Separation and Purification Technology 194 (2018) 281–300

Contents lists available at ScienceDirect

Separation and Purification Technology

journal homepage: www.elsevier.com/locate/seppur

Review

# Methodologies for screening and selection of crystalline microporous materials in mixture separations

Rajamani Krishna

*Van 't Hoff Institute for Molecular Sciences, University of Amsterdam, Science Park 904, 1098 XH Amsterdam, The Netherlands*

ARTICLE INFO

*Keywords:*
Screening metrics
Adsorption selectivity
Uptake capacity
Diffusion selectivity
Membranes
PSA units

ABSTRACT

Ordered crystalline microporous materials such as zeolites, metal-organic frameworks (MOFs), and zeolitic imidazolate frameworks (ZIFs) offer considerable potential for separating a wide variety of mixtures. There are basically two different separation technologies that can be employed: (1) pressure swing adsorption (PSA) unit with a fixed bed of adsorbent particles, and (2) membrane device, wherein the mixture is allowed to permeate through thin micro-porous crystalline layers. The fundamental physico-chemical principles underlying the separations in these two devices are fundamentally different. In fixed bed adsorbers, diffusional effects are usually undesirable because these tend to produce distended breakthroughs and diminished productivities. For membrane separations, both intra-crystalline diffusion and mixture adsorption equilibrium determine permeation selectivities, and diffusion selectivities are often the primary drivers for separations.

Using Configurational-Bias Monte Carlo (CBMC) simulations of mixture adsorption equilibrium, and Molecular Dynamics (MD) simulations of guest diffusivities in a wide number of guest/host combinations, we demonstrate that adsorption and diffusion do not, in general, proceed hand-in-hand. Strong adsorption often implies lowered mobility. Consequently, the best material for use in fixed bed adsorbers does not always coincide with the ideal choice for use as thin layers in membrane devices. Methodologies for screening microporous materials for use in fixed-bed units and membrane devices are discussed using a large number of examples of industrially important separations.

## 1. Introduction

Ordered crystalline microporous materials such as zeolites (crystalline aluminosilicates), metal-organic frameworks (MOFs), and zeolitic imidazolate frameworks (ZIFs) offer potential for separation of a wide variety of mixtures: $CO_2/CH_4$, $CO_2/N_2$, $CO_2/H_2$, $CH_4/H_2$, $CH_4/N_2$, $CO_2/CO/CH_4/H_2$, $CO_2/C_2H_2$, $O_2/N_2$, Xe/Kr, fluorocarbons, alkane/alkenes, alkyne/alkene, butane isomers, alkane isomers, xylene isomers, benzene/cyclohexane, and ethylbenzene/styrene [1–35]. Particularly potent in many separations are MOFs with exposed $M^{2+}$ cation sites such as $M_2$(dobdc) [M = Mg, Mn, Co, Ni, Zn, Fe; dobdc$^{4-}$ = 2,5- dioxido-1,4-benzenedicarboxylate]; these MOFs are also referred to as M-MOF-74 and CPO-27-M (see framework in Fig. 1). M-MOF-74 has one-dimensional (1D) hexagonal-shaped channels of approximately 11 Å. Another important MOF with exposed cation sites is $M_3(BTC)_2$ [M = Cu, Cr, Mo; BTC$^{3-}$ = 1,3,5-benzenetricarboxylate]; $Cu_3(BTC)_2$ is also known as HKUST-1. In ZIFs, the Zn or Co atoms are linked through N atoms of ditopic imidazolates to form a range of neutral framework structures. The frameworks of ZIF compounds can be represented by M $(Im)_2$ [M = tetrahedrally coordinated metal atom; Im = imidazolate and its derivative], similar to that of $(AlO_2)_x(SiO_2)_y$ zeolites. The M-Im-M angle of 145° is close to the Si—O—Si angle typically found in zeolites. ZIF-8, for example, has the structural topology of SOD (sodalite), and consists of cages separated by narrow windows of 3.3 Å size.

In comparison to traditionally used porous materials such as zeolites, MOFs offer significantly higher surface areas and porosities. The structural details and pore landscapes of all the zeolites and MOFs considered in this MOF are provided in the Supplementary material accompanying this publication. As illustration, Fig. 2 presents data for surface areas, pore volumes, framework densities, and characteristic pore dimensions of some representative adsorbents. The commonly known MFI zeolite, for example, has a channel dimension of 5.5 Å, pore volume of 0.165 $cm^3\,g^{-1}$, and surface area of 490 $m^2\,g^{-1}$. Significantly higher surface areas are available with MOFs; for example MOF-177 has a surface area of 4800 $m^2\,g^{-1}$. The accessible pore volumes of MOFs are commonly in the 0.5–2 $cm^3\,g^{-1}$ range. For any given separation application, there is a need to identify the microporous material with the ideal pore size, and surface area that offers the right degree of interactions (van der Waals, electrostatic, π-electron exchange) with the guest molecules.

*E-mail address:* r.krishna@contact.uva.nl.

https://doi.org/10.1016/j.seppur.2017.11.056
Received 21 October 2017; Received in revised form 20 November 2017; Accepted 20 November 2017
Available online 22 November 2017

**Nomenclature**

| | |
|---|---|
| $D_{i,self}$ | self-diffusivity of species *i*, $m^2\ s^{-1}$ |
| $Đ_i$ | Maxwell-Stefan diffusivity, $m^2\ s^{-1}$ |
| $Đ_i(0)$ | zero-loading M-S diffusivity, $m^2\ s^{-1}$ |
| $f_i$ | partial fugacity of species *i*, Pa |
| $N_i$ | molar flux of species *i*, mol $m^{-2}\ s^{-1}$ |
| $p_i$ | partial pressure of species *i*, Pa |
| $p_t$ | total system pressure, Pa |
| $q_A$ | gravimetric uptake of species A, mol $kg^{-1}$ |
| $Q_A$ | volumetric uptake of species A, mol $m^{-3}$ |
| $\Delta Q$ | separation potential, mol $m^{-3}$ |
| $Q_{st}$ | isosteric heat of adsorption, J $mol^{-1}$ |
| $S_{ads}$ | adsorption selectivity, dimensionless |
| $S_{diff}$ | diffusion selectivity, dimensionless |
| $S_{perm}$ | permeation selectivity, dimensionless |
| $t$ | time, s |
| $T$ | temperature, K |
| $y_A$ | fluid phase mole fraction of species A, dimensionless |

*Greek letters*

| | |
|---|---|
| $\delta$ | thickness of membrane, m |
| $\Pi_i$ | membrane permeability of species *i*, mol $m^{-1}\ s^{-1}\ Pa^{-1}$ |
| $\rho$ | framework density, kg $m^{-3}$ |

*Subscripts*

| | |
|---|---|
| A | referring to component A |
| B | referring to component B |
| i | referring to component *i* |
| t | referring to total mixture |

In practice, separations using zeolites, MOFs and ZIFs are conducted in either pressure swing adsorption (PSA) units consisting of fixed beds packed with adsorbent, or membrane permeation devices that consist of thin microporous crystalline layers, typically a few micrometers in thickness. PSA units are operated in a cyclical manner, with adsorption and desorption cycles [13,14,36–39]. Most commonly, the separation performance in a fixed-bed adsorber is dictated by mixture adsorption equilibrium. The separation effectiveness of fixed-bed devices is dictated by a combination of adsorption selectivity and uptake capacities. For separation of a binary mixture of components A and B, the adsorption selectivity is defined by

$$S_{ads} = \frac{q_A/q_B}{y_A/y_B} \tag{1}$$

where the $q_A$, and $q_B$ represent the molar loadings within the zeolite or MOF that is in equilibrium with a bulk fluid mixture with mole fractions

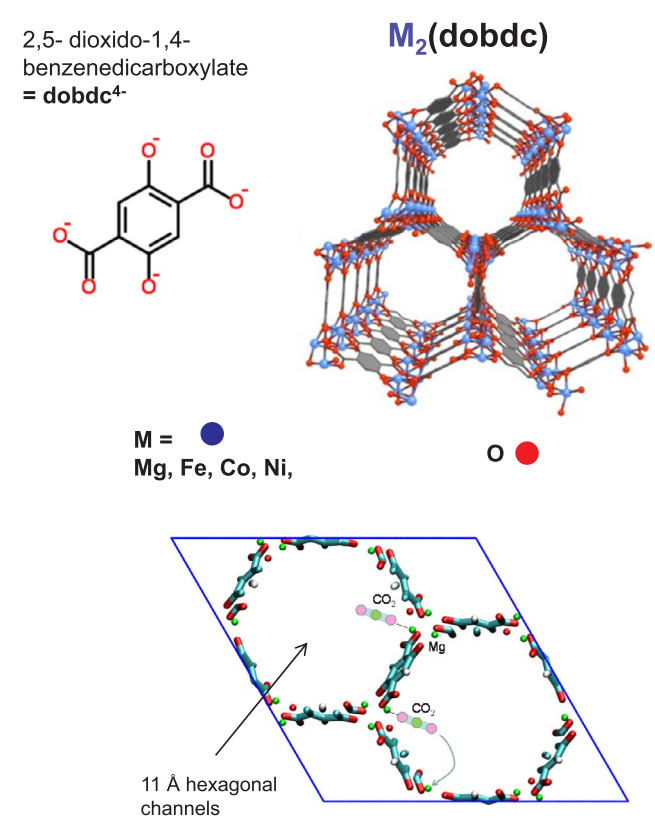


**Fig. 1.** M-MOF-74 has 1D hexagonal-shaped channels of 11 Å size.

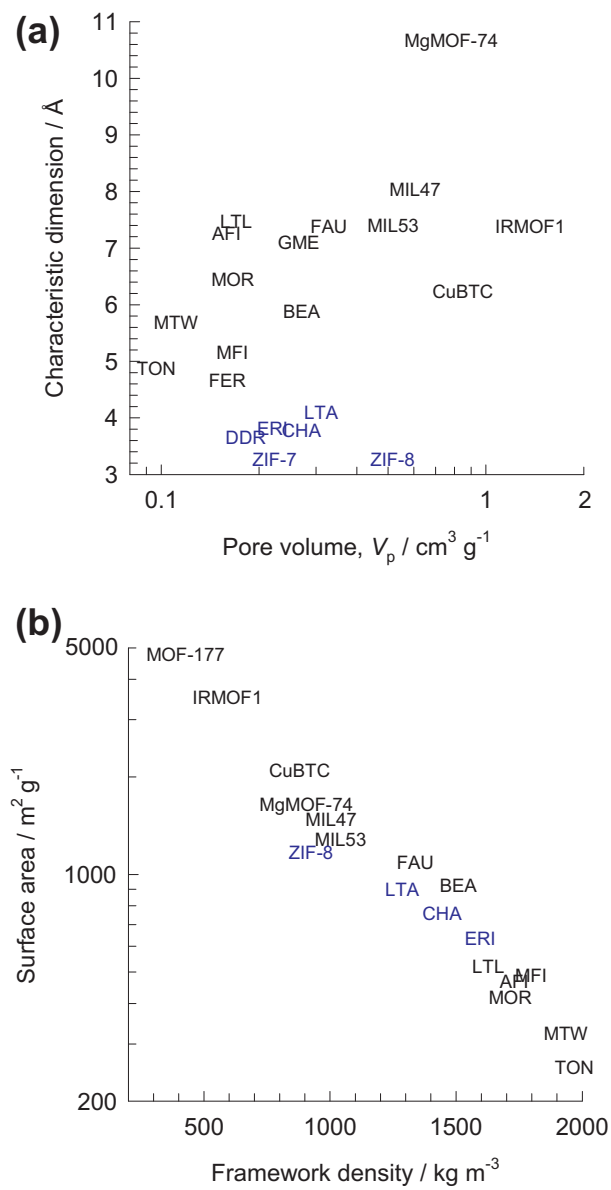


**Fig. 2.** Comparison of surface area, pore volumes, framework densities, and characteristic dimensions of some representative zeolites, MOFs and ZIFs.

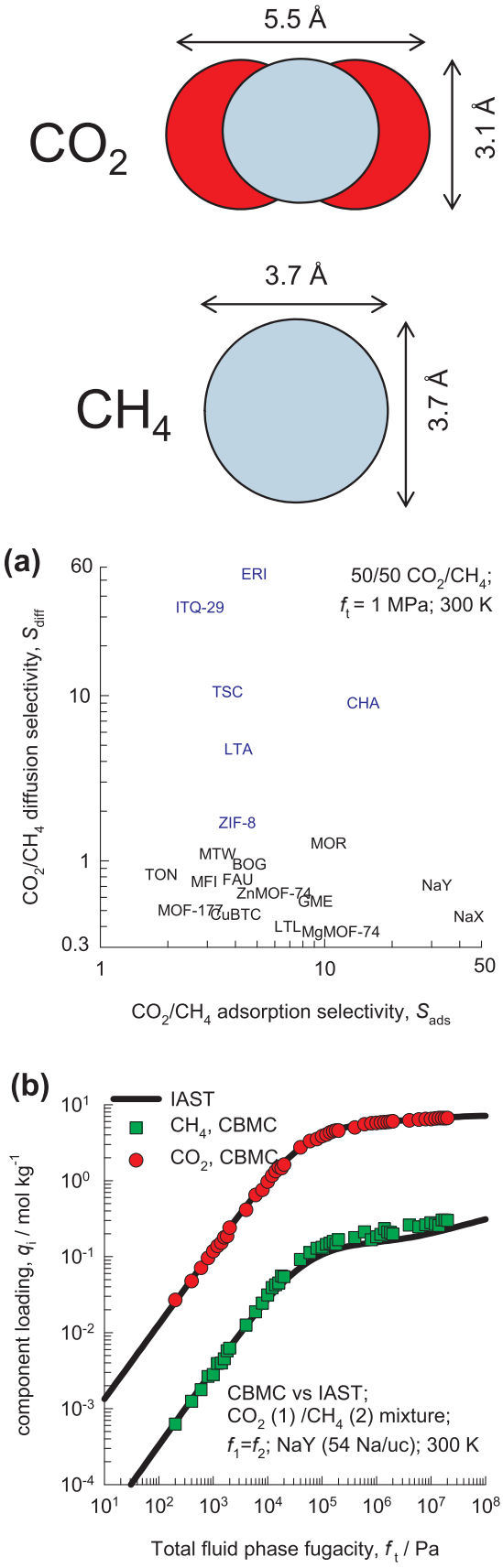


**Fig. 3.** (a) Comparison of diffusion selectivities, $S_{diff}$ (obtained from MD simulations for binary mixtures), and adsorption selectivities, $S_{ads}$ (obtained from CBMC simulations for binary mixtures), for 50/50 $CO_2/CH_4$ mixtures. The conditions correspond to bulk fluid phase fugacity $f_t = f_1 + f_2 = 1$ MPa and 300 K. The data on $S_{diff}$ and $S_{ads}$ are collected from earlier published material [15,16,41,44,45]. The symbols marked blue are cage-type structures with narrow windows. (b) Comparison of CBMC data with IAST estimations of the component loadings for adsorption of 50/50 $CO_2/CH_4$ mixtures in NaY zeolite at 300 K.

$y_A$, and $y_B = 1 - y_A$. The molar loadings, also called *gravimetric uptake capacities*, are usually expressed with the units mol kg$^{-1}$. The *volumetric uptake capacities* are

$$Q_A = \rho q_A; \quad Q_B = \rho q_B \tag{2}$$

where ρ is the crystal framework density of the zeolite or MOF, expressed say in units of kg m$^{-3}$, or kg L$^{-1}$. The selectivity $S_{ads}$ may be calculated on the basis of experimental data on unary isotherms, along with the Ideal Adsorbed Solution Theory (IAST) of Myers and Prausnitz [40] for mixture adsorption equilibrium.

High uptake capacities are desirable because these result in longer breakthrough times, and reduced frequency of bed regeneration. Higher values of $S_{ads}$ are desired because they lead to sharper breakthrough fronts and larger differences between the breakthrough times of individual constituents. If high product purities are desired, then this also demands $S_{ads} >> 1$. Most commonly, however, high uptake capacities do not go hand-in-hand with high selectivities [13,14].

For membrane separations, both adsorption equilibrium, and intracrystalline diffusion determine membrane permeation selectivities

$$S_{perm} = \frac{N_A/N_B}{f_A/f_B} \tag{3}$$

In Eq. (3), $N_A$ and $N_B$ are the permeation fluxes; $f_A$ and $f_B$ are the partial fugacities in the upstream compartment. The permeation selectivity can be expressed as

$$S_{perm} = S_{ads} \times S_{diff} \tag{4}$$

where $S_{diff}$ is the diffusion selectivity that can be taken, as a good approximation, equal to the ratio of the self-diffusivities $D_{i,self}$ in the mixture [15,41]

$$S_{diff} = \frac{D_{A,self}}{D_{B,self}} \tag{5}$$

To set the scene, and define the objectives of this review article, let us consider the separation of $CO_2$ from $CH_4$ that is relevant to the purification of natural gas, which can contain up to 92% $CO_2$ impurity at its source [42]. Removal of $CO_2$, which is most commonly accomplished using amines, is conducted at pressures ranging between 2 MPa and 7 MPa [43]. The separation requirements for production of liquefied natural gas (LNG) are rather stringent, often requiring the achievement of impurity levels of less than 500 ppm $CO_2$. Fig. 3a provides a comparison of $CO_2/CH_4$ adsorption selectivities $S_{ads}$ and $CO_2/CH_4$ diffusion selectivities $S_{diff}$ for 50/50 $CO_2/CH_4$ mixtures for selected zeolites and MOFs at a total fugacity $f_t = 1$ MPa, and temperature $T = 300$ K. The data on $S_{ads}$ are determined from Configurational-Bias Monte Carlo (CBMC) simulations of mixture adsorption equilibrium [15,16,41,44,45]. For the guest molecules $CO_2$ and $CH_4$, the CBMC simulation methodology is equivalent to Grand Canonical Monte Carlo (GCMC) simulations. The binding of $CO_2$ molecules to open metal sites is often influenced by orbital interactions and polarization effects; such effects are particularly strong in the low pressure region; the influence of polarization is of lesser importance at higher pressures. Polarization effects are not adequately catered for in GCMC simulations, and this often leads to deviations of GCMC simulations from experimental data on unary isotherms [16,46]. The data on $S_{diff}$ are determined by Molecular Dynamics (MD) simulations of the self-diffusivities in the mixture and use of Eq. (5).

For most adsorbents, the CBMC simulations of component loadings in the mixture are in good agreement with the IAST estimations, based on CBMC simulations of unary isotherms. As illustration, Fig. 3b compares CBMC data with IAST estimations for NaY zeolite; the agreement between the CBMC data and IAST estimates is very good. There are, however, instances of some quantitative failures of the IAST for cases of segregated adsorption caused by preferential location of $CO_2$ molecules at window regions of cage-type zeolites [47,48].

There appear to be two fundamentally different categories of behaviors in Fig. 3a. The adsorption and diffusion selectivities of CHA, DDR, ERI, ITQ-29, ZIF-8, and TSC (indicated in blue) serve to complement each other; we obtain $S_{ads} > 1$ and $S_{diff} > 1$. These materials have cage-type topologies in which adjacent cages are separated by narrow windows in the 3.3 Å–4.3 Å size range; see Supplementary material for pore landscapes of CHA, DDR, TSC, ERI, ITQ-29, and ZIF-8. In all such structures, $CO_2$ jumps length-wise across the narrow windows as evidenced in video animations [49,50]. Since the cross-sectional dimension of $CO_2$ is smaller than that of $CH_4$, this accounts for the significantly higher diffusion selectivities in favor of $CO_2$.

In the second category of materials (indicated by black symbols in Fig. 3a) there is lack of synergy between adsorption and diffusion, i.e. we find $S_{ads} > 1$ but $S_{diff} < 1$, i.e. the diffusion selectivity favors the more poorly adsorbing $CH_4$; these materials fall into four sub-classes of materials, in all of which the channel dimensions are larger than about 5 Å.

- One-dimensional (1D) channels (e.g. TON, LTL, MTW, MgMOF-74, MIL-53)
- 1D channels with side pockets (e.g. FER, MOR)
- Intersecting channels (e.g. MFI, BEA, ISV, Zn(bdc)dabco)
- "Open" structures with large cavities (e.g. NaY, NaX, IRMOF-1, CuBTC, MOF-177)

The question arises: In these four topologies, why is the diffusion selectivity in favor of $CH_4$ that has the *larger* kinetic diameter?Another interesting observation is that the hierarchy of $CO_2/CH_4$ diffusion selectivities $S_{diff}$: FAU (=all-silica Faujasite) > NaY > NaX. These three materials have the same pore size and topology; the structure has cavities that are about 11 Å in size. Adjacent cavities are separated by 10-ring windows of 7.3 Å size; the window aperture does not offer significant free-energy barriers for inter-cage hopping. The only differences reside in the Si/Al ratio, and the number of extra-framework $Na^+$ cations; for each unit cell (uc) of these materials, we have FAU (192 Si, 0 Al, 0 $Na^+$, Si/Al = ∞); NaY (138 Si, 54 Al, 54 $Na^+$, Si/Al = 2.56); NaX (106 Si, 86 Al, 86 $Na^+$, Si/Al = 1.23). Clearly, the diffusion characteristics are determined by factors other than pore size and guest confinement. Particularly noteworthy is the fact that NaX zeolite, commonly known by its trade name 13X, has the highest adsorption selectivity, but the lowest diffusion selectivity. What is the rationalization for this strong dependence of the diffusion selectivity on the Si/Al ratio, in *disfavor* of $CO_2$?

What screening criteria should we use to select the best material for use in fixed bed adsorbers? How do we conduct the analogous screening and selection of materials for use as thin layers in membrane permeation units?

The primary objective of this article is to address the set of four questions posed above, and obtain answers that will help in the choice of the ideal material for a given separation task. For illustration of the suggested methodology for screening, we undertake detailed analyses of a wide number of different separations that are of importance in the process industries.

## 2. $CO_2/CH_4$ mixture separations

Fig. 4a, b present MD simulation data on the loading dependence of the self-diffusivities of $CO_2$, and $CH_4$ in FAU, NaY, and NaX. The self-

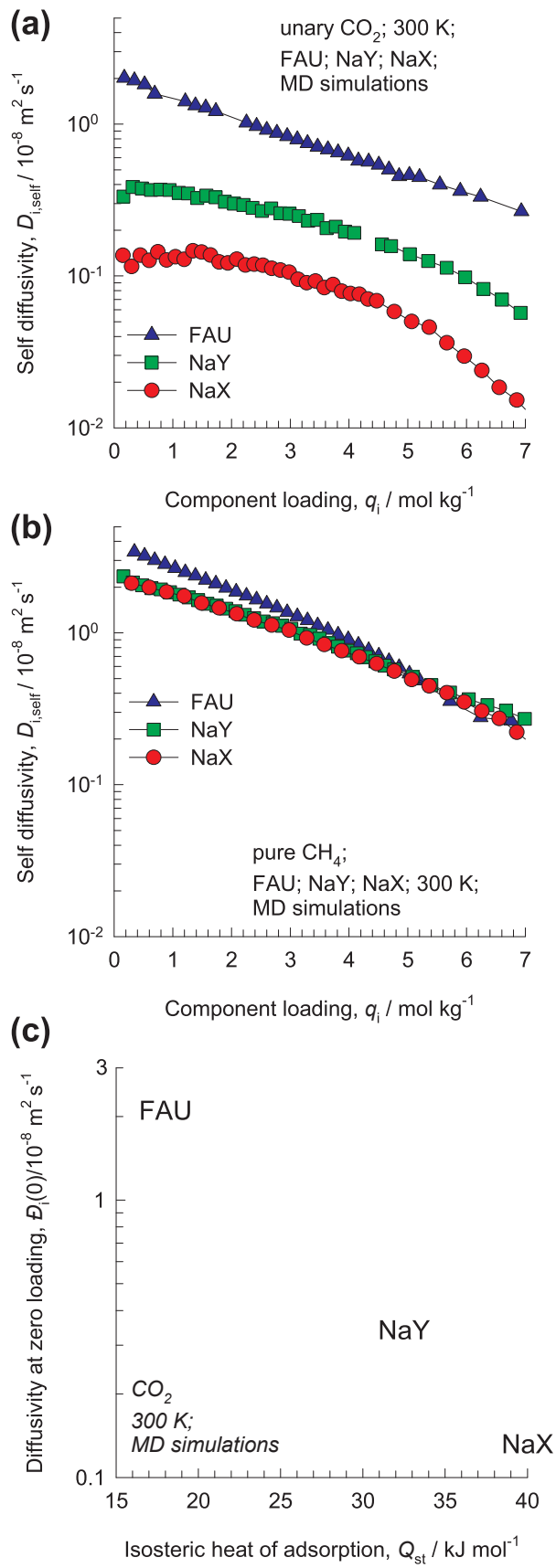


**Fig. 4.** (a, b) Loading dependence of the self-diffusivities of (a) $CO_2$, and (b) $CH_4$ in FAU-Si, NaY, and NaX. (c) Zero-loading diffusivities $Đ_i(0)$ of $CO_2$ in FAU-Si (all silica), NaY (54 $Na^+$/u.c.), and NaX (86 $Na^+$/u.c.) zeolites, plotted with the corresponding values of $Q_{st}$. These data are based on CBMC and MD simulations, reported in earlier works [41,45,122].

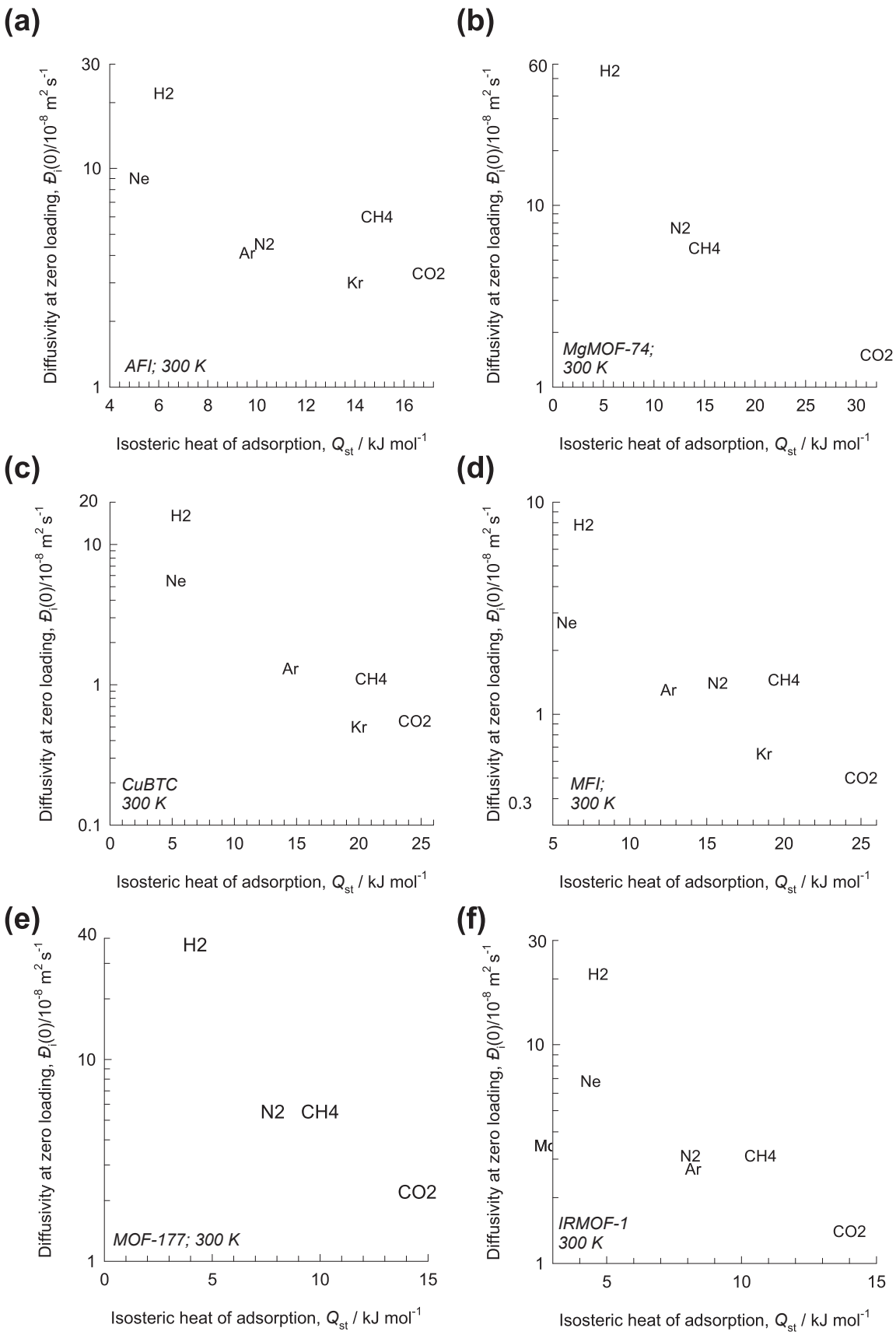


**Fig. 5.** Zero-loading diffusivities $Đ_i(0)$ of light gases in (a) AFI, (b) MgMOF-74, (c) MFI, (d) CuBTC, (e) MOF-177, and (f) IRMOF-1, plotted as a function of the corresponding values of the isosteric heats of adsorption, $Q_{st}$. These data are based on CBMC and MD simulations, reported in earlier works [41,45,122].

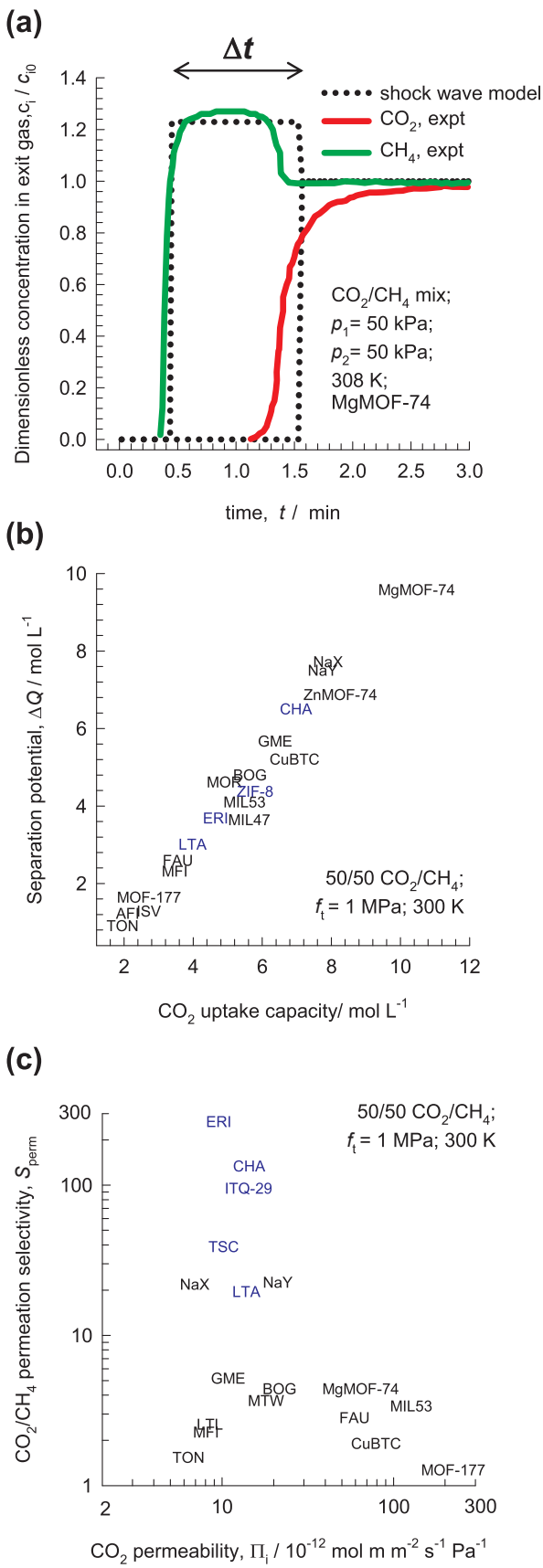


**Fig. 6.** (a) Experimental data of Remy et al. [52] for transient breakthrough of equimolar $CO_2/CH_4$ mixtures through fixed bed adsorber packed with MgMOF-74 operating at 308 K. The dotted lines represent the shock-wave model for breakthroughs. (b) Plot of the separation potential, $\Delta Q$, calculated using the formula $\Delta Q$ versus the volumetric $CO_2$ uptake capacity for 50/50 $CO_2/CH_4$ mixture separations in different zeolites, and MOFs. (c) Robeson plot for separation of $CO_2/CH_4$ mixtures; the permeation selectivities, $S_{perm}$, for different microporous materials are plotted against the $CO_2$ permeability.

diffusivity of $CO_2$ strongly decreases as the number of extra-framework cations increases, whereas the self-diffusivity of $CH_4$ is practically the same in the three materials. Due to strong electrostatic interactions, the binding strength of $CO_2$ increases with increasing number of $Na^+$ cations. The isosteric heats of adsorption, $Q_{st}$, is an appropriate measure of the binding strength and can be determined from CBMC simulations using fluctuation formula as described in earlier works [41,45]. In Fig. 4c, the zero-loading diffusivities $Đ_i(0)$ of $CO_2$ in FAU, NaY (54 $Na^+$/uc), and NaX (86 $Na^+$/uc) zeolites are plotted against the corresponding values of the $Q_{st}$, extrapolated to zero-loadings; the stronger the binding, the lower the diffusivity. The data in Fig. 4 rationalizes the hierarchy of $CO_2/CH_4$ diffusion selectivities $S_{diff}$: FAU > NaY > NaX.

Plots of zero-loading diffusivities $Đ_i(0)$ of light gases ($H_2$, $N_2$, $CH_4$, $CO_2$, He, Ne, Kr) versus the corresponding values of the isosteric heats of adsorption $Q_{st}$ are shown in Fig. 5 for AFI, MgMOF-74, MFI, CuBTC, MOF-177, and IRMOF-1. The values of $Q_{st}$ were determined from CBMC simulations In each of these materials, the strongest binding is with $CO_2$; this explains why the $CO_2/CH_4$ diffusion selectivities are lower than unity in all these six materials (cf. Fig. 3a). Of these six materials examined in Fig. 5, we also note that the $Q_{st}$ value for $CO_2$ in MgMOF-74 is the highest, indicating strong $CO_2$ binding. Neutron diffraction data [51] establish that $CO_2$ molecules attach strongly via O atoms to the unsaturated $Mg^{2+}$ atoms of MgMOF-74 (see Fig. 1); this strong binding accounts for the high adsorption selectivity (≈12) in favor of $CO_2$ (cf. Fig. 3a).For effective use of the three materials with the highest values of $S_{ads}$, i.e. NaX, NaY, and MgMOF-74, in PSA units, the crystal size must be chosen to be small enough to minimize the negative influence of intra-crystalline diffusional resistances. Adsorbent materials suitable for use in fixed bed adsorbers are usually those with characteristic pore dimensions larger than about 6 Å; the Supplementary material contains information on pore sizes of all of the host structures discussed in this article. The experimental data of Remy et al. [52] for transient breakthroughs of $CO_2/CH_4$ mixtures through a fixed bed adsorber packed with MgMOF-74 are shown in Fig. 6a. There is a slight distention in the breakthrough characteristics; this distention is undesirable because it leads to diminished productivities of purified $CH_4$ that is recovered during the time interval $\Delta t$. The maximum achievable productivity of pure $CH_4$ is realized when both intra-crystalline diffusion and axial dispersion effects are completely absent and the concentrations "fronts" of the fluid mixture traverse the fixed bed in the form of shock waves [14,53]. The shock-wave model solution is indicated by the dotted lines in Fig. 6a. For a binary mixture with mole fractions $y_A$, and $y_B = 1-y_A$, in the feed mixture, the maximum achievable productivity, $\Delta Q$, can be calculated using the shock-wave model; the result is [14]

$$\Delta Q = Q_A \frac{y_B}{1-y_B} - Q_B \tag{6}$$

The physical significance of $\Delta Q$, conveniently expressed in the units of mol per L of adsorbent, is that it represents the *maximum* amount of pure component B (less strongly adsorbed component) that can be recovered during the *adsorption* phase of fixed bed separations. The quantity $\Delta Q$ is an appropriate combination of selectivity and uptake capacity that is reflective of the *separation potential* of separations in fixed beds packed with a specific adsorbent [14]. The quantity $\Delta Q$ is distinctly different from the *working capacity*, whose evaluation requires us to additionally specify the regeneration strategy. Using the CBMC data on mixture adsorption equilibrium (cf. Fig. 3), Fig. 6b plots the

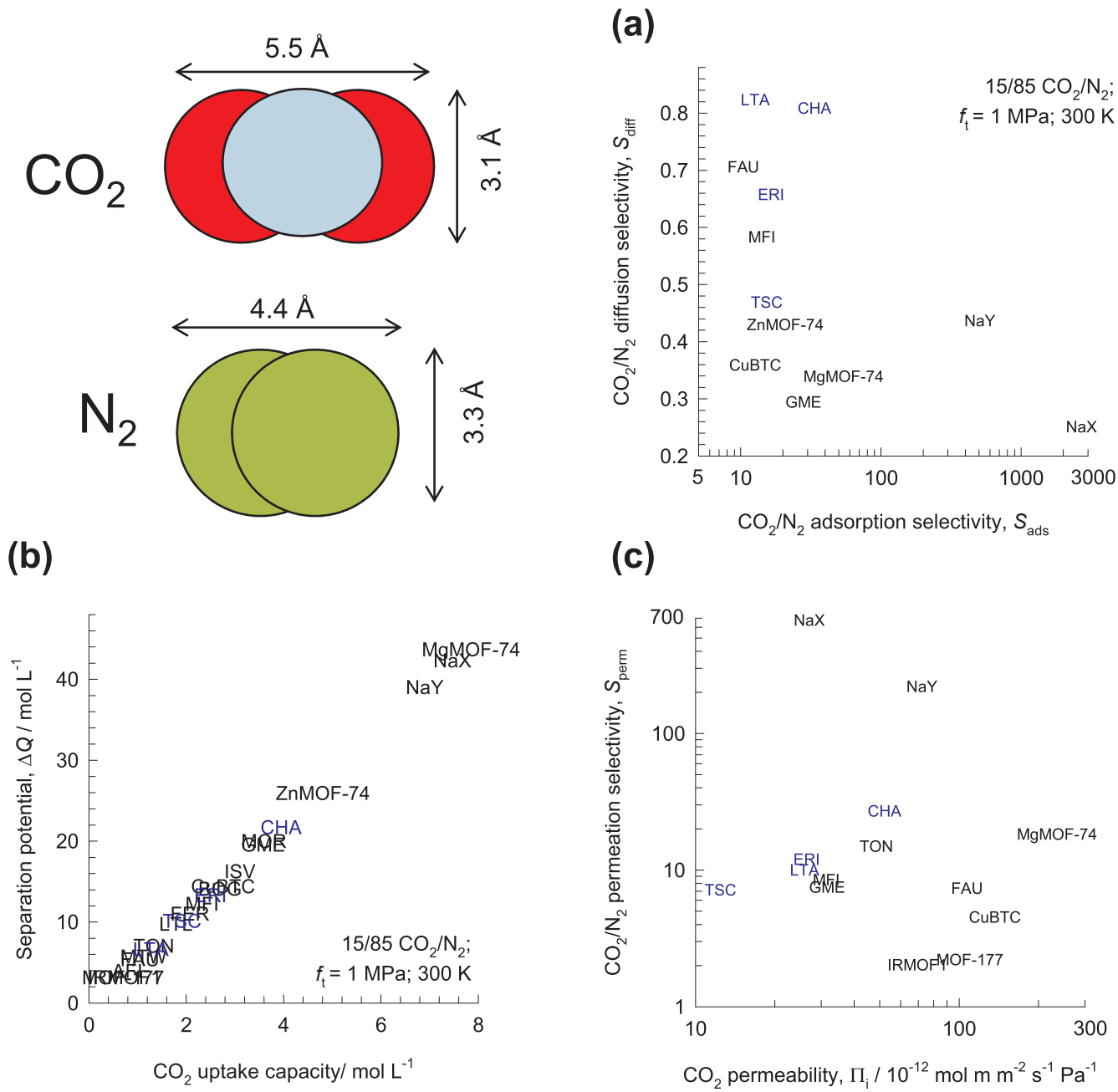


**Fig. 7.** (a) Comparison of diffusion selectivities, $S_{diff}$, and adsorption selectivities, $S_{ads}$ for 15/85 $CO_2/N_2$ mixtures. The conditions correspond to $f_t$ = 1 MPa and 300 K. (b) Plot of the separation potential, $\Delta Q$, versus the volumetric $CO_2$ uptake capacity for 15/85 $CO_2/N_2$ mixture separations in different zeolites, and MOFs. (c) Robeson plot for separation of $CO_2/N_2$ mixtures; the permeation selectivities, $S_{perm}$, for different microporous materials are plotted against the $CO_2$ permeability. The plotted data are culled from earlier published works [15,16,41,44,45].

separation potential, $\Delta Q$, versus the volumetric $CO_2$ uptake capacity for different materials. Based on this screening methodology, the three best materials to use in PSA units are MgMOF-74, NaX, and NaY. Other factors such as framework stability, resistance to moisture in the feed, material and regeneration costs, need to be taken into consideration in the final choice of adsorbent; discussions on these factors are beyond the scope of this article.

For use of the materials in membrane constructs, the screening needs to be done differently because the membrane performance is strongly influenced, often dominated, by diffusional influences. In the literature the performance of membranes is judged on the basis of the Robeson plot [54] of the permeation selectivity $S_{perm} = S_{ads} \times S_{diff}$ versus the $CO_2$ permeability of the membrane, $\Pi_i$, defined by

$$\Pi_i = \frac{N_i}{\Delta f_i / \delta} \tag{7}$$

where $\delta$ is the thickness of the crystalline layer on the membrane; $\Delta f_i = f_{i0} - f_{i\delta}$ is the difference in the partial fugacities in the bulk fluid mixtures in the upstream ($z = 0$) and downstream ($z = \delta$) compartments. If the downstream conditions are such that the loadings are negligibly small, the $CO_2$ permeability can be determined from MD simulations by using the following expression [15]

$$\Pi_i = \frac{\rho D_{i,self}\, q_i}{f_i} \tag{8}$$

Fig. 6c presents the Robeson plot for $CO_2/CH_4$ mixture separation in the various microporous structures, for an upstream membrane fugacity

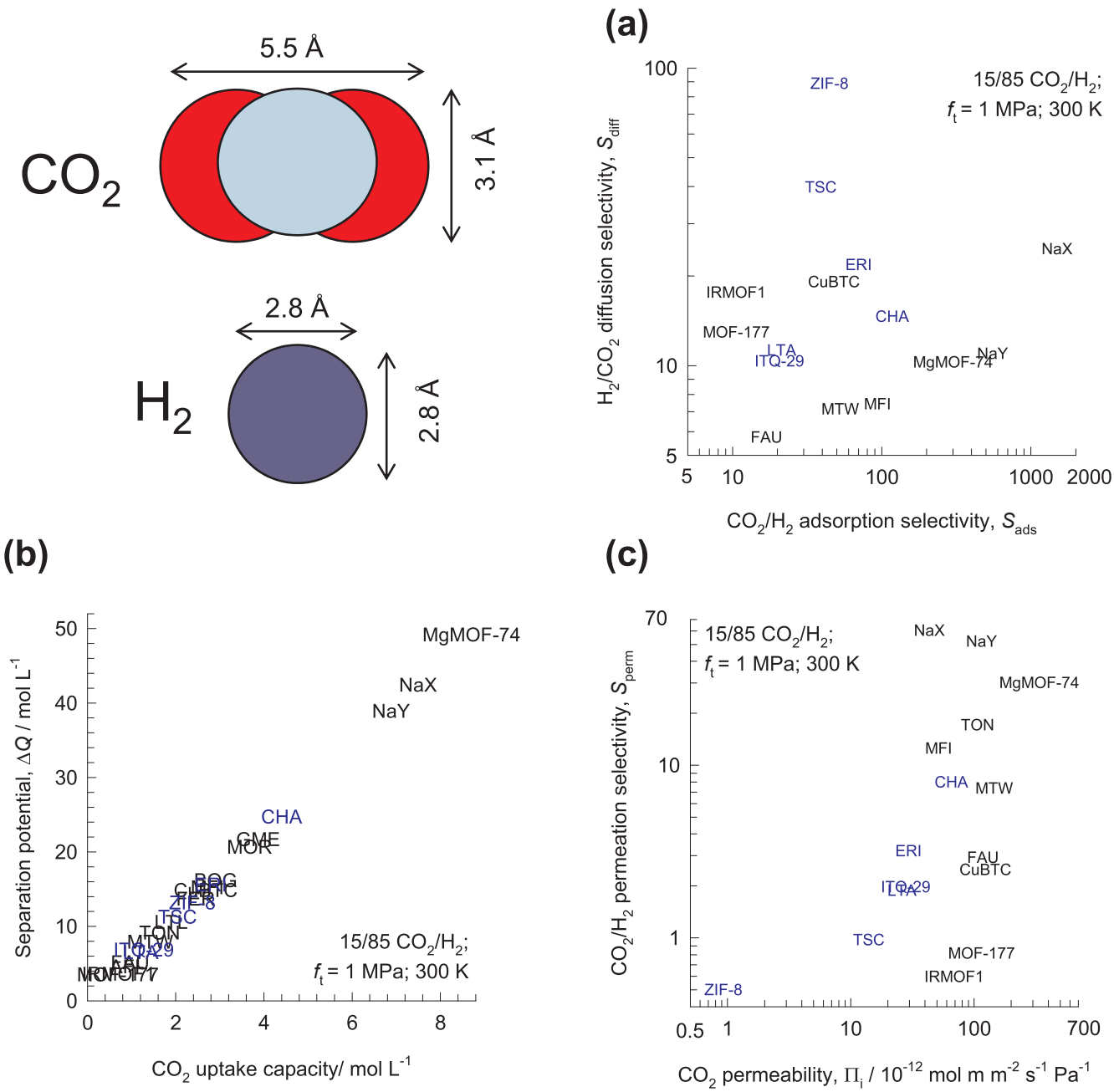


**Fig. 8.** (a) Comparison of $H_2/CO_2$ diffusion selectivities, $S_{diff}$, and $CO_2/H_2$ adsorption selectivities, $S_{ads}$ for 15/85 $CO_2/H_2$ mixtures. The conditions correspond to $f_t$ = 1 MPa and 300 K. (b) Plot of the separation potential, $\Delta Q$, versus the volumetric $CO_2$ uptake capacity for $CO_2/H_2$ mixture separations in different zeolites, and MOFs. (c) Robeson plot for separation of $CO_2/H_2$ mixtures; the $CO_2/H_2$ permeation selectivities, $S_{perm}$, for different microporous materials are plotted against the $CO_2$ permeability. The plotted data are culled from earlier published works [15,16,41,44,45].

$f_t = f_A + f_B$ = 1 MPa, typical of natural gas sweetening applications. The highest permeation selectivities for $CO_2/CH_4$ separation with $S_{perm}$ > 100 are obtained with zeolites with 8-ring windows such as DDR, CHA, and ERI; in these cases $S_{ads}$, and $S_{diff}$ complement each other. For DDR and CHA, there is experimental evidence that such high permeation selectivities can be realized in practice [47,55–61]. For MFI, the $S_{perm}$ value of 2.3 is in agreement with experiment [58]. Open, large pore, structures such as MOF-177, CuBTC have high $\Pi_i$ but low $S_{perm}$. On the other hand, ERI, DDR, and CHA have significantly higher $S_{perm}$ values but with lower $\Pi_i$. High values of $S_{perm}$ rarely go hand in hand with high $\Pi_i$. For technological applications, a compromise has to be made. The compromise structure could perhaps be NaY with reasonably high permeability and permeation selectivity. There is considerable scope for development of novel materials that would lead to a performance at the top right corner of the Robeson plot, using mixed-matrix membranes that attempts to profit from both adsorption and diffusion characteristics of the constituent materials.

## 3. $CO_2/N_2$ mixture separations

The capture of $CO_2$ from flue gases emanating from power plants involves separation of 15/85 $CO_2/N_2$ mixtures [6,18]. Due to its lower polarizability and quadrupole moment, the adsorption strength of $N_2$ is lower than that of $CO_2$ in all materials; therefore, the adsorption selectivity $S_{ads}$ > 10 in all adsorbents. The smaller molecular dimensions of $N_2$, coupled with its poor adsorption strength, ensures that the $CO_2$ diffusivity is lower than that of $N_2$ in all materials. Fig. 7a presents a comparison of diffusion selectivities, $S_{diff}$, and adsorption selectivities,

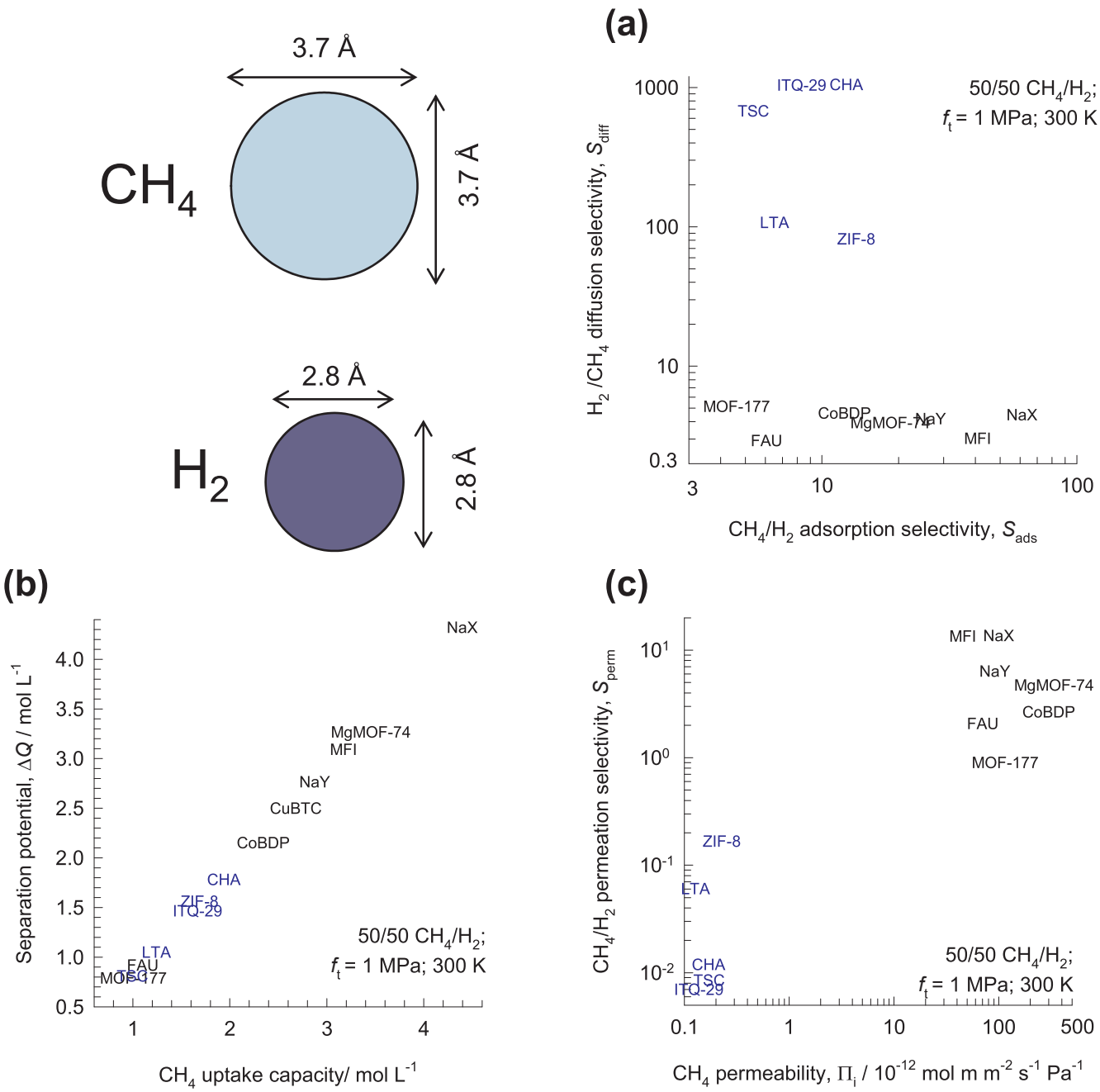


**Fig. 9.** (a) Comparison of $H_2/CH_4$ diffusion selectivities, $S_{diff}$, and $CH_4/H_2$ adsorption selectivities, $S_{ads}$ for 50/50 $CH_4/H_2$ mixtures. The conditions correspond to $f_t$ = 1 MPa and 300 K. (b) Plot of the separation potential $\Delta Q$ versus the volumetric $CH_4$ uptake capacity for 50/50 $CH_4/H_2$ mixture separations in different zeolites, and MOFs. (c) Robeson plot for separation of $CH_4/H_2$ mixtures; the $CH_4/H_2$ permeation selectivities, $S_{perm}$, for different microporous materials are plotted against the $CH_4$ permeability. The plotted data are culled from earlier published works [15,16,41,44,45].

$S_{ads}$ for 15/85 $CO_2/N_2$ mixtures. The highest adsorption selectivities are realized with NaX zeolite. As with $CO_2/CH_4$ mixtures, the hierarchy FAU > NaY > NaX holds for $CO_2/N_2$ diffusion selectivities for the same reasons as elucidated in the foregoing section.For use in fixed bed units, screening on the basis of the plot of $\Delta Q$ versus volumetric $CO_2$ uptake capacity leads to the hierarchy MgMOF-74 > NaX > NaY; see Fig. 7b. The superior performance of MgMOF-74 is primarily due to its higher $CO_2$ uptake capacity. However, Pirngruber et al. [62] argue that the material with the strongest affinity for $CO_2$ is not necessarily the best adsorbent because of the difficulty of regeneration.

For selection of materials for use in membrane devices, the Robeson plot is presented in Fig. 7c. The $S_{perm}$ estimate for MFI of 8.2 is in reasonable agreement with the experiments of Bernal et al. [63]. The best combination of $S_{perm}$ and $\Pi_i$. values are obtained with NaX, NaY, and MgMOF-74. There is experimental evidence that the predicted permeation selectivities for NaY can indeed be realized in practice [64–67].

## 4. $CO_2/H_2$ mixture separations

The separation of $CO_2/H_2$ mixtures is important in the context of $H_2$ purification and $H_2$ production processes that are commonly operated at high pressures [42,68,69]. Due its smaller molecular dimensions, and lower adsorption strength the diffusion selectivity favors $H_2$ whereas the adsorption selectivity favors $CO_2$; see Fig. 8a. The highest $H_2/CO_2$ diffusion selectivity is with ZIF-8, whereas the highest $CO_2/H_2$

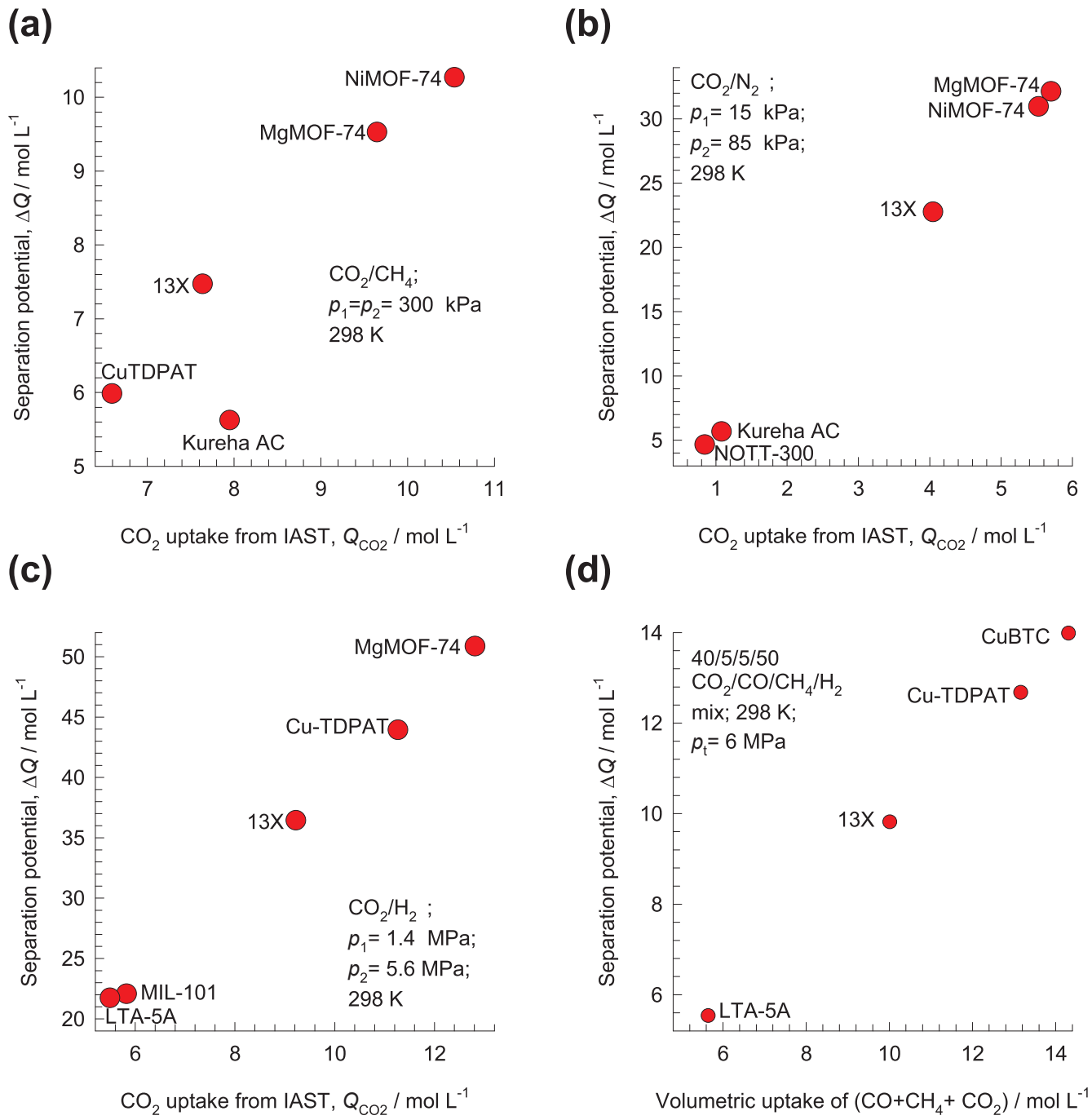


**Fig. 10.** Plot of the separation potential $\Delta Q$ versus the volumetric uptake capacity for (a) 50/50 $CO_2(1)/CH_4(2)$ mixture separations at $p_t$ = 600 kPa, (b) 15/85 $CO_2/N_2$ mixture separations at $p_t$ = 100 kPa, (c) 20/80 $CO_2/H_2$ mixture separations at $p_t$ = 7 MPa, and (d) 40/5/5/50 $CO_2/CO/CH_4/H_2$ mixture separations at $p_t$ = 6 MPa. The IAST calculations are based on the pure experimental component isotherm data for the various zeolites and MOFs, as compiled in our previous work [14].

adsorption selectivity is exhibited by NaX zeolite.For $CO_2/H_2$ separations in fixed bed units for production of pure $H_2$, screening on the basis of the plot of $\Delta Q$ versus volumetric $CO_2$ uptake capacity leads to the hierarchy MgMOF-74 > NaX > NaY; see Fig. 8b; this hierarchy is precisely the same as for $CO_2/CH_4$ and $CO_2/N_2$ mixtures.

For screening materials for use in membrane devices, the Robeson plot is presented in Fig. 8c. The best materials for $CO_2$-selective membrane operations are NaX, NaY, and MgMOF-74 that lie in the top right corner. For $H_2$-selective membrane operations, ZIF-8 is the suitable choice. There is recent experimental evidence in the literature to show that $H_2$-selective separation is possible with ZIF-7 and ZIF-8 membranes [70,71]. The $H_2/CO_2$ permeation selectivity value for ZIF-8 reported by Zhang et al. [71] is 4.6, in reasonably good agreement with the predictions based on molecular simulations as presented in Fig. 8c.

## 5. $CH_4/H_2$ mixture separations

The separation of $CH_4/H_2$ mixtures is important in the context of $H_2$

purification, recovery, and production processes [42,68,69]. In all materials, the diffusion selectivity favors $H_2$ whereas the adsorption selectivity favors $CH_4$; see Fig. 9a. The highest $H_2/CH_4$ diffusion selectivity is with ITQ-29 and CHA, whereas the highest $CH_4/H_2$ adsorption selectivity is exhibited by NaX zeolite.For separations in fixed bed units for production of pure $H_2$, screening on the basis of the plot of $\Delta Q$ versus volumetric $CH_4$ uptake capacity leads to the hierarchy NaX > MgMOF-74 > MFI > NaY; see Fig. 9b.

For screening materials for use in membrane devices, the Robeson plot is presented in Fig. 9c. The best materials for $CH_4$-selective membrane operations are MFI, NaX, NaY, and MgMOF-74 that lie in the top right corner. For $H_2$-selective membrane operations, suitable choices are cage-window structures: ZIF-8, ITQ-29, CHA, and LTA. For ZIF-8 membranes, Zhang et al. [71] have reported $H_2/CH_4$ permeation selectivities of 10, in good agreement with the predictions based on molecular simulations presented in Fig. 9c.

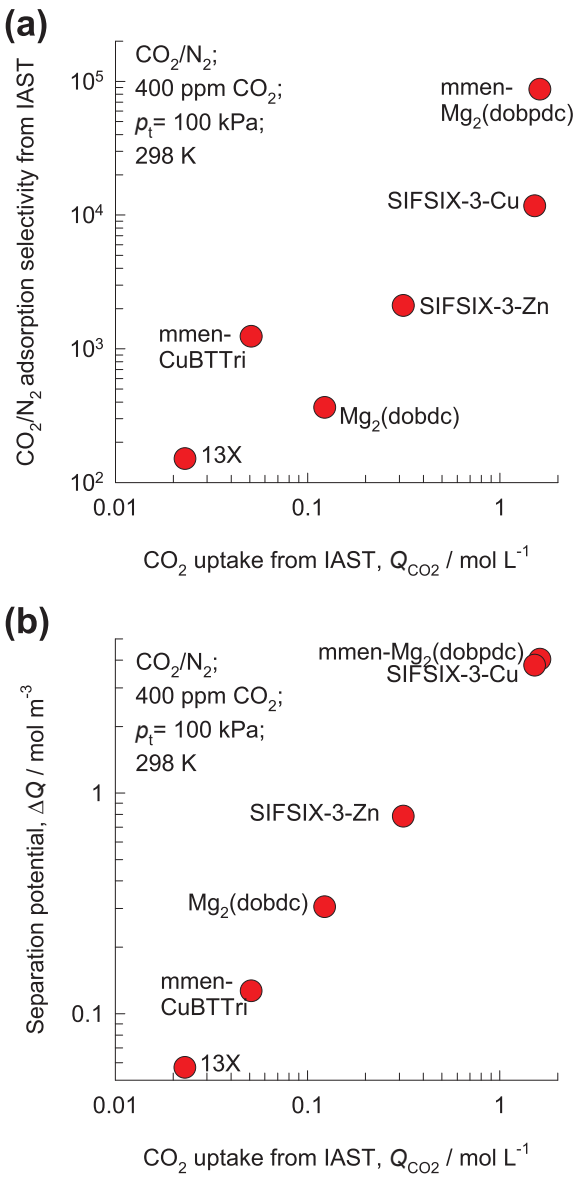


**Fig. 11.** (a) Plot of adsorption selectivity versus volumetric $CO_2$ uptake capacity for $CO_2/N_2$ mixtures containing 400 ppm $CO_2$. (b) Plot of the separation potential, $\Delta Q$, calculated using the formula $\Delta Q$ versus the volumetric $CO_2$ uptake capacity. The materials evaluated are $Mg_2$(dobdc)[ = MgMOF-74] [18], 13X zeolite [6,18], mmen-CuBTTri [formed by the incorporation of the incorporation of *N*,*N*-dimethylethylenediamine (mmen) into $H_3[(Cu_4Cl)_3(BTTri)_8$ (CuBTTri; $H_3$BTTri = 1,3,5-tri(1*H*-1,2,3-triazol-4-yl)benzene)] [82], mmen-$Mg_2$(dopbdc) [(dopbdc)$^{4-}$ = 4,4′-dioxido-3,3′-biphenyldicarboxylate] [81], SIFSIX-3-Cu [based on pyrazine/copper(II) two-dimensional periodic $4^4$ square grids pillared by silicon hexafluoride anions] [83], and SIFSIX-3-Zn [83].

## 6. Screening materials for CO2 capture on the basis of experimental data on unary isotherms

An important conclusion to be drawn from the screening of materials for $CO_2$ capture in fixed bed operations is that the material possessing the highest potential for production of pure $CH_4$ (cf. Fig. 6b), $N_2$ (cf. Fig. 7b), or $H_2$ (cf. Fig. 8b) is not the one that possesses the highest adsorption selectivity (i.e. NaX zeolite), but MgMOF-74 that has the right combination of selectivity and uptake capacity. This is an important conclusion that needs to be validated on the basis of experimental data. Towards this end, we compare the separation potentials $\Delta Q$ using calculations based on the IAST model, along with experimental data on the unary isotherms of $CO_2$, $CH_4$, $N_2$, and $H_2$. For 50/50 $CO_2/CH_4$ mixtures at a total of 600 kPa, the plot of $\Delta Q$ versus volumetric $CO_2$ uptake capacity is presented in Fig. 10a. The three best materials are NiMOF-74, MgMOF-74 and 13X zeolite, in agreement with the screening results using molecular simulations presented in Fig. 6b. The screening results for 15/85 $CO_2/N_2$ mixture separations at total pressure of 100 kPa are shown in Fig. 10b. The obtained hierarchy of $\Delta Q$ values: MgMOF-74 ≈ NiMOF-74 > 13X, is the same as that in Fig. 7b, deduced on the basis of molecular simulations. The screening results for 20/80 $CO_2/H_2$ mixture separations at total pressure of 6 MPa are shown in Fig. 10c. In this case, the hierarchy of $\Delta Q$ values is: MgMOF-74 > CuTDPAT > 13X, agreeing with the corresponding hierarchy in Fig. 8b while noting that there are no molecular simulation results available for CuTDPAT [69]. The reliability of molecular simulation data for screening materials, especially zeolites, for $CO_2$ capture applications is due to the fact that the force fields for $CO_2$, $CH_4$, $N_2$, and $H_2$ used in the simulations have been developed on the basis of extensive experimental data on unary isotherms [72,73]. For MOFs and ZIFs, the generic UFF [74] and DREIDING [75] force fields were used; consequently the results are somewhat less reliable, especially for host materials with open metal sites.

For industrial production of pure $H_2$, steam-methane reformer off-gas, after it has been further treated in a water-gas shift reactor, is a commonly used feed gas stream, with typical compositions 70–80% $H_2$, 15–25% $CO_2$, 3–6% $CH_4$, and 1–3% CO [76–78]. For most adsorbents, the sequence of breakthroughs in fixed bed adsorbers follows the increasing hierarchy of adsorption strengths, i.e. $H_2$, $CH_4$, CO, and $CO_2$. This implies that the $CH_4/H_2$, and $CO/H_2$ adsorption selectivities are far more relevant than the $CO_2/H_2$ selectivity. The precise definition of selectivity to be used for multicomponent gas mixtures that are relevant to fixed bed operations is ambiguous. In this case, the proper metric is the separation potential quantifying the maximum achievable productivity of pure $H_2$ is derived from the shock-wave model [14]

$$\Delta Q = (Q_{CH4} + Q_{CO} + Q_{CO2})\frac{y_{H2}}{1-y_{H2}} - Q_{H2} \tag{9}$$

Fig. 10d presents plot of $\Delta Q$ vs volumetric uptake capacity for four different adsorbents. The best MOF for this separation task is CuBTC; this is because $CO_2/H_2$ selectivity is largely irrelevant for $H_2$ production processes even though $CO_2$ may be the present as the largest impurity in the feed mixture.

## 7. $CO_2$ capture from ambient air

The majority of research on $CO_2$ capture with MOFs has its focus on flue gas mixtures that typically contain 15% $CO_2$, and 85% $N_2$

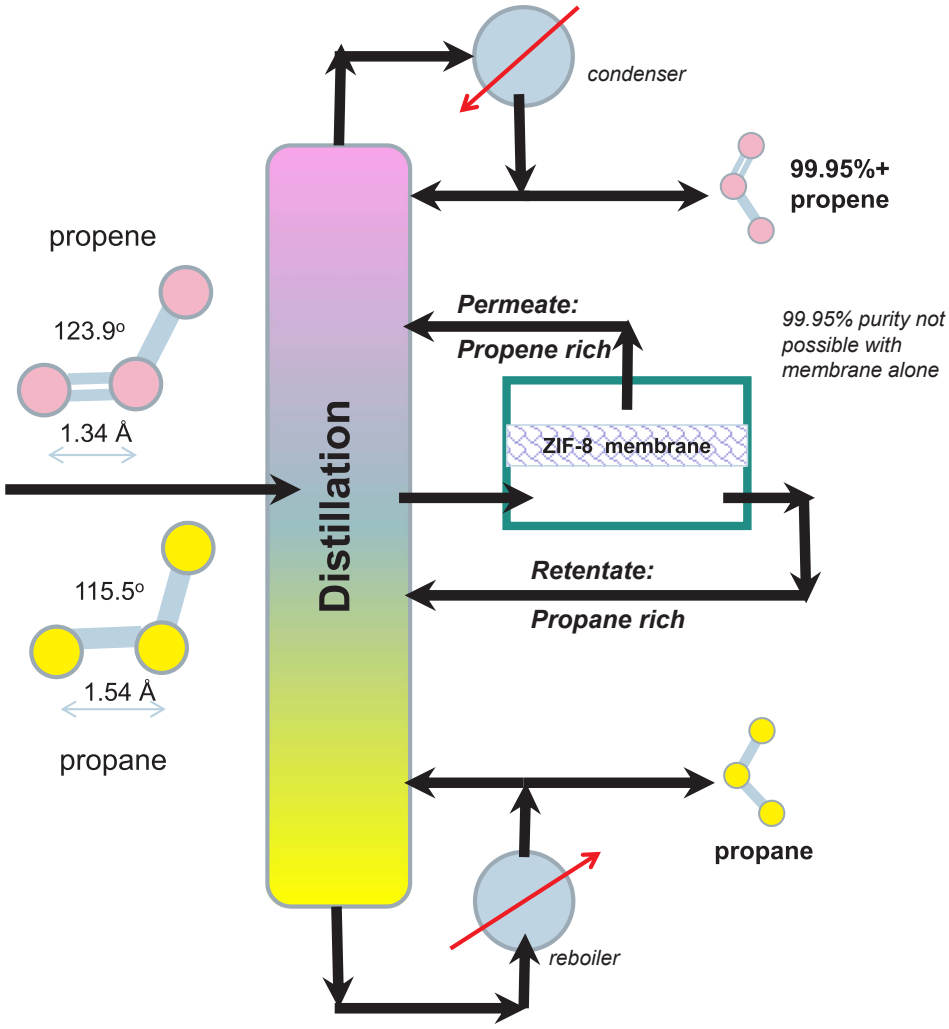


**Fig. 12.** Separation of propene and propane using a hybrid scheme consisting of ZIF-8 membrane and conventional distillation.

[6,18,19]. More recently, the potential of MOFs for $CO_2$ capture from ambient air has been the subject of a number of investigations [79–83]. Typically, the $CO_2$ concentrations in ambient air are about 400 ppm (=0.04%). Higher $CO_2$ concentrations, up to about 0.5%, are encountered in confined spaces such as in aeroplanes, submarines, space vehicles, and inside space suits of astronauts [84]. There is anecdotal evidence of curtailment of a space walk due to increase of $CO_2$ levels inside a space suit, that uses canisters containing lithium hydroxide for $CO_2$ capture [85].

Fig. 11a presents a plot of the adsorption selectivity versus volumetric $CO_2$ uptake capacity for $CO_2/N_2$ mixtures containing 400 ppm $CO_2$; the objective of the separation task is to produce $N_2$ containing less than 40 ppm $CO_2$. All six materials have selectivity values exceeding 100; the highest selectivity is achieved with mmen-$Mg_2$(dopbdc) [81]. There are, however, large differences in the $CO_2$ uptake capacities, ranging from 0.023 mol $L^{-1}$ for 13X zeolite to 1.6 mol $L^{-1}$ for mmen-$Mg_2$(dopbdc) [81], and SIFSIX-3-Cu [83]. The maximum productivity of pure $N_2$ (< 40 ppm $CO_2$) may be determined for each MOF using Eq. (6). The two best performing MOFs are mmen-$Mg_2$(dopbdc) and SIFSIX-3-Cu, that have both high uptake capacities; see Fig. 11b.

## 8. Alkene/alkane, and alkyne/alkene separations

There are stringent purity constraints of > 99.95% on $C_2H_4$ and $C_3H_6$ used as feedstocks to polymerization reactors. In order to meet required purity levels, distillation columns in currently used technologies for $C_2H_4/C_2H_6$ and $C_3H_6/C_3H_8$ separations need to operate at high pressures and cryogenic temperatures, employing high reflux ratios. The alkene/alkane distillation units are some of the largest and tallest distillation columns used in the petrochemical industries. Consequently, there is considerable economic incentive for development of energy efficient alternatives. One technological option is to employ a hybrid distillation-membrane scheme such as the one pictured in Fig. 12. Based on literature information, ZIF-8 membranes have potential applications for separation of both $C_2H_4/C_2H_6$, and $C_3H_6/C_3H_8$ mixtures [86–88]. The separations using ZIF-8 membranes is primarily based on differences in the diffusivities of the alkenes and alkanes; such differences arise due to subtle differences in bond lengths and bond angles [41]. The adsorption selectivities for $C_2H_4/C_2H_6$, and $C_3H_6/C_3H_8$ mixtures using ZIF-8 favor the saturated alkane [37,86,89]; this implies that adsorption and diffusion do not proceed hand in hand. The diffusion selectivities over-ride the adsorption selectivities, yielding permeation selectivities in favor of the unsaturated alkene [37,86]. The experiments of Bux et al. [86] for a ZIF-8 membrane show that the $C_2H_4/C_2H_6$ permeation selectivity is in the range of 2–3. For $C_3H_6/C_3H_8$ permeation across ZIF-8 membrane, the permeation selectivities, $S_{perm}$, reported in the experiments of Pan et al. [87] and Liu et al. [88] show values in the range of 30–35. These permeation selectivity values are significantly higher than the relative volatility of 1.14 for $C_3H_6/C_3H_8$; consequently, the hybrid process can be expected to have superior separation capability when compared to distillation alone. Importantly, the hybrid scheme in Fig. 12 contributes to alleviating the load on the condensers and reboilers.

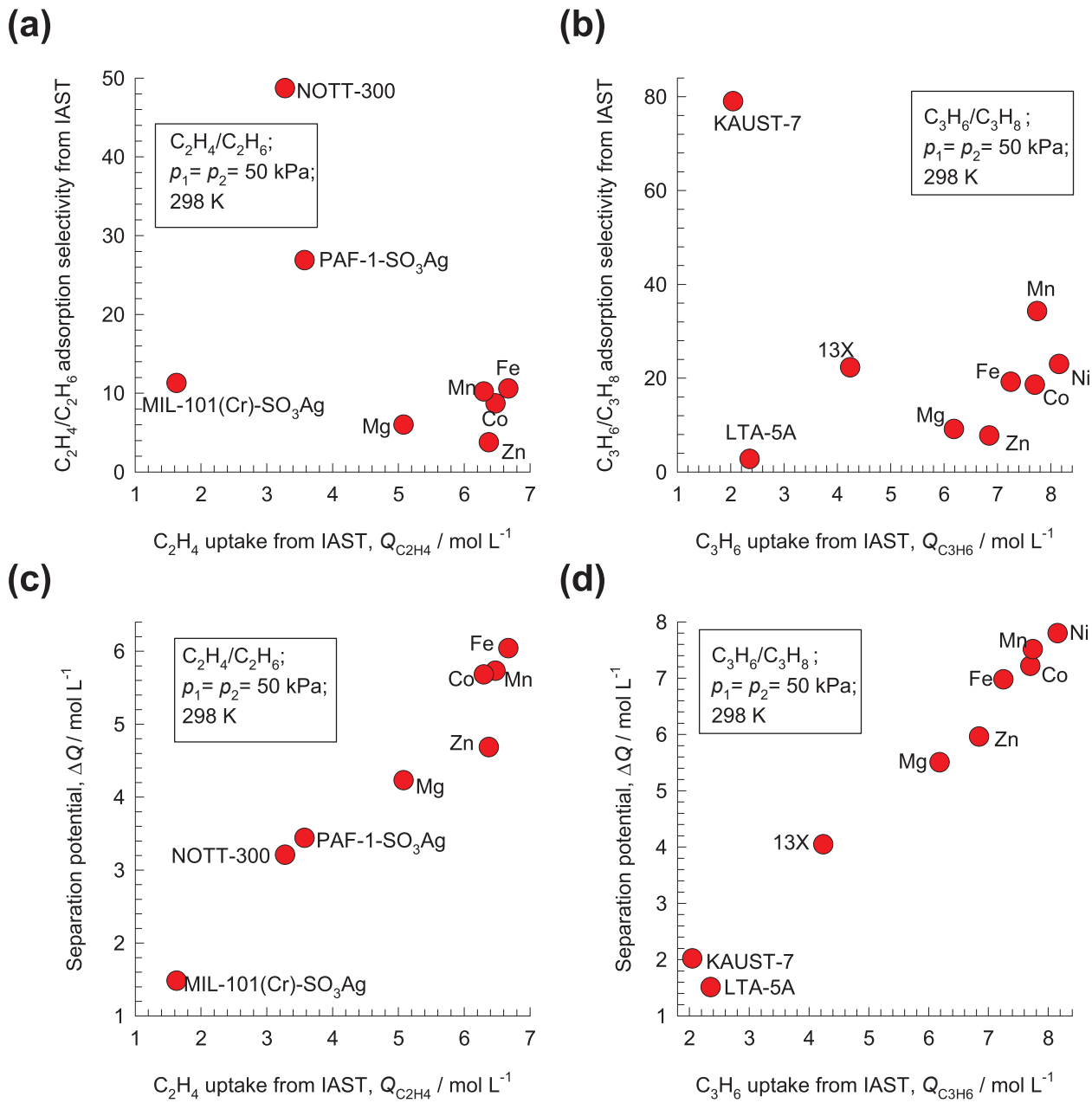


**Fig. 13.** (a, b) Plot of adsorption selectivity versus volumetric alkene uptake capacity, and (c, d) plot of the separation potential, $\Delta Q$, versus the volumetric alkene uptake capacity for (a, c) 50/50 $C_2H_4/C_2H_6$ mixtures using M-MOF-74 (M = Fe, Co, Mn, Mg, Zn), PAF-1-$SO_3Ag$, MIL-101-Cr-$SO_3Ag$, and NOTT-300, and (b, d) 50/50 $C_3H_6/C_3H_8$ mixtures using M-MOF-74 (M = Fe, Co, Ni, Mn, Mg, Zn), 13X zeolite, LTA-5A zeolite, and KAUST-7. In all cases, the temperature $T$ = 298 K, and total pressure $p_t$ = 100 kPa. The calculations are based on the pure component isotherm data for the various zeolites and MOFs, as compiled in our previous work [14].

For $C_2H_4/C_2H_6$, and $C_3H_6/C_3H_8$ separations in fixed-bed adsorption devices, a vast majority of the MOFs reported in the literature selectively adsorb the unsaturated alkenes [1–3,90]; see the plots of selectivity vs alkene uptake capacity for a few selected MOFs in Fig. 13a,b. Simultaneous and cooperative hydrogen-bonding, and $\pi \cdots \pi$ stacking interactions account for the stronger binding of $C_2H_4$ in NOTT-300. The $\pi$-complexation of the alkenes with Ag (I) ions of PAF-1-$SO_3Ag$, account for its high $C_2H_4/C_2H_6$ selectivity. Cadiau et al. [91] report the synthesis of NbOFFIVE-1-Ni (=KAUST-7), whose effective aperture permits ingress of the $C_3H_6$ molecules, but practically excludes $C_3H_8$ on the basis of subtle differences in bond lengths and bond angles. The separation capability of M-MOF-74 [M = Mg, Mn, Co, Ni, Zn, Fe] has been established in laboratory studies [3,90]; $C_2H_4$, and $C_3H_6$ can selective bind with $M^{2+}$ of M-MOF-74, with side-on attachment and $\pi$-coordination [3]. Mukherjee et al.[12] also show that $\pi$-complexation triggered Lewis acid–base interactions between the open metal sites of M-MOF-74 and the $\pi$-electron rich benzene molecules can be exploited to achieve benzene/cyclohexane separations with high selectivities towards benzene; see Figs. S94 and S95 of Supplementary material for further details.

An important point to note is that the desired pure alkene can only be recovered during the desorption phase [3] of PSA operations. Using the shock-wave model, the maximum productivity of the more strongly adsorbed alkene (component A) is given by [14]

$$\Delta Q = Q_A - Q_B \frac{y_A}{1-y_A} \tag{10}$$

The plots of the separation potential versus the alkene uptake capacity for 50/50 $C_2H_4/C_2H_6$, and 50/50 $C_3H_6/C_3H_8$ mixtures are presented in Fig. 13c,d. It is interesting to note that the MOFs with the highest selectivities, NOTT-30 and KAUST-7, are not the ones displaying the highest productivity for production of pure alkene. For both mixtures, M-MOF-74 (M = Fe, Mn, Co, Ni) yield the best separations.

There are, however, practical technological issues associated with achieving the required > 99.95% purities in PSA units in the *desorption* phase. It becomes necessary to operate with multiple beds involving five different steps; the alkene product of the desired purity is recovered in the final step by counter-current vacuum blowdown [92,93]. Purely from a technological view point, it is preferable to use adsorbents that are selective to the saturated alkanes, so that the desired alkenes are recoverable in the adsorption cycle [94]. The preferential adsorption of alkanes is only possible if separations are based on van der Waals interactions alone. However, the adsorption selectivities cannot be expected to be high. Indeed, computational screening of 300000 all-silica zeolite structures by Kim et al.[95] results in the discovery of SOF zeolite, that has a $C_2H_6/C_2H_4$ selectivity of only 2.9. This selectivity value of 2.9 can be matched by ZIF-7 [94,96], and ZIF-8 [89]. Two recent publications, also report ethane-selective adsorption with Ni(bdc)(ted)$_{0.5}$ [97] and PCN-250 [98] but our IAST estimates of the adsorption selectivities at 298 K yield values close to 2; this value is too low for achievement of the desired purity levels.

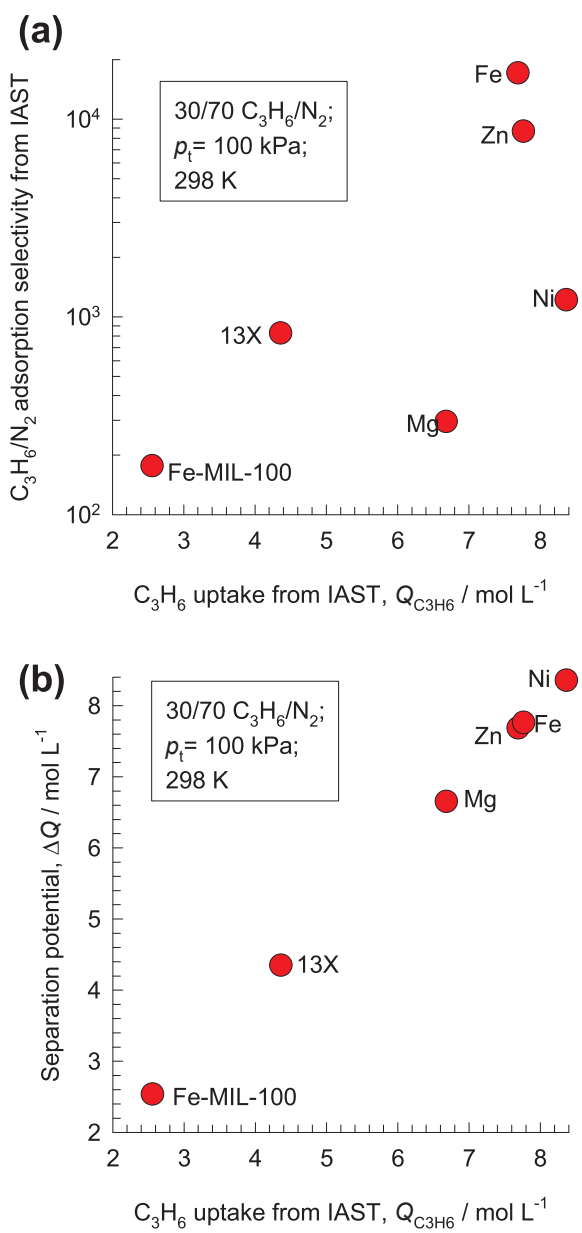


**Fig. 14.** Plot of the separation potential $\Delta Q$. versus the volumetric uptake capacity of $C_2H_2$ for separation of 1/99 $C_2H_2/C_2H_4$ mixtures using SIFSIX-(1-Cu, 2-Cu, 3-Zn, 2-Cu-i, 3-Ni, 14-Cu-i), M′MOF-3a, and UTSA-100a. The total pressure, $p_t$ = 100 kPa, and temperature $T$ = 298 K. The unary isotherm data for other MOFs are from the published literature [13,14,100].

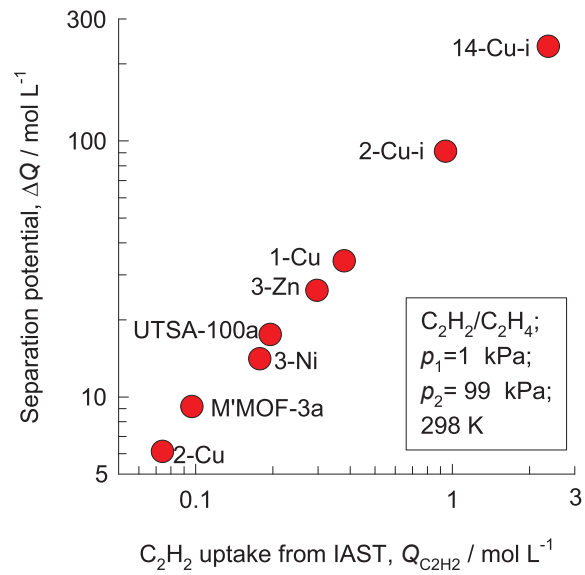


**Fig. 15.** (a) Plot of adsorption selectivity vs volumetric uptake capacity of $C_3H_6$ for separation of 30/70 $C_3H_6/N_2$ mixtures using M-MOF-74 (M = Fe, Ni, Mg, Zn), 13X zeolite, and Fe-MIL-100. The total pressure, $p_t$ = 100 kPa, and temperature $T$ = 298 K. (b) Plot of the separation potential $\Delta Q$ versus the volumetric uptake capacity of $C_3H_6$. For Fe-MIL-100, the unary isotherm data are taken from Ribeiro et al. [102]; the unary isotherm data for other MOFs are from previous works [10,13,14].

The $C_2H_4$ and $C_3H_6$ feedstocks to the polymerization reactors are also subject to strict constraints on the presence of the corresponding alkynes, $C_2H_2$ (ethyne) and $C_3H_4$ (propyne). Typically, the alkyne content of alkyne/alkene feed mixtures is 1%. The presence of alkyne impurities higher than 40 ppm may poison the polymerization catalyst and have a deleterious effect on the polymer product. Current technologies for separation of $C_2H_2/C_2H_4$ and $C_3H_4/C_3H_6$ use absorption in dimethyl formamide (DMF); solvent regeneration is energy consuming. There is considerable research effort expended in recent years on the development of MOFs for this separation task [5,24–28,31,99]. Fig. 14 presents a plot of the separation potential $\Delta Q$ versus the volumetric uptake capacity of $C_2H_2$ for separation of 1/99 $C_2H_2/C_2H_4$ mixtures using eight different adsorbents. The highest productivity of purified $C_2H_4$ is shown by SIFSIX-14-Cu-i (also called UTSA-200) with an interpenetrated network that has an effective pore size of 3.3 Å–4 Å, small enough to prevent the ingress of $C_2H_4$ [100]; furthermore, the $SiF_6^{2-}$ sites enhance the adsorption of ethyne.

## 9. Propene/nitrogen separations

Subsequent to the polymerization of propene, the solid polymer product is purged with nitrogen, yielding a nitrogen-rich purge gas containing unreacted $C_3H_6$; typical composition of the purge gas is 30% $C_3H_6$, 70% $N_2$ [101,102]. There is considerable economic incentive to separate the 30/70 $C_3H_6/N_2$ mixtures and recycle the recovered $C_3H_6$ to the polymerization reactor [101,102]. Narin et al. [101], and Ribeiro et al. [102] demonstrate the potential of Fe-MIL-100 for this separation

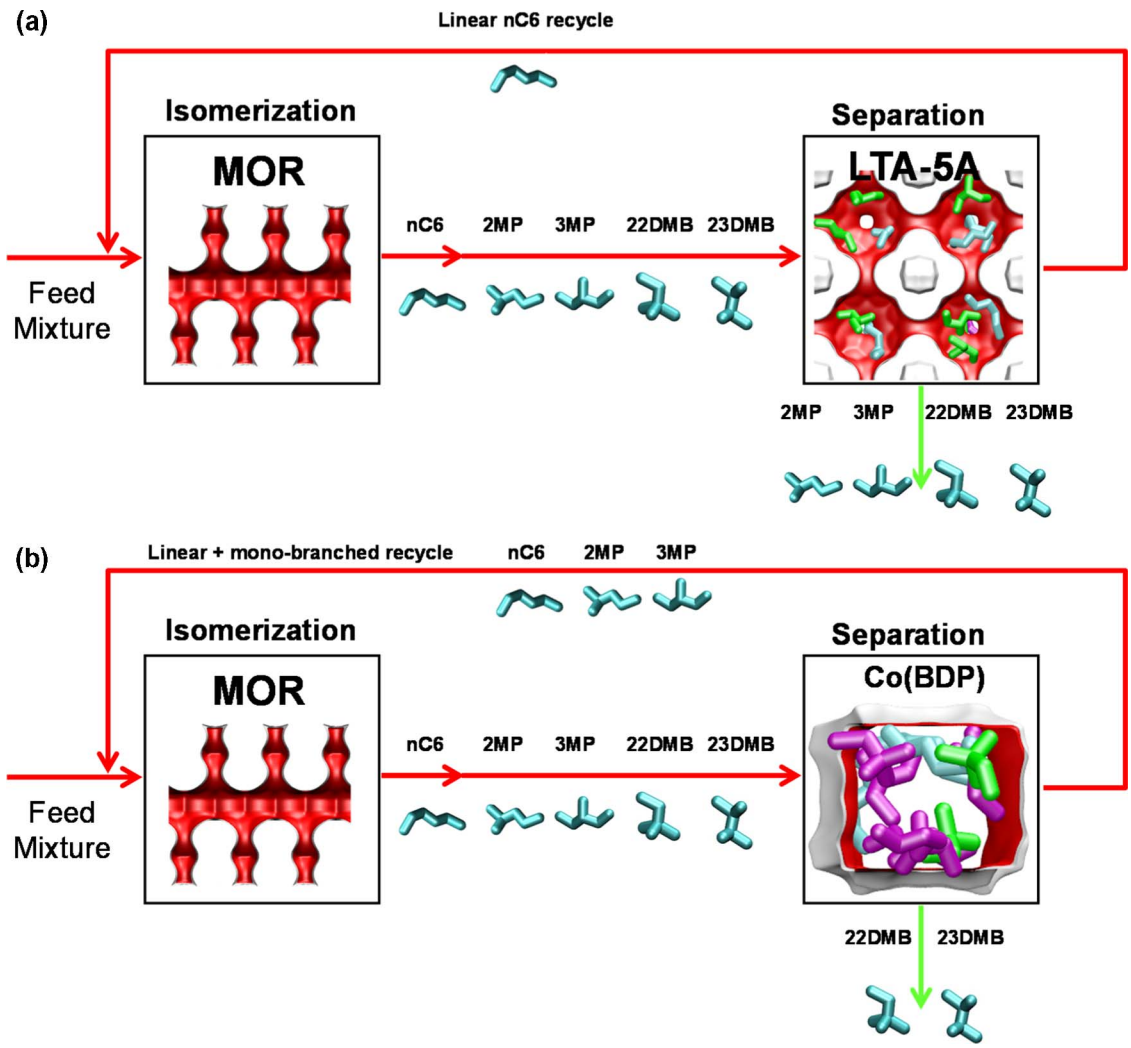


**Fig. 16.** (a) Currently employed processing scheme for nC6 isomerization and subsequent separation step using LTA-5A zeolite. (b) Improved processing scheme for the nC6 isomerization process.

task by use of laboratory scale breakthrough experiments. We shall examine whether significant improvements in separation performance can be achieved by use of other materials. To meet this objective, we perform IAST calculations of mixture adsorption equilibrium. Fig. 15a presents a plot of the adsorption selectivity vs volumetric uptake capacity of $C_3H_6$ for separation of 30/70 $C_3H_6/N_2$ mixtures using M-MOF-74 (M = Fe, Ni, Mg, Zn), 13X zeolite, and Fe-MIL-100. The highest selectivity is achieved with Fe-MOF-74 [3], whereas the highest volumetric uptake capacity of $C_3H_6$ is with NiMOF-74. The desired product $C_3H_6$ can be recovered in the desorption phase; the maximum productivity of each MOF, calculated using Eq. (10), is presented in Fig. 15b as a function of the volumetric uptake capacity of $C_3H_6$. The best separation potential is offered by NiMOF-74 that has the highest uptake capacity for $C_3H_6$. It is also interesting to note that lowest productivity of pure $C_3H_6$ is with Fe-MIL-100, whose productivity is even lower than that of the commercially available 13X zeolite.

## 10. Separation of mixtures of hexane isomers

The separation of hexane isomers is required for production of high-octane gasoline. The values of the Research Octane Number (RON) increases with the degree of branching; the RON values are: n-hexane (nC6) = 30, 2-methylpentane (2MP) = 74.5, 3-methylpentane (3MP) = 75.5, 2,2 dimethylbutane (22DMB) = 94, and 2,3 dimethylbutane (23DMB) = 105. The di-branched isomers are therefore the preferred products for incorporation into the high-octane gasoline pool [7,37,103]. Currently, the separation of hexane isomers is performed using LTA-5A zeolite that operates on the principle of molecular sieving; see the process flow diagram in Fig. 16a. Linear nC6 can hop from one cage to the adjacent cage through the 4 Å windows of LTA-5A, but branched alkanes are largely excluded. A more efficient process scheme (cf. Fig. 16b), requires the "discovery" of a MOF adsorbent that would separate the di-branched isomers 22DMB and 23DMB from the nC6, 2MP, and 3MP, these low-RON components are recycled back to the reactor. Typically, in such a processing scheme the aim would be to produce a product stream from the separation step with RON value > 92. This requirement of 92 + RON implies that the product stream will contain predominantly the di-branched isomers 22DMB and 23DMB, while allowing a small proportion of 2MP and 3MP to be incorporated into the product stream. Since high-octane gasoline is sold on the basis of the product octane value, there are no strict constraints on the product compositions and purities; i.e. sharp separations between mono- and di- branched isomers are not demanded. CBMC simulations are particularly potent tools for screening of zeolite and MOF adsorbents

for separation of alkane isomers because the force fields for alkane molecules are well established [7,15,72,103–105].

As illustration, Fig. 17a shows the transient development of exit gas compositions from a bed packed with Co(BDP) with an equimolar 5-component feed mixture. Product gas with 92 + RON can be recovered from the displacement interval in which the di-branched isomers 22DMB and 23DMB are eluted, as indicated. When the mono-branched isomers break through, there is a sharp decrease in the RON of the product exiting the fixed bed. The desired separation is between (22DMB + 23DMB), and (nC6 + 2MP + 3MP) the appropriate expression for the separation potential is [14]

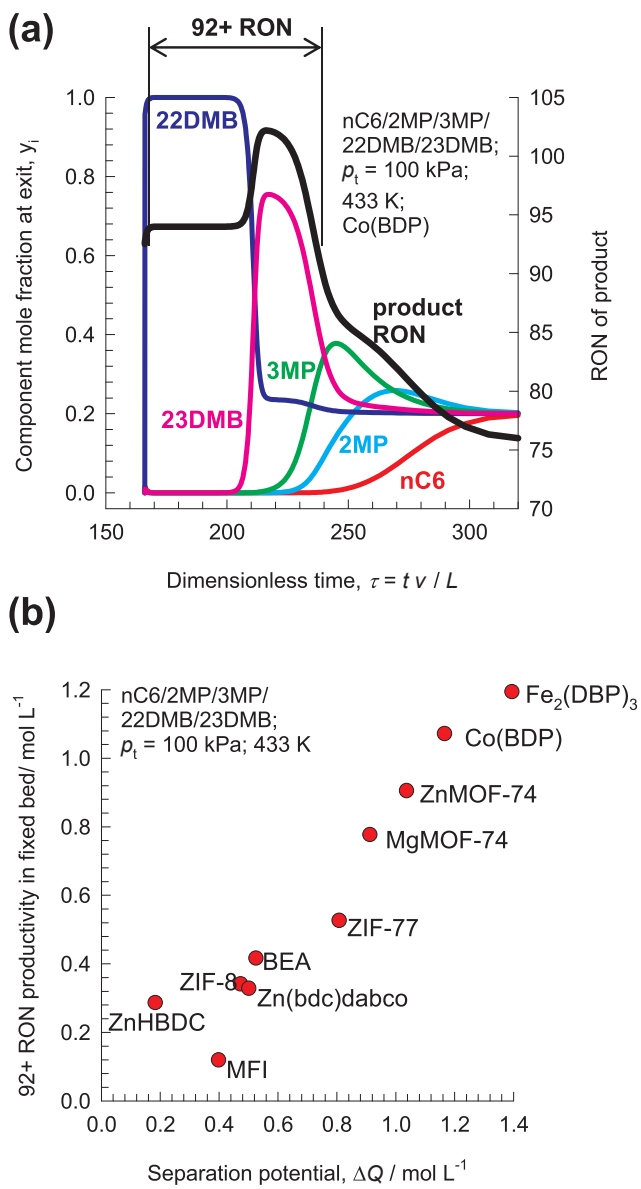


**Fig. 17.** (a) Transient breakthrough simulations for separation of equimolar nC6/2MP/3MP/22DMB/23DMB mixtures at 433 K and 100 kPa in fixed bed adsorber packed with Co(BDP). Also shown (right y-axis) is the RON of product gas at the outlet of fixed bed. (b) The 92 + RON productivity for ten different adsorbent materials: ZnMOF-74, MgMOF-74, Co(BDP), $Fe_2(BDP)_3$, MFI, BEA, ZIF-8, ZnHBDC, Zn(bdc)dabco, and ZIF-77, plotted as a function of the separation potential $\Delta Q$, calculated from Eq. (9). The unary isotherm data and calculation details are provided in earlier works [13,14,37]. The computational details of the transient breakthroughs, and calculations of product RON, are provided in earlier works [13,14,37,123]; these are also summarized in the Supplementary material.

$$\Delta Q = (Q_{nC6} + Q_{2MP} + Q_{3MP})\frac{y_{22MB} + y_{23DMB}}{1-y_{22MB}-y_{23DMB}} - (Q_{22DMB} + Q_{23DMB}) \tag{11}$$

Fig. 17b compares 92 + RON productivities for ten different adsorbent materials, plotted as a function of the separation potential $\Delta Q$; the interdependence is linear and we conclude that the best performing MOF for this separation duty is $Fe_2(BDP)_3$; this conclusion is in line with the earlier work of Herm et al. [4].

## 11. Separation of mixtures of xylene isomers

Aromatic hydrocarbons, that are valuable feedstocks in the petrochemical industries, are most commonly obtained from catalytic reforming of naphtha. The xylene isomers, o-xylene, m-xylene and in particular p-xylene, are important chemical intermediates. In a commonly used separation scheme (cf. Fig. 18), the xylenes rich stream from the bottom of the reformer splitter is routed to a xylenes splitter. Here, the heavier aromatics (C9+) are removed from the bottom of the column. The overhead stream from the xylenes splitter needs to be separated for recovery of p-xylene. In current technology, this mixture is separated in a Simulated Moving Bed (SMB) adsorption separation unit, that operates under conditions in which the bulk fluid phase is in the liquid state and the pores of the adsorbent are saturated with guest aromatic molecules. The typical composition of a mixed xylenes feed to a simulated moving bed (SMB) adsorber is 19% ethylbenzene, 44% m-xylene, 20% o-xylene, and 17% p-xylene. As pointed out by Peralta et al. [106], adsorbents selective to p-xylene are desirable for high productivities; they need to adsorb only about 20% of the feed, whereas an adsorbent that rejects p-xylene would have to adsorb 80% of the feed. In current industrial practice the adsorbent used is BaX zeolite, that selectively adsorbs p-xylene. The hierarchy of adsorption strengths in BaX is dictated by molecular packing, or entropy, effects that prevail under pore saturation [107,108]. For realizing improvements in the SMB adsorber, there is considerable scope for development of MOFs that have both higher uptake capacity and selectivity to p-xylene as compared to BaX zeolite. Improved MOF adsorbents will result in lower recirculation flows of eluent, and solid adsorbent in the SMB unit and this will result in significant economic advantages.

Since there is no unambiguous definition of the adsorption selectivity, the screening and ranking of MOFs is appropriately done using the separation potential $\Delta Q$ for preferential adsorption of p-xylene, and rejection of o-xylene, m-xylene, and ethylbenzene [14]

$$\Delta Q = Q_{pX}\left(\frac{1-y_{pX}}{y_{pX}}\right) - (Q_{oX} + Q_{mX} + Q_{EthBz}) \tag{12}$$

Fig. 19a presents the plot of $\Delta Q$, versus the volumetric uptake of p-xylene for a few selected MOFs. Significant improvements over BaX zeolite are offered by DynaMOF-100 [11,109], and Co-CUK-1 [110,111]. DynaMOF-100 is a Zn(II)-based dynamic coordination framework that undergoes guest-induced structural changes so as to allow selective uptake of p-xylene within the cavities (see Fig. 19b). Co-CUK-1 is comprised of cobalt(II) cations and the dianion of dicarboxylic acid; the 1D zig-zag shaped channels of Co-CUK-1 allow optimal vertical stacking of p-xylene (cf. Fig. 19c).

Mukherjee et al. [11] also demonstrate that DynaMOF-100 has the ability to selectively encapsulate styrene from mixtures with ethylbenzene; this separation is currently carried out in vacuum distillation columns (see top right corner of Fig. 18). The Supplementary material provides further background on styrene/ethylbenzene separations; see Figs. S92, and S93.

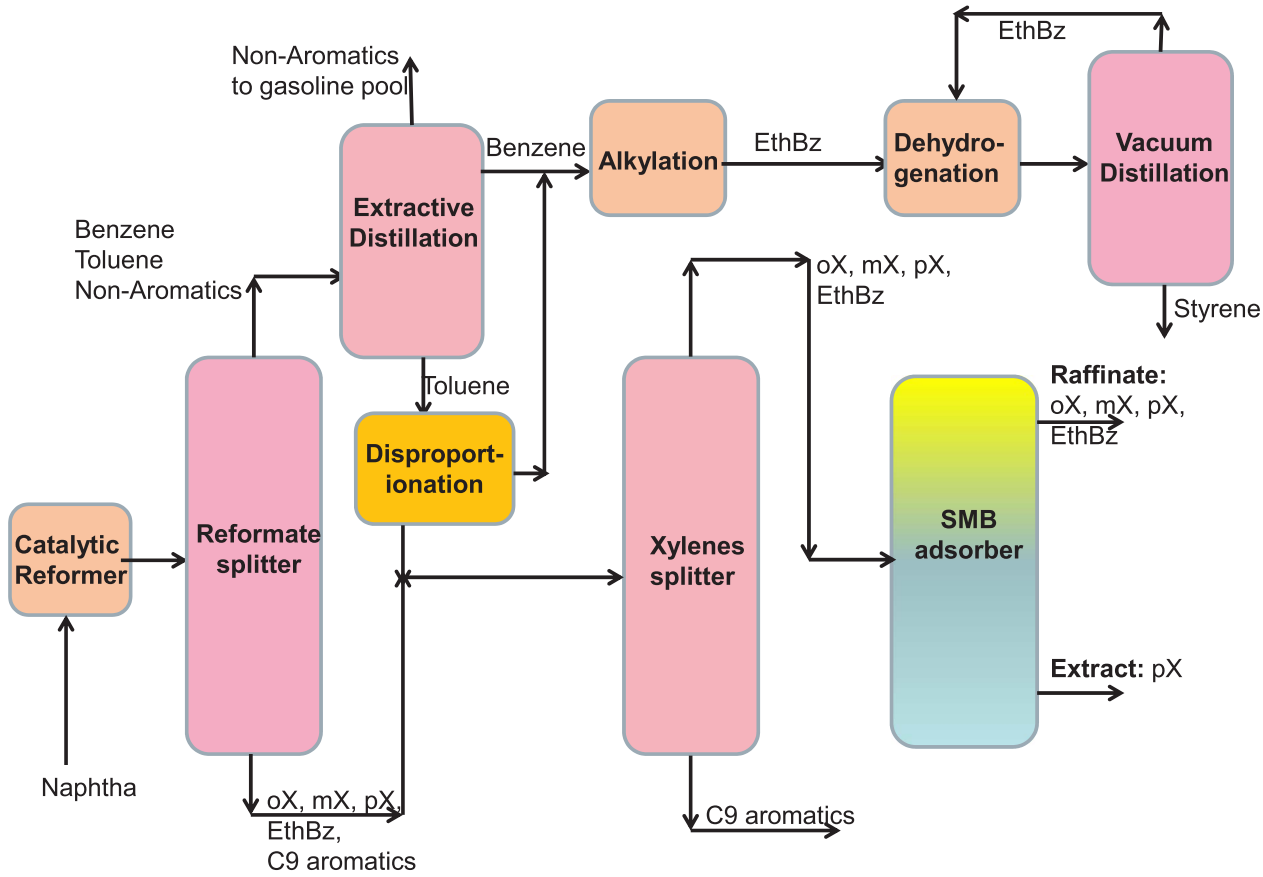


**Fig. 18.** Schematic showing the separations of the products from a catalytic reforming unit. Further process background details are provided in the Supplementary material.

## 12. Conclusions

The following major conclusions emerge from the data and analysis presented in this article.

(1). The principles governing separations in fixed bed adsorbers and membrane permeation devices are distinctly different. The selection of the "ideal" microporous crystalline material for use in either of these devices is governed by distinctly different considerations.

(2). The membrane permeation selectivity is a product of the diffusion selectivity and the adsorption selectivity: $S_{perm} = S_{diff} \times S_{ads}$. Membrane separations are primarily "driven" by $S_{diff}$. Cage-type structures with narrow 3.3 Å to 4.3 Å windows are particularly suited for exploitation of differences in guest mobilities, as required for $H_2$-selective and alkene-selective permeation characteristics.

(3). Except for cage-type structures with narrow 3.3 Å to 4.3 Å windows, in all other structural topologies, adsorption strength and intra-crystalline diffusivity do not normally proceed hand-in-hand; strong adsorption almost invariably implies low mobility.

(4). Most commonly, intra-crystalline diffusion influences are undesirable in fixed bed adsorption units because these result in distended breakthroughs and reduced productivities. In case of negligible diffusional influences, the separation effectiveness for binary mixtures is dictated by a combination of adsorption selectivity, $S_{ads}$, and uptake capacities.

(5). The combined selectivity/capacity metric $\Delta Q$, derived using the idealized shock-wave model is an appropriate screening tool for selecting materials for use in PSA units. In most of the separations analyzed, the adsorbent that offers the highest value of the separation potential $\Delta Q$ is not the one that possesses the highest value of $S_{ads}$.

(6). Screening of the materials on the basis of $\Delta Q$ is particularly convenient for multicomponent separations (e.g. $H_2$ purification, separation of alkane isomers, and xylenes) for which there is no unambiguous definition of $S_{ads}$.

(7). For alkene/alkane separations, most of the materials developed selectively adsorb the unsaturated alkene. From a practical perspective, to meet the required 99.95%+ alkene purity target it is desirable to synthesize MOFs that selectively adsorb the saturated alkane.

Not considered in this article are separations of mixtures of polar compounds, such as water/alcohol, and alcohol/aromatic mixtures. In such cases, molecular clustering effects are of significant importance and this causes significant failure of the IAST [112,113]. There is a need for development of reliable methods for prediction of thermodynamic non-ideality effects in mixture adsorption.

Also not considered in this review are diffusion-selective separations in fixed bed adsorbers, e.g. selective uptake of $N_2$ from $N_2/CH_4$ mixtures using LTA-4A zeolite and Ba-ETS-4 [114–116], and selective uptake of $O_2$ from $O_2/N_2$ mixtures using LTA-4A zeolite and carbon molecular sieve [39,117–120]. The screening of adsorbents requires reliable experimental data on intra-crystalline diffusivities [121].

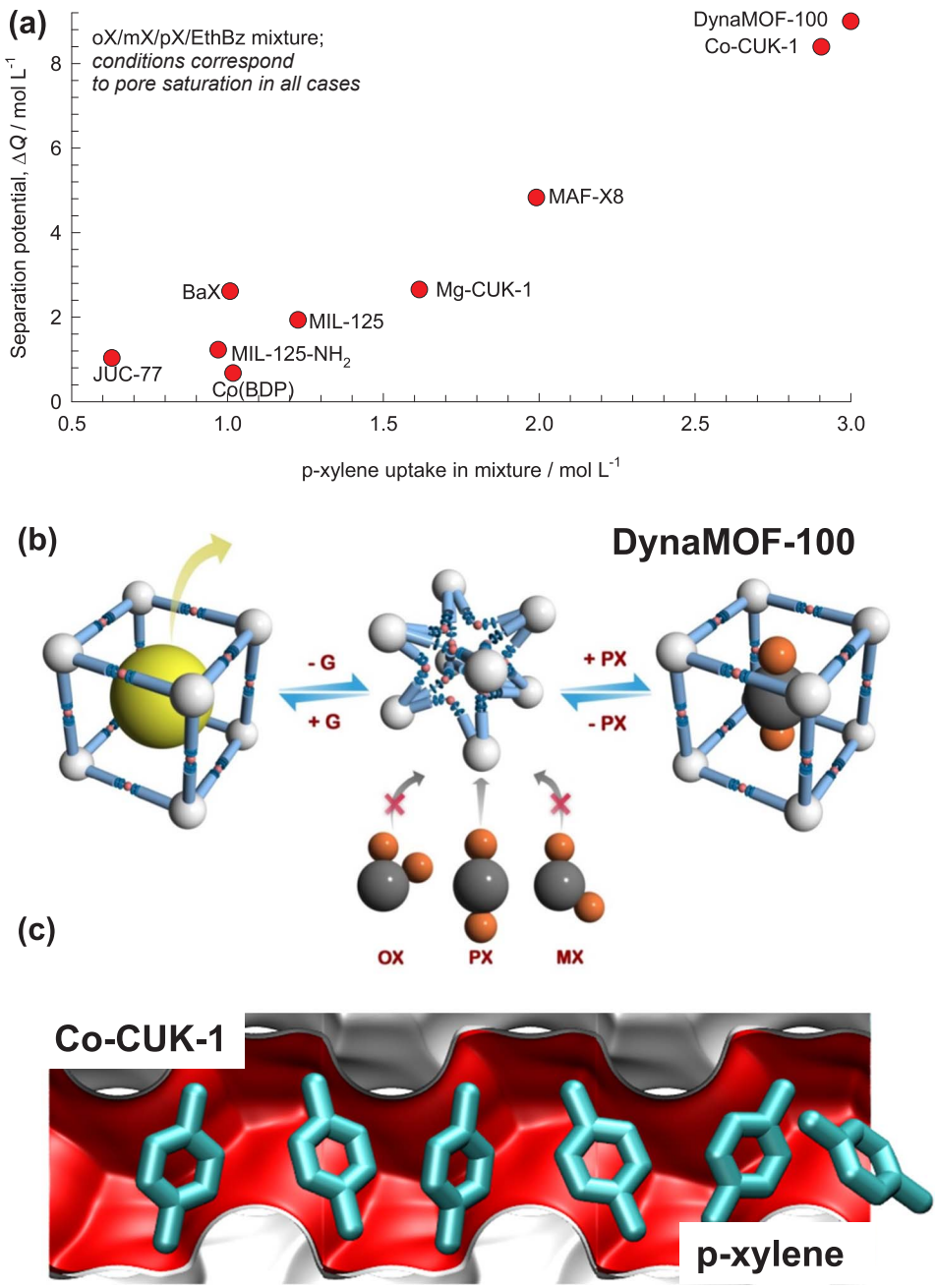


**Fig. 19.** (a) Plot of the separation potential, $\Delta Q$, versus the volumetric uptake of p-xylene. The bulk fluid phase consists of equimolar oX/mX/pX/EthBz mixtures, operating at temperatures that ensure pore saturation. The isotherm data for BaX, MAF-X8 [8], JUC-77, Co (BDP), MIL-125, and MIL-125-$NH_2$ are from Torres-Knoop et al. [8] The isotherm data for DynaMOF-100 are from Mukherjee et al. [11,109]. The isotherm data for Mg-CUK-1 are from Saccoccia et al. [124]. The isotherm data for Co-CUK-1 are from Yoon et al. [111]. (b) Schematic representation of the framework flexibility of DynaMOF-100 with selective accommodation of p-xylene from xylenes mixture [109]. (c) Snapshots showing the stacking of p-xylene, and ethylbenzene within the 1D zig-zag shaped channels of Co-CUK-1. The calculation details are provided in the Supplementary material.

## Appendix A. Supplementary material

Supplementary data associated with this article can be found, in the online version, at http://dx.doi.org/10.1016/j.seppur.2017.11.056.

## References

[1] Y. He, R. Krishna, B. Chen, Metal-organic frameworks with potential for energy-efficient adsorptive separation of light hydrocarbons, Energy Environ. Sci. 5 (2012) 9107–9120.
[2] Z. Bao, G. Chang, H. Xing, R. Krishna, Q. Ren, B. Chen, Potential of microporous metal-organic frameworks for separation of hydrocarbon mixtures, Energy Environ. Sci. 9 (2016) 3612–3641.
[3] E.D. Bloch, W.L. Queen, R. Krishna, J.M. Zadrozny, C.M. Brown, J.R. Long, Hydrocarbon separations in a metal-organic framework with open iron(II) coordination sites, Science 335 (2012) 1606–1610.
[4] Z.R. Herm, B.M. Wiers, J.M. Van Baten, M.R. Hudson, P. Zajdel, C.M. Brown, N. Maschiocchi, R. Krishna, J.R. Long, Separation of hexane isomers in a metal-organic framework with triangular channels, Science 340 (2013) 960–964.
[5] X. Cui, K. Chen, H. Xing, Q. Yang, R. Krishna, Z. Bao, H. Wu, W. Zhou, X. Dong, Y. Han, B. Li, Q. Ren, M.J. Zaworotko, B. Chen, Pore chemistry and size control in hybrid porous materials for acetylene capture from ethylene, Science 353 (2016) 141–144.
[6] S.C. Xiang, Y. He, Z. Zhang, H. Wu, W. Zhou, R. Krishna, B. Chen, Microporous metal-organic framework with potential for carbon dioxide capture at ambient conditions, Nat. Commun 3 (2012) 954, http://dx.doi.org/10.1038/ncomms1956.
[7] D. Dubbeldam, R. Krishna, S. Calero, A.Ö. Yazaydın, Computer-assisted screening of ordered crystalline nanoporous adsorbents for separation of alkane isomers, Angew. Chem. Int. Ed. 51 (2012) 11867–11871.
[8] A. Torres-Knoop, R. Krishna, D. Dubbeldam, Separating xylene isomers by commensurate stacking of p-Xylene within channels of MAF-X8, Angew. Chem. Int. Ed. 53 (2014) 7774–7778.
[9] A. Torres-Knoop, J. Heinen, R. Krishna, D. Dubbeldam, Entropic separation of styrene/ethylbenzene mixtures by exploitation of subtle differences in molecular configurations in ordered crystalline nanoporous adsorbents, Langmuir 31 (2015) 3771–3778.
[10] D. Banerjee, A.J. Cairns, J. Liu, R. Krishna, P.K. Thallapally, D.M. Strachan, Potential of metal-organic frameworks for capture of noble gases, Acc. Chem. Res. 48 (2015) 211–219.
[11] S. Mukherjee, B. Joarder, A.V. Desai, B. Manna, R. Krishna, S.K. Ghosh, Exploiting framework flexibility of a metal-organic framework for selective adsorption of styrene over ethylbenzene, Inorg. Chem. 54 (2015) 4403–4408.

[12] S. Mukherjee, B. Manna, A.V. Desai, Y. Yin, R. Krishna, R. Babarao, S.K. Ghosh, Harnessing Lewis acidic open metal sites of metal-organic frameworks: foremost route to achieve highly selective benzene sorption over cyclohexane, Chem. Commun. 52 (2016) 8215–8218.
[13] R. Krishna, Methodologies for evaluation of metal-organic frameworks in separation applications, RSC Adv. 5 (2015) 52269–52295.
[14] R. Krishna, Screening metal-organic frameworks for mixture separations in fixed-bed adsorbers using a combined selectivity/capacity metric, RSC Adv. 7 (2017) 35724–35737.
[15] R. Krishna, J.M. van Baten, In silico screening of zeolite membranes for $CO_2$ capture, J. Membr. Sci. 360 (2010) 323–333.
[16] R. Krishna, J.M. van Baten, In silico screening of metal-organic frameworks in separation applications, Phys. Chem. Chem. Phys. 13 (2011) 10593–10616.
[17] H. Liu, Y. He, J. Jiao, D. Bai, D.-L. Chen, R. Krishna, B. Chen, A porous zirconium-based metal-organic framework with the potential for the separation of butene isomers, Chem. Eur. J. 12 (2016) 14988–14997.
[18] J.A. Mason, K. Sumida, Z.R. Herm, R. Krishna, J.R. Long, Evaluating metal-organic frameworks for post-combustion carbon dioxide capture via temperature swing adsorption, Energy Environ. Sci. 4 (2011) 3030–3040.
[19] K. Sumida, D.L. Rogow, J.A. Mason, T.M. McDonald, E.D. Bloch, Z.R. Herm, T.-H. Bae, J.R. Long, Carbon dioxide capture in metalorganic frameworks, Chem. Rev. 112 (2012) 724–781.
[20] T. Hähnel, G. Kalies, R. Krishna, J. Möllmer, J. Hofmann, M. Kobalz, H. Krautscheid, Adsorptive separation of C2/C3/C4-hydrocarbons on a flexible Cu-MOF: the influence of temperature, chain length and bonding character, Microporous Mesoporous Mater. 224 (2016) 392–399.
[21] J. Yang, R. Krishna, J. Li, J. Li, Experiments and simulations on separating a $CO_2$/$CH_4$ mixture using K-KFI at low and high pressures, Microporous Mesoporous Mater. 184 (2014) 21–27.
[22] X. Chen, A.M. Plonka, D. Banerjee, R. Krishna, H.T. Schaef, D. Ghose, P.K. Thallapally, J.B. Parise, Direct observation of Xe and Kr adsorption in a Xe-selective microporous metal organic framework, J. Am. Chem. Soc. 137 (2015) 7007–7010.
[23] D.-L. Chen, N. Wang, F.-F. Wang, J. Xie, Y. Zhong, W. Zhu, J.K. Johnson, R. Krishna, Utilizing gate-opening mechanism in ZIF-7 for adsorption discrimination between $N_2O$ and $CO_2$, J. Phys. Chem. C 118 (2014) 17831–17838.
[24] C.B. Fan, L.L. Gong, L. Huang, F. Luo, R. Krishna, X.F. Yi, A.M. Zheng, L. Zhang, S.Z. Pu, X.F. Feng, M.B. Luo, G.C. Guo, Significant enhancement of $C_2H_2$/$C_2H_4$ separation by a photochromic diarylethene unit: a temperature- and light-responsive separation switch, Angew. Chem. Int. Ed. 56 (2017) 7900–7906.
[25] L. Li, R. Krishna, Y. Wang, X. Wang, J. Yang, J. Li, Flexible metal–organic frameworks with discriminatory gate-opening effect for separation of acetylene from ethylene/acetylene mixtures, Eur. J. Inorg. Chem. 2016 (2016) 4457–4462, http://dx.doi.org/10.1002/ejic.201600182.
[26] L. Li, R. Krishna, Y. Wang, J. Yang, X. Wang, J. Li, Exploiting the gate opening effect in a flexible MOF for selective adsorption of propyne from C1/C2/C3 hydrocarbons, J. Mater. Chem. A 4 (2016) 751–755.
[27] L. Li, R.-B. Lin, R. Krishna, X. Wang, B. Li, H. Wu, J. Li, W. Zhou, B. Chen, Flexible − robust metal − organic framework for efficient removal of propyne from propylene, J. Am. Chem. Soc. 139 (2017) 7733–7736.
[28] L. Li, R.-B. Lin, R. Krishna, X. Wang, B. Li, H. Wu, J. Li, W. Zhou, B. Chen, Efficient separation of ethylene from acetylene/ethylene mixtures by a flexible-robust metal–organic framework, J. Mater. Chem. A 5 (2017) 18984–18988, http://dx.doi.org/10.1039/c7ta05598f.
[29] F. Luo, C. Yan, L. Dang, R. Krishna, W. Zhou, H. Wu, X. Dong, Y. Han, T.-L. Hu, M. O'Keeffe, L. Wang, M. Luo, R.-B. Lin, B. Chen, UTSA-74: A MOF-74 isomer with two accessible binding sites per metal center for highly selective gas separation, J. Am. Chem. Soc. 138 (2016) 5678–5684.
[30] W. Zhang, D. Banerjee, J. Liu, H.T. Schaef, J.V. Crum, C.A. Fernandez, R.K. Kukkadapu, Z. Nie, S.K. Nune, R.K. Motkuri, K.W. Chapman, M.H. Engelhard, J.C. Hayes, K.L. Silvers, R. Krishna, B.P. McGrail, J. Liu, P.K. Thallapally, Redox-active metal-organic composites for highly selective oxygen separation applications, Adv. Mater. 28 (2016) 3572–3577.
[31] J.W. Yoon, J.S. Lee, S. Lee, K.H. Cho, Y.K. Hwang, M. Daturi, C.-H. Jun, R. Krishna, J.-S. Chang, Adsorptive separation of acetylene from light hydrocarbons by mesoporous iron trimesate MIL-100(Fe), Chem. Eur. J. 21 (2015) 18431–18438.
[32] B. Manna, S. Mukherjee, A.V. Desai, S. Sharma, R. Krishna, S.K. Ghosh, A π-electron deficient diaminotriazine functionalized MOF for selective sorption of benzene over cyclohexane, Chem. Commun. 51 (2015) 15386–15389.
[33] R.K. Motkuri, H.V.R. Annapureddy, M. Vijaykumar, T. Schaef, P.F. Martin, B.P. McGrail, L.X. Dang, R. Krishna, P.K. Thallapally, Fluorocarbon adsorption in hierarchical porous frameworks, Nat. Commun. 5 (2014) 4368, http://dx.doi.org/10.1038/ncomms5368.
[34] J. Duan, M. Higuchi, R. Krishna, T. Kiyonaga, Y. Tsutsumi, Y. Sato, Y. Kubota, M. Takata, S. Kitagawa, High $CO_2$/$N_2$/$O_2$/CO separation in a chemically robust porous coordination polymer with low binding energy, Chem. Sci. 5 (2014) 660–666.
[35] J. Duan, W. Jin, R. Krishna, Natural gas purification using a porous coordination polymer with water and chemical stability, Inorg. Chem. 54 (2015) 4279–4284.
[36] D.M. Ruthven, S. Farooq, K.S. Knaebel, Pressure Swing Adsorption, VCH Publishers, New York, 1994.
[37] R. Krishna, The Maxwell-Stefan description of mixture diffusion in nanoporous crystalline materials, Microporous Mesoporous Mater. 185 (2014) 30–50.
[38] R.T. Yang, Gas Separation by Adsorption Processes, Butterworth, Boston, 1987.
[39] R.T. Yang, Adsorbents: Fundamentals and Applications, John Wiley & Sons Inc, Hoboken, New Jersey, 2003.
[40] A.L. Myers, J.M. Prausnitz, Thermodynamics of Mixed Gas Adsorption, A.I.Ch.E.J. 11 (1965) 121–130.
[41] R. Krishna, J.M. van Baten, Investigating the relative influences of molecular dimensions and binding energies on diffusivities of guest species inside nanoporous crystalline materials, J. Phys. Chem. C 116 (2012) 23556–23568.
[42] Z.R. Herm, J.A. Swisher, B. Smit, R. Krishna, J.R. Long, Metal-organic frameworks as adsorbents for hydrogen purification and pre-combustion carbon dioxide capture, J. Am. Chem. Soc. 133 (2011) 5664–5667.
[43] G.T. Rochelle, Amine scrubbing for $CO_2$ capture, Science 325 (2009) 1652–1654.
[44] R. Krishna, J.M. van Baten, Investigating the validity of the knudsen prescription for diffusivities in a mesoporous covalent organic framework, Ind. Eng. Chem. Res. 50 (2011) 7083–7087.
[45] R. Krishna, J.M. van Baten, Influence of adsorption thermodynamics on guest diffusivities in nanoporous crystalline materials, Phys. Chem. Chem. Phys. 15 (2013) 7994–8016.
[46] R. Krishna, J.M. van Baten, Investigating the potential of MgMOF-74 membranes for $CO_2$ capture, J. Membr. Sci. 377 (2011) 249–260.
[47] R. Krishna, J.M. van Baten, Segregation effects in adsorption of $CO_2$ containing mixtures and their consequences for separation selectivities in cage-type zeolites, Sep. Purif. Technol. 61 (2008) 414–423.
[48] C. Chmelik, J.M. van Baten, R. Krishna, Hindering effects in diffusion of $CO_2$/$CH_4$ mixtures in ZIF-8 crystals, J. Membr. Sci. 397–398 (2012) 87–91.
[49] R. Krishna, J.M. van Baten, Using molecular dynamics simulations for elucidation of molecular traffic in ordered crystalline microporous materials, Microporous Mesoporous Mater. 258 (2018) 151–169, http://dx.doi.org/10.1016/j.micromeso.2017.09.014).
[50] R. Krishna, J.M. van Baten, A molecular dynamics investigation of the diffusion characteristics of cavity-type zeolites with 8-ring windows, Microporous Mesoporous Mater. 137 (2011) 83–91.
[51] H. Wu, J.M. Simmons, G. Srinivas, W. Zhou, T. Yildrim, Adsorption sites and binding nature of $CO_2$ in prototypical metal-organic frameworks: a combined neutron diffraction and first-principles study, J. Phys. Chem. Lett. 1 (2010) 1946–1951.
[52] T. Remy, S.A. Peter, S. Van der Perre, P. Valvekens, D.E. De Vos, G.V. Baron, J.F.M. Denayer, Selective dynamic $CO_2$ separations on Mg-MOF-74 at low pressures: a detailed comparison with 13X, J. Phys. Chem. C 117 (2013) 9301–9310.
[53] G. Kluge, T. Franke, R. Schöllner, G. Nagel, Estimation of component loadings in fixed-bed adsorption from breakthrough curves of binary gas mixtures in nontrace systems, Chem. Eng. Sci. 46 (1991) 368–371.
[54] L.M. Robeson, The upper bound revisited, J. Membr. Sci. 320 (2008) 390–400.
[55] S. Himeno, T. Tomita, K. Suzuki, K. Nakayama, S. Yoshida, Synthesis and permeation properties of a DDR-type zeolite membrane for separation of $CO_2$/$CH_4$ gaseous mixtures, Ind. Eng. Chem. Res. 46 (2007) 6989–6997.
[56] J. van den Bergh, W. Zhu, J. Gascon, J.A. Moulijn, F. Kapteijn, Separation and permeation characteristics of a DD3R zeolite membrane, J. Membr. Sci. 316 (2008) 35–45.
[57] R. Krishna, J.M. van Baten, E. García-Pérez, S. Calero, Incorporating the loading dependence of the Maxwell-Stefan diffusivity in the modeling of $CH_4$ and $CO_2$ permeation across zeolite membranes, Ind. Eng. Chem. Res. 46 (2007) 2974–2986.
[58] R. Krishna, S. Li, J.M. van Baten, J.L. Falconer, R.D. Noble, Investigation of slowing-down and speeding-up effects in binary mixture permeation across SAPO-34 and MFI membranes, Sep. Purif. Technol. 60 (2008) 230–236.
[59] S. Li, J.L. Falconer, R.D. Noble, R. Krishna, Modeling permeation of $CO_2$/$CH_4$, $CO_2$/$N_2$, and $N_2$/$CH_4$ mixtures across SAPO-34 membrane with the Maxwell-Stefan equations, Ind. Eng. Chem. Res. 46 (2007) 3904–3911.
[60] S. Li, J.L. Falconer, R.D. Noble, R. Krishna, Interpreting unary, binary and ternary mixture permeation across a SAPO-34 membrane with loading-dependent Maxwell-Stefan diffusivities, J. Phys. Chem. C 111 (2007) 5075–5082.
[61] R. Krishna, J.M. van Baten, Onsager coefficients for binary mixture diffusion in nanopores, Chem. Eng. Sci. 63 (2008) 3120–3140.
[62] G.D. Pirngruber, V. Carlier, D. Leinekugel-le-Cocq, Post-combustion $CO_2$ capture by vacuum swing adsorption using Zeolites – a feasibility study, Oil Gas Sci. Technol. 69 (2014) 989–1003.
[63] M.P. Bernal, J. Coronas, M. Menendez, J. Santamaria, Separation of $CO_2$/$N_2$ mixtures using MFI-type zeolite membranes, AIChE J. 50 (2004) 127–135.
[64] K. Kusakabe, T. Kuroda, A. Murata, S. Morooka, Formation of a Y-type zeolite membrane on a porous α-alumina tube for gas separation, Ind. Eng. Chem. Res. 36 (1997) 649–655.
[65] Y. Hasegawa, T. Tanaka, K. Watanabe, B.H. Jeong, K. Kusakabe, S. Morooka, Separation of $CO_2$-$CH_4$ and $CO_2$-$N_2$ systems using ion-exchanged FAU-type zeolite membranes with different Si/Al ratios, Korean J. Chem. Eng. 19 (2002) 309–313.
[66] Y. Hasegawa, K. Watanabe, K. Kusakabe, S. Morooka, Influence of alkali cations on permeation properties of Y-type zeolite membranes, J. Membr. Sci. 208 (2002) 415–418.
[67] J.C. White, P.K. Dutta, K. Shqau, H. Verweij, Synthesis of ultrathin zeolite Y membranes and their application for separation of carbon dioxide and nitrogen gases, Langmuir 26 (2010) 10287–10293.
[68] Z.R. Herm, R. Krishna, J.R. Long, $CO_2$/$CH_4$, $CH_4$/$H_2$ and $CO_2$/$CH_4$/$H_2$ separations at high pressures using $Mg_2$(dobdc), Microporous Mesoporous Mater. 151 (2012) 481–487.
[69] H. Wu, K. Yao, Y. Zhu, B. Li, Z. Shi, R. Krishna, J. Li, Cu-TDPAT, an *rht*-type dual-functional metal-organic framework offering significant potential for use in $H_2$ and natural gas purification processes operating at high pressures, J. Phys. Chem. C 116 (2012) 16609–16618.
[70] Y. Li, F. Liang, H. Bux, W. Yang, J. Caro, Zeolitic imidazolate framework ZIF-7 based molecular sieve membrane for hydrogen separation, J. Membr. Sci. 354

(2010) 48–54.
[71] X. Zhang, Y. Liu, S. Li, L. Kong, H. Liu, Y. Li, W. Han, K.L. Yeung, W. Zhu, W. Yang, J. Qiu, New membrane architecture with high performance: ZIF-8 membrane supported on vertically aligned ZnO nanorods for gas permeation and separation, Chem. Mater. 26 (2014) 1975–1981.
[72] D. Dubbeldam, S. Calero, T.J.H. Vlugt, R. Krishna, T.L.M. Maesen, B. Smit, United atom forcefield for alkanes in nanoporous materials, J. Phys. Chem. B 108 (2004) 12301–12313.
[73] E. García-Pérez, J.B. Parra, C.O. Ania, A. García-Sánchez, J.M. Van Baten, R. Krishna, D. Dubbeldam, S. Calero, A computational study of $CO_2$, $N_2$ and $CH_4$ adsorption in zeolites, Adsorption 13 (2007) 469–476.
[74] A.K. Rappé, C.J. Casewit, K.S. Colwel, W.A. Goddard, W.M. Skiff, UFF, A full periodic table force field for molecular mechanics and molecular dynamics simulations, J. Am. Chem. Soc. 114 (1992) 10024–10035.
[75] S.L. Mayo, B.D. Olafson, W.A. Goddard, DREIDING: a generic force field for molecular simulations, J. Phys. Chem. 94 (1990) 8897–8909.
[76] S. Sircar, T.C. Golden, Purification of hydrogen by pressure swing adsorption, Sep. Sci. Technol. 35 (2000) 667–687.
[77] A.M. Ribeiro, C.A. Grande, F.V.S. Lopes, J.M. Loureiro, A.E. Rodrigues, A parametric study of layered bed PSA for hydrogen purification, Chem. Eng. Sci. 63 (2008) 5258–5273.
[78] A.M. Banu, D. Friedrich, S. Brandani, T. Düren, A Multiscale study of MOFs as adsorbents in $H_2$ PSA purification, Ind. Eng. Chem. Res. 52 (2013) 9946–9957.
[79] W. Lu, J.P. Sculley, D. Yuan, R. Krishna, Z. Wei, H.C. Zhou, Polyamine-tethered porous polymer networks for carbon dioxide capture from flue gas, Angew. Chem. Int. Ed. 51 (2012) 7480–7484.
[80] W. Lu, J.P. Sculley, D. Yuan, R. Krishna, H.C. Zhou, Carbon dioxide capture from air using amine-grafted porous polymer networks, J. Phys. Chem. C 117 (2013) 4057–4061.
[81] T.M. McDonald, W.R. Lee, J.A. Mason, B.M. Wiers, C.S. Hong, J.R. Long, Capture of carbon dioxide from air and flue gas in the alkylamine-appended metal-organic framework mmen-$Mg_2$(dobpdc), J. Am. Chem. Soc. 134 (2012) 7056–7065.
[82] T.M. McDonald, D.M. D'Alessandro, R. Krishna, J.R. Long, Enhanced carbon dioxide capture upon incorporation of *N*, N′- dimethylethylenediamine in the metal-organic framework CuBTTri, Chem. Sci. 2 (2011) 2022–2028.
[83] O. Shekhah, Y. Belmabkhout, Z. Chen, V. Guillerm, A. Cairns, K. Adil, M. Eddaoudi, Made-to-order metal-organic frameworks for trace carbon dioxide removal and air capture, Nat. Commun. 5 (2014) 4228, http://dx.doi.org/10.1038/ncomms5228.
[84] E.S. Sanz-Pérez, C.R. Murdock, S.A. Didas, C.W. Jones, Direct capture of $CO_2$ from ambient air, Chem. Rev. 116 (2016) 11840–11876.
[85] W. Harwood, Spacewalk Cut Short by Spacesuit CO2 Buildup, CNET, California, < https://www.cnet.com/news/spacewalk-cut-short-by-spacesuit-co2-buildup/ > , 22 July 2009.
[86] H. Bux, C. Chmelik, R. Krishna, J. Caro, Ethene/ethane separation by the MOF membrane ZIF-8: molecular correlation of permeation, adsorption, diffusion, J. Membr. Sci. 369 (2011) 284–289.
[87] Y. Pan, T. Li, G. Lestari, Z. Lai, Effective separation of propylene/propane binary mixtures by ZIF-8 membranes, J. Membr. Sci. 390–391 (2012) 93–98.
[88] D. Liu, X. Ma, H. Xi, Y.S. Lin, Gas transport properties and propylene/propane separation characteristics of ZIF-8 membranes, J. Membr. Sci. 451 (2014) 85–93.
[89] U. Böhme, B. Barth, C. Paula, A. Kuhnt, W. Schwieger, A. Mundstock, J. Caro, M. Hartmann, Ethene/ethane and propene/propane separation via the olefin and paraffin selective metal – organic framework adsorbents CPO-27 and ZIF-8, Langmuir 29 (2013) 8592–8600.
[90] S.J. Geier, J.A. Mason, E.D. Bloch, W.L. Queen, M.R. Hudson, C.M. Brown, J.R. Long, Selective adsorption of ethylene over ethane and propylene over propane in the metal–organic frameworks $M_2$(dobdc) (M = Mg, Mn, Fe Co, Ni, Zn), Chem. Sci. 4 (2013) 2054–2061.
[91] A. Cadiau, K. Adil, P.M. Bhatt, Y. Belmabkhout, M. Eddaoudi, A metal-organic framework-based splitter for separating propylene from propane, Science 353 (2016) 137–140.
[92] F.A. Da Silva, A.E. Rodrigues, Propylenepropane separation by vacuum swing adsorption using 13X zeolite, AIChE J. 47 (2001) 341–357.
[93] C.A. Grande, F. Poplow, A.E. Rodrigues, Vacuum pressure swing adsorption to produce polymer-grade polypropylene, Sep. Sci. Technol. 45 (2010) 1252–1259.
[94] C. Gücüyener, J. van den Bergh, J. Gascon, F. Kapteijn, Ethane/ethene separation turned on its head: selective ethane adsorption on the metal-organic framework ZIF-7 through a gate-opening mechanism, J. Am. Chem. Soc. 132 (2010) 17704–17706.
[95] J. Kim, L.-C. Lin, R.L. Martin, J.A. Swisher, M. Haranczyk, B. Smit, Large-scale computational screening of zeolites for ethane/ethene separation, Langmuir 28 (2012) 11914–11919.
[96] D.-L. Chen, N. Wang, C. Xu, G. Tu, W. Zhu, R. Krishna, A combined theoretical and experimental analysis on transient breakthroughs of $C_2H_6/C_2H_4$ in fixed beds packed with ZIF-7, Microporous Mesoporous Mater. 208 (2015) 55–65.
[97] W. Liang, F. Xu, X. Zhou, J. Xiao, Q. Xia, Y. Li, Z. Li, Ethane selective adsorbent Ni(bdc)$(ted)_{0.5}$ with high uptake and its significance in adsorption separation of ethane and ethylene, Chem. Eng. Sci. 148 (2016) 275–281.
[98] Y. Chen, Z. Qiao, H. Wu, D. Lv, R. Shi, Q. Xia, J. Zhou, Z. Li, An ethane-trapping MOF PCN-250 for highly selective adsorption of ethane over ethylene, Chem. Eng. Sci. 175 (2018) 110–117, http://dx.doi.org/10.1016/j.ces.2017.09.032.
[99] T.L. Hu, H. Wang, B. Li, R. Krishna, H. Wu, W. Zhou, Y. Zhao, Y. Han, X. Wang, W. Zhu, Z. Yao, S.C. Xiang, B. Chen, A microporous metal-organic framework with dual functionalities for highly efficient removal of acetylene from ethylene/acetylene mixtures at room temperature, Nat. Commun. 6 (2015) 7328, http://dx.doi.org/10.1038/ncomms8328.
[100] B. Li, X. Cui, D. O'Nolan, H.-M. Wen, M. Jiang, R. Krishna, H. Wu, R.-B. Lin, Y.-S. Chen, D. Yuan, H. Xing, W. Zhou, Q. Ren, G. Qian, M.J. Zaworotko, B. Chen, An ideal molecular sieve for acetylene removal from ethylene with record selectivity and productivity, Adv. Mater. 2017 (2017) 1704210, http://dx.doi.org/10.1002/adma.201704210).
[101] G. Narin, A.M. Ribeiro, A. Ferreira, Y.K. Hwang, U.-H. Lee, J.M. Loureiro, J.-S. Chang, A.E. Rodrigues, Propylene/nitrogen separation in a by-stream of the polypropylene production: from pilot test and model validation to industrial scale process design and optimization, Ind. Eng. Chem. Res. 53 (2014) 9199–9213.
[102] A.M. Ribeiro, M.C. Campo, G. Narin, J.C. Santos, A. Ferreira, J.-S. Chang, Y.K. Hwang, Y.-K. Seo, U.-H. Lee, J.M. Loureiro, A.E. Rodrigues, Pressure swing adsorption process for the separation of nitrogen and propylene with a MOFadsorbent MIL-100(Fe), Sep. Purif. Technol. 110 (2013) 101–111.
[103] R. Krishna, J.M. van Baten, Screening of zeolite adsorbents for separation of hexane isomers: a molecular simulation study, Sep. Purif. Technol. 55 (2007) 246–255.
[104] T.J.H. Vlugt, R. Krishna, B. Smit, Molecular simulations of adsorption isotherms for linear and branched alkanes and their mixtures in silicalite, J. Phys. Chem. B 103 (1999) 1102–1118.
[105] D. Dubbeldam, S. Calero, T.J.H. Vlugt, R. Krishna, T.L.M. Maesen, E. Beerdsen, B. Smit, Force field parametrization through fitting on inflection points in isotherms, Phys. Rev. Lett. 93 (2004) 088302.
[106] D. Peralta, K. Barthelet, J. Pérez-Pellitero, C. Chizallet, G. Chaplais, A. Simon-Masseron, G.D. Pirngruber, Adsorption and separation of Xylene isomers: CPO-27-Ni vs HKUST-1 vs NaY, J. Phys. Chem. C 116 (2012) 21844–21855.
[107] R. Krishna, Separating mixtures by exploiting molecular packing effects in microporous materials, Phys. Chem. Chem. Phys. 17 (2015) 39–59.
[108] R. Krishna, J.M. van Baten, Commensurate-incommensurate adsorption and diffusion in ordered crystalline microporous materials, Phys. Chem. Chem. Phys. 19 (2017) 20320–20337.
[109] S. Mukherjee, B. Joarder, B. Manna, A.V. Desai, A.K. Chaudhari, S.K. Ghosh, Framework-flexibility driven selective sorption of p-Xylene over other isomers by a dynamic metal-organic framework, Sci. Rep. 4 (2014) 5761, http://dx.doi.org/10.1038/srep05761.
[110] S.M. Humphrey, J.-S. Chang, S.H. Jhung, J.W. Yoon, P.T. Wood, Porous cobalt (II)–organic frameworks with corrugated walls: structurally robust gas-sorption materials, Angew. Chem. Int. Ed. 46 (2007) 272–275.
[111] J.W. Yoon, J.S. Lee, G.W. Piburn, K.H. Cho, K. Jeon, H.-K. Lim, H. Kim, C.-H. Jun, S.M. Humphrey, R. Krishna, J.-S. Chang, Highly Selective Adsorption of p-Xylene over other C8 Aromatic Hydrocarbons by Co-CUK-1: A Combined Experimental and Theoretical Assessment, Dalton Trans. 5 (2017) 5–50, http://dx.doi.org/10.1039/C7DT03304D.
[112] J.J. Gutierrez-Sevillano, S. Calero, R. Krishna, Selective adsorption of water from mixtures with 1-alcohols by exploitation of molecular packing effects in CuBTC, J. Phys. Chem. C 119 (2015) 3658–3666.
[113] J.J. Gutierrez-Sevillano, S. Calero, R. Krishna, Separation of benzene from mixtures with water, methanol, ethanol, and acetone: highlighting hydrogen bonding and molecular clustering influences in CuBTC, Phys. Chem. Chem. Phys. 17 (2015) 20114–20124.
[114] H.W. Habgood, The kinetics of molecular sieve action. Sorption of nitrogen-methane mixtures by linde molecular sieve 4A, Canad. J. Chem. 36 (1958) 1384–1397.
[115] S.J. Bhadra, S. Farooq, Separation of methanenitrogen mixture by pressure swing adsorption for natural gas upgrading, Ind. Eng. Chem. Res. 50 (2011) 14030–14045.
[116] B. Majumdar, S.J. Bhadra, R.P. Marathe, S. Farooq, Adsorption and diffusion of methane and nitrogen in barium exchanged ETS-4, Ind. Eng. Chem. Res. 50 (2011) 3021–3034.
[117] S. Farooq, M.N. Rathor, K. Hidajat, A Predictive model for a kinetically controlled pressure swing adsorption separation process, Chem. Eng. Sci. 48 (1993) 4129–4141.
[118] S. Farooq, Sorption and diffusion of oxygen and nitrogen in molecular- sieve RS-10, Gas Sep. Purif. 9 (1995) 205–212.
[119] Y.D. Chen, R.T. Yang, P. Uawithya, Diffusion of oxygen, nitrogen and their mixtures in carbon molecular-sieve, AIChE J. 40 (1994) 577–585.
[120] S. Sircar, A.L. Myers, Gas Separation by zeolites, Handbook of Zeolite Science and Technology Vol. pp (2003) 1063–1104.
[121] R. Krishna, A Maxwell-Stefan-glueckauf description of transient mixture uptake in microporous adsorbents, Sep. Purif. Technol. 191 (2018) 392–399, http://dx.doi.org/10.1016/j.seppur.2017.09.057.
[122] R. Krishna, Diffusion in porous crystalline materials, Chem. Soc. Rev. 41 (2012) 3099–3118.
[123] R. Krishna, J.M. van Baten, Screening metal-organic frameworks for separation of pentane isomers, Phys. Chem. Chem. Phys. 19 (2017) 8380–8387.
[124] B. Saccoccia, A.M. Bohnsack, N.W. Waggoner, K.H. Cho, J.S. Lee, D.-Y. Hong, V.M. Lynch, J.-S. Chang, S.M. Humphrey, Separation of p-divinylbenzene by selective room-temperature adsorption inside Mg-CUK-1 prepared by aqueous microwave synthesis, Angew. Chem. Int. Ed. 54 (2015) 5394–5398.

*Supplementary Material to accompany:*

# Methodologies for Screening and Selection of Crystalline Microporous Materials in Mixture Separations

**Rajamani Krishna**

Van 't Hoff Institute for Molecular Sciences, University of Amsterdam, Science Park 904,

1098 XH Amsterdam, The Netherlands

*CORRESPONDING AUTHOR Tel +31 20 6270990; Fax: + 31 20 5255604;

email: r.krishna@contact. uva.nl

**Table of Contents**

# 1. Preamble

This Supplementary material accompanying our manuscript *Methodologies for Screening and Selection of Crystalline Microporous Materials in Mixture Separations* provides:

(a) Detailed structural information on all of the zeolites, and MOFs analyzed and discussed in the article

(b) Details of the IASTcalculations for mixture adsorption equilibrium,

(c) Summary of the Maxwel-Stefan formulation for mixture diffusion in zeolites and MOFs

(d) Modeling of transient breakthroughs in fixed bed adsorbers

(e) Influence of intra-crystalline diffusion on separations in fixed beds

(f) Further background details of screening of MOFs for separation of hexane isomers, xylene isomers, ethylbenzene/styrene, and benzene/cyclohexane mixtures.

# 2. Structural topology and connectivity of some common zeolites, MOFs, and ZIFs

The pore landscape, topology, and connectivity of the microporous host structures also show a wide diversity. These include: one-dimensional (1D) channels (e.g. AFI, LTL, MTW, TON, MIL-47, MIL-53, Co(BDP), $Fe_2(BDP)_3$), 1D zig-zag channels (e.g. CoFormate, MnFormate), 1D channels with side pockets (e.g. MOR, FER), intersecting channels (e.g. MFI, BEA, BOG, Zn(bdc)dabco, Co(bdc)dabco), cavities with large windows (e.g. FAU, NaX, NaY, IRMOF-1, CuBTC), and cages separated by narrow windows (e.g. LTA, CHA, DDR, TSC, ERI, ZIF-8).

The crystallographic data are available on the zeolite atlas website of the International Zeolite Association (IZA).[1, 2] Further details on the structure, landscape, pore dimensions of a very wide variety of micro-porous materials are available in the published literature.[3-10]

The pore topology and structural details of the crystalline structures that are discussed and analyzed in this article are provided in the accompanying Figures as indicated below; further details are provided by Krishna and van Baten.[11-13]

## 3. Structural information for 1D channel structures

The pore landscape and structural details of all-silica AFI are provided in Figure 1.

The pore landscape and structural details of all-silica LTL are provided in Figure 2.

The pore landscape and structural details of all-silica MTW are provided in Figure 3.

The pore landscape and structural details of all-silica TONW are provided in Figure 4.

Co-Formate (Figure 5). Its synthesis is reported by Li et al.[14] The network exhibits diamondoid connectivity and the overall framework gives rise to zig-zag channels along the *b* axis. The effective pore size of these one-dimensional channels is 5 – 6 Å; one unit cell of Co-FA comprises a total of four distinct channel "segments"; each channel segment forms part of the repeat zig-zag structure.

The pore landscape and structural details for MIL-47 are provided in Figure 6.

The pore landscape and structural data for MIL-53(Cr) are shown in Figure 7.

The structural information for Co(BDP) with ($BDP^{2-}$ = 1,4-benzenedipyrazolate) is from Choi et al.[15] and Salles et al.[16] The structural data, and pore landscapes a are provided in Figures 8, and 9.

The structural information for CuBTT is from Demessence et al.[17] The structural data, and pore landscapes are provided in Figures 10, and 11.

For $Fe_2(BDP)_3$ ($BDP^{2-}$ = 1,4-benzenedipyrazolate), we used the structural data published by Herm et al.[18] For appreciation of the pore structure of $Fe_2(BDP)_3$ the pore landscapes were constructed using the structural information. The channels are triangular in shape, with a pore size of 4.9 Å, as determined from molecular simulations. The structural data, and pore landscapes along with snapshots of pentane and hexane isomers are provided in Figures 12, 13, 14.

The structural information on MgMOF-74 ( = $Mg_2$(dobdc) = Mg\(dobdc) with dobdc = ($dobdc^{4-}$ = 1,4-dioxido-2,5-benzenedicarboxylate)), ZnMOF-74 (= $Zn_2$(dobdc) = Zn\(dobdc)), were obtained from a variety of references.[19-24] The structural data, and pore landscapes of MgMOF-74 are provided in Figures 15, and 16. The structural data, and pore landscapes of ZnMOF- are provided in Figures 17, and 18.

The pore landscapes and structural details of CoMOF-74, NiMOF-74, and FeMOF-74 are shown in Figures 19, 20, and 21.

The pore landscape and structural details of ZnHBDC are provided in Figure 22.

The structural data for ZIF-77 were taken from Dubbeldam et al.[25] The characteristic pore size of ZIF-77 is 4.5 Å, significantly smaller than the 4.9 Å sized triangular channels of $Fe_2(BDP)_3$. The structural data, and pore landscapes are provided in Figures 23, 24.

## 4. Structural information for 1D channel structures with side pockets

MOR zeolite (Mordenite) consists of 12-ring (7.0 Å × 6.5 Å) 1D channels, connected to 8-ring (5.7 Å × 2.6 Å) pockets; the pore landscapes and structural details are provided in Figures 25, and 26.

FER zeolite; see Figures 27, 28.

## 5. Structural information for cage structures with narrow windows

AFX zeolite consists of cages of volume 490 $Å^3$, separated by 3.4 Å × 3.9 Å windows; the cages are also connected to pockets of 98$Å^3$ by 3.1 Å × 4.62 Å windows; see Figures 29, and 30.

CHA zeolite consists of cages of volume 316 $Å^3$, separated by 3.8 Å × 4.2 Å 8-ring windows as shown in Figure 31. SAPO-34 has the same structural topology of CHA zeolite.

DDR (cages of 277.8 $Å^3$ volume, separated by 3.65 Å × 4.37 Å 8-ring windows; the pore landscapes and structural details are provided in Figure 32).

ERI (cages of 408.7 $Å^3$ volume, separated by 3.8 Å × 4.9 Å 8-ring windows; the pore landscapes and structural details are provided in Figure 33).

The pore landscape and structural details of ITQ-29 are provided in Figure 34.

LTA, LTA-5A, LTA-4A (cages of 743 $Å^3$ volume, separated by 4.11 Å × 4.47 Å 8-ring windows; the pore landscapes and structural details are provided in Figures 35, 36, and 37).

Per unit cell, LTA-5 has 96 Si, 96 Al, 32 $Na^+$, 32 $Ca^{++}$ with Si/Al=1.

Per unit cell LTA-4A has 96 Si, 96 Al, 96 $Na^+$, Si/Al=1.

The pore landscape and structural details for ZIF-7 are provided in Figure 38.

ZIF-8 (cages of 1168 $Å^3$ volume, separated by 3.3 Å windows; the pore landscapes and structural details are provided in Figure 39).

Customized for $C_3H_6/C_3H_8$ separations, Cadiau et al.[26] report the synthesis of NbOFFIVE-1-Ni (= KAUST-7), that belongs to the same class of SIFSIX materials, using pyrazine as the organic linker; see Figure 40. The $(SiF_6)^{2-}$ pillars in the cage are replaced with somewhat bulkier $(NbOF_5)^{2-}$ pillars. This causes tilting of the pyrazine molecule on the linker, effectively reducing the aperture opening from 0.50 nm [with $(SiF_6)^{2-}$ pillars] to 0.30 nm. The small aperture permits ingress of the smaller $C_3H_6$ molecules, but practically excludes $C_3H_8$ on the basis of subtle differences in bond lengths and bond angles.

# 6. Structural information for intersecting channel structures

MFI zeolite (also called silicalite-1) has a topology consisting of a set of intersecting straight channels, and zig-zag (or sinusoidal) channels of 5.4 Å × 5.5 Å and 5.4 Å × 5.6 Å size. The pore landscapes and structural details are provided in Figures 41, and 42. The crystal framework density $\rho = 1796$ kg m$^{-3}$. The pore volume $V_p = 0.165$ cm$^3$/g.

The pore landscapes and structural details for ISV zeolite are provided in Figure 43.

The pore landscapes and structural details for BEA zeolite are provided in Figures 44, 45.

The pore landscapes and structural details for BOG zeolite are provided in Figures 46, 47.

The pore landscape and structural details of GME zeolite are provided in Figure 48.

The structural information for Zn(bdc)dabco is from Bárcia et al.[27] and Lee et al. [28] The structural data, and pore landscapes, are provided in Figures 49, 50, and 51.

Cui et al. [29] report a series of coordination networks composed of inorganic anions of $(SiF_6)^{2-}$ (hexafluorosilicate, SIFSIX), that offer potential for separation of $C_2H_2/C_2H_4$ mixtures. In these SIFSIX materials, two-dimensional (2D) nets of organic ligand (= pyridine) and metal (Cu, Ni, or Zn) node are pillared with $(SiF_6)^{2-}$ anions in the third dimension to form 3D coordination networks that have primitive cubic topology; Figure 52a shows the structure of SIFSIX-1-Cu (1

= 4,4'-bipyridene). The pore sizes within this family of materials can be systematically tuned by changing the length of the organic linkers, the metal node, and/or the framework interpenetration. Figure 52b shows the structure SIFSIX-2-Cu-i (2 = 4,4'-dipyridylacetylene, i = interpenetrated); in this case, each $C_2H_2$ molecule is bound by two F atoms from different nets. The binding of $C_2H_4$ with the F atoms is weaker because it is far less acidic than $C_2H_2$.

## 7. Structural information for cages separated by large windows

FAU-Si (= all-silica FAU) (cages of 408.7 $Å^3$ volume, separated by 3.8 Å × 4.9 Å 8-ring windows; See Figure 53.

Figure 54 provides structural details of NaY zeolite with 138 Si, 54 Al, 54 $Na^+$, Si/Al=2.55.

Figure 55 shows the structural details of NaX (= 86 $Na^+$/uc = 13X) zeolite. Per unit cell of NaX zeolite we have 106 Si, 86 Al, 86 $Na^+$ with Si/Al=1.23. Also shown are the snapshots of $CO_2$ and $CH_4$ in the cages.

For IRMOF-1 (= MOF 5 = $Zn_4O(BDC)_3$ with $BDC^{2-}$ = 1-4 benzenedicarboxylate), we used the structural data published by Dubbeldam et al. [30, 31] The structural data, and pore landscapes are provided in Figures **56**, and 57.

CuBTC (= $Cu_3(BTC)_2$ with BTC = 1,3,5-benzenetricarboxylate, also known as HKUST-1) framework is composed of copper atoms connected by benzene-1,3,5-tricarboxylate (BTC) linkers, which form a characteristic paddle-wheel structure: two copper atoms bonded to the oxygen atoms of four BTC linkers, generating four-connected square-planar vertexes; see Figures 58, and 59. The framework contains two types of large cavities (9 Å diameter) and small cavities (of 5 Å diameter). The larger cavities ($L_2$ and $L_3$) are similar in size and shape but as a result of the paddle-wheel, the copper atoms are only accessible from the $L_3$ cages. $L_2$ and $L_3$ cavities are connected through triangular-shaped windows. The small cavities ($T_1$) are tetrahedral

pockets enclosed by the benzene rings; these are connected to $L_3$ cages by small triangular windows (3.5 Å in size), as shown in Figure 60.

The structural information for MOF-177 (= $Zn_4O(BTB)_2$ with ($BTB^{3-}$ = 1,3,5-benzenetribenzoate)) is provided by Chae et al.[32] The structural data, and pore landscapes, along with snapshots of alkanes are provided in Figures 61, 62, 63.

# 8. Summary of IAST calculation methodology

Within microporous crystalline materials, the guest molecules exist in the adsorbed phase. The Gibbs adsorption equation[33] in differential form is

$$Ad\pi = \sum_{i=1}^{n} q_i d\mu_i \qquad (1)$$

The quantity $A$ on the left side of Equation (1) is the surface area per kg of framework, with units of $m^2$ per kg of the framework of the crystalline material; $q_i$ is the molar loading of component $i$ in the adsorbed phase with units moles per kg of framework; $\mu_i$ is the molar chemical potential of component $i$. The spreading pressure $\pi$ has the same units as surface tension, i.e. N $m^{-1}$.

The chemical potential of any component in the adsorbed phase, $\mu_i$, equals that in the bulk fluid phase. If the partial fugacities in the bulk fluid phase are $f_i$, we have

$$d\mu_i = RTd \ln f_i \qquad (2)$$

where $R$ is the gas constant (= 8.314 J $mol^{-1}$ $K^{-1}$).

Briefly, the basic equation of Ideal Adsorbed Solution Theory (IAST) of Myers and Prausnitz[34] is the analogue of Raoult's law for vapor-liquid equilibrium, i.e.

$$f_i = P_i^0 x_i; \quad i = 1,2,...n \qquad (3)$$

where $x_i$ is the mole fraction in the adsorbed phase

$$x_i = \frac{q_i}{q_1 + q_2 + ...q_n} \tag{4}$$

and $P_i^0$ is the pressure for sorption of every component *i*, which yields the same spreading pressure, $\pi$ for each of the pure components, as that for the mixture:

$$\frac{\pi A}{RT} = \int_0^{P_1^0} \frac{q_1^0(f)}{f} df = \int_0^{P_2^0} \frac{q_2^0(f)}{f} df = \int_0^{P_3^0} \frac{q_3^0(f)}{f} df = ... \tag{5}$$

where $q_i^0(f)$ is the *pure* component adsorption isotherm. The molar loadings $q_i^0(f)$ are expressed in the units of moles adsorbed per kg of framework, i.e. mol kg$^{-1}$. The units of $\frac{\pi A}{RT}$, also called the adsorption potential,[35] are mol kg$^{-1}$. If the isotherm fits are expressed in terms of molecules per unit cell, then the units of $\frac{\pi A}{RT}$ are also in molecules per unit cell.

The unary isotherm may be described by say the 1-site Langmuir isotherm

$$q^0(f) = q_{sat} \frac{bf}{1+bf}; \quad \theta = \frac{bf}{1+bf} \tag{6}$$

where we define the fractional *occupancy* of the adsorbate molecules, $\theta = q^0(f)/q_{sat}$. The superscript 0 is used to emphasize that $q^0(f)$ relates the *pure component* loading to the bulk fluid fugacity. More generally, the unary isotherms may need to be described by the dual-Langmuir-Freundlich model

$$q^0(f) = q_{A,sat} \frac{b_A f^{\nu A}}{1+b_A f^{\nu A}} + q_{B,sat} \frac{b_B f^{\nu B}}{1+b_B f^{\nu B}} \tag{7}$$

or the 3-site Langmuir-Freundlich model:

$$q^0 = q_{A,sat}\frac{b_A f^{\nu_A}}{1+b_A f^{\nu_A}} + q_{B,sat}\frac{b_B f^{\nu_B}}{1+b_B f^{\nu_B}} + q_{c,sat}\frac{b_C f^{\nu_C}}{1+b_C f^{\nu_C}} \tag{8}$$

Each of the integrals in Equation (5) can be evaluated analytically. For the 3-site Langmuir-Freundlich isotherm, the integration yields for component *i*,

$$\begin{aligned}
\int_{f=0}^{P_i^0} \frac{q^0(f)}{f}df &= \frac{q_{A,sat}}{\nu_A}\ln\left(1+b_A\left(P_i^0\right)^{\nu_A}\right) + \frac{q_{B,sat}}{\nu_B}\ln\left(1+b_B\left(P_i^0\right)^{\nu_B}\right) + \frac{q_{c,sat}}{\nu_C}\ln\left(1+b_C\left(P_i^0\right)^{\nu_C}\right) \\
\int_{f=0}^{P_i^0} \frac{q^0(f)}{f}df &= \frac{q_{A,sat}}{\nu_A}\ln\left(1+b_A\left(\frac{f_i}{x_i}\right)^{\nu_A}\right) + \frac{q_{B,sat}}{\nu_B}\ln\left(1+b_B\left(\frac{f_i}{x_i}\right)^{\nu_B}\right) + \frac{q_{c,sat}}{\nu_C}\ln\left(1+b_C\left(\frac{f_i}{x_i}\right)^{\nu_C}\right)
\end{aligned} \tag{9}$$

The right hand side of equation (9) is a function of $P_i^0$. For multicomponent mixture adsorption, each of the equalities on the right hand side of Equation (5) must satisfied. For specified partial fugacities in the bulk fluid phase, $f_i$, these constraints may be solved using a suitable root-finder, to yield the set of values of the adsorbed phase mole fractions, $x_i$, and $P_i^0$, all of which must satisfy Equation (5). The corresponding values of the integrals using these as upper limits of integration must yield the same value of $\frac{\pi A}{RT}$ for each component; this ensures that the obtained solution is the correct one.

A key assumption of the IAST is that the enthalpies and surface areas of the adsorbed molecules do not change upon mixing. If the total mixture loading is $q_t$, the area covered by the adsorbed mixture is $\frac{A}{q_t}$ with units of $m^2$ (mol mixture)$^{-1}$. Therefore, the assumption of no surface area change due to mixture adsorption translates as $\frac{A}{q_t} = \frac{Ax_1}{q_1^0\left(P_1^0\right)} + \frac{Ax_2}{q_2^0\left(P_2^0\right)} + \cdots \frac{Ax_n}{q_n^0\left(P_n^0\right)}$; the total mixture loading is $q_t$ is calculated from

$$q_t \equiv q_1 + q_2 ... + q_n = \frac{1}{\frac{x_1}{q_1^0(P_1^0)} + \frac{x_2}{q_2^0(P_2^0)} + .... + \frac{x_n}{q_n^0(P_n^0)}} \tag{10}$$

in which $q_1^0(P_1^0)$, $q_2^0(P_2^0)$,… $q_n^0(P_n^0)$ are determined from the unary isotherm fits, using the sorption pressures for each component $P_1^0$, $P_2^0$, $P_3^0$,.. $P_n^0$ that are available from the solutions to equations (9), and (10).

The set of equations (3), (4), (5), (7), (8), (9), and (10) need to be solved numerically to obtain the loadings, $q_i$ of the individual components in the mixture.

## 9. The Maxwell-Stefan description of *n*-component mixture permeation across microporous membranes

The Maxwell-Stefan (M-S) equations represent a balance between the force exerted per mole of species *i* with the drag, or friction, experienced with each of the partner species in the mixture. The M-S equations for *n*-component diffusion in zeolites, MOFs, and ZIFs take the form[4, 36, 37]

$$-\rho \frac{q_i}{RT} \frac{d\mu_i}{dz} = \sum_{\substack{j=1 \\ j \neq i}}^{n} \frac{x_j N_i - x_i N_j}{Đ_{ij}} + \frac{N_i}{Đ_i}; \quad i = 1,2,..n \tag{11}$$

The $N_i$ as the number of moles of species *i* transported per m$^2$ of crystalline material per second

$$N_i \equiv \rho q_i u_i \tag{12}$$

where $\rho$ is the framework density with units of kg m$^{-3}$. The mole fractions of the components in the adsorbed phase, $x_i = q_i / q_t$ where $q_i$ is the molar loading of adsorbate, and $q_t$ is the *total* mixture loading $q_t = \sum_{i=1}^{n} q_i$. The M-S diffusivity $Đ_{ij}$ has the units m$^2$ s$^{-1}$ and the physical

significance of an *inverse* drag coefficient. At the molecular level, the $Đ_{ij}$ reflect how the facility for transport of species *i correlates* with that of species *j*; they are also termed *exchange coefficients*. An important, persuasive, argument for the use of the M-S formulation for mixture diffusion is that the M-S diffusivity $Đ_i$ in mixtures can be estimated using information on the loading dependence of the corresponding unary diffusivity values.

The Maxwell-Stefan diffusion formulation is consistent with the theory of irreversible thermodynamics. The Onsager Reciprocal Relations imply that the M-S pair diffusivities are symmetric

$$Đ_{ij} = Đ_{ji} \tag{13}$$

At thermodynamic equilibrium, the chemical potential of component *i* in the bulk gas mixture equals the chemical potential of that component in the adsorbed phase within the membrane at both upstream and downstream faces. For the bulk gas phase mixture we have

$$\frac{1}{RT}\frac{d\mu_i}{dz} = \frac{d\ln f_i}{dz} = \frac{1}{p_i}\frac{df_i}{dz}; \quad i = 1,2 \tag{14}$$

The chemical potential gradients $d\mu_i/dz$ can be related to the gradients of the molar loadings, $q_i$, by defining thermodynamic correction factors $\Gamma_{ij}$

$$\frac{q_i}{RT}\frac{d\mu_i}{dz} = \sum_{j=1}^{n}\Gamma_{ij}\frac{dq_j}{dz}; \quad \Gamma_{ij} = \frac{q_i}{f_i}\frac{\partial f_i}{\partial q_j}; \quad i, j = 1,....n \tag{15}$$

The thermodynamic correction factors $\Gamma_{ij}$ can be calculated by numerical differentiation of the RAST model describing mixture adsorption equilibrium. In some special cases, the mixed-gas Langmuir model

$$\frac{q_i}{q_{i,sat}} = \theta_i = \frac{b_i f_i}{1 + \sum_{i=1}^{n} b_i f_i}; \quad i = 1,2,...n \tag{16}$$

may be of adequate accuracy. Analytic differentiation of equation (16) yields

$$\Gamma_{ij} = \delta_{ij} + \left(\frac{q_{i,sat}}{q_{j,sat}}\right)\left(\frac{\theta_i}{\theta_V}\right); \quad i, j = 1,2 \ldots n \tag{17}$$

where the fractional vacancy $\theta_V$ is defined as

$$\theta_V = 1 - \theta_t = 1 - \sum_{i=1}^{n} \theta_i \tag{18}$$

The elements of the matrix of thermodynamic factors $\Gamma_{ij}$ can be calculated explicitly from information on the component loadings $q_i$ in the adsorbed phase; this is the persuasive advantage of the use of the mixed-gas Langmuir model. By contrast, the IAST does not allow the calculation of $\Gamma_{ij}$ explicitly from knowledge on the component loadings $q_i$ in the adsorbed phase; an numerical procedure is required.

Specifically for binary mixtures, the mixed-gas Langmuir model is

$$\theta_i = \frac{q_i}{q_{i,sat}} = \frac{b_i f_i}{1 + b_1 f_1 + b_2 f_2}; \quad i = 1,2 \tag{19}$$

and the four elements of the matrix of thermodynamic factors $\begin{bmatrix} \Gamma_{11} & \Gamma_{12} \\ \Gamma_{21} & \Gamma_{22} \end{bmatrix}$ are:[38]

$$\begin{bmatrix} \Gamma_{11} & \Gamma_{12} \\ \Gamma_{21} & \Gamma_{22} \end{bmatrix} = \frac{1}{1 - \theta_1 - \theta_2} \begin{bmatrix} 1 - \theta_2 & \frac{q_{1,sat}}{q_{2,sat}} \theta_1 \\ \frac{q_{2,sat}}{q_{1,sat}} \theta_2 & 1 - \theta_1 \end{bmatrix} \tag{20}$$

The persuasive advantage of equation (20) is that the matrix of thermodynamic correction factors can be determined explicitly from the component loadings, and occupancies, without the need for numerical differentiation.

For binary mixture diffusion inside zeolites, MOFs, and ZIFs, the Maxwell-Stefan equations (11) are written as

$$\begin{aligned} -\rho \frac{q_1}{RT}\frac{d\mu_1}{dz} &= \frac{x_2 N_1 - x_1 N_2}{Đ_{12}} + \frac{N_1}{Đ_1} \\ -\rho \frac{q_2}{RT}\frac{d\mu_2}{\partial z} &= \frac{x_1 N_2 - x_2 N_1}{Đ_{12}} + \frac{N_2}{Đ_2} \end{aligned} \tag{21}$$

The first members on the right hand side of Equation (21) are required to quantify slowing-down effects that characterize binary mixture diffusion.[3, 5, 7] There is no experimental technique for direct determination of the exchange coefficients $Đ_{12}$, that quantify molecule-molecule interactions.

Let us define the square matrix $[B]$

$$[B] = \begin{bmatrix} \frac{1}{Đ_1} + \frac{x_2}{Đ_{12}} & -\frac{x_1}{Đ_{12}} \\ -\frac{x_2}{Đ_{12}} & \frac{1}{Đ_2} + \frac{x_1}{Đ_{12}} \end{bmatrix} \tag{22}$$

Equation (21) can be re-cast into 2-dimensional matrix notation

$$-\rho \begin{pmatrix} \frac{q_1}{RT}\frac{d\mu_1}{dz} \\ \frac{q_2}{RT}\frac{d\mu_2}{dz} \end{pmatrix} = [B]\begin{pmatrix} N_1 \\ N_2 \end{pmatrix}; \quad \begin{pmatrix} N_1 \\ N_2 \end{pmatrix} = -\rho [B]^{-1} \begin{pmatrix} \frac{q_1}{RT}\frac{d\mu_1}{dz} \\ \frac{q_2}{RT}\frac{d\mu_2}{dz} \end{pmatrix} \tag{23}$$

We define the square matrix $[\Lambda] \equiv [B]^{-1}$; The inverse of the square matrix $[B]$ can be obtained explicitly

$$[\Lambda] \equiv [B]^{-1} = \frac{1}{1+\frac{x_1 Đ_2}{Đ_{12}}+\frac{x_2 Đ_1}{Đ_{12}}} \begin{bmatrix} Đ_1\left(1+\frac{x_1 Đ_2}{Đ_{12}}\right) & \frac{x_1 Đ_1 Đ_2}{Đ_{12}} \\ \frac{x_2 Đ_1 Đ_2}{Đ_{12}} & Đ_2\left(1+\frac{x_2 Đ_1}{Đ_{12}}\right) \end{bmatrix} \tag{24}$$

Combining equations (21), (23), and (24) we obtain

$$\begin{pmatrix} N_1 \\ N_2 \end{pmatrix} = -\rho\,[\Lambda][\Gamma] \begin{pmatrix} \frac{dq_1}{dz} \\ \frac{dq_2}{dz} \end{pmatrix};$$

$$\begin{pmatrix} N_1 \\ N_2 \end{pmatrix} = -\frac{\rho}{1+\frac{x_1 Đ_2}{Đ_{12}}+\frac{x_2 Đ_1}{Đ_{12}}} \begin{bmatrix} Đ_1\left(1+\frac{x_1 Đ_2}{Đ_{12}}\right) & \frac{x_1 Đ_1 Đ_2}{Đ_{12}} \\ \frac{x_2 Đ_1 Đ_2}{Đ_{12}} & Đ_2\left(1+\frac{x_2 Đ_1}{Đ_{12}}\right) \end{bmatrix} \begin{bmatrix} \Gamma_{11} & \Gamma_{12} \\ \Gamma_{21} & \Gamma_{22} \end{bmatrix} \begin{pmatrix} \frac{dq_1}{dz} \\ \frac{dq_2}{dz} \end{pmatrix} \tag{25}$$

Extensive Molecular Dynamics (MD) simulations have shown that correlation effects are of negligible importance for mixture diffusion across materials such as LTA, ZIF-8, CHA, DDR, ERI that consist of cages separated by windows in the 3.4 Å – 4.2 Å size range.[3, 5, 7, 39] Molecules jump one-at-a-time across the narrow windows, and the assumption of negligible correlations is justified.

In the limiting scenario in which correlations effects are of negligible importance:

$$\frac{Đ_i}{Đ_{ij}} \to 0; \quad \text{correlations negligible}$$

In cases in which correlations are negligible, Equation (25) simplifies to yield

$$N_i = -\rho\, Đ_i \frac{q_i}{RT}\frac{d\mu_i}{dz}; \quad i = 1,2$$

$$[\Lambda] \to \begin{bmatrix} Đ_1 & 0 \\ 0 & Đ_2 \end{bmatrix}; \quad \begin{pmatrix} N_1 \\ N_2 \end{pmatrix} = -\rho \begin{bmatrix} Đ_1 & 0 \\ 0 & Đ_2 \end{bmatrix} \begin{bmatrix} \Gamma_{11} & \Gamma_{12} \\ \Gamma_{21} & \Gamma_{22} \end{bmatrix} \begin{pmatrix} \frac{dq_1}{dz} \\ \frac{dq_2}{dz} \end{pmatrix} \tag{26}$$

# 10. Simulation methodology for transient breakthrough in fixed bed adsorbers

Fixed beds, packed with crystals of microporous materials, are commonly used for separation of mixtures (see schematic in Figure 64); such adsorbers are commonly operated in a transient mode, and the compositions of the gas phase, and component loadings within the crystals, vary with position and time. During the initial stages of the transience, the pores are loaded up gradually, and only towards the end of the adsorption cycle are conditions corresponding to pore saturation attained. Put another way, separations in fixed bed adsorbers are influenced by both the Henry regime of adsorption as well as the conditions corresponding to pore saturation. For a given separation task, transient breakthroughs provide more a realistic evaluation of the efficacy of a material, as they reflect the combined influence of adsorption selectivity, and adsorption capacity.[4, 40]

We describe below the simulation methodology used to perform transient breakthrough calculations that are presented in this work. This simulation methodology is the same as that used in our previous published works.[4, 40]

Assuming plug flow of an *n*-component gas mixture through a fixed bed maintained under isothermal, isobaric, conditions, the molar concentrations in the gas phase at any position and instant of time are obtained by solving the following set of partial differential equations for each of the species *i* in the gas mixture.[38]

$$\frac{\partial c_i(t,z)}{\partial t} + \frac{\partial\left(v(t,z)c_i(t,z)\right)}{\partial z} + \frac{\left(1-\varepsilon\right)}{\varepsilon}\rho\frac{\partial \bar{q}_i(t,z)}{\partial t} = 0; \quad i = 1,2,...n \tag{27}$$

In equation (27), $t$ is the time, $z$ is the distance along the adsorber, $\rho$ is the framework density, $\varepsilon$ is the bed voidage, $v$ is the interstitial gas velocity, and $\bar{q}_i(t,z)$ is the *spatially averaged* molar

loading within the crystallites of radius $r_c$, monitored at position $z$, and at time $t$. The time $t = 0$, corresponds to the time at which the feed mixture is injected at the inlet to the fixed bed. Prior to injection of the feed, it is assumed that an inert, non-adsorbing, gas flows through the fixed bed.

At any time $t$, during the transient approach to thermodynamic equilibrium, the spatially averaged molar loading within the crystallite $r_c$ is obtained by integration of the radial loading profile

$$\bar{q}_i(t) = \frac{3}{r_c^3}\int_0^{r_c} q_i(r,t) r^2 dr \tag{28}$$

For transient unary uptake within a crystal at any position and time with the fixed bed, the radial distribution of molar loadings, $q_i$, within a spherical crystallite, of radius $r_c$, is obtained from a solution of a set of differential equations describing the uptake

$$\frac{\partial q_i(r,t)}{\partial t} = -\frac{1}{\rho}\frac{1}{r^2}\frac{\partial}{\partial r}\left(r^2 N_i\right) \tag{29}$$

The molar flux $N_i$ of component $i$ may be described by the appropriate formulations of Maxwell-Stefan equations, discussed in the foregoing.

Summing equation (**28**) over all $n$ species in the mixture allows calculation of the *total average* molar loading of the mixture within the crystallite

$$\bar{q}_t(t,z) = \sum_{i=1}^{n} \bar{q}_i(t,z) \tag{30}$$

The *interstitial* gas velocity is related to the *superficial* gas velocity by

$$v = \frac{u}{\varepsilon} \tag{31}$$

The adsorber bed is assumed to be initially free of adsorbates, i.e. we have the initial condition

$$t = 0; \quad q_i(0,z) = 0 \tag{32}$$

Equation (32) is relevant to the operation of the transient breakthrough experiments on a laboratory scale, but are not truly reflective of industrial operations.

At time, $t = 0$, the inlet to the adsorber, $z = 0$, is subjected to a step input of the $n$-component gas mixture and this step input is maintained till the end of the adsorption cycle when steady-state conditions are reached.

$$t \geq 0; \quad p_i(0,t) = p_{i0}; \quad u(0,t) = u_0 \tag{33}$$

where $u_0 = v_0\varepsilon$ is the superficial gas velocity at the inlet to the adsorber.

If the value of $\frac{Đ_i}{r_c^2}$ is large enough to ensure that intra-crystalline gradients are absent and the entire crystallite particle can be considered to be in thermodynamic equilibrium with the surrounding bulk gas phase at that time $t$, and position $z$ of the adsorber

$$\bar{q}_i(t,z) = q_i(t,z) \tag{34}$$

The molar loadings at the *outer surface* of the crystallites, i.e. at $r = r_c$, are calculated on the basis of adsorption equilibrium with the bulk gas phase partial pressures $p_i$ at that position $z$ and time $t$. The adsorption equilibrium can be calculated on the basis of the IAST description of mixture adsorption equilibrium.

For convenience, the set of equations describing the fixed bed adsorber are summarized in Figure 65. Typically, the adsorber length is divided into 100 – 200 slices. Combination of the discretized partial differential equations (PDEs) along with the algebraic IAST equilibrium model, results in a set of differential-algebraic equations (DAEs), which are solved using BESIRK.[41] BESIRK is a sparse matrix solver, based on the semi-implicit Runge-Kutta method

originally developed by Michelsen,[42] and extended with the Bulirsch-Stoer extrapolation method.[43] Use of BESIRK improves the numerical solution efficiency in solving the set of DAEs. The evaluation of the sparse Jacobian required in the numerical algorithm is largely based on analytic expressions.[38] Further details of the numerical procedures used in this work, are provided by Krishna and co-workers;[38, 44-46] interested readers are referred to our website that contains the numerical details.[44]

For presenting the breakthrough simulation results, we use the dimensionless time, $\tau = \frac{tu}{L\varepsilon}$, obtained by dividing the actual time, $t$, by the characteristic time, $\frac{L\varepsilon}{u}$, where $L$ is the length of adsorber, $u$ is the superficial fluid velocity, $\varepsilon$ is the bed voidage.[47]

For all the simulations reported in this article we choose the following: adsorber length, $L$ = 0.3 m; cross-sectional area, $A$ = 1 m$^2$; superficial gas velocity in the bed, $u_0$ = 0.04 m s$^{-1}$; voidage of the packed bed, $\varepsilon$ = 0.4. Also, the total pressures is assumed to be constant along the length of the fixed bed. Please note that since the superficial gas velocity is specified, the specification of the cross-sectional area of the tube, $A$, is not relevant in the simulation results presented. The total volume of the bed is $V_{bed} = LA$. The volume of MOF used in the simulations is $V_{ads} = LA(1-\varepsilon)$ = 0.18 m$^3$. If $\rho$ is the framework density, the mass of the adsorbent in the bed is $m_{ads} = \rho LA(1-\varepsilon)$ kg. It is important to note that the volume of adsorbent, $V_{ads}$, includes the pore volume of the adsorbent material. In these breakthrough simulations we use the same volume of adsorbent in the breakthrough apparatus, i.e. (1 - $\varepsilon$) $A$ $L$ = 0.18 m$^3$ = 180 L.

# 11. Influence of intra-crystalline diffusion on Xe/Kr separations

As illustration of the influence of intra-crystalline diffusion influences on the separation performance of fixed bed adsorbers, we analyze the separation of noble gases that is of importance in the nuclear industry.[48] Adsorption separations of noble gases rely on the differences in the polarizabilities, that increase with the molar masses and the kinetic diameters; see Figures 66a,b. Figure 67 plots the adsorption selectivities vs volumetric uptake capacity of Xe for separation of 20/80 Xe(1)/Kr(2) mixtures using a variety of MOFs. The highest selectivity is realized with CoFormate (= $Co_3(HCOO)_6$); Wang et al.[49] attribute the highly selective adsorption of Xe in Co-Formate to commensurate positioning of Xe within the channels that are approximately 5-6 Å in size. The hierarchy of Xe uptake capacities is Ag@NiMOF-74 > Co-Formate > NiMOF-74 > SBMOF-2 > CuBTC > SAPO-34. The higher uptake capacity of Ag@NiMOF-74 is partly attributable to its higher pore volume and larger channel dimensions (11 Å).

Should we select MOFs for Xe/Kr separations on the basis of adsorption selectivity or on the basis of uptake capacity? For separations in fixed bed adsorbers, the more poorly adsorbed Kr can be recovered in nearly pure form during the adsorption phase; pure Xe is recovered during the desorption phase. Clearly, the best MOF is one that leads to the highest productivities of pure Kr, and pure Xe; to determine the productivities we need to perform transient breakthrough simulations in fixed bed adsorbers using the simulation methodology described in the literature [4, 37, 40, 50].

Figure 68 presents the transient breakthroughs of 20/80 Xe/Kr mixture in fixed bed packed with Co(Formate), the MOF with the highest selectivity for this separation task. The commensurate positioning of Xe in the channels implies that the intra-crystalline diffusivity of

Xe will be significantly lower than that of Kr [5, 48, 51]. The continuous solid lines in Figure 68 presents the transient breakthrough simulations that include the influence of intra-crystalline effects with the values $Đ_{Xe}/r_c^2 = 2\times10^{-3}$ s$^{-1}$; $Đ_{Kr}/r_c^2 = 1\times10^{-2}$ s$^{-1}$ where $Đ_i$ is the intra-crystalline Maxwell-Stefan diffusivity, and $r_c$ is the radius of the crystallites. During the time interval $\Delta\tau$, indicated in Figure 68, pure Kr, containing < 1000 ppm Xe, can be recovered as demanded by the process requirements. From a material balance on the adsorber the productivity of pure Kr, expressed as the mol of pure Kr recovered per L of adsorbent can be determined; this value is 5.5 mol L$^{-1}$. If intra-crystalline diffusion effects are absent, i.e. the values of $\frac{Đ_i}{r_c^2}$ are large enough to ensure that intra-crystalline gradients are absent, equation (34) applies.

The dashed lines in Figure 68 represent the transient breakthrough simulations in which is invoked; in this scenario, the breakthroughs are sharper and the productivity of pure Kr is determined to be 6.5 mol L$^{-1}$.

The maximum achievable productivity is realized when equation (34) holds and the concentration "fronts" traverse the fixed bed in the form of shock waves [50, 52]. The shock-wave model solution is indicated by the dotted lines in Figure 68. For a binary (1, 2) mixture with mole fractions $y_1$, and $y_2 = 1 - y_1$, in the feed mixture, the maximum achievable productivity, $\Delta Q$, also termed the separation potential,[50] can be calculated using the formula

$$\Delta Q = \left( q_1 \frac{y_2}{1 - y_2} - q_2 \right) \rho \qquad (35)$$

where $\rho$ is the framework density. Equation (35) is derived using the shock-wave model for fixed beds, with sharp, vertical, breakthrough "fronts" [50, 52]. The physical significance of $\Delta Q$, conveniently expressed in the units of mol per L of adsorbent, is that it represents the *maximum*

amount of pure component 2 (= the more poorly adsorbed component) that can be recovered during the adsorption phase of fixed bed separations. For 20/80 Xe/Kr mixtures, the maximum achievable productivity of Co(Formate) is 7.5 mol $L^{-1}$. Intra-crystalline diffusion effects reduce the productivity of pure Kr in fixed bed operations, due to the distended nature of the breakthroughs.

The separation potential, $\Delta Q$, is a combined selectivity/capacity metric that quantifies the separation capability of a zeolite or MOF in fixed bed operations; it is an appropriate tool for initial screening and selection of adsorbent materials for any separation application. Figure 67b presents a plot of the separation potential $\Delta Q$ versus the volumetric uptake capacity of Xe, $q_1\rho = Q_1$. The highest separation potential is achieved with Ag@NiMOF-74, with hexagonal channels that are sufficiently large in size (≈ 11 Å) to offer no diffusional limitations [48, 50]; it possesses the right combination of selectivity and capacity to achieve the highest productivity of pure Kr during the adsorption phase of PSA operations.

## 12. Influence of intra-crystalline diffusion on pentane isomers separations

In order to further illustrate the influence of intra-particle diffusion limitations on the separation performance of fixed bed adsorbers, let us consider the separation of the pentane isomers n-pentane (nC5) and 2-methylbutane (2MB) using ZIF-8 in a packed adsorber operating at 100 kPa and 433 K. The objective of the separation is to produce say 99% pure 2MB for inclusion in the high-octane gasoline pool. The windows of ZIF-8 are about 3.3 Å, and therefore intra-crystalline diffusion effects are likely to significantly influence the transient breakthroughs in fixed-bed adsorbers. The diffusivity values used in the simulations are $Đ_{nC5}/r_c^2 = 2.5\times10^{-5}$ $s^{-1}$; $Đ_{2NB}/r_c^2 = 5\times10^{-5}$ $s^{-1}$; $Đ_{nC5}/Đ_{2MB}$ =50. The chosen diffusivity values are based on our earlier

publication [4] which contains a thorough re-analysis of the experimental data of Peralta et al.[53] for breakthrough of hexane isomers in an adsorber packed with ZIF-8. The red lines in Figure 69 are the simulations that include the influence of intra-crystalline diffusion. From a material balance on the adsorber, the productivity of 99% pure 2MB is determined to be 0.44 mol $L^{-1}$.

The blue lines in Figure 69 are the simulations in which the values of $\frac{Đ_i}{r_c^2}$ are large enough to ensure intra-crystalline diffusion effects are negligible. In this case the productivity of 99% pure 2MB is determined to be 0.52 mol $L^{-1}$; this value is 15% higher than the productivity obtained for the scenario including diffusional effects.

The maximum achievable productivity of pure 2MB is realized when both intra-crystalline diffusion and axial dispersion effects are completely absent and the concentrations "fronts" of the fluid mixture traverse the fixed bed in the form of shock waves [50, 52]. The shock-wave model solution is indicated by the dotted lines in Figure 69. The expression for the maximum productivity of pure 2MB is

$$\Delta Q = Q_{nC5}\frac{y_{2MB}}{y_{nC5}} - Q_{2MB} \tag{36}$$

In equation (36), $y_{nC5}$, and $y_{2MB}$ are the mole fractions of nC5 and 2MB in the feed mixture entering the fixed bed adsorber; in our simulations we use equimolar mixtures, i.e. $y_{nC5} = y_{2MB} = 0.5$. $Q_{nC5}$, and $Q_{2MB}$ are the *volumetric uptake capacities* of nC5 and 2MB, obtained by multiplying the molar loadings $q_{nC5}$, and $q_{2MB}$ by the framework density, $\rho$:

$$Q_{nC5} = \rho q_{nC5}; \quad Q_{2MB} = \rho q_{2MB} \tag{37}$$

Therefore, the quantity $\Delta Q$, termed the *separation potential*, is to be viewed as a *combined* selectivity/capacity metric.[50] For equimolar feed mixtures, $\Delta Q = Q_{nC5} - Q_{2MB}$. The quantity $\Delta Q$ can be determined from simple IAST calculations for mixture adsorption equilibrium; the value thus obtained is 0.706 mol $L^{-1}$. The metric is the suitable metric for comparing the separation potential of different adsorbents for a given separation task.

## 13. Screening of MOFs for separation of hexane isomers

The separation of hexane isomers, n-hexane (nC6), 2-methylpentane (2MP), 3-methylpentane (3MP), 2,2 dimethylbutane (22DMB), and 2,3 dimethylbutane (23DMB) is required for production of high-octane gasoline. The values of the Research Octane Number (RON) increases with the degree of branching; the RON values are: nC6 = 30, 2MP = 74.5, 3MP = 75.5, 22DMB = 94, 23DMB = 105. Therefore, di-branched isomers are preferred products for incorporation into the high-octane gasoline pool.[4, 25, 54] Currently, the separation of hexane isomers is performed using LTA-5A zeolite that operates on the principle of molecular sieving; see Figure 70. Linear nC6 can hop from one cage to the adjacent cage through the 4 Å windows of LTA-5A, but branched alkanes are largely excluded. An improved separation scheme, pictured in Figure 71 would require an adsorbent that would separate the di-branched isomers 22DMB and 23DMB from the nC6, 2MP, and 3MP; this would allow the low-RON components to be recycled back to the isomerization reactor. The separation of 22DMB and 23DMB from the remaining isomers is a difficult task because it requires distinguishing molecules on the *degree* of branching; such a separation is not feasible with the currently used LTA-5A. Typically, in such a processing scheme the aim would be to produce a product stream from the separation step with RON value > 92. This requirement of 92+ RON implies that the product stream will contain predominantly the di-branched isomers 22DMB and 23DMB, while allowing a small proportion

of 2MP and 3MP to be incorporated into the product stream. Sharp separations between mono- and di- branched isomers is not a strict requirement.

Figures 72 ($Fe_2(BDP)_3$), 73 (ZIF-77), 74 (MFI), 75 (Co(BDP)), 76 (MgMOF-74), 77 (Zn(MOF-74), 78 (ZIF-8), 79 (BEA zeolite), 80 (Zn(bdc)dabco), and 81 (ZnHBDC) shows the transient breakthrough simulations for separation of equimolar nC6/2MP/3MP/22DMB/23DMB mixtures at 433 K and 100 kPa in fixed bed adsorber packed with different adsorbents. The sequence of breakthroughs is di-branched isomers, mon-branched isomers, and linear nC6. Also shown is the RON of product gas at the outlet of fixed bed; the RON values are calculated from the pure component values, weighted with the mole fractions in the exit gas stream at any time, *t*. There is a time interval during which product gas exiting the fixed bed has an average RON value higher than 92, the target RON value. Since the RON values of both 22DMB and 23DMB are higher than 92, the desired separation is between 23DMB and 3MP. The appropriate expression for the separation potential is [50]

$$\Delta Q = \left(Q_{nC6} + Q_{2MP} + Q_{3MP}\right)\frac{y_{22MB} + y_{23DMB}}{1 - y_{22MB} - y_{23DMB}} - \left(Q_{22DMB} + Q_{23DMB}\right) \tag{38}$$

Figure 82 compares 92+ RON productivity for a total of nine different adsorbent materials: ZnMOF-74, MgMOF-74, Co(BDP), $Fe_2(BDP)_3$, MFI, BEA, ZIF-8, Zn(bdc)dabco, and ZIF-77, plotted as a function of the separation potential $\Delta Q$, calculated from IAST. The productivity is linearly related to the separation potential. The best performing MOF for this separation duty is $Fe_2(BDP)_3$, in line with the earlier work of Herm et al.[18]

For the UiO-66, and CFI, the di-branched isomers are most strongly adsorbed and these can be recovered only during the desorption phase; see the adsorption/desorption simulations in Figure

83 (UiO-66), and Figure 84 (CFI). The separation potential that describes the recovery of the di-branched isomers is [50]

$$\Delta Q = \left(Q_{22DMB} + Q_{23DMB}\right) - \left(Q_{nC6} + Q_{2MP} + Q_{3MP}\right)\frac{1 - y_{22MB} - y_{23DMB}}{y_{22MB} + y_{23DMB}} \tag{39}$$

The plot of the 92+ RON productivity vs separation potential, calculated using equation (39), for UiO-66, and CFI are indicated by the blue symbols in Figure 82. It is interesting to note that UiO-66 exhibits a comparable separation performance as $Fe_2(BDP)_3$. The important disadvantage of the use of UiO-66 is that the desired dibranched isomers can only be recovered during the desorption phase.

## 14. Separations of xylene isomers: Process background

Mixtures of xylene isomers o-xylene, m-xylene, and p-xylene are most commonly obtained from catalytic reforming of naphtha. The demand for p-xylene is several times that of m-xylene and o-xylene. The largest use of p-xylene is in its oxidation to make terephthalic acid, that is used in turn to make polymers such as polyethylene terephthalate (PET) and polybutylene terephthalate (PBT). PET is one of the largest volume polymers in the world, and is used to produce fibers, resins, films, and blown beverage bottles. In a commonly used separation scheme used to recover p-xylene (cf. Figure 85), the xylenes rich stream from the bottom of the reformer splitter is routed to a xylenes splitter. Here, the heavier aromatics (C9+) are removed from the bottom of the column. The overhead stream from the xylenes splitter containing o-xylene, m-xylene, p-xylene, and ethylbenzene need to be separated for recovery of p-xylene. Due to the very small differences in boiling points, p-xylene recovery form o-xylene/m-xylene/p-xylene/ethylbenzene mixtures is not possible by use of distillation technology. There are, however, significant differences in the freezing points (see Figure 86) that allow fractional

crystallization to be used for separations. The differences in the freezing points arise because of differences in the stacking efficiencies of molecules. Para-xylene has the highest freezing point because these molecules stack most efficiently; pure p-xylene crystals are the first to emerge from the solution upon cooling. However, the energy requirements for fractional crystallization are high because of the need to cool to temperatures of about 220 K. Selective adsorption of xylene isomers within the pores of ordered crystalline micro-porous materials is an energy-efficient alternative to fractional crystallization. In currently used technology the separation is carried out using cation-exchanged Faujasite (FAU) zeolite in a Simulated Moving Bed (SMB) adsorption separation unit.

An SMB unit consists of a set of interconnected columns in series; countercurrent flow of the solid and liquid phases is simulated by the periodic shifting of the inlets and outlets in the direction of the liquid flow. Commonly used SMB technologies are UOP's Parex, Axens' Eluxyl, and Toray's Aromax.[55, 56]\ In Figures 87a,b, the SMB process for separation of a feed mixture containing o-xylene/m-xylene/p-xylene/ethylbenzene is depicted in its (mathematically) equivalent form of true moving bed with counter-current contacting between the down-flowing adsorbent material and up-flowing desorbent (eluent) liquid.

The typical composition of a mixed xylenes feed to a simulated moving bed (SMB) adsorber is 19% ethylbenzene, 44% m-xylene, 20% o-xylene, and 17% p-xylene. Since the adsorbent particles are in contact with a mixture in the *liquid* phase, the pores of the adsorbent material are practically saturated with guest molecules. The hierarchy of adsorption strengths is dictated by molecular packing, or entropy, effects. Binding energies of guest molecules with the framework walls or non-framework cations do not solely determine the separation performance. As pointed out by Peralta et al.,[57] adsorbents selective to p-xylene are desirable for high productivities; they

need to adsorb only ~20% of the feed, whereas an adsorbent that rejects p-xylene would have to adsorb 80% of the feed. In current industrial practice the adsorbent used is BaX zeolite, that selectively adsorbs p-xylene. Typically, BaX zeolite also contains other cations such as $K^+$.

The discovery of MOFs that are selective to p-xylene and have higher separation potential than BaX zeolite will result in lower recirculation flows of eluent, and solids in the SMB unit and this will result in significant economic advantages.

## 15. Screening of MOFs for separation of xylene isomers

The height and width of the C8 aromatics are: o-xylene: 8 Å × 7.4 Å; m-xylene: 8.9 Å × 7.4 Å; p-xylene: 9.3 Å × 6.7 Å; ethylbenzene: 9.5 Å × 6.7 Å; styrene: 9.3 Å × 6.7 Å; see dimensions provided in Figure 86. A further point to note is that xylene isomers are flat; these isomers can align themselves parallel to the channel walls, affording better van der Waals interactions with the framework atoms. By contrast, ethylbenzene is not a flat molecule; the ethyl branch is not in the same plane as the benzene ring.

Due to the differences in the molecular dimensions of the xylene isomers, the efficiencies with which the xylene isomers stack within the channels of different dimensions are different. We can deliberately choose a material with a specified channel dimension in order to allow the optimum stacking of one or other of the xylene isomers.

Experimental data [58-60] for MIL-47 and MIL-53 with 1D rhombohedric channels of 8.5 Å show that these MOFs are selective to adsorption of o-xylene when operating at conditions close to pore saturation. The snapshots in Figure 88a, obtained from CBMC simulations,[61] clearly show the optimal stacking of o-xylene within 8.5 Å channels of MIL-47.

Experimental data of Niekiel et al.[62] for adsorption isotherms for xylene isomers in CAU-13 show strong selectivity towards o-xylene that has optimal stacking within the 8.46 Å channels.

Fang et al.[63] report pulse breakthrough simulations for 4-component o-xylene/m-xylene/p-xylene/ethylbenzene in MOF-CJ3 that indicate adsorption selectivity towards o-xylene. MOF-CJ3 has that has square channels of approximately 8 Å size that is adequate for commensurate stacking of o-xylene.

Clearly, MIL-47, MIL-53, CAU-13, and MOF-CJ3 are not suitable for replacement of BaX zeolite in SMB units.

Torres-Knoop et al.[61] have adopted a conceptual approach, using CBMC simulations for selecting MOFs that have the desired selectivity to p-xylene. Within the one-dimensional 10 Å channels of MAF-X8, we have commensurate stacking of p-xylene; see snapshots in Figure 88b. Co(BDP), that has 10 Å square-shaped 1D channels of Co(BDP), also allows p-xylene to stack vertically (cf. Figure 88c), resulting in selectivity in favor of p-xylene.[61]

Figure 89 presents snapshots of stacking of o-xylene, m-xylene, p-xylene, and ethylbenzene within the 1D zig-zag shaped channels of Co-CUK-1, which is comprised of cobalt(II) cations and the dianion of dicarboxylic acid $[Co_3(2,4\text{-pdc})_2(\mu 3\text{-OH})_2]$ (2,4-pdc = pyridine-2,4-dicarboxylic acid dianion); the synthesis of this MOF is described by Humphrey et al.[64, 65] The p-xylene molecules can stack vertically, and this results in a higher saturation capacity for the para-isotherm, as demonstrated by the experimental data on unary isotherms in Figure 89.

Mukherjee et al.[66] have presented pure component adsorption isotherm data at 298 K for o-xylene, m-xylene, p-xylene, and ethylbenzene in a Zn(II)-based dynamic coordination framework, $[Zn_4O(L)_3]$ where the ligand L = 4, 4'- ((4-(tert-butyl) - 1,2-phenylene)bis(oxy))dibenzoate). The MOF structure gets transformed in such a manner as to allow optimal packing of p-xylene within the cavities; see Figure 90.

The production of *p*-xylene involves the separation of 4-component equimolar o-xylene(1)/m-xylene(2)/p-xylene(3)/ethylbenzene(4) mixtures.[13, 40, 61] We calculate the *volumetric separation potential* for preferential adsorption of p-xylene, and rejection of o-xylene, m-xylene, and ethylbenzene as follows [50]

$$\Delta Q = \left(Q_{pX}\right)\frac{y_{oX} + y_{mX} + y_{EthBz}}{1 - y_{oX} - y_{mX} - y_{EthBz}} - \left(Q_{oX} + Q_{mX} + Q_{EthBz}\right) \tag{40}$$

In equation (40), the *volumetric* loadings of each of the four aromatics, $Q_i$, expressed in mol per L of crystalline adsorbent, are obtained by multiplying the molar loadings, $q_i$, with the framework density, $\rho$. The separation potential for various MOFs can be calculated using the IAST for mixture adsorption equilibrium.

Adopting the methodology described in earlier work,[40] we compare the performances of all MOFs at conditions corresponding to pore saturation. Let us compare the separation performance of BaX zeolite with other MOFs that show selectivity towards p-xylene: DynaMOF-100 [66, 67] Mg-CUK-1 [68], Co-CUK-1[65] MAF-X8 [61], JUC-77, Co(BDP), MIL-125, and MIL-125-$NH_2$. The isotherm data for MAF-X8,[61] JUC-77, Co(BDP), MIL-125, and MIL-125-$NH_2$ are taken from Torres-Knoop et al.[61] The isotherm data for DynaMOF-100 are taken from Mukherjee et al.[66, 67] The isotherm data for Mg-CUK-1 are taken from Saccoccia et al.[68] The isotherm data for Co-CUK-1 are taken from the Yoon et al.[65]

Figure 91 is a plot of $\Delta Q$ as a function of the volumetric uptake of p-xylene in the mixture. A combination of high separation potential and high p-xylene capacity provides the best separation capability in a SMB adsorber. According to Figure 91, the best separation performance is realized with DynaMOF-100. The next best performance is that of Co-CUK-1. Both these MOFs offer significantly higher separation potential than the commercially used BaX zeolite.

# 16. Separation of ethylbenzene/styrene mixtures

Alkylation of benzene with ethene produces ethyl benzene (cf. Figure 85), which is dehydrogenated to styrene, a monomer used in the manufacture of many commercial polymers and co-polymers The conversion of ethylbenzene to styrene is only partial, and the reactor product contains a large fraction, in the range of 20%-40%, of unreacted ethylbenzene. Due to the small, 9 K, difference in their boiling points, the distillation separation of styrene and ethylbenzene has to be carried out in tall distillation columns operating under vacuum and at high reflux ratios; the energy demands are therefore very high. Adsorptive separations using microprous metal-organic frameworks offer energy-efficient alternatives.

Maes et al.[69] and Remy et al.[70] have demonstrated that MIL-47 (V) and MIL-53 (Al) also have the potential for separation of mixtures of styrene and ethylbenzene. Styrene is a flat molecule; by contrast, ethylbenzene is not a flat molecule; the ethyl branch is not in the same plane as the benzene ring. Due to differences in the flatness, styrene has stronger interactions with the metal framework. Being flat, styrene molecules stack more efficiently within the 1D channels of MIL-47 (V) and MIL-53 (Al). The pure component isotherm data of Maes et al.[69], measured for bulk liquid phases show that the adsorption loadings of styrene are higher than that of ethylbenzene. The experimental data of Maes et al.[69] for transient breakthroughs of ethylbenzene/styrene mixtures in MIL-47(V) and MIL-53(Al) demonstrate that styrene is selectively adsorbed. Let us now compare the performance of MIL-47(V) and MIL-53(Al) with DynaMOF-100 that undergoes guest-induced structural changes to selectively encapsulate styrene (cf. Figure 92).

For comparing the separation performance of MIL-47(V) and MIL-53(Al) with DynaMOF-100, we adopt the concept of the separation potential: $\Delta Q = Q_{St} - Q_{EthBz}$ , where $Q_i$, expressed in

mol per L of crystalline adsorbent, are obtained by multiplying the molar loadings, $q_i$, with the framework density, $\rho$.

Figure 93 presents a plot of the separation potential, $\Delta Q = Q_{St} - Q_{EthBz}$, versus the volumetric styrene uptake capacity. The clear superiority of DynaMOF-100 for styrene/ethylbenzene separations needs, however, to be established by experiments in fixed beds.

## 17. Separation of benzene/cyclohexane mixtures

Cyclohexane, and important industrial chemical, is produced by catalytic hydrogenation of benzene. The unreacted benzene is present in the effluent from the reactor must be removed from the desired product. The separation of benzene (Bz) and cyclohexane (CC6) is difficult because the differences in the boiling points is only 0.6 K. Currently technologies use extractive distillation with entrainers such as sulpholane, dimethylsulfoxide, N-methylpyrrolidone, and N-formylmorpholine; such processes are energy intensive. Adsorptive separations offer the energy-efficient alternatives to extractive distillation, especially for mixtures containing small percentage of benzene, as is commonly encountered.

Adsorption separation of benzene/cyclohexane mixtures can rely either on (a) selective adsorption of benzene due to π-complexation because cyclohexane does not form π-complexes, or (b) molecular packing effects, exploiting the concept that stacking of flat benzene molecules is easier than stacking cyclohexanes in either the boat or chair configurations.

Ren et al.[71] has suggested the use of a porous aromatic framework, PAF-2. The pure component isotherm data for PAF-2 shown in Figure 2b of Ren et al.[71] indicate that the saturation capacity of benzene is much higher than that of cyclohexane; this is perhaps due to molecular packing effects. In addition to molecular packing effects, the higher π–π interaction

between the benzene molecule and the aromatic framework of PAF-2 also contributes to good separations.

The pure component isotherm data of Lin et al.[72] for benzene and cyclohexane in Mn triazolate indicates the possibility of selective adsorption of benzene that has a higher saturation capacity.

The work of Manna et al.[73] shows the potential of diaminotriazine functionalized MOF, named DAT-MOF-1, for Bz/CC6 separations due to its π-electron deficient pore surface,

Karmakar et al.[74] demonstrate the potential of a covalent triazine framework CTF-IP10 for Bz/CC6 separations by exploiting its π-electron deficient pore characteristics.

Mukherjee et al.[75] have presented pure component isotherm data for Bz and CC6 in M-MOF-74 ( = $M_2$(dobdc) = M\(dobdc) with dobdc = (dobdc$^{4-}$ = 1,4-dioxido-2,5-benzenedicarboxylate)) with different metal atoms M = Mn, Ni, Mg, Cu, Zn, Co. Their data show that π-complexation triggered Lewis acid–base interactions between the open metal sites of M-MOF-74 and the π-electron rich benzene molecules can be exploited to achieve Bz/CC6 separations with high selectivities towards benzene.

Let us define the adsorption selectivity

$$S_{ads} = \frac{q_{Bz}/q_{CC6}}{y_{Bz}/y_{CC6}} = \frac{Q_{Bz}/Q_{CC6}}{y_{Bz}/y_{CC6}} \tag{41}$$

where the $q_A$, and $q_B$ represent the molar loadings within MOF that is in equilibrium with a bulk fluid mixture with mole fractions $y_A$, and $y_B = 1 - y_A$. The molar loadings, also called *gravimetric uptake capacities*, are usually expressed with the units mol kg$^{-1}$. The *volumetric uptake capacities* are

$$Q_{Bz} = \rho q_{Bz}; \quad Q_{CC6} = \rho q_{CC6} \tag{42}$$

where $\rho$ is the crystal framework density of MOF, expressed say in units of kg $m^{-3}$, or kg $L^{-1}$. The selectivity $S_{ads}$ may be calculated on the basis of experimental data on unary isotherms, along with the Ideal Adsorbed Solution Theory (IAST) of Myers and Prausnitz[34] for mixture adsorption equilibrium.

During the adsorption phase of fixed bed separations, the poorly adsorbed cyclohexane can be recovered in nearly pure form during a certain time interval during the transient breakthrough. As illustration, Figure 94a presents transient breakthrough simulations for separation of benzene/cyclohexane mixtures in a fixed bed packed with DAT-MOF-1. The total pressure is maintained constant at $p_t$ = 10 kPa, and the temperature is 298 K. Let us assume that the purity demanded of the cyclohexane product is 99.95%+. From a material balance on the adsorber, the productivity of 99.95%+ pure cyclohexane is determined to be 0.506 moles per L of crystalline adsorbent packed in the adsorber. The maximum achievable productivity of pure cyclohexane is realized when both intra-crystalline diffusion and axial dispersion effects are completely absent and the concentrations "fronts" of the fluid mixture traverse the fixed bed in the form of shock waves [50, 52]. The shock-wave model solution is indicated by the dotted lines in Figure 94b. The expression for the maximum productivity of pure CC6 is

$$\Delta Q = Q_{Bz}\frac{y_{CC6}}{y_{Bz}} - Q_{CC6} \tag{43}$$

In equation (43), $Q_{Bz}$, and $Q_{CC6}$ are the volumetric uptake capacities of benzene and cyclohexane, obtained by multiplying the molar loadings by the framework density, $\rho$.; $y_{Bz}$, and $y_{CC6}$ are the mole fractions of benzene and cyclohexane in the feed mixture entering the fixed bed adsorber. In view of equation (41), we may also write equation (43) in the form

$$\Delta Q = Q_{Bz} \frac{y_{CC6}}{y_{Bz}} \left( 1 - \frac{1}{S_{ads}} \right) \tag{44}$$

Therefore, the quantity $\Delta Q$, termed the separation potential, is to be viewed as a combined selectivity/capacity metric. For equimolar feed mixtures, $\Delta Q = Q_{Bz} - Q_{CC6}$. The quantity $\Delta Q$ can be determined from simple IAST calculations for mixture adsorption equilibrium; the value thus obtained is 0.596 mol $L^{-1}$; this value is slightly higher than the value obtained from the breakthrough simulations in Figure 94a; this reduction is attributable to the slight distention in the breakthrough characteristics. For a wide range of mixtures, it has been established that the separation potential can be used to screen the separation performance of MOFs

The Bz/CC6 separation performance of M-MOF-74, with PAF-2, MnTriazolate, DAT-MOF-1, and CTF-IP10 can be compared using $\Delta Q$, Figure 95 presents a plot of the separation potential, $\Delta Q_{CC6/Bz} = Q_{Bz} - Q_{CC6}$ vs benzene uptake capacity, $Q_{Bz}$, for M-MOF-74 (M = Mn, Ni, Mg, Cu, Zn, Co), and PAF-2, MnTriazolate, DAT-MOF-1, and CTF-IP10. The best separation performance is achieved with Mn-MOF-74 and Ni-MOF-74. It is interesting to note that there is an order of magnitude difference between the separation performance of Mn-MOF-74, and Ni-MOF-74 and DAT-MOF-1 and PAF-2.

# 18. Notation

| | |
|---|---|
| $A$ | surface area per kg of framework, $m^2\ kg^{-1}$ |
| $b_i$ | parameter in the pure component Langmuir adsorption isotherm, $Pa^{-1}$ |
| $[B]$ | M-S matrix, $m^{-2}\ s$ |
| $c_i$ | molar concentration of species $i$, mol $m^{-3}$ |
| $c_t$ | total molar concentration in mixture, mol $m^{-3}$ |
| $c_{i0}$ | molar concentration of species $i$ in fluid mixture at inlet to adsorber, mol $m^{-3}$ |
| $Đ_i$ | M-S diffusivity of component $i$ for molecule-pore interactions, $m^2\ s^{-1}$ |
| $Đ_i(0)$ | M-S diffusivity at zero-loading, $m^2\ s^{-1}$ |
| $Đ_{ij}$ | M-S exchange coefficient, $m^2\ s^{-1}$ |
| $Đ_{12}$ | M-S exchange coefficient for binary mixture, $m^2\ s^{-1}$ |
| $E$ | energy parameter, J $mol^{-1}$ |
| $f_i$ | partial fugacity of species $i$, Pa |
| $f_t$ | total fugacity of bulk fluid mixture, Pa |
| $[I]$ | Identity matrix with elements $\delta_{ij}$, dimensionless |
| $L$ | length of packed bed adsorber, m |
| $n$ | number of species in the mixture, dimensionless |
| $N_i$ | molar flux of species $i$ defined in terms of the membrane area, mol $m^{-2}\ s^{-1}$ |
| $p_i$ | partial pressure of species $i$, Pa |
| $p_t$ | total system pressure, Pa |
| $P_i^0$ | sorption pressure, Pa |
| $q_A$ | molar loading species A, mol $kg^{-1}$ |
| $q_{i,sat}$ | molar loading of species $i$ at saturation, mol $kg^{-1}$ |
| $q_t$ | total molar loading of mixture, mol $kg^{-1}$ |
| $Q_A$ | volumetric uptake of species A, mol $m^{-3}$ |

| | |
|---|---|
| $\Delta Q$ | separation potential, mol m$^{-3}$ |
| $r$ | radial coordinate, m |
| $r_c$ | radius of crystallite, m |
| $R$ | gas constant, 8.314 J mol$^{-1}$ K$^{-1}$ |
| $S_{ads}$ | adsorption selectivity, dimensionless |
| $S_{perm}$ | permeation selectivity, dimensionless |
| $t$ | time, s |
| $T$ | absolute temperature, K |
| $u_i$ | velocity of motion of $i$, m s$^{-1}$ |
| $u$ | superficial gas velocity in packed bed, m s$^{-1}$ |
| $v$ | interstitial gas velocity in packed bed, m s$^{-1}$ |
| $V_p$ | pore volume, m$^3$ kg$^{-1}$ |
| $x_i$ | mole fraction of species $i$ in adsorbed phase, dimensionless |
| $y_i$ | mole fraction of species $i$ in bulk fluid mixture, dimensionless |
| $z$ | distance along the adsorber, and along membrane layer, m |

***Greek letters***

| | |
|---|---|
| $\gamma_i$ | activity coefficient of component $i$ in adsorbed phase, dimensionless |
| $\Gamma_{ij}$ | thermodynamic factors, dimensionless |
| $[\Gamma]$ | matrix of thermodynamic factors, dimensionless |
| $\delta$ | thickness of membrane, m |
| $\delta_{ij}$ | Kronecker delta, dimensionless |
| $\varepsilon$ | voidage of packed bed, dimensionless |
| $\eta$ | dimensionless distance, dimensionless |
| $\theta_i$ | fractional occupancy of component $i$, dimensionless |
| $\theta_t$ | fractional occupancy of adsorbed mixture, dimensionless |
| $\theta_V$ | fractional vacancy, dimensionless |

| | |
|---|---|
| $\Theta_i$ | loading of species *i*, molecules per unit cage, or per unit cell |
| $\Theta_{i,sat}$ | saturation loading of species *i*, molecules per unit cage, or per unit cell |
| $\Theta_t$ | total mixture loading, molecules per unit cage, or per unit cell |
| $[\Lambda]$ | matrix of Maxwell-Stefan diffusivities, $m^2\ s^{-1}$ |
| $\Lambda_{ij}$ | Wilson parameters, dimensionless |
| $\mu_i$ | molar chemical potential, $J\ mol^{-1}$ |
| $\pi$ | spreading pressure, $N\ m^{-1}$ |
| $\rho$ | framework density, $kg\ m^{-3}$ |
| $\tau$ | time, dimensionless |

***Subscripts***

| | |
|---|---|
| 0 | upstream face of membrane |
| 1 | referring to species 1 |
| 2 | referring to species 2 |
| i,j | components in mixture |
| $\eta$ | position along membrane |
| $\delta$ | downstream face of membrane |
| i | referring to component *i* |
| t | referring to total mixture |
| s | referring to surface at position $\xi = 1$. |
| sat | referring to saturation conditions |
| V | vacancy |

***Superscripts***

| | |
|---|---|
| 0 | referring to pure component loading |
| excess | referring to excess parameter |

***Vector and Matrix Notation***

| | |
|---|---|
| ( ) | component vector |
| [ ] | square matrix |

# 19. References


(1) Baerlocher, C.; Meier, W. M.; Olson, D. H. *Atlas of Zeolite Framework Types*; 5th Edition, Elsevier: Amsterdam, 2002.

(2) Baerlocher, C.; McCusker, L. B. Database of Zeolite Structures. http://www.iza-structure.org/databases/, International Zeolite Association, 10 January 2002.

(3) Krishna, R. Diffusion in Porous Crystalline Materials. *Chem. Soc. Rev.* **2012**, *41*, 3099-3118.

(4) Krishna, R. The Maxwell-Stefan Description of Mixture Diffusion in Nanoporous Crystalline Materials. *Microporous Mesoporous Mater.* **2014**, *185*, 30-50.

(5) Krishna, R. Describing the Diffusion of Guest Molecules inside Porous Structures. *J. Phys. Chem. C* **2009**, *113*, 19756-19781.

(6) Krishna, R.; van Baten, J. M. Investigating the Relative Influences of Molecular Dimensions and Binding Energies on Diffusivities of Guest Species Inside Nanoporous Crystalline Materials *J. Phys. Chem. C* **2012**, *116*, 23556-23568.

(7) Krishna, R.; van Baten, J. M. Investigating the Influence of Diffusional Coupling on Mixture Permeation across Porous Membranes *J. Membr. Sci.* **2013**, *430*, 113-128.

(8) Krishna, R.; van Baten, J. M. Influence of Adsorption Thermodynamics on Guest Diffusivities in Nanoporous Crystalline Materials. *Phys. Chem. Chem. Phys.* **2013**, *15*, 7994-8016.

(9) Krishna, R.; van Baten, J. M. Insights into diffusion of gases in zeolites gained from molecular dynamics simulations. *Microporous Mesoporous Mater.* **2008**, *109*, 91-108.

(10) Krishna, R.; van Baten, J. M. Diffusion of alkane mixtures in MFI zeolite. *Microporous Mesoporous Mater.* **2008**, *107*, 296-298.

(11) Krishna, R.; van Baten, J. M. Separating n-alkane mixtures by exploiting differences in the adsorption capacity within cages of CHA, AFX and ERI zeolites. *Sep. Purif. Technol.* **2008**, *60*, 315-320.

(12) Krishna, R.; van Baten, J. M. Entropy-based Separation of Linear Chain Molecules by Exploiting Differences in the Saturation Capacities in Cage-type Zeolites. *Sep. Purif. Technol.* **2011**, *76*, 325-330.

(13) Krishna, R. Separating Mixtures by Exploiting Molecular Packing Effects in Microporous Materials. *Phys. Chem. Chem. Phys.* **2015**, *17*, 39-59.

(14) Li, K.; Olson, D. H.; Lee, J. Y.; Bi, W.; Wu, K.; Yuen, T.; Xu, Q.; Li, J. Multifunctional Microporous MOFs Exhibiting Gas/Hydrocarbon Adsorption Selectivity, Separation Capability and Three-Dimensional Magnetic Ordering. *Adv. Funct. Mater.* **2008**, *18*, 2205-2214.

(15) Choi, H. J.; Dincă, M.; Long, J. R. Broadly Hysteretic $H_2$ Adsorption in the Microporous Metal-Organic Framework Co(1,4-benzenedipyrazolate). *J. Am. Chem. Soc.* **2008**, *130*, 7848-7850.

(16) Salles, F.; Maurin, G.; Serre, C.; Llewellyn, P. L.; Knöfel, C.; Choi, H. J.; Filinchuk, Y.; Oliviero, L.; Vimont, A.; Long, J. R.; Férey, G. Multistep $N_2$ Breathing in the Metal-Organic Framework Co(1,4-benzenedipyrazolate). *J. Am. Chem. Soc.* **2010**, *132*, 13782-13788.

(17) Demessence, A.; D'Alessandro, D. M.; Foo, M. W.; Long, J. R. Strong $CO_2$ Binding in a Water-Stable, Triazolate-Bridged Metal-Organic Framework Functionalized with Ethylenediamine. *J. Am. Chem. Soc.* **2009**, *131*, 8784-8786.

(18) Herm, Z. R.; Wiers, B. M.; Van Baten, J. M.; Hudson, M. R.; Zajdel, P.; Brown, C. M.; Maschiocchi, N.; Krishna, R.; Long, J. R. Separation of Hexane Isomers in a Metal-Organic Framework with Triangular Channels *Science* **2013**, *340*, 960-964.

(19) Britt, D.; Furukawa, H.; Wang, B.; Glover, T. G.; Yaghi, O. M. Highly efficient separation of carbon dioxide by a metal-organic framework replete with open metal sites. *Proc. Natl. Acad. Sci. U.S.A.* **2009**, *106*, 20637-20640.

(20) Rosi, N. L.; Kim, J.; Eddaoudi, M.; Chen, B.; O'Keeffe, M.; Yaghi, O. M. Rod Packings and Metal-Organic Frameworks Constructed from Rod-Shaped Secondary Building Units. *J. Am. Chem. Soc.* **2005**, *127*, 1504-1518.

(21) Dietzel, P. D. C.; Panella, B.; Hirscher, M.; Blom, R.; Fjellvåg, H. Hydrogen adsorption in a nickel based coordination polymer with open metal sites in the cylindrical cavities of the desolvated framework. *Chem. Commun.* **2006**, 959-961.

(22) Dietzel, P. D. C.; Besikiotis, V.; Blom, R. Application of metal–organic frameworks with coordinatively unsaturated metal sites in storage and separation of methane and carbon dioxide. *J. Mater. Chem.* **2009**, *19*, 7362-7370.

(23) Caskey, S. R.; Wong-Foy, A. G.; Matzger, A. J. Dramatic Tuning of Carbon Dioxide Uptake via Metal Substitution in a Coordination Polymer with Cylindrical Pores. *J. Am. Chem. Soc.* **2008**, *130*, 10870-10871.

(24) Yazaydın, A. Ö.; Snurr, R. Q.; Park, T. H.; Koh, K.; Liu, J.; LeVan, M. D.; Benin, A. I.; Jakubczak, P.; Lanuza, M.; Galloway, D. B.; Low, J. J.; Willis, R. R. Screening of Metal-Organic Frameworks for Carbon Dioxide Capture from Flue Gas using a Combined Experimental and Modeling Approach. *J. Am. Chem. Soc.* **2009**, *131*, 18198-18199.

(25) Dubbeldam, D.; Krishna, R.; Calero, S.; Yazaydın, A. Ö. Computer-Assisted Screening of Ordered Crystalline Nanoporous Adsorbents for Separation of Alkane Isomers. *Angew. Chem. Int. Ed.* **2012**, *51*, 11867-11871.

(26) Cadiau, A.; Adil, K.; Bhatt, P. M.; Belmabkhout, Y.; Eddaoudi, M. A Metal-Organic Framework–Based Splitter for Separating Propylene from Propane. *Science* **2016**, *353*, 137-140.

(27) Bárcia, P. S.; Zapata, F.; Silva, J. A. C.; Rodrigues, A. E.; Chen, B. Kinetic Separation of Hexane Isomers by Fixed-Bed Adsorption with a Microporous Metal-Organic Framework. *J. Phys. Chem. B* **2008**, *111*, 6101-6103.

(28) Lee, J. Y.; Olson, D. H.; Pan, L.; Emge, T. J.; Li, J. Microporous Metal–Organic Frameworks with High Gas Sorption and Separation Capacity. *Adv. Funct. Mater.* **2007**, *17*, 1255-1262.

(29) Cui, X.; Chen, K.; Xing, H.; Yang, Q.; Krishna, R.; Bao, Z.; Wu, H.; Zhou, W.; Dong, X.; Han, Y.; Li, B.; Ren, Q.; Zaworotko, M. J.; Chen, B. Pore Chemistry and Size Control in Hybrid Porous Materials for Acetylene Capture from Ethylene. *Science* **2016**, *353*, 141-144.

(30) Dubbeldam, D.; Walton, K. S.; Ellis, D. E.; Snurr, R. Q. Exceptional Negative Thermal Expansion in Isoreticular Metal–Organic Frameworks. *Angew. Chem. Int. Ed.* **2007**, *46*, 4496-4499.

(31) Dubbeldam, D.; Frost, H.; Walton, K. S.; Snurr, R. Q. Molecular simulation of adsorption sites of light gases in the metal-organic framework IRMOF-1. *Fluid Phase Equilib.* **2007**, *261*, 152-161.

(32) Chae, H. K.; Siberio-Pérez, D. Y.; Kim, J.; Go, Y. B.; Eddaoudi, M.; Matzger, A. J.; O'Keeffe, M.; Yaghi, O. M. A route to high surface area, porosity and inclusion of large molecules in crystals. *Nature* **2004**, *427*, 523-527.

(33) Ruthven, D. M. *Principles of Adsorption and Adsorption Processes*; John Wiley: New York, 1984.

(34) Myers, A. L.; Prausnitz, J. M. Thermodynamics of Mixed Gas Adsorption. *A.I.Ch.E.J.* **1965**, *11*, 121-130.

(35) Siperstein, F. R.; Myers, A. L. Mixed-Gas Adsorption. *A.I.Ch.E.J.* **2001**, *47*, 1141-1159.

(36) Krishna, R.; van Baten, J. M. Maxwell-Stefan modeling of slowing-down effects in mixed gas permeation across porous membranes. *J. Membr. Sci.* **2011**, *383*, 289-300.

(37) Krishna, R. Tracing the Origins of Transient Overshoots for Binary Mixture Diffusion in Microporous Crystalline Materials. *Phys. Chem. Chem. Phys.* **2016**, *18*, 15482-15495.

(38) Krishna, R.; Baur, R. Modelling Issues in Zeolite Based Separation Processes. *Sep. Purif. Technol.* **2003**, *33*, 213-254.

(39) Krishna, R.; van Baten, J. M. A molecular dynamics investigation of the diffusion characteristics of cavity-type zeolites with 8-ring windows. *Microporous Mesoporous Mater.* **2011**, *137*, 83-91.

(40) Krishna, R. Methodologies for Evaluation of Metal-Organic Frameworks in Separation Applications. *RSC Adv.* **2015**, *5*, 52269-52295.

(41) Kooijman, H. A.; Taylor, R. A dynamic nonequilibrium model of tray distillation columns. *A.I.Ch.E.J.* **1995**, *41*, 1852-1863.

(42) Michelsen, M. An efficient general purpose method of integration of stiff ordinary differential equations. *A.I.Ch.E.J.* **1976**, *22*, 594-597.

(43) Bulirsch, R.; Stoer, J. Numerical treatment of ordinary differential equations by extrapolation methods. *Numer. Math.* **1966**, *8*, 1-14.

(44) Krishna, R.; Baur, R. Diffusion, Adsorption and Reaction in Zeolites: Modelling and Numerical Issues. http://krishna.amsterchem.com/zeolite/, University of Amsterdam, Amsterdam, 1 January 2015.

(45) Krishna, R.; van Baten, J. M. Investigating the potential of MgMOF-74 membranes for $CO_2$ capture. *J. Membr. Sci.* **2011**, *377*, 249-260.

(46) He, Y.; Krishna, R.; Chen, B. Metal-Organic Frameworks with Potential for Energy-Efficient Adsorptive Separation of Light Hydrocarbons. *Energy Environ. Sci.* **2012**, *5*, 9107-9120.

(47) Krishna, R.; Long, J. R. Screening metal-organic frameworks by analysis of transient breakthrough of gas mixtures in a fixed bed adsorber. *J. Phys. Chem. C* **2011**, *115*, 12941-12950.

(48) Banerjee, D.; Cairns, A. J.; Liu, J.; Krishna, R.; Thallapally, P. K.; Strachan, D. M. Potential of Metal-Organic Frameworks for Capture of Noble Gases. *Acc. Chem. Res.* **2015**, *48*, 211-219.

(49) Wang, H.; Yao, K.; Zhang, Z.; Jagiello, J.; Gong, Q.; Han, Y.; Li, J. The First Example of Commensurate Adsorption of Atomic Gas in a MOF and Effective Separation of Xenon from Other Noble Gases. *Chem. Sci.* **2014**, *5*, 620-624.

(50) Krishna, R. Screening Metal-Organic Frameworks for Mixture Separations in Fixed-Bed Adsorbers using a Combined Selectivity/Capacity Metric. *RSC Adv.* **2017**, *7*, 35724-35737.

(51) Krishna, R.; van Baten, J. M. A molecular simulation study of commensurate – incommensurate adsorption of n-alkanes in cobalt formate frameworks. *Molecular Simulation* **2009**, *35*, 1098-1104.

(52) Kluge, G.; Franke, T.; Schöllner, R.; Nagel, G. Estimation of Component Loadings in Fixed-Bed Adsorption from Breakthrough Curves of Binary Gas Mixtures in Nontrace Systems. *Chem. Eng. Sci.* **1991**, *46*, 368-371.

(53) Peralta, D.; Chaplais, G.; Simon-Masseron, A.; Barthelet, K.; Pirngruber, G. D. Separation of C6 paraffins using Zeolitic Imidazolate Frameworks: comparison with zeolite 5A. *Ind. Eng. Chem. Res.* **2012**, *51*, 4692-4702.

(54) Krishna, R.; van Baten, J. M. Screening of zeolite adsorbents for separation of hexane isomers: A molecular simulation study. *Sep. Purif. Technol.* **2007**, *55*, 246-255.

(55) Minceva, M.; Rodrigues, A. E. Modeling and Simulation of a Simulated Moving Bed for the Separation of *p*-Xylene. *Ind. Eng. Chem. Res.* **2002**, *41*, 3454-3461.

(56) Minceva, M.; Rodrigues, A. E. Understanding and Revamping of Industrial Scale SMB Units for p-Xylene Separation. *A.I.Ch.E.J.* **2007**, *53*, 138-149.

(57) Peralta, D.; Barthelet, K.; Pérez-Pellitero, J.; Chizallet, C.; Chaplais, G.; Simon-Masseron, A.; Pirngruber, G. D. Adsorption and Separation of Xylene Isomers: CPO-27-Ni vs HKUST-1 vs NaY. *J. Phys. Chem. C* **2012**, *116*, 21844-21855.

(58) El Osta, R.; Carlin-Sinclair, A.; Guillou, N.; Walton, R. I.; Vermoortele, F.; Maes, M.; De Vos, D.; Millange, F. Liquid-Phase Adsorption and Separation of Xylene Isomers by the Flexible Porous Metal−Organic Framework MIL-53(Fe). *Chem. Mater.* **2012**, *24*, 2781-2791.

(59) Finsy, V.; Verelst, H.; Alaerts, L.; De Vos, D.; Jacobs, P. A.; Baron, G. V.; Denayer, J. F. M. Pore-Filling-Dependent Selectivity Effects in the Vapor-Phase Separation of Xylene Isomers on the Metal-Organic Framework MIL-47. *J. Am. Chem. Soc.* **2008**, *130*, 7110-7118.

(60) Remy, T.; Baron, G. V.; Denayer, J. F. M. Modeling the Effect of Structural Changes during Dynamic Separation Processes on MOFs. *Langmuir* **2011**, *27*, 13064-13071.

(61) Torres-Knoop, A.; Krishna, R.; Dubbeldam, D. Separating Xylene Isomers by Commensurate Stacking of p-Xylene within Channels of MAF-X8. *Angew. Chem. Int. Ed.* **2014**, *53*, 7774-7778.

(62) Niekiel, F.; Lannoeye, J.; Reinsch, H.; Munn, A. S.; Heerwig, A.; Zizak, I.; Kaskel, S.; Walton, R. I.; de Vos, D.; Llewellyn, P.; Lieb, A.; Maurin, G.; Stock, N. Conformation-Controlled Sorption Properties and Breathing of the Aliphatic Al-MOF [Al(OH)(CDC)]. *Inorg. Chem.* **2012**, *53*, 4610-4620.

(63) Fang, Z. L.; Zheng, S. R.; Tan, J. B.; Cai, S. L.; Fan, J.; Yan, X.; Zhang, W. G. Tubular metal–organic framework-based capillary gas chromatography column for separation of alkanes and aromatic positional isomers. *J. Chromatogr. A* **2013**, *1285*, 132-138.

(64) Humphrey, S. M.; Chang, J.-S.; Jhung, S. H.; Yoon, J. W.; Wood, P. T. Porous Cobalt(II)–Organic Frameworks with Corrugated Walls: Structurally Robust Gas-Sorption Materials. *Angew. Chem. Int. Ed.* **2007**, *46*, 272-275.

(65) Yoon, J. W.; Lee, J. S.; Piburn, G. W.; Cho, K. H.; Jeon, K.; Lim, H.-K.; Kim, H.; Jun, C.-H.; Humphrey, S. M.; Krishna, R.; Chang, J.-S. Highly Selective Adsorption of p-Xylene

over other C8 Aromatic Hydrocarbons by Co-CUK-1: A Combined Experimental and Theoretical Assessment. *Dalton Trans.* **2017**, *XX*, XXX-XXX. http://dx.doi.org/10.1039/C7DT03304D.

(66) Mukherjee, S.; Joarder, B.; Manna, B.; Desai, A. V.; Chaudhari, A. K.; Ghosh, S. K. Framework-Flexibility Driven Selective Sorption of p-Xylene over Other Isomers by a Dynamic Metal-Organic Framework. *Sci. Rep.* **2014**, *4*, 5761. http://dx.doi.org/10.1038/srep05761

(67) Mukherjee, S.; Joarder, B.; Desai, A. V.; Manna, B.; Krishna, R.; Ghosh, S. K. Exploiting Framework Flexibility of a Metal-Organic Framework for Selective Adsorption of Styrene over Ethylbenzene. *Inorg. Chem.* **2015**, *54*, 4403-4408.

(68) Saccoccia, B.; Bohnsack, A. M.; Waggoner, N. W.; Cho, K. H.; Lee, J. S.; Hong, D.-Y.; Lynch, V. M.; Chang, J.-S.; Humphrey, S. M. Separation of p-Divinylbenzene by Selective Room-Temperature Adsorption Inside Mg-CUK-1 Prepared by Aqueous Microwave Synthesis. *Angew. Chem. Int. Ed.* **2015**, *54*, 5394-5398.

(69) Maes, M.; Vermoortele, F.; Alaerts, L.; Couck, S.; Kirschhock, C. E. A.; Denayer, J. F. M.; De Vos, D. E. Separation of Styrene and Ethylbenzene on Metal-Organic Frameworks: Analogous Structures with Different Adsorption Mechanisms. *J. Am. Chem. Soc.* **2010**, *132*, 15277-15285.

(70) Remy, T.; Ma, L.; Maes, M.; De Vos, D. E.; Baron, G. V.; Denayer, J. F. M. Vapor-Phase Adsorption and Separation of Ethylbenzene and Styrene on the Metal−Organic Frameworks MIL-47 and MIL-53(Al). *Ind. Eng. Chem. Res.* **2012**, *51*, 14824-14833.

(71) Ren, H.; Ben, T.; Wang, E.; Jing, X.; Xue, M.; Liu, B.; Cui, Y.; Qui, S.; Zhu, G. Targeted synthesis of a 3D porous aromatic framework for selective sorption of benzene. *Chem. Commun.* **2010**, *46*, 291-293.

(72) Lin, J.-B.; Zhang, J.-P.; Zhang, W.-X.; Wei Xue, W.; Xue, D.-X.; Chen, X.-M. Porous Manganese(II) 3-(2-Pyridyl)-5-(4-Pyridyl)-1,2,4-Triazolate Frameworks: Rational Self-Assembly, Supramolecular Isomerism, Solid-State Transformation, and Sorption Properties. *Inorg. Chem.* **2009**, *46*, 6652-6660.

(73) Manna, B.; Mukherjee, S.; Desai, A. V.; Sharma, S.; Krishna, R.; Ghosh, S. K. A π-electron Deficient Diaminotriazine Functionalized MOF for Selective Sorption of Benzene Over Cyclohexane. *Chem. Commun.* **2015**, *51*, 15386-15389.

(74) Karmakar, A.; Kumar, A.; Chaudhari, A. K.; Samantha, P.; Desai, A. V.; Krishna, R.; Ghosh, S. K. Bimodal functionality in a porous covalent triazine framework by rational integration of electron rich and deficient pore surface. *Chem. Eur. J.* **2016**, *22*, 4931-4937.

(75) Mukherjee, S.; Manna, B.; Desai, A. V.; Yin, Y.; Krishna, R.; Babarao, R.; Ghosh, S. K. Harnessing Lewis Acidic Open Metal Sites of Metal-organic Frameworks: Foremost Route to Achieve Highly Selective Benzene Sorption over Cyclohexane. *Chem. Commun.* **2016**, *52*, 8215-8218.

(76) Lin, Y. S. Molecular Sieves for Gas Separation. *Science* **2016**, *353*, 121-122.

(77) Krishna, R. A Maxwell-Stefan-Glueckauf Description of Transient Mixture Uptake in Microporous Adsorbents. *Sep. Purif. Technol.* **2018**, *191*, 392-399. https://doi.org/10.1016/j.seppur.2017.09.057.

(78) Krishna, R.; van Baten, J. M. Screening Metal-Organic Frameworks for Separation of Pentane Isomers. *Phys. Chem. Chem. Phys.* **2017**, *19*, 8380-8387.

## 20. Captions for Figures

Figure 1. Pore landscape and structural details of all-silica AFI zeolite.

Figure 2. Pore landscape and structural details of all-silica LTL zeolite.

Figure 3. Pore landscape and structural details of all-silica MTW zeolite.

Figure 4. Pore landscape of all-silica TON zeolite.

Figure 5. Pore landscape, and structural details of Co-Formate.

Figure 6. Pore landscape and structural data for MIL-47.

Figure 7. Pore landscape and structural data for MIL-53(Cr).

Figure 8. Pore landscape and structural data for Co(BDP).

Figure 9. Pore landscape and structural data for Co(BDP).

Figure 10. Pore landscape and structural data for CuBTT.

Figure 11. Pore landscape and structural data for CuBTT.

Figure 12. Pore landscape and structural data for $Fe_2(BDP)_3$.

Figure 13. Pore landscape and structural data for $Fe_2(BDP)_3$.

Figure 14. Snapshot of nC5, 2MB, and neo-P within the triangular channels of $Fe_2(BDP)_3$. Also shown are the snapshots of the hexane isomers: n-hexane (nC6), 2-methylpentane (2MP), 3-methylpentane (3MP), 2,2-dimethylbutane (22DMB) and 2,3-dimethylbutane (23DMB).

Figure 15. Pore landscape and structural data for MgMOF-74.

Figure 16. Pore landscape and structural data for MgMOF-74.

Figure 17. Pore landscape and structural data for ZnMOF-74.

Figure 18. Pore landscape and structural data for ZnMOF-74.

Figure 19. Pore landscape and structural data for CoMOF-74.

Figure 20. Pore landscape and structural data for NiMOF-74.

Figure 21. Pore landscape and structural data for FeMOF-74.

Figure 22. Pore landscapes and structural details of ZnHBDC.

Figure 23. Pore landscape and structural data for ZIF-77.

Figure 24. Pore landscape and structural data for ZIF-77.

Figure 25. Pore landscape of all-silica MOR zeolite.

Figure 26. Structural details for MOR zeolite.

Figure 27. Pore landscape of all-silica FER zeolite.

Figure 28. Structural details for FER zeolite.

Figure 29. Pore landscape of all-silica AFX zeolite.

Figure 30. Structural details for AFX zeolite.

Figure 31. Pore landscape and structural details of all-silica CHA zeolite.

Figure 32. Pore landscape and structural details of all-silica DDR zeolite.

Figure 33. Pore landscape and structural details of all-silica ERI zeolite.

Figure 34. Pore landscape and structural details of ITQ-29.

Figure 35. Pore landscape and structural details of all-silica LTA zeolite.

Figure 36. Structural details for LTA-5A zeolite.

Figure 37. Structural details for LTA-4A zeolite.

Figure 38. Pore landscape and structural data for ZIF-7.

Figure 39. Pore landscape and structural data for ZIF-8.

Figure 40. Structure of NbOFFIVE-1-Ni (= KAUST-7), highlighting the $C_3H_6$ binding with $(NbOF_5)^{2-}$ anions. Adapted from Lin.[76]

Figure 41. Pore landscape and structural data for MFI zeolite.

Figure 42. Pore landscape and structural data for MFI zeolite.

Figure 43. Pore landscape and structural data for ISV zeolite.

Figure 44. Pore landscape of all-silica BEA zeolite.

Figure 45. Structural details for BEA zeolite.

Figure 46. Pore landscape of all-silica BOG zeolite.

Figure 47. Structural details for BOG zeolite.

Figure 48. Pore landscape and structural details of all-silica GME zeolite.

Figure 49. Pore landscape and structural data for Zn(bdc)dabco.

Figure 50. Pore landscape and structural data for Zn(bdc)dabco.

Figure 51. Pore landscape and structural data for Zn(bdc)dabco.

Figure 52. (a) Structures of (a) SIFSIX-1-Cu, and (b) SIFSIX-2-Cu-i, highlighting the $C_2H_2$ binding with $(SiF_6)^{2-}$ anions. Adapted from Lin [76] and Cui et al. [29]

Figure 53. Pore landscape and structural details of all-silica FAU zeolite.

Figure 54. Structural details of NaY zeolite with 138 Si, 54 Al, 54 $Na^+$, Si/Al=2.55.

Figure 55. Structural details of NaX (= 86 $Na^+$/uc = 13X) zeolite. Snapshots of $CO_2$ and $CH_4$ in the cages.

Figure 56. Pore landscape and structural data for IRMOF-1.

Figure 57. Pore landscape and structural data for IRMOF-1.

Figure 58. Pore landscape of all-silica CuBTC.

Figure 59. Structural details for CuBTC.

Figure 60. Cage connectivity of CuBTC framework.

Figure 61. Pore landscape and structural data for MOF-177.

Figure 62. Pore landscape and structural data for MOF-177.

Figure 63. Snapshot of hexane isomers within the pore topology of MOF-177.

Figure 64. Schematic of a packed bed adsorber, showing two different discretization schemes for a single spherical crystallite.

Figure 65. Summary of model equations describing packed bed adsorber, along with discretization scheme.

Figure 66. (a, b) Polarizability of noble gases as a function of (a) molar mass, and (b) kinetic diameter.

Figure 67. (a) Plot of adsorption selectivity vs volumetric uptake capacity of Xe for separation of 20/80 Xe(1)/Kr(2) mixtures using NiMOF-74, Ag@NiMOF-74, CuBTC, SBMOF-2, CoFormate, and SAPO-34. The total pressure, $p_t$ = 100 kPa, and temperature $T$ = 298 K. (b) Plot of the separation potential $\Delta Q = \left( q_1 \frac{80}{20} - q_2 \right) \rho$ versus the volumetric uptake capacity of Xe. The unary isotherm data are culled from our previous works.[40, 48, 50]

Figure 68. Transient breakthrough of 20/80 Xe/Kr mixtures in fixed bed adsorber packed with CoFormate. The total pressure, $p_t$ = 100 kPa, and temperature $T$ = 298 K. Simulations that include intra-crystalline diffusion effects are indicated by the continuous solid lines. The chosen diffusivity values are $Đ_{Xe}/r_c^2$ = 2×10$^{-3}$ s$^{-1}$; $Đ_{Kr}/r_c^2$ = 1×10$^{-2}$ s$^{-1}$. The dotted lines represent the shock-wave models solution. The calculation details are presented in earlier works.[40, 50, 77]

Figure 69. Transient nC5(1)/2MB(2) breakthrough simulations for fixed bed adsorber packed with ZIF-8 and operating at 433 K. The partial fugacities in the feed gas mixture at the inlet, $f_1$= $f_2$= 50 kPa. The dimensionless concentration of nC5 and 2MB, normalized with respect to the molar concentrations at the adsorber inlet, are plotted against the dimensionless time, $\tau = \frac{tu}{L\varepsilon}$. The red lines are the simulations that include the influence of intra-crystalline diffusion; the diffusivity values used in the simulations are $Đ_{nC5}/r_c^2$ = 2.5×10$^{-5}$ s$^{-1}$; $Đ_{2NB}/r_c^2$ = 5×10$^{-5}$ s$^{-1}$; $Đ_{nC5}/Đ_{2MB}$ =50. The blue lines are the simulations in which the values of $\frac{Đ_i}{r_c^2}$ are large enough to ensure intra-crystalline diffusion effects are negligible. The dotted lines are the breakthroughs following the shock wave model.

Figure 70. Currently employed processing scheme for nC6 isomerization and subsequent separation step using LTA-5A zeolite.

Figure 71. Improved processing scheme for the nC6 isomerization process.

Figure 72. Simulations of breakthrough characteristics for 5-component nC6/2MP/3MP/22DMB/23DMB mixture in a fixed bed adsorber packed with $Fe_2(BDP)_3$, (framework density $\rho$ = 1.145 kg $L^{-1}$). The breakthrough simulations are the same as those presented in earlier works. [4, 50, 78]

Figure 73. Simulations of breakthrough characteristics for 5-component nC6/2MP/3MP/22DMB/23DMB mixture in a fixed bed adsorber packed with ZIF-77 (framework density $\rho$ = 1.552 kg $L^{-1}$). The breakthrough simulations are the same as those presented in earlier works. [4, 50, 78]

Figure 74. Simulations of breakthrough characteristics for 5-component nC6/2MP/3MP/22DMB/23DMB mixture in a fixed bed adsorber packed with MFI (framework density $\rho$ = 1.796 kg $L^{-1}$). The breakthrough simulations are the same as those presented in earlier works. [4, 50, 78]

Figure 75. Simulations of breakthrough characteristics for 5-component nC6/2MP/3MP/22DMB/23DMB mixture in a fixed bed adsorber packed with Co(BDP). The breakthrough simulations are the same as those presented in earlier works. [4, 50, 78]

Figure 76. Simulations of breakthrough characteristics for 5-component nC6/2MP/3MP/22DMB/23DMB mixture in a fixed bed adsorber packed with MgMOF-74. The breakthrough simulations are the same as those presented in earlier works. [4, 50, 78]

Figure 77. Simulations of breakthrough characteristics for 5-component nC6/2MP/3MP/22DMB/23DMB mixture in a fixed bed adsorber packed with ZnMOF-74. The breakthrough simulations are the same as those presented in earlier works. [4, 50, 78]

Figure 78. Simulations of breakthrough characteristics for 5-component nC6/2MP/3MP/22DMB/23DMB mixture in a fixed bed adsorber packed with ZIF-8. The breakthrough simulations are the same as those presented in earlier works. [4, 50, 78]

Figure 79. Simulations of breakthrough characteristics for 5-component nC6/2MP/3MP/22DMB/23DMB mixture in a fixed bed adsorber packed with BEA. The breakthrough simulations are the same as those presented in earlier works.[4, 50, 78]

.

Figure 80. Simulations of breakthrough characteristics for 5-component nC6/2MP/3MP/22DMB/23DMB mixture in a fixed bed adsorber packed with with Zn(bdc)dabco. The breakthrough simulations are the same as those presented in earlier works.[4, 50, 78]

Figure 81. Simulations of breakthrough characteristics for 5-component nC6/2MP/3MP/22DMB/23DMB mixture in a fixed bed adsorber packed with ZnHBDC. The breakthrough simulations are the same as those presented in earlier works.[4, 50, 78]

Figure 82. Separation of equimolar nC6/2MP/3MP/22DMB/23DMB mixtures at 433 K and 100 kPa in fixed bed adsorber. Comparison of 92+ RON productivity, plotted as a function of the separation potential $\Delta Q$, calculated using IAST. The plotted data are culled from previous work.[50]

Figure 83. Simulations of breakthrough characteristics for 5-component nC6/2MP/3MP/22DMB/23DMB mixture in a fixed bed adsorber packed with UiO-66. The breakthrough simulations are the same as those presented in earlier works.[4, 50, 78]

Figure 84. Simulations of breakthrough characteristics for 5-component nC6/2MP/3MP/22DMB/23DMB mixture in a fixed bed adsorber packed with CFI. The breakthrough simulations are the same as those presented in earlier works.[4, 50, 78]

Figure 85. Schematic showing the separations of the products from a catalytic reforming unit.

Figure 86. Boiling points, and freezing points of C8 hydrocarbons, along with the molecular dimensions, culled from Torres-Knoop et al.[61]

Figure 87. (a) Moving bed adsorption technology for separation of feed mixture containing o-xylene/m-xylene/p-xylene/ethylbenzene. The simulated moving bed technology, used in industrial practice, is depicted here in its (mathematically) equivalent form of true moving bed with counter-current contacting between the downflowing adsorbent material and upflowing desorbent (eluent) liquid. (b) Qualitative representation of the liquid phase concentrations of a mixture of o-xylene/m-xylene/p-xylene/ethylbenzene in a SMB adorption unit with zeolite selective to p-xylene. The data shown are plotted using the information presented by Minceva and Rodrigues.[55]

Figure 88. Snapshots, obtained from CBMC simulations [61], showing (a) stacking of o-xylene within 8.5 Å channels of MIL-47, (b) stacking of p-xylene within 10 Å channels of MAF-X8, and (c) Snapshots showing the stacking of p-xylene within 10 Å channels of Co(BDP).

Figure 89. Snapshots, obtained from CBMC simulations, showing the stacking of o-xylene, m-xylene, p-xylene, and ethylbenzene within the 1D zig-zag shaped channels of Co-CUK-1. Also shown are the experimental data presented by Yoon et al.[65]

Figure 90. Schematic representation of the framework flexibility of DynaMOF-100 with selective accommodation of p-xylene from xylenes mixture.[66]

Figure 91. The separation potential, $\Delta Q$ for separation of equimolar 4-component o-xylene/m-xylene/p-xylene/ethylbenzene mixtures plotted against the volumetric uptake of p-xylene. For each adsorbent, the conditions correspond to pore saturation.

Figure 92. Schematic representation of the framework flexibility of DynaMOF-100 with selective accommodation of styrene from mixtures with ethylbenzene.[67]

Figure 93. Plot of the separation potential, $\Delta Q = Q_{St} - Q_{EthBz}$ vs styrene uptake capacity for equimolar styrene/ethylbenzene mixtures in MIL-47(V), MIL-53(Al), and DynaMOF-100. The calculations are from Krishna.[50]

Figure 94. (a) Transient breakthrough simulations for separation of benzene/cyclohexane mixtures in a fixed bed packed with DAT-MOF-1. The total pressure is maintained constant at $p_t$ = 10 kPa, and the temperature is 298 K. The unary isotherm data are provided by Manna et al.[73] (b) The dotted lines represent the shock wave model for fixed bed adsorbers. [50]

Figure 95. Plot of the separation potential, $\Delta Q = Q_{Bz} - Q_{CC6}$ vs volumetric uptake capacity of benzene, $Q_{Bz}$ for variety of MOFs carrying out benzene/cyclohexane separations.

# AFI

Figure S1

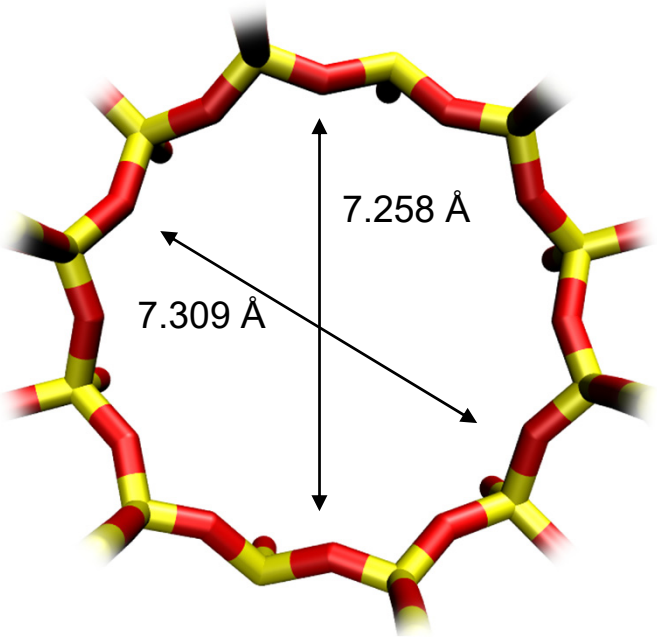


| | AFI |
|---|---|
| *a* /Å | 23.774 |
| *b* /Å | 13.726 |
| *c* /Å | 8.484 |
| Cell volume / Å$^3$ | 2768.515 |
| conversion factor for [molec/uc] to [mol per kg Framework] | 0.3467 |
| conversion factor for [molec/uc] to [kmol/m$^3$] | 2.1866 |
| $\rho$ [kg/m3] | 1729.876 |
| MW unit cell [g/mol(framework)] | 2884.07 |
| $\phi$, fractional pore volume | 0.274 |
| open space / Å$^3$/uc | 759.4 |
| Pore volume / cm$^3$/g | 0.159 |
| Surface area /m$^2$/g | 466.0 |
| DeLaunay diameter /Å | 7.26 |

Snapshots of $CH_4$ and $CO_2$

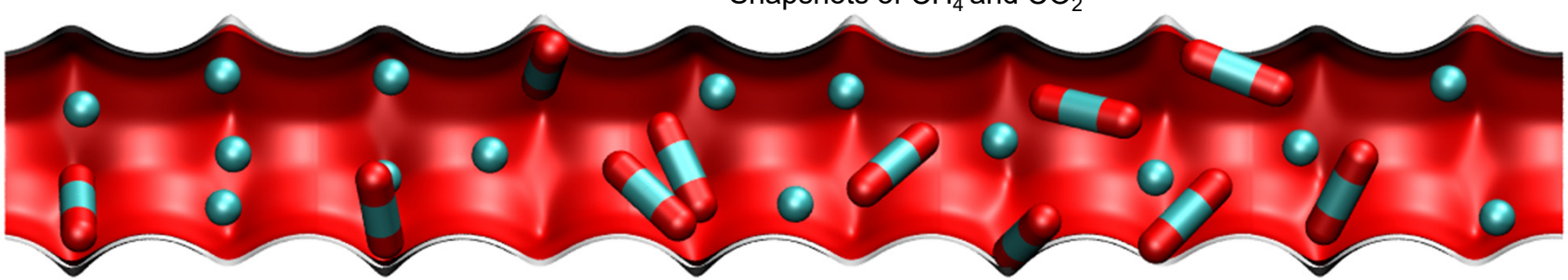

Structural information from: C. Baerlocher, L.B. McCusker, Database of Zeolite Structures, International Zeolite Association, http://www.iza-structure.org/databases/

# LTL

Figure S2

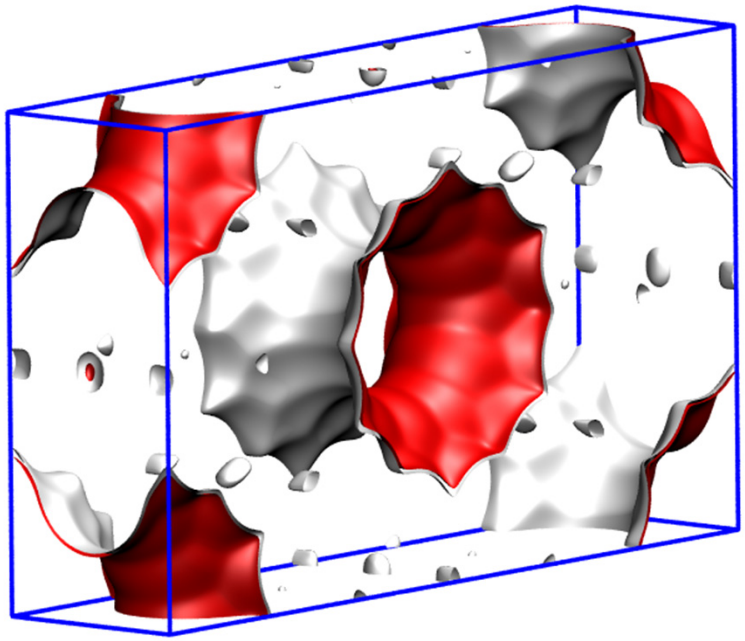

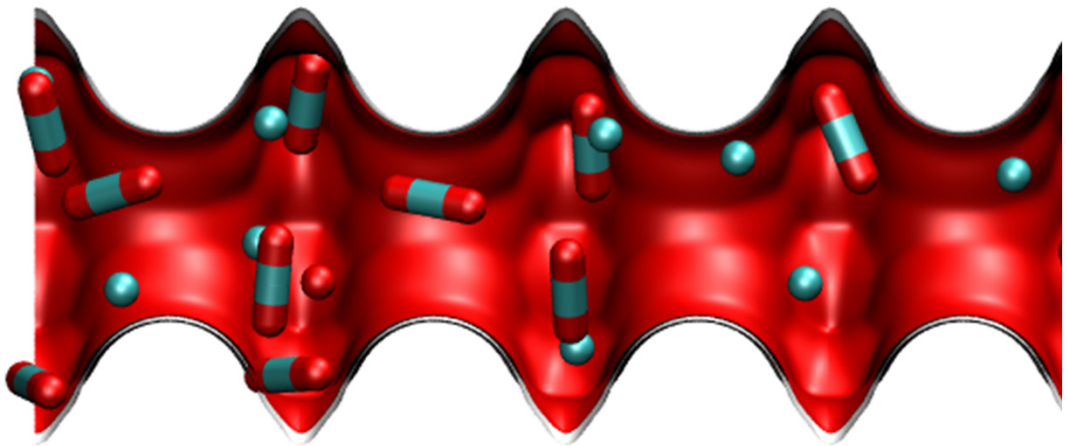

| | LTL |
|---|---|
| *a* /Å | 31.984 |
| *b* /Å | 18.466 |
| *c* /Å | 7.476 |
| Cell volume / Å$^3$ | 4415.449 |
| conversion factor for [molec/uc] to [mol per kg Framework] | 0.2312 |
| conversion factor for [molec/uc] to [kmol/m$^3$] | 1.3597 |
| $\rho$ [kg/m3] | 1626.965 |
| MW unit cell [g/mol(framework)] | 4326.106 |
| $\phi$, fractional pore volume | 0.277 |
| open space / Å$^3$/uc | 1221.3 |
| Pore volume / cm$^3$/g | 0.170 |
| Surface area /m$^2$/g | 521.0 |
| DeLaunay diameter /Å | 7.47 |

# MTW

Figure S3

MTW has 1D, 12-ring channels

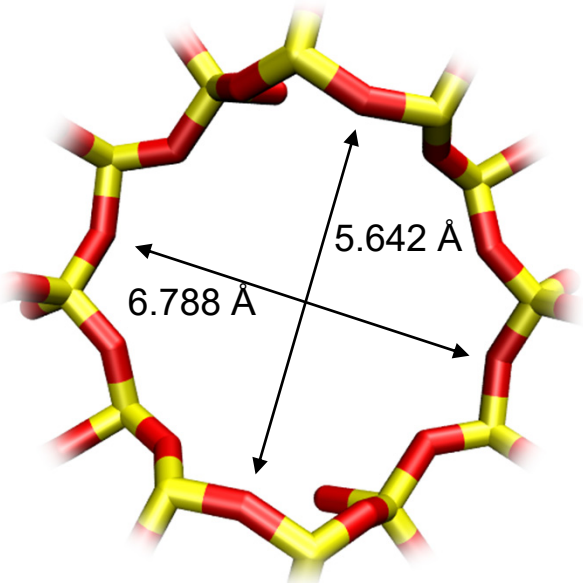


| | MTW |
|---|---|
| *a* /Å | 24.863 |
| *b* /Å | 5.012 |
| *c* /Å | 24.326 |
| Cell volume / Å$^3$ | 2887.491 |
| conversion factor for [molec/uc] to [mol per kg Framework] | 0.2972 |
| conversion factor for [molec/uc] to [kmol/m$^3$] | 2.6759 |
| $\rho$ [kg/m3] | 1935.031 |
| MW unit cell [g/mol(framework)] | 3364.749 |
| $\phi$, fractional pore volume | 0.215 |
| open space / Å$^3$/uc | 620.6 |
| Pore volume / cm$^3$/g | 0.111 |
| Surface area /m$^2$/g | 323.0 |
| DeLaunay diameter /Å | 5.69 |

# TON

Figure S4

10-ring channel of TON

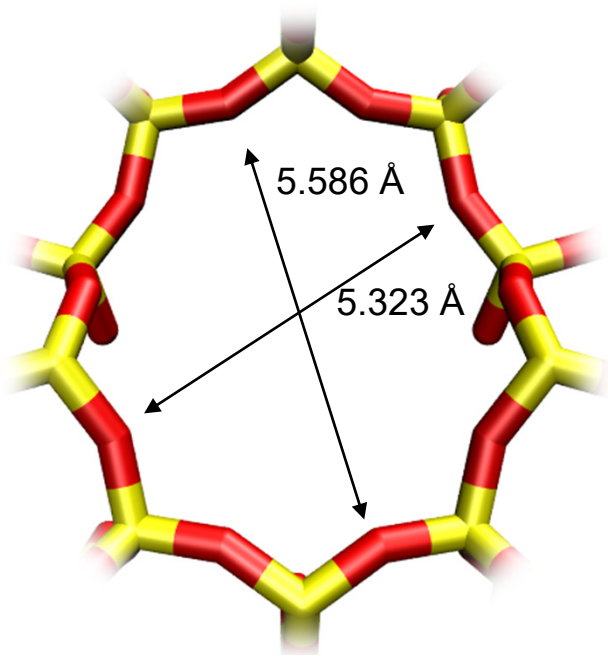


| | TON |
|---|---|
| *a* /Å | 13.859 |
| *b* /Å | 17.42 |
| *c* /Å | 5.038 |
| Cell volume / Å$^3$ | 1216.293 |
| conversion factor for [molec/uc] to [mol per kg Framework] | 0.6935 |
| conversion factor for [molec/uc] to [kmol/m$^3$] | 7.1763 |
| $\rho$ [kg/m3] | 1968.764 |
| MW unit cell [g/mol(framework)] | 1442.035 |
| $\phi$, fractional pore volume | 0.190 |
| open space / Å$^3$/uc | 231.4 |
| Pore volume / cm$^3$/g | 0.097 |
| Surface area /m$^2$/g | 253.0 |
| DeLaunay diameter /Å | 4.88 |

# Co-Formate pore landscapes

Figure S5

1 unit cell of Co-FA

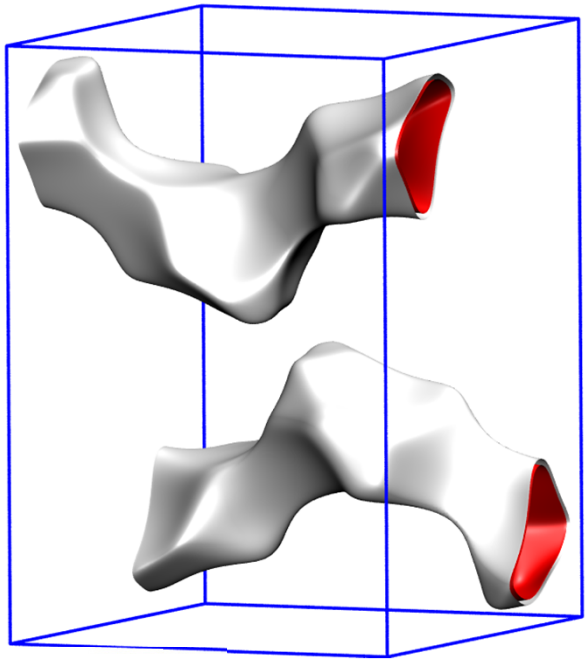

| | Co-FA |
|---|---|
| *a* /Å | 11.3834 |
| *b* /Å | 9.9292 |
| *c* /Å | 14.4324 |
| Cell volume / Å$^3$ | 1631.27 |
| conversion factor for [molec/uc] to [mol per kg Framework] | 0.5595 |
| $\rho$ [kg/m3] | 1819.46 |
| MW unit cell [g/mol(framework)] | 1787.36 |
| Pore volume / cm$^3$/g | 0.139 |

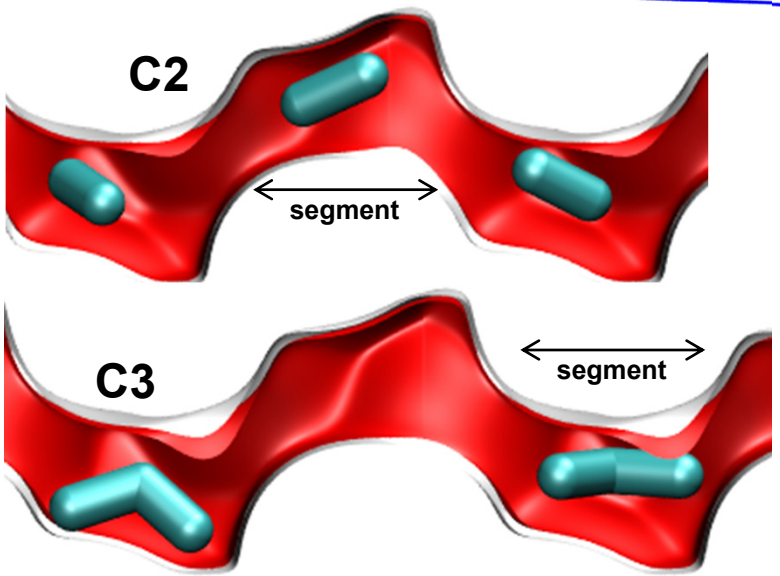


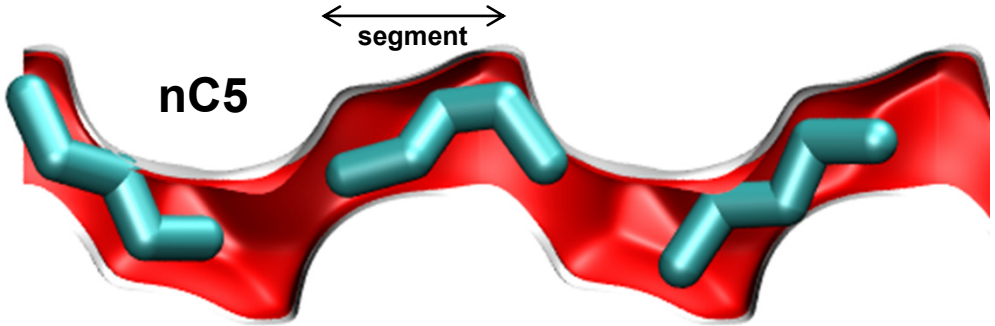

# MIL–47

Figure S6

**Stacking o-xylene in MIL-47**

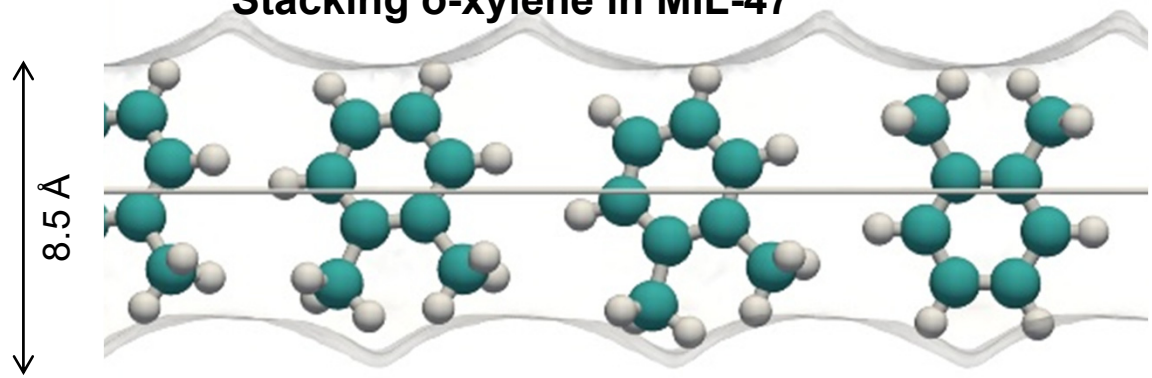


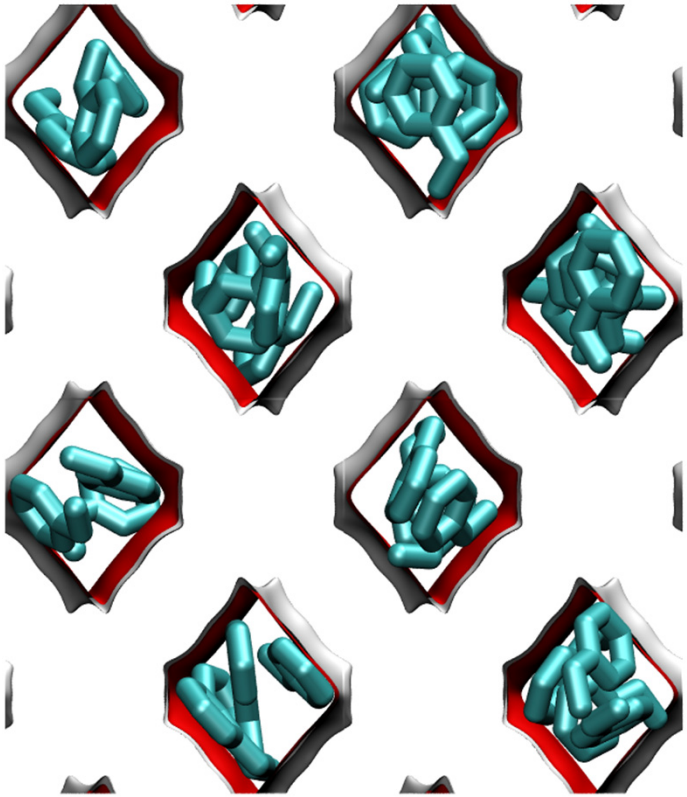

| | MIL-47 |
|---|---|
| *a* /Å | 6.808 |
| *b* /Å | 16.12 |
| *c* /Å | 13.917 |
| Cell volume / Å$^3$ | 1527.321 |
| conversion factor for [molec/uc] to [mol per kg Framework] | 1.0824 |
| conversion factor for [molec/uc] to [kmol/m$^3$] | 1.7868 |
| $\rho$ [kg/m3] | 1004.481 |
| MW unit cell [g/mol(framework)] | 923.881 |
| $\phi$, fractional pore volume | 0.608 |
| open space / Å$^3$/uc | 929.3 |
| Pore volume / cm$^3$/g | 0.606 |
| Surface area /m$^2$/g | 1472.8 |
| DeLaunay diameter /Å | 8.03 |

Figure S7

# MIL–53 (Cr)

**Simulation results**
**presented are for –lp structure, i.e. large pore**

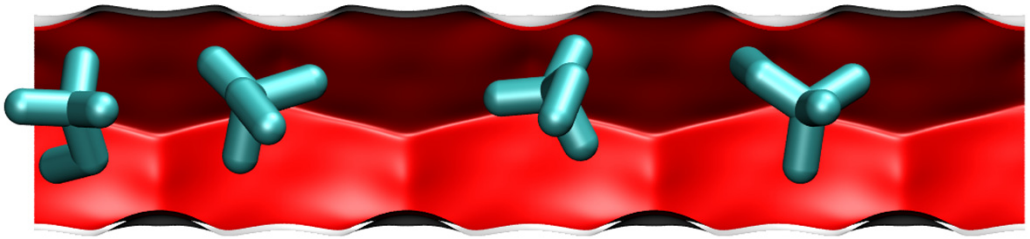

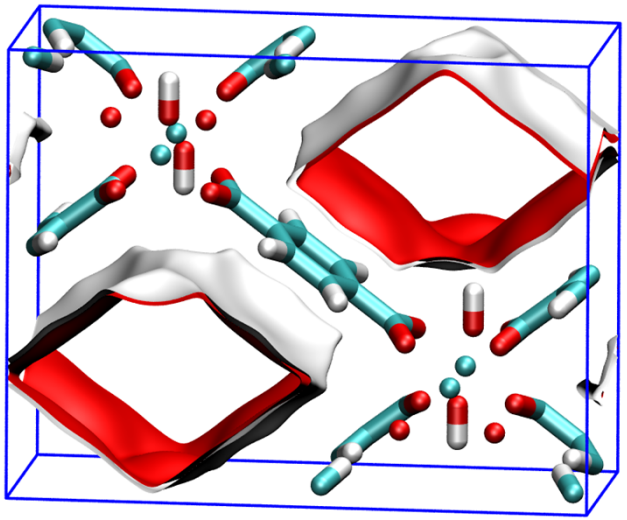

| | MIL53(Cr)-lp |
|---|---|
| *a* /Å | 16.733 |
| *b* /Å | 13.038 |
| *c* /Å | 6.812 |
| Cell volume / Å$^3$ | 1486.139 |
| conversion factor for [molec/uc] to [mol per kg Framework] | 1.0728 |
| conversion factor for [molec/uc] to [kmol/m$^3$] | 2.0716 |
| $\rho$ [kg/m3] | 1041.534 |
| MW unit cell [g/mol(framework)] | 932.1312 |
| $\phi$, fractional pore volume | 0.539 |
| open space / Å$^3$/uc | 801.6 |
| Pore volume / cm$^3$/g | 0.518 |
| Surface area /m$^2$/g | 1280.5 |
| DeLaunay diameter /Å | 7.40 |

# Co(BDP) pore landscapes

Figure S8

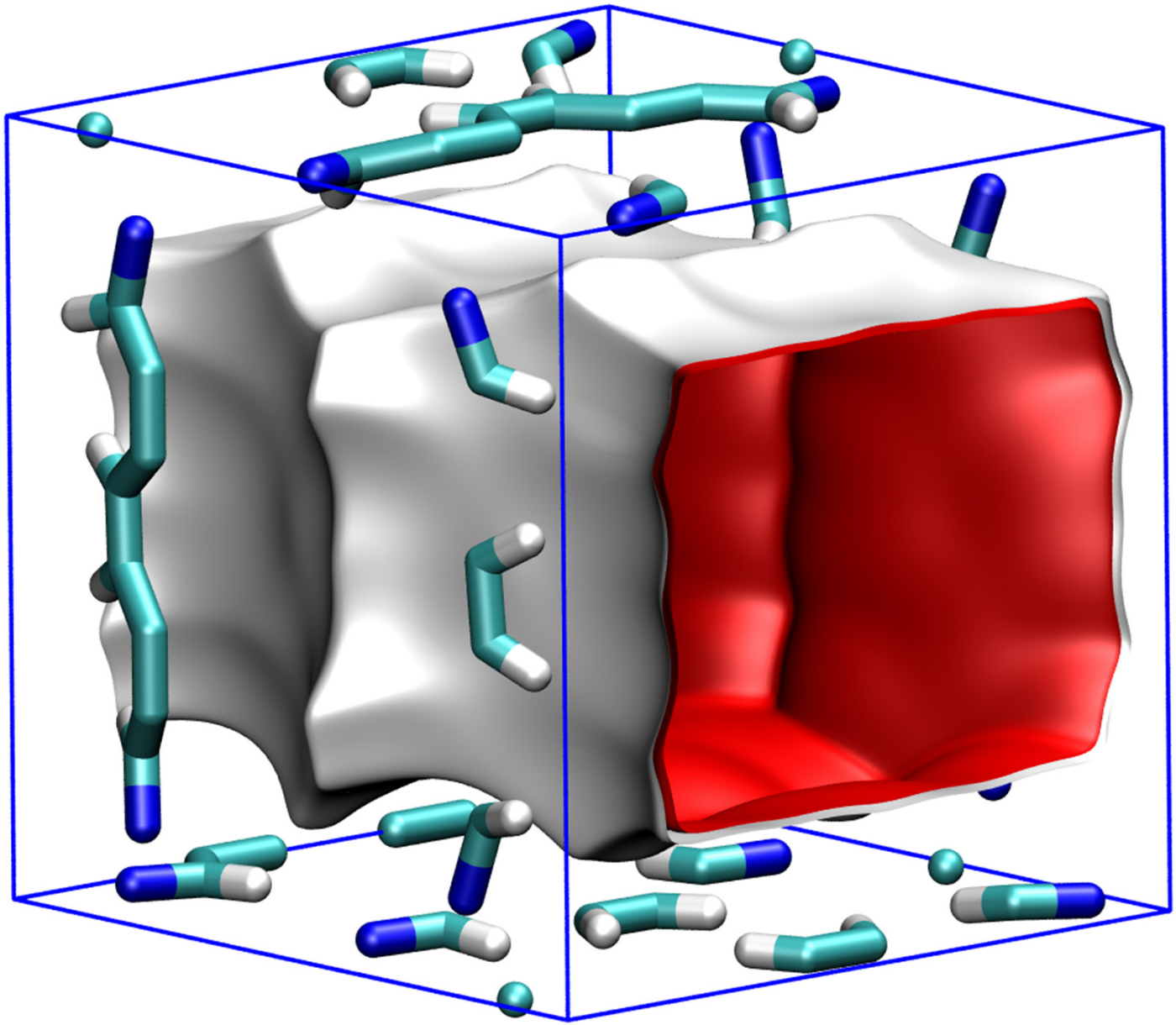

# Co(BDP) pore dimensions

Figure S9

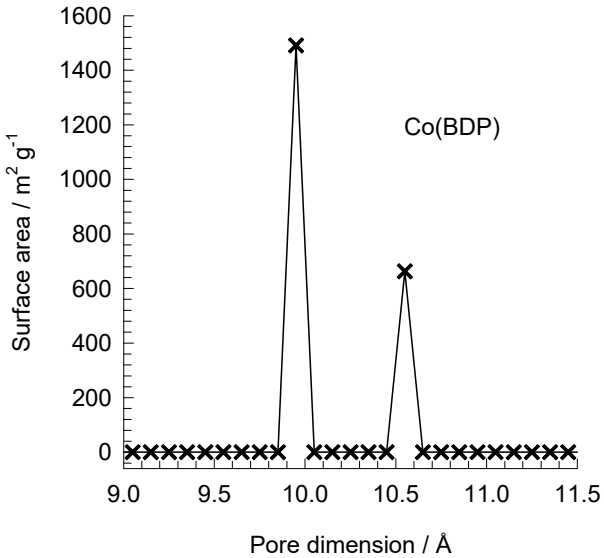


This plot of surface area versus pore dimension is determined using a combination of the DeLaunay triangulation method for pore dimension determination, and the procedure of Düren for determination of the surface area.

| | CoBDP |
|---|---|
| *a* /Å | 13.2529 |
| *b* /Å | 13.253 |
| *c* /Å | 13.995 |
| Cell volume / $Å^3$ | 2458.091 |
| conversion factor for [molec/uc] to [mol per kg Framework] | 0.9362 |
| conversion factor for [molec/uc] to [kmol/$m^3$] | 1.0102 |
| $\rho$ [kg/m3] | 721.5517 |
| MW unit cell [g/mol(framework)] | 1068.094 |
| $\phi$, fractional pore volume | 0.669 |
| open space / $Å^3$/uc | 1643.9 |
| Pore volume / $cm^3$/g | 0.927 |
| Surface area /$m^2$/g | 2148.8 |
| DeLaunay diameter /Å | 10 |

# CuBTT pore landscapes

Figure S10

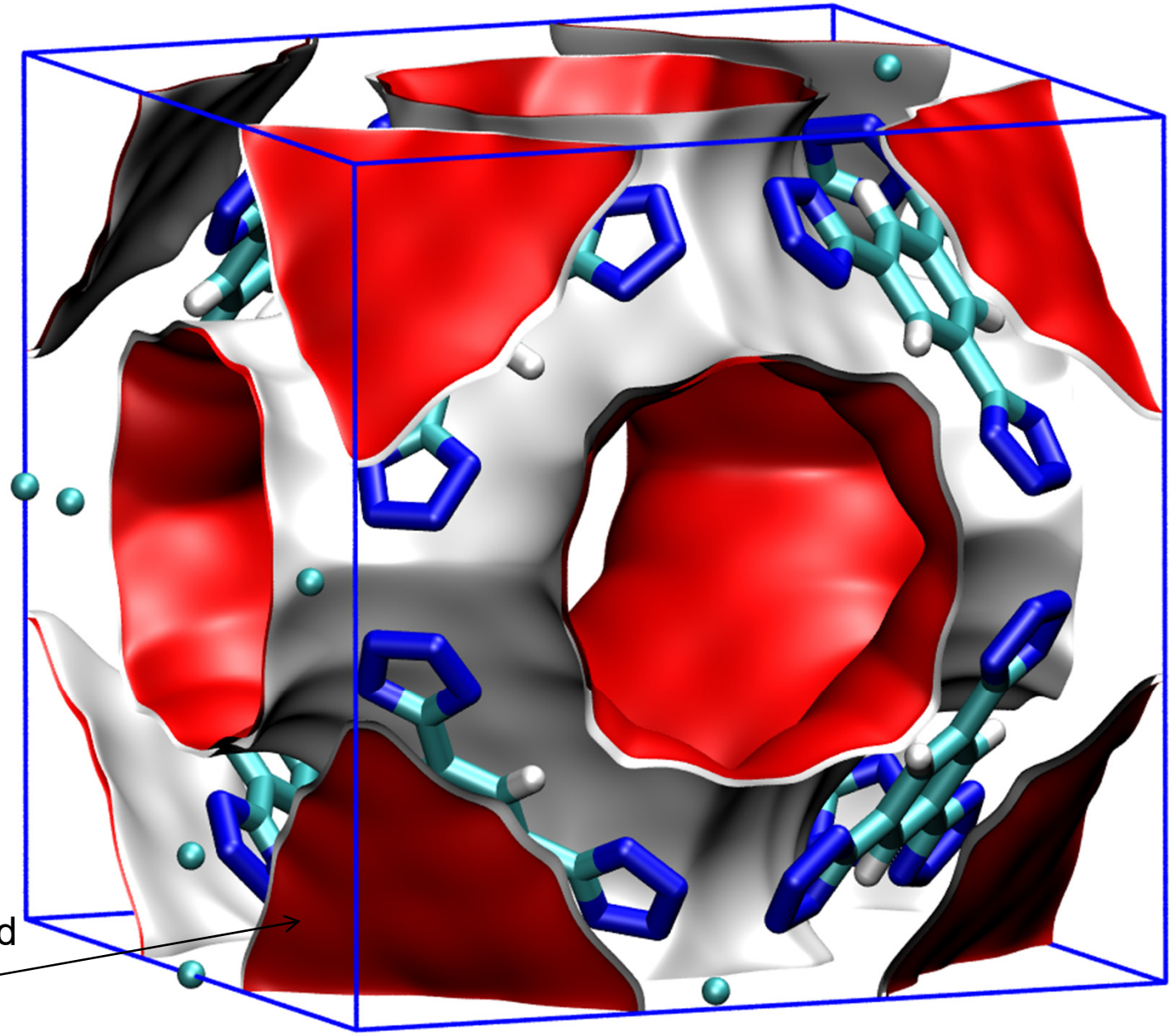

These inaccessible pockets were blocked in our simulations

# CuBTT pore dimensions

Figure S11

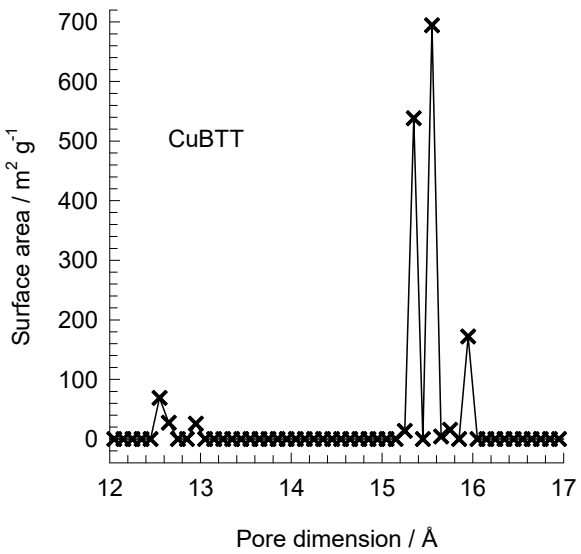


This plot of surface area versus pore dimension is determined using a combination of the DeLaunay triangulation method for pore dimension determination, and the procedure of Düren for determination of the surface area.

| | CuBTT (blocked) |
|---|---|
| *a* /Å | 18.595 |
| *b* /Å | 18.595 |
| *c* /Å | 18.595 |
| Cell volume / Å$^3$ | 6429.668 |
| conversion factor for [molec/uc] to [mol per kg Framework] | 0.3224 |
| conversion factor for [molec/uc] to [kmol/m$^3$] | 0.4547 |
| $\rho$ [kg/m3] | 801.0756 |
| MW unit cell [g/mol(framework)] | 3101.745 |
| $\phi$, fractional pore volume | 0.568 |
| open space / Å$^3$/uc | 3652.1 |
| Pore volume / cm$^3$/g | 0.709 |
| Surface area /m$^2$/g | 1564.6 |
| DeLaunay diameter /Å | 9.99 |

# $Fe_2(BDP)_3$ pore landscapes

Figure S12

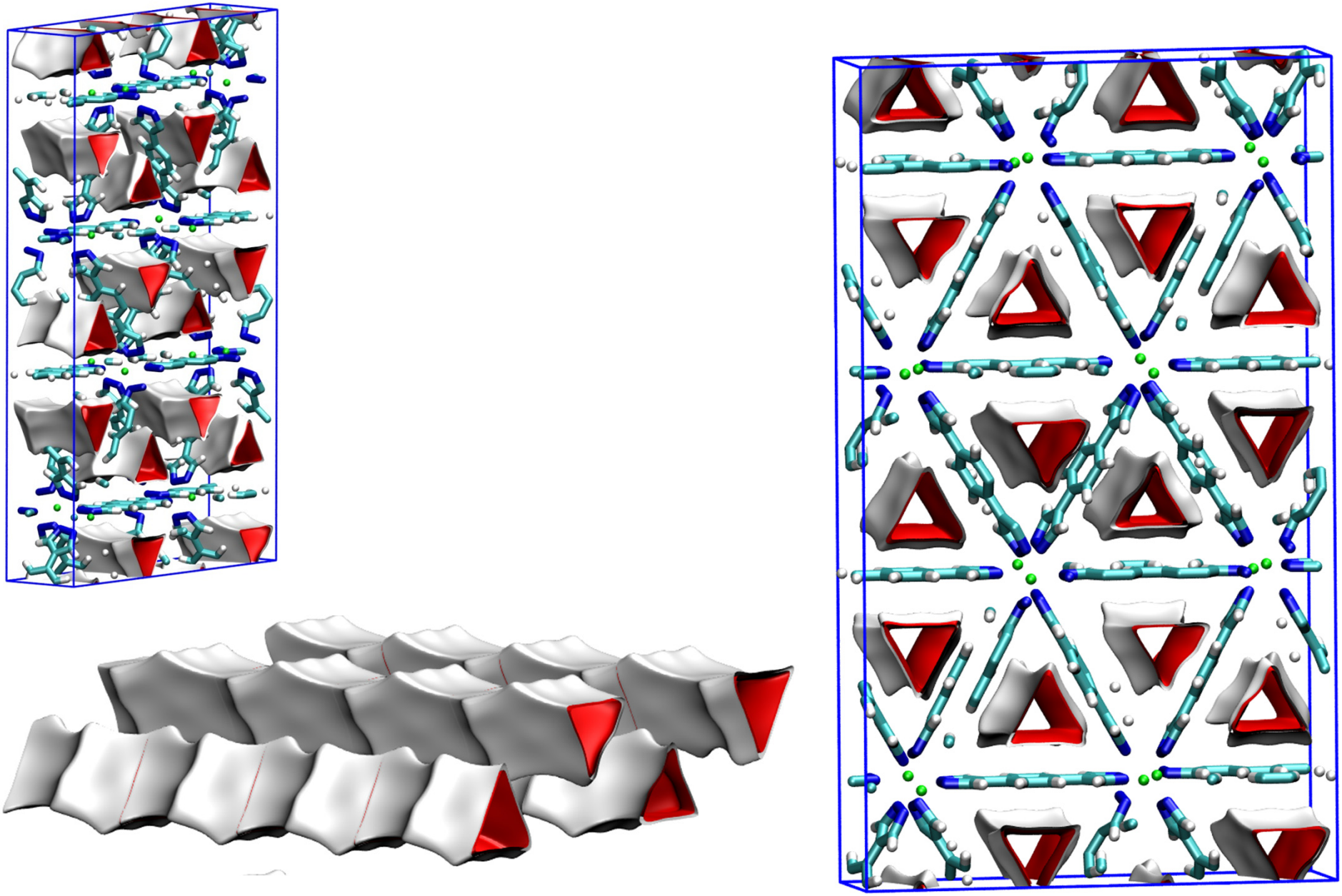

# $Fe_2(BDP)_3$ pore dimensions

Figure S13

| | $Fe_2(BDP)_3$ |
|---|---|
| *a* /Å | 7.104 |
| *b* /Å | 26.491 |
| *c* /Å | 45.353 |
| Cell volume / $Å^3$ | 8535.33 |
| $\rho$ [kg/m3] | 1145.46 |
| Pore volume / $cm^3/g$ | 0.4 |
| Surface area/ $cm^2/g$ | 1230 |
| DeLaunay diameter /Å | 4.9 |

Figure S14

# $Fe_2(BDP)_3$ snapshots of C5, C6 isomers

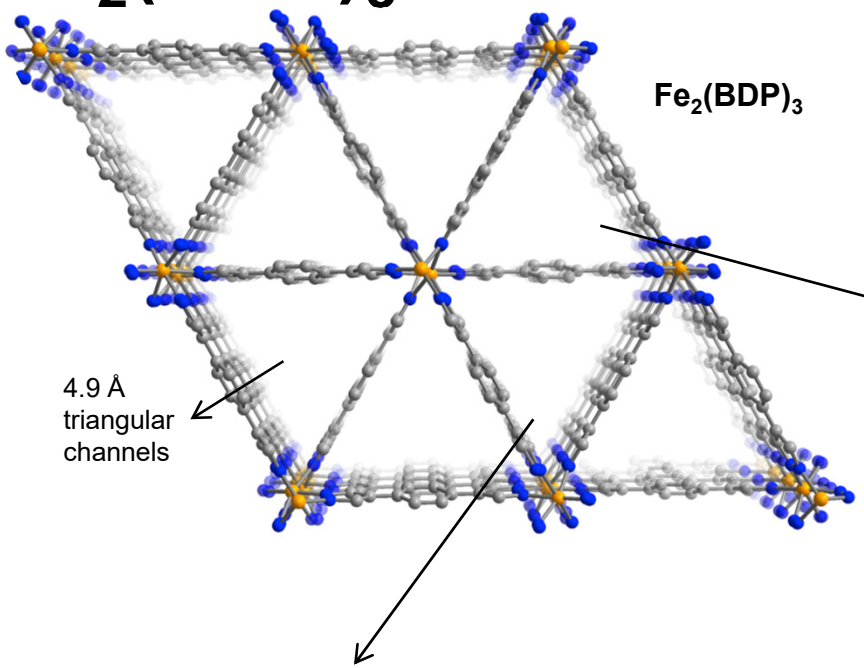


Side-view of C6 isomers in the gutters

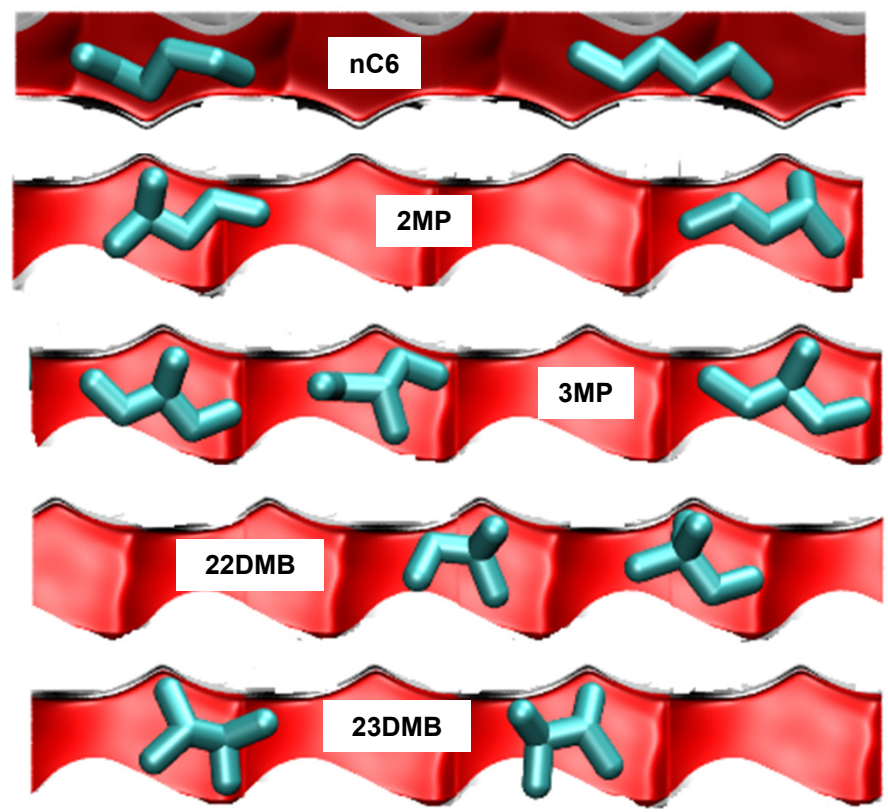


Side-view of C5 isomers in the gutters

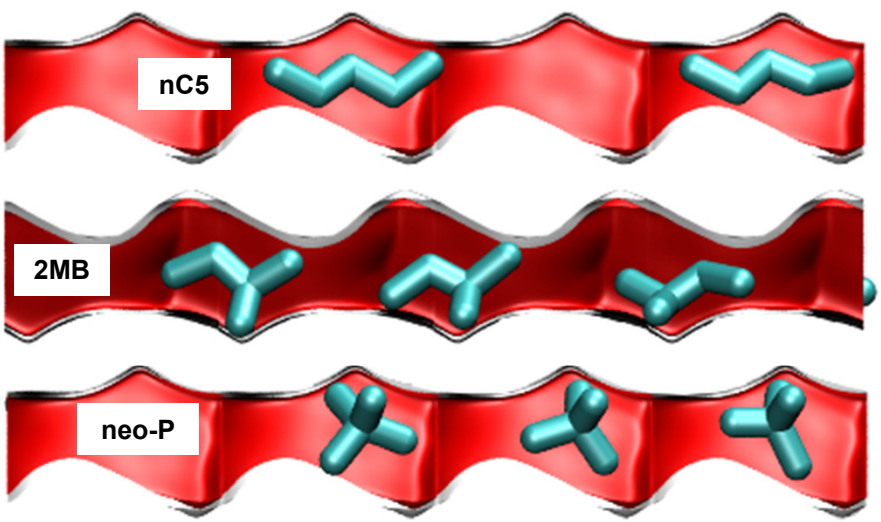

# MgMOF-74 pore landscapes

Figure S15

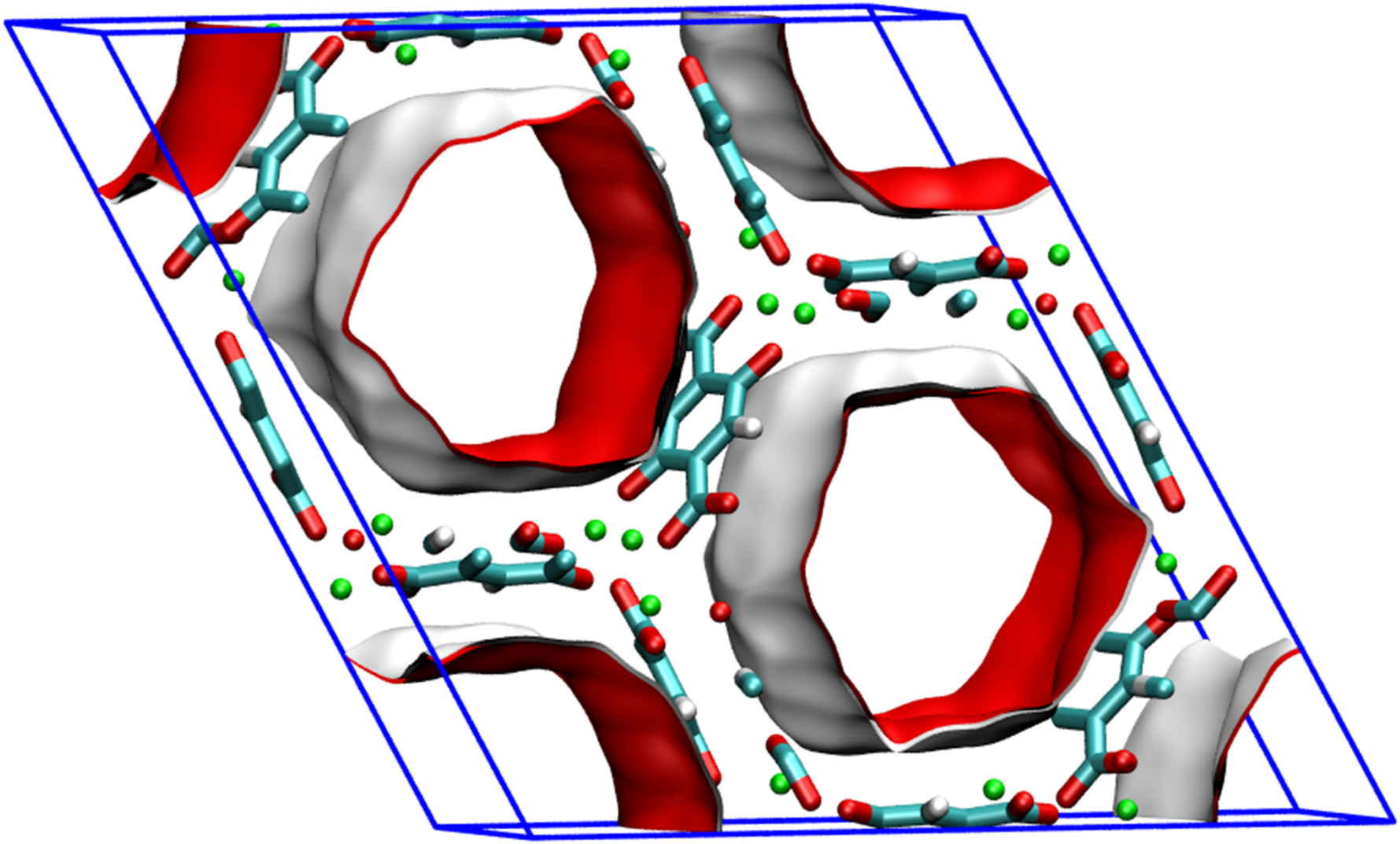

# MgMOF-74 pore dimensions

Figure S16

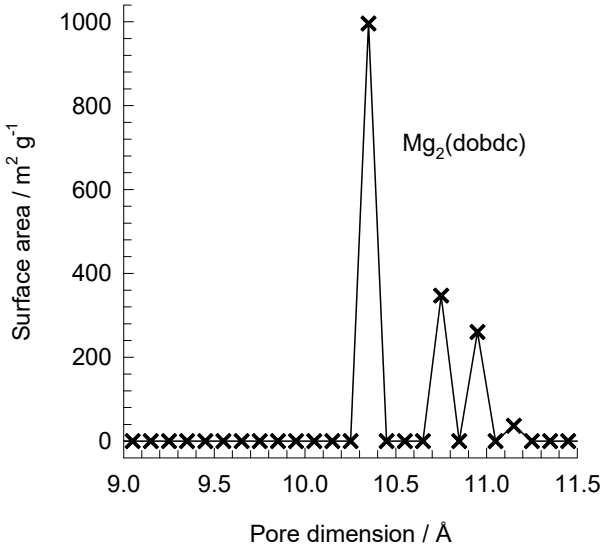


This plot of surface area versus pore dimension is determined using a combination of the DeLaunay triangulation method for pore dimension determination, and the procedure of Düren for determination of the surface area.

| | MgMOF-74 |
|---|---|
| *a* /Å | 25.8621 |
| *b* /Å | 25.8621 |
| *c* /Å | 6.91427 |
| Cell volume / Å$^3$ | 4005.019 |
| conversion factor for [molec/uc] to [mol per kg Framework] | 0.4580 |
| conversion factor for [molec/uc] to [kmol/m$^3$] | 0.5856 |
| $\rho$ [kg/m3] | 905.367 |
| MW unit cell [g/mol(framework)] | 2183.601 |
| $\phi$, fractional pore volume | 0.708 |
| open space / Å$^3$/uc | 2835.6 |
| Pore volume / cm$^3$/g | 0.782 |
| Surface area /m$^2$/g | 1640.0 |
| DeLaunay diameter /Å | 10.66 |

# ZnMOF-74 pore landscapes

Figure S17

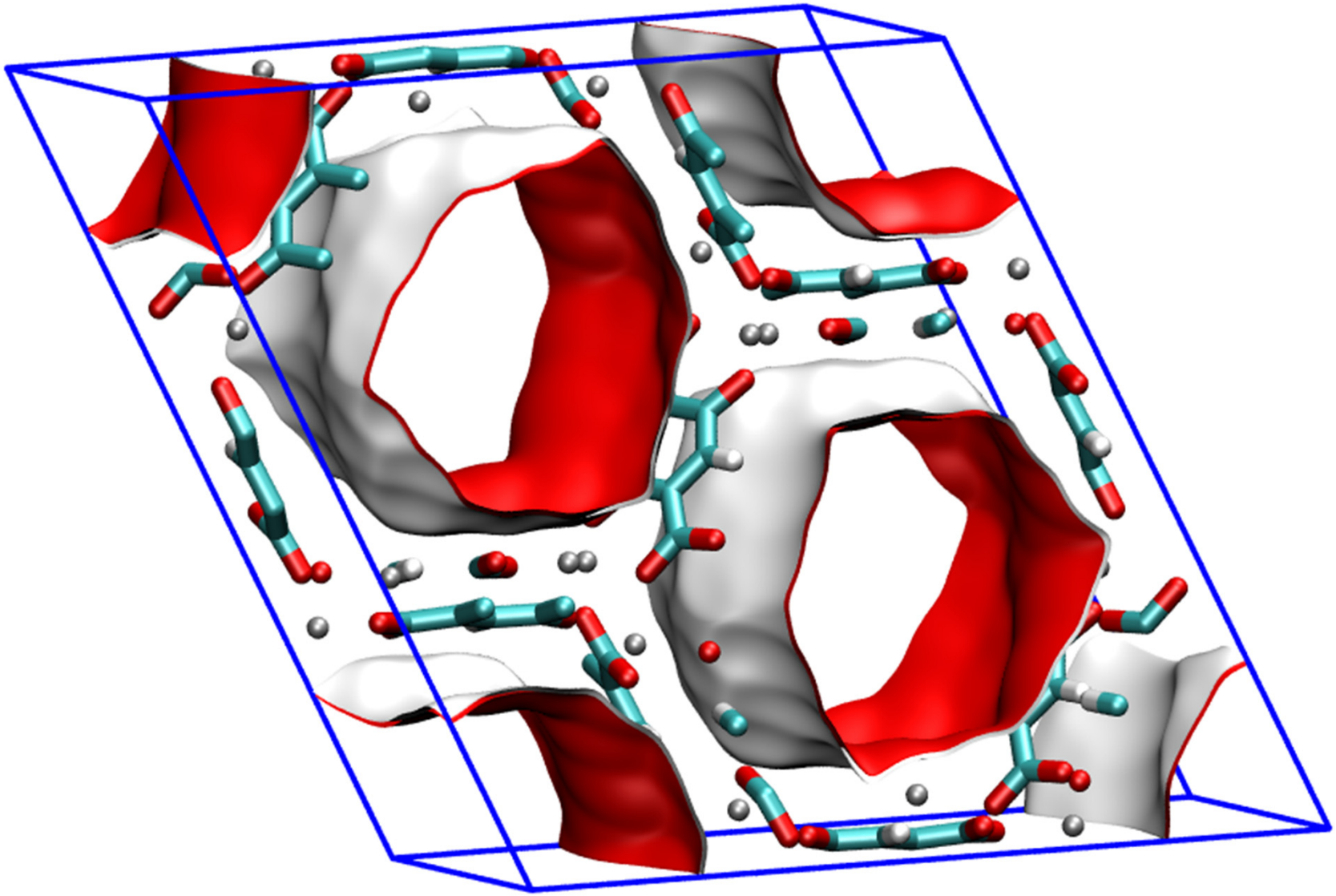

# ZnMOF-74 pore dimensions

Figure S18

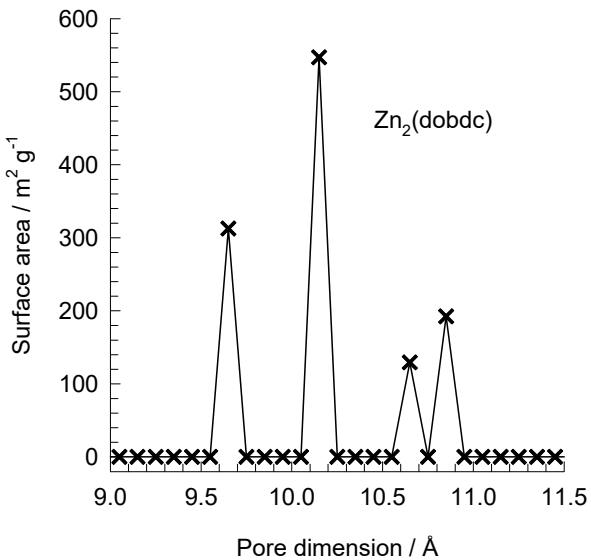


This plot of surface area versus pore dimension is determined using a combination of the DeLaunay triangulation method for pore dimension determination, and the procedure of Düren for determination of the surface area.

| | ZnMOF-74 |
|---|---|
| *a* /Å | 25.9322 |
| *b* /Å | 25.9322 |
| *c* /Å | 6.8365 |
| Cell volume / Å$^3$ | 3981.467 |
| conversion factor for [molec/uc] to [mol per kg Framework] | 0.3421 |
| conversion factor for [molec/uc] to [kmol/m$^3$] | 0.5881 |
| $\rho$ [kg/m3] | 1219.304 |
| MW unit cell [g/mol(framework)] | 2923.473 |
| $\phi$, fractional pore volume | 0.709 |
| open space / Å$^3$/uc | 2823.8 |
| Pore volume / cm$^3$/g | 0.582 |
| Surface area /m$^2$/g | 1176.0 |
| DeLaunay diameter /Å | 9.49 |

# CoMOF-74

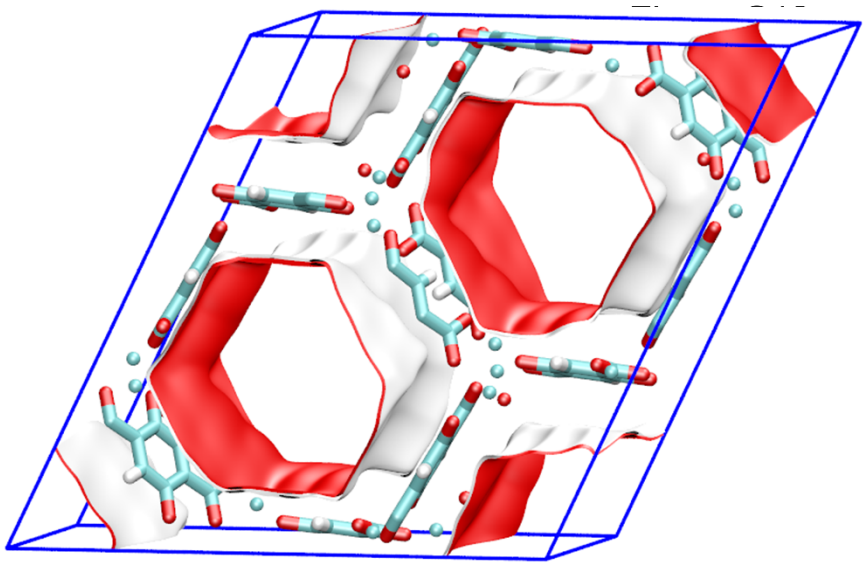

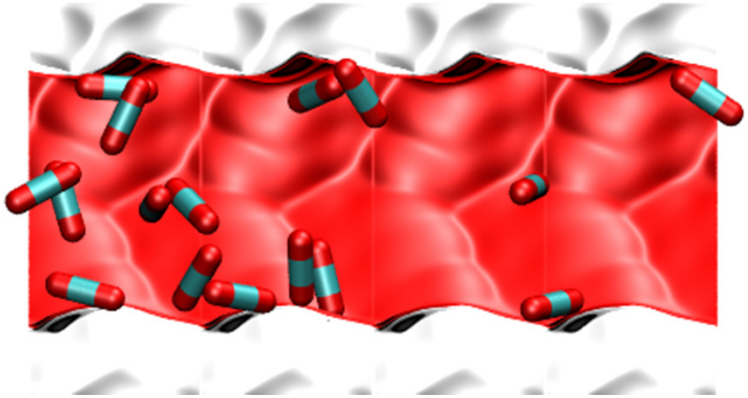

| | CoMOF-74 |
|---|---|
| *a* /Å | 25.885 |
| *b* /Å | 25.885 |
| *c* /Å | 6.8058 |
| Cell volume / Å$^3$ | 3949.173 |
| conversion factor for [molec/uc] to [mol per kg Framework] | 0.3563 |
| conversion factor for [molec/uc] to [kmol/m$^3$] | 0.5945 |
| $\rho$ [kg/m3] | 1180.261 |
| MW unit cell [g/mol(framework)] | 2806.908 |
| $\phi$, fractional pore volume | 0.707 |
| open space / Å$^3$/uc | 2793.1 |
| Pore volume / cm$^3$/g | 0.599 |
| Surface area /m$^2$/g | 1274.0 |
| DeLaunay diameter /Å | 9.52 |

# NiMOF-74

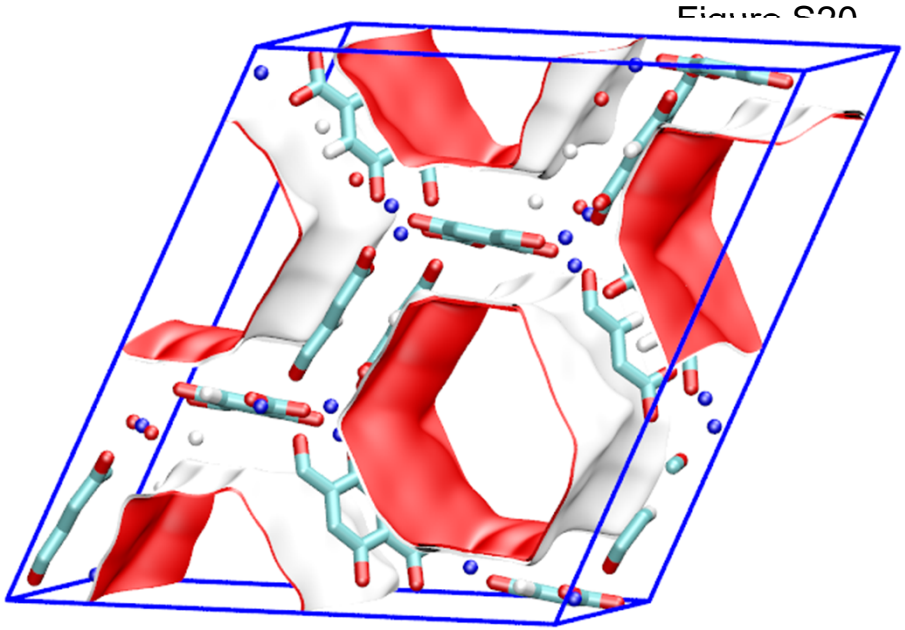

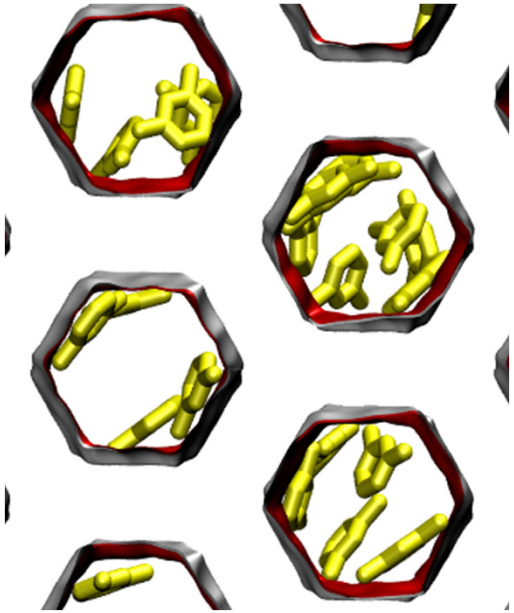

| | NiMOF-74 |
|---|---|
| *a* /Å | 25.7856 |
| *b* /Å | 25.7856 |
| *c* /Å | 6.7701 |
| Cell volume / Å$^3$ | 3898.344 |
| conversion factor for [molec/uc] to [mol per kg Framework] | 0.3568 |
| conversion factor for [molec/uc] to [kmol/m$^3$] | 0.6133 |
| $\rho$ [kg/m3] | 1193.811 |
| MW unit cell [g/mol(framework)] | 2802.592 |
| $\phi$, fractional pore volume | 0.695 |
| open space / Å$^3$/uc | 2707.6 |
| Pore volume / cm$^3$/g | 0.582 |
| Surface area /m$^2$/g | 1239.0 |
| DeLaunay diameter /Å | 9.80 |

# FeMOF-74

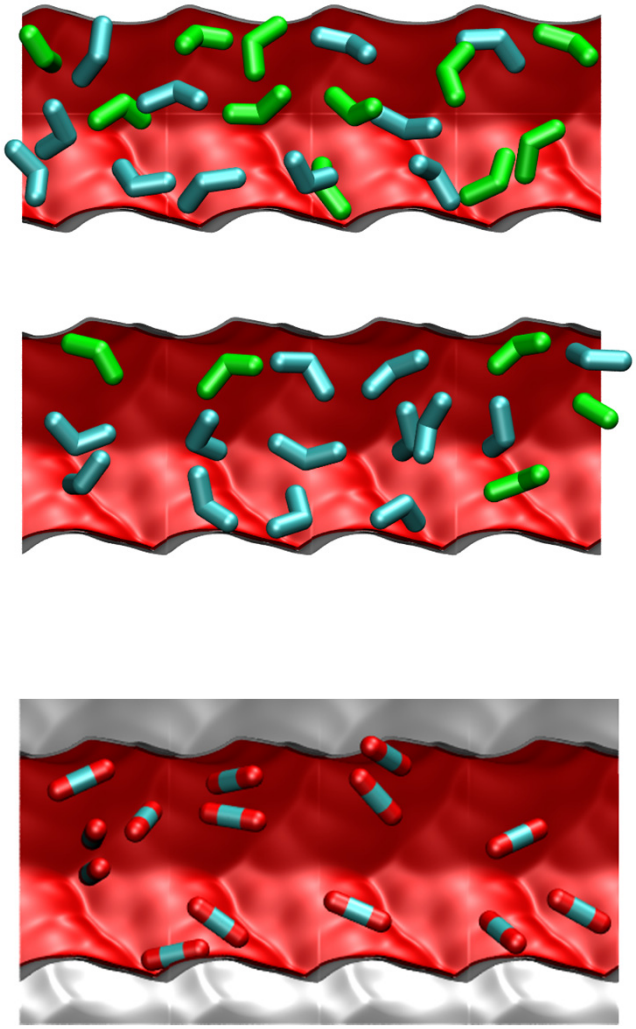

Figure S21

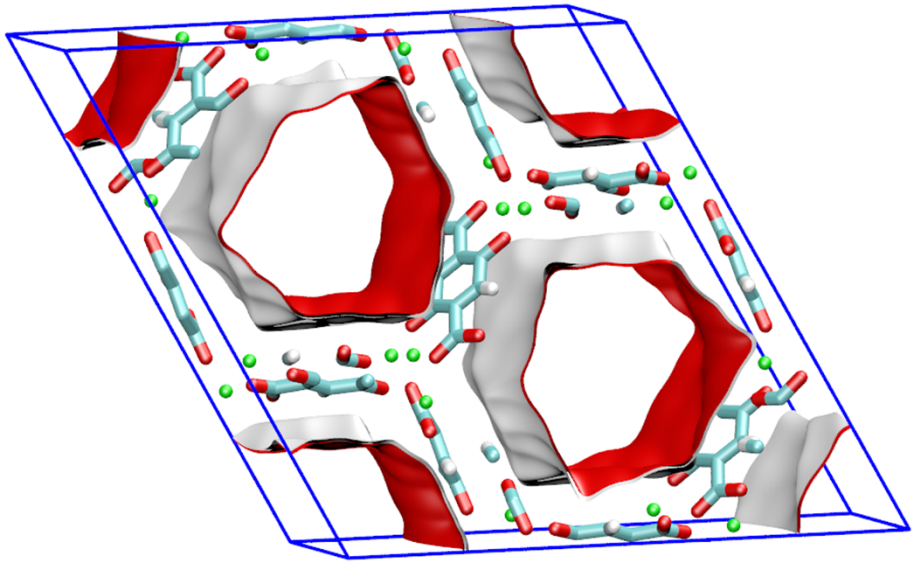

| | FeMOF-74 |
|---|---|
| *a* /Å | 26.1627 |
| *b* /Å | 26.1627 |
| *c* /Å | 6.8422 |
| Cell volume / Å$^3$ | 4055.94 |
| conversion factor for [molec/uc] to [mol per kg Framework] | 0.3635 |
| conversion factor for [molec/uc] to [kmol/m$^3$] | 0.5807 |
| $\rho$ [kg/m3] | 1126.434 |
| MW unit cell [g/mol (framework)] | 2751.321 |
| $\phi$, fractional pore volume | 0.705 |
| open space / Å$^3$/uc | 2859.7 |
| Pore volume / cm$^3$/g | 0.626 |
| Surface area /m$^2$/g | 1277.4 |
| DeLaunay diameter /Å | 11.12 |

# ZnHBDC

Figure S22

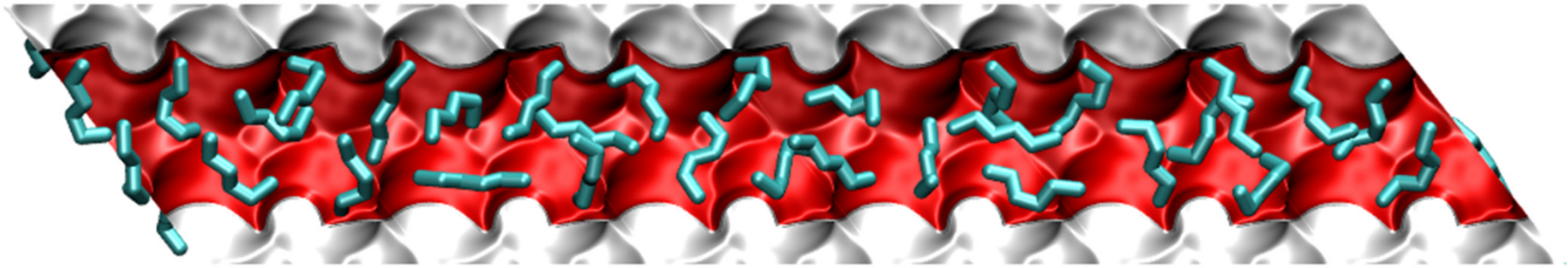

| | ZnHBDC |
|---|---|
| *a* /Å | 21.222 |
| *b* /Å | 17.716 |
| *c* /Å | 14.376 |
| Cell volume / Å$^3$ | 4269.518 |
| conversion factor for [molec/uc] to [mol per kg Framework] | 0.4489 |
| conversion factor for [molec/uc] to [kmol/m$^3$] | 0.6099 |
| $\rho$ [kg/m3] (with cations) | 866.4858 |
| MW unit cell [g/mol(framework+cations)] | 2227.841 |
| $\phi$, fractional pore volume | 0.638 |
| open space / Å$^3$/uc | 2722.7 |
| Pore volume / cm$^3$/g | 0.736 |
| Surface area /m$^2$/g | 1738.0 |
| DeLaunay diameter /Å | |

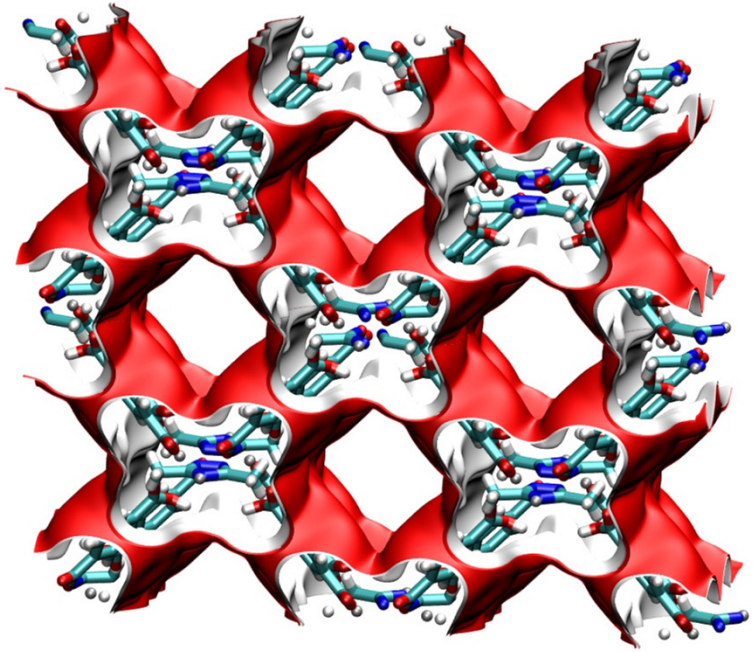

**The detailed structural information is provided in Dubbeldam, D.; Krishna, R.; Calero, S.; Yazaydın, A. Ö. Computer-Assisted Screening of Ordered Crystalline Nanoporous Adsorbents for Separation of Alkane Isomers. Angew. Chem. Int. Ed. 2012, 51, 11867-11871.**

# ZIF-77

## pore landscapes

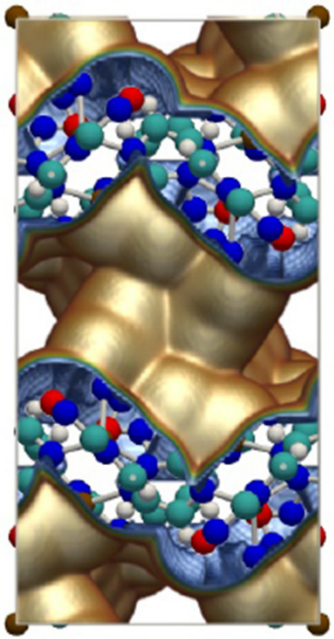

Single unit cell: x-y view

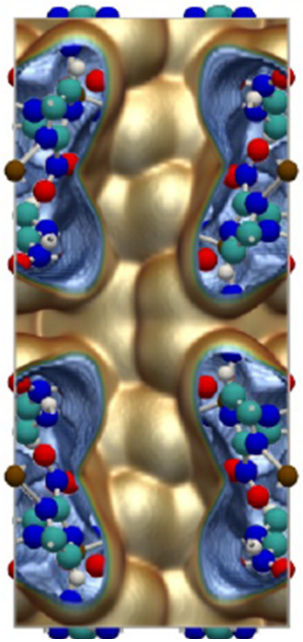

Single unit cell: x-z view

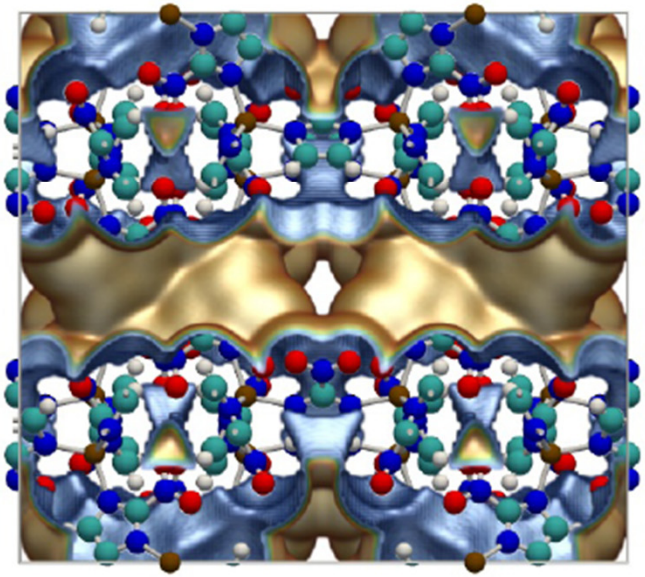

Single unit cell: y-z view

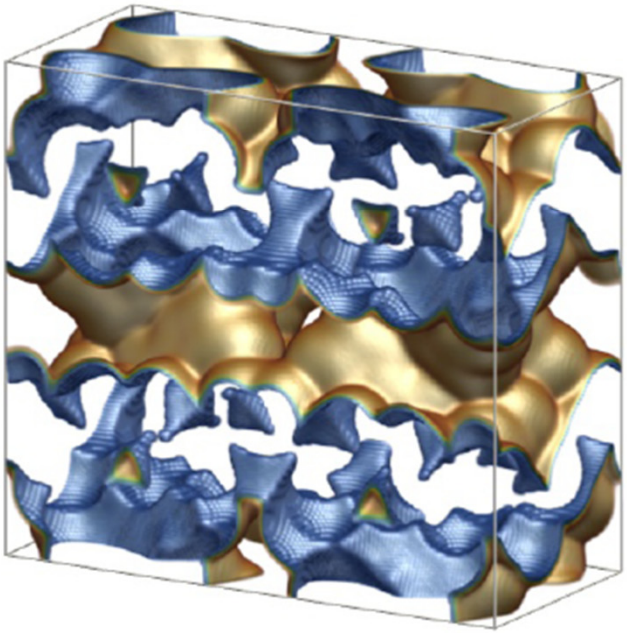

Single unit cell: x-y-z view

# ZIF-77 dimensions

Figure S24

| | ZIF-77 |
|---|---|
| *a* /Å | 11.1248 |
| *b* /Å | 22.3469 |
| *c* /Å | 24.9087 |
| $\rho$ [kg/m3] | 1552.86 |
| MW unit cell [g/mol(framework)] | 2730.182 |
| $\phi$, fractional pore volume | 0.293 |
| Pore volume / $cm^3/g$ | 0.189 |
| Surface area /$m^2/g$ | 541 |
| DeLaunay diameter /Å | 4.5 |

Figure S25

# MOR pore landscape

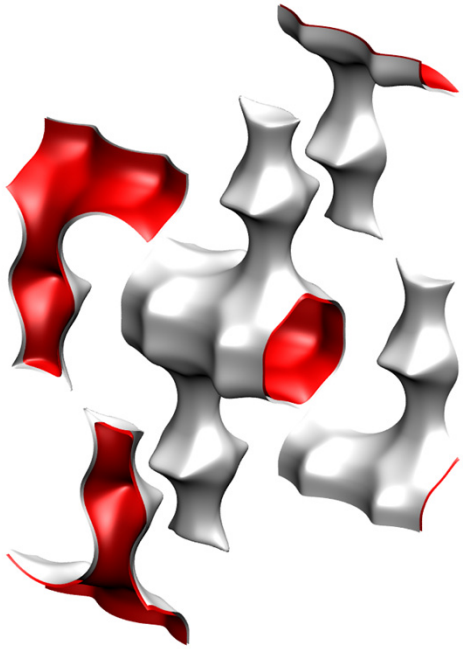

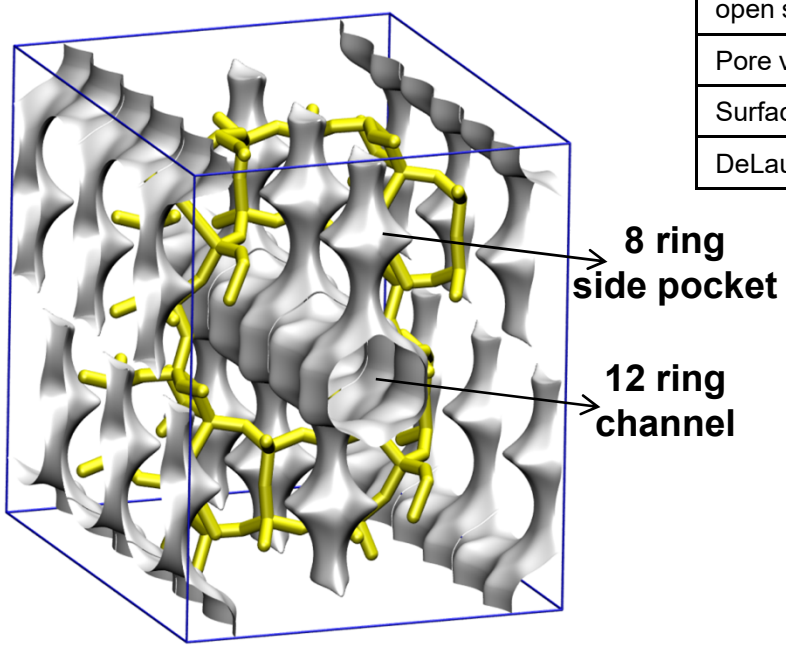


| | MOR |
|---|---|
| *a* /Å | 18.094 |
| *b* /Å | 20.516 |
| *c* /Å | 7.524 |
| Cell volume / Å$^3$ | 2793.033 |
| conversion factor for [molec/uc] to [mol per kg Framework] | 0.3467 |
| conversion factor for [molec/uc] to [kmol/m$^3$] | 2.0877 |
| $\rho$ [kg/m3] | 1714.691 |
| MW unit cell [g/mol(framework)] | 2884.07 |
| $\phi$, fractional pore volume | 0.285 |
| open space / Å$^3$/uc | 795.4 |
| Pore volume / cm$^3$/g | 0.166 |
| Surface area /m$^2$/g | 417.0 |
| DeLaunay diameter /Å | 6.44 |

# MOR pore dimensions

Figure S26

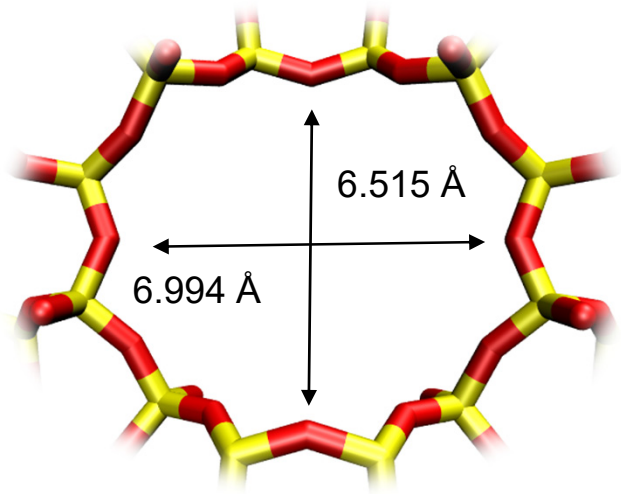


MOR Channel [1 0 0]

12-ring
main channels

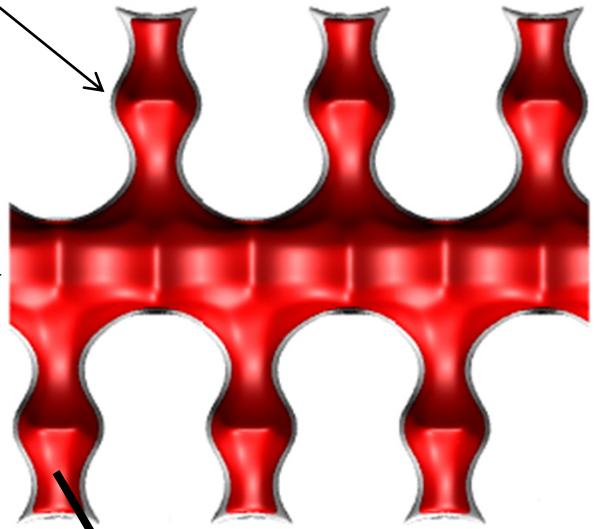


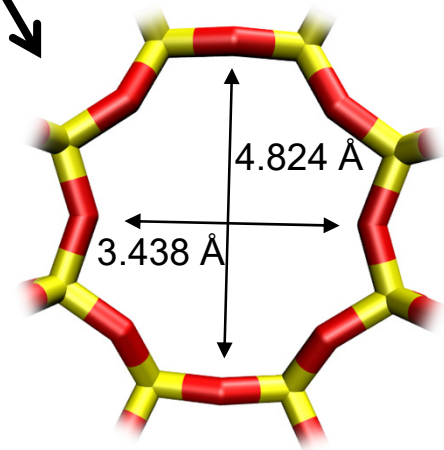


MOR [0 1 0]

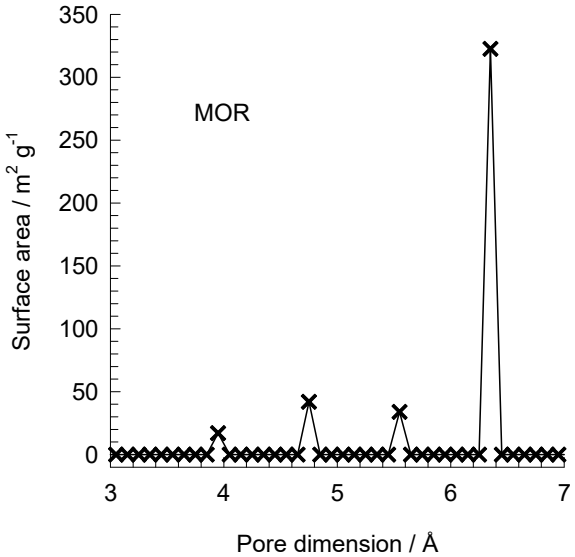


This plot of surface area versus pore dimension is determined using a combination of the DeLaunay triangulation method for pore dimension determination, and the procedure of Düren for determination of the surface area.

# FER pore landscape

Figure S27

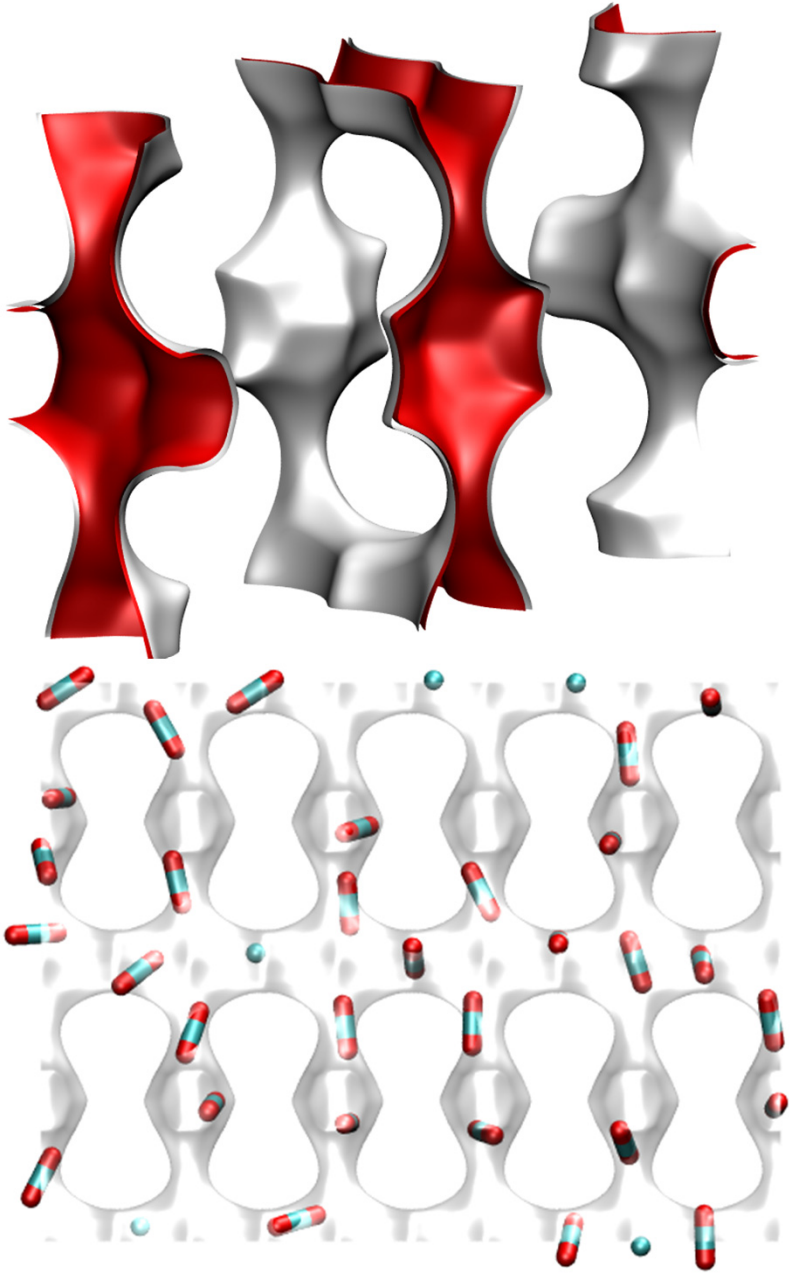

| | FER |
|---|---|
| *a* /Å | 19.156 |
| *b* /Å | 14.127 |
| *c* /Å | 7.489 |
| Cell volume / Å$^3$ | 2026.649 |
| conversion factor for [molec/uc] to [mol per kg Framework] | 0.4623 |
| conversion factor for [molec/uc] to [kmol/m$^3$] | 2.8968 |
| $\rho$ [kg/m3] | 1772.33 |
| MW unit cell [g/mol (framework)] | 2163.053 |
| $\phi$, fractional pore volume | 0.283 |
| open space / Å$^3$/uc | 573.2 |
| Pore volume / cm$^3$/g | 0.160 |
| Surface area /m$^2$/g | 403.0 |
| DeLaunay diameter /Å | 4.65 |

# FER pore dimensions

Figure S28

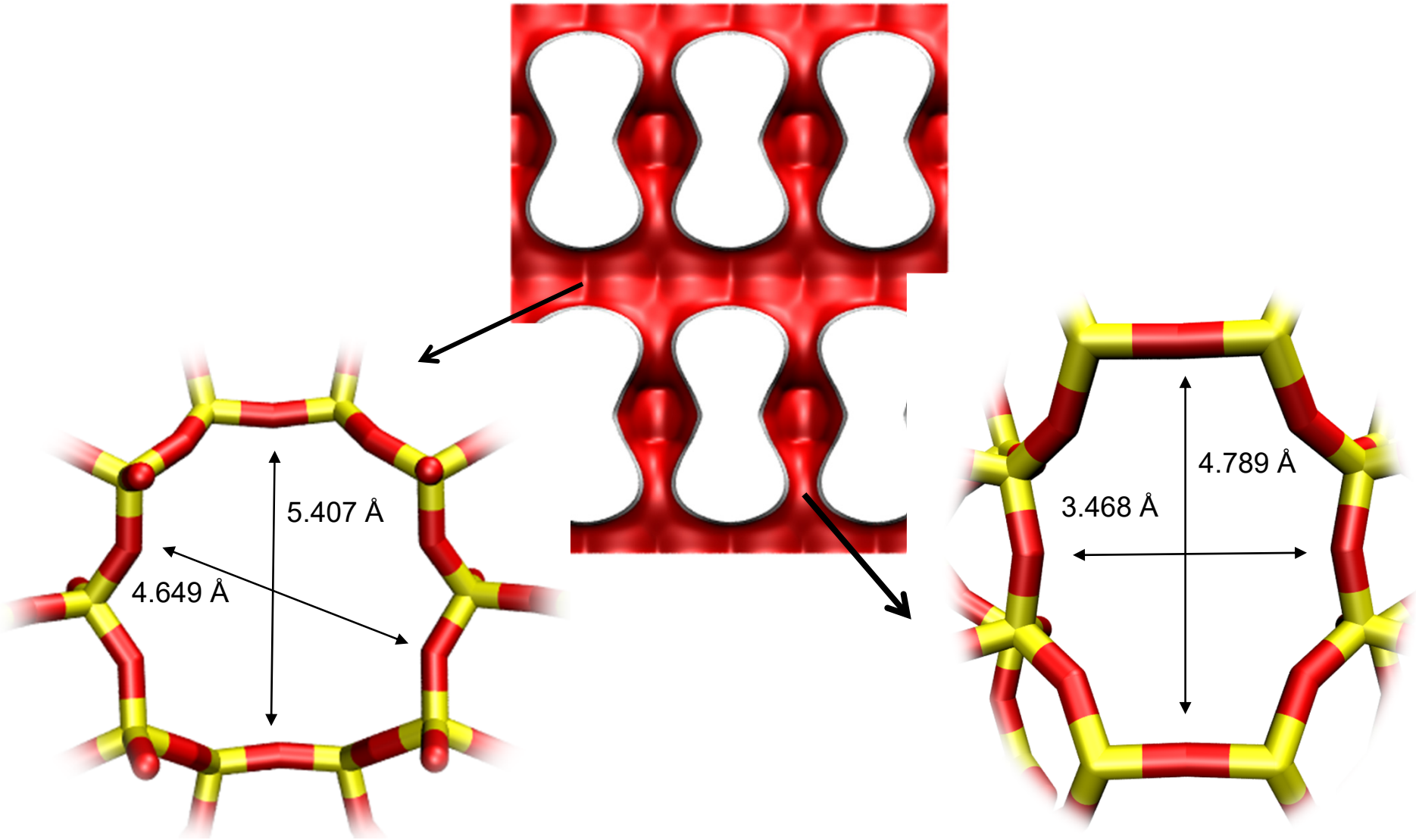


FER channel [0 0 1]

FER [0 1 0]

# AFX pore landscape

Figure S29

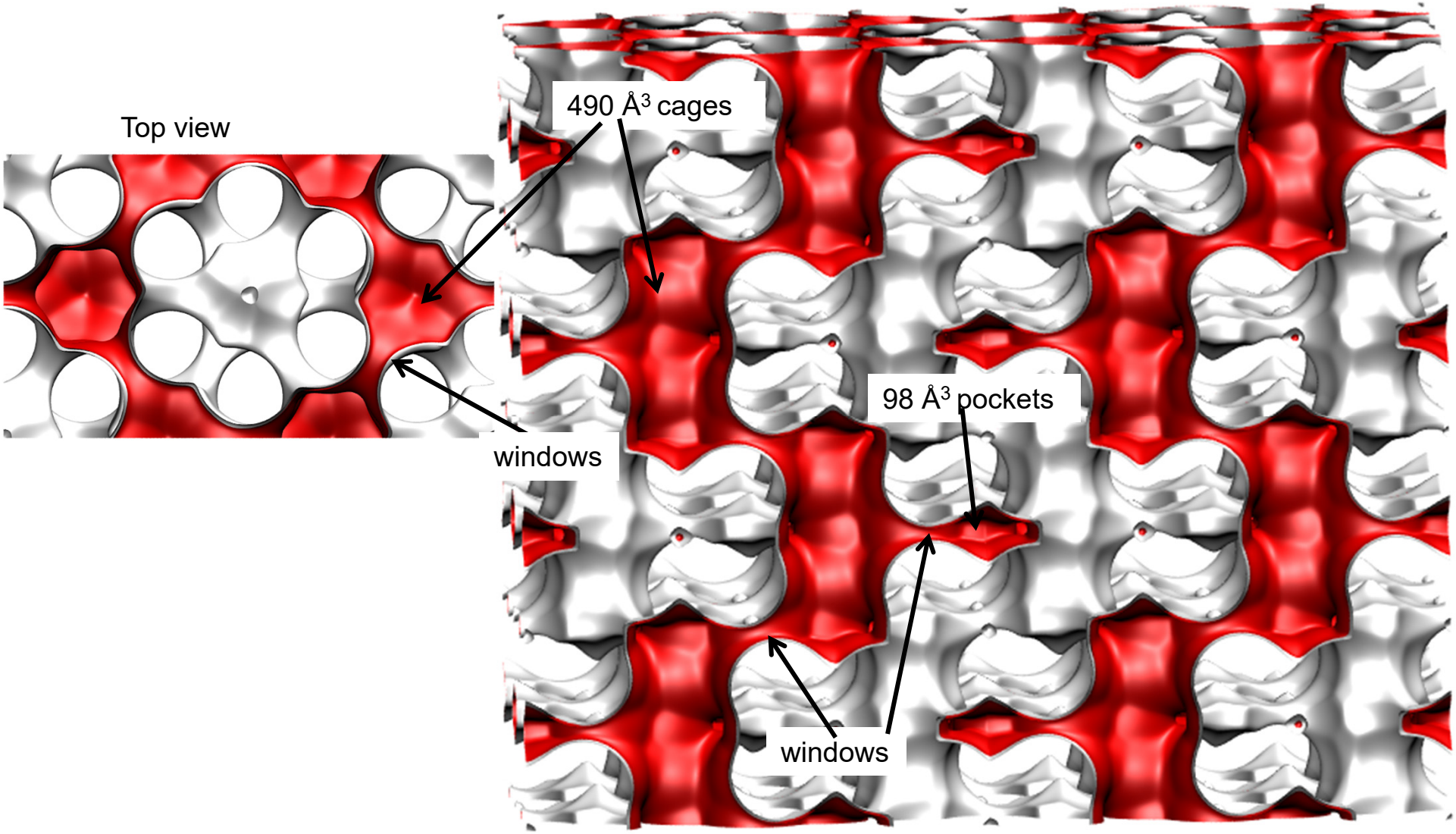


Structural information from: C. Baerlocher, L.B. McCusker, Database of Zeolite Structures, International Zeolite Association, http://www.iza-structure.org/databases/

# AFX window sizes and pore dimensions

Figure S30

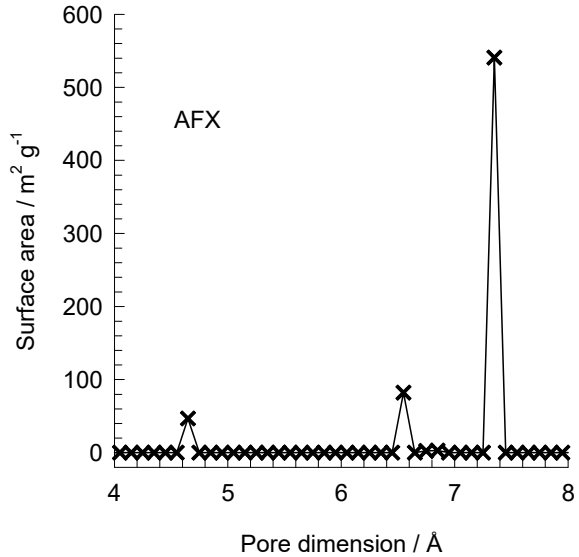


| | AFX |
|---|---|
| *a* /Å | 23.836 |
| *b* /Å | 13.762 |
| *c* /Å | 19.949 |
| Cell volume / Å$^3$ | 6543.891 |
| conversion factor for [molec/uc] to [mol per kg Framework] | 0.1734 |
| conversion factor for [molec/uc] to [kmol/m$^3$] | 0.7059 |
| $\rho$ [kg/m3] | 1463.713 |
| MW unit cell [g/mol(framework)] | 5768.141 |
| $\phi$, fractional pore volume | 0.359 |
| open space / Å$^3$/uc | 2352.5 |
| Pore volume / cm$^3$/g | 0.246 |
| Surface area /m$^2$/g | 674.0 |
| DeLaunay diameter /Å | 3.44 |

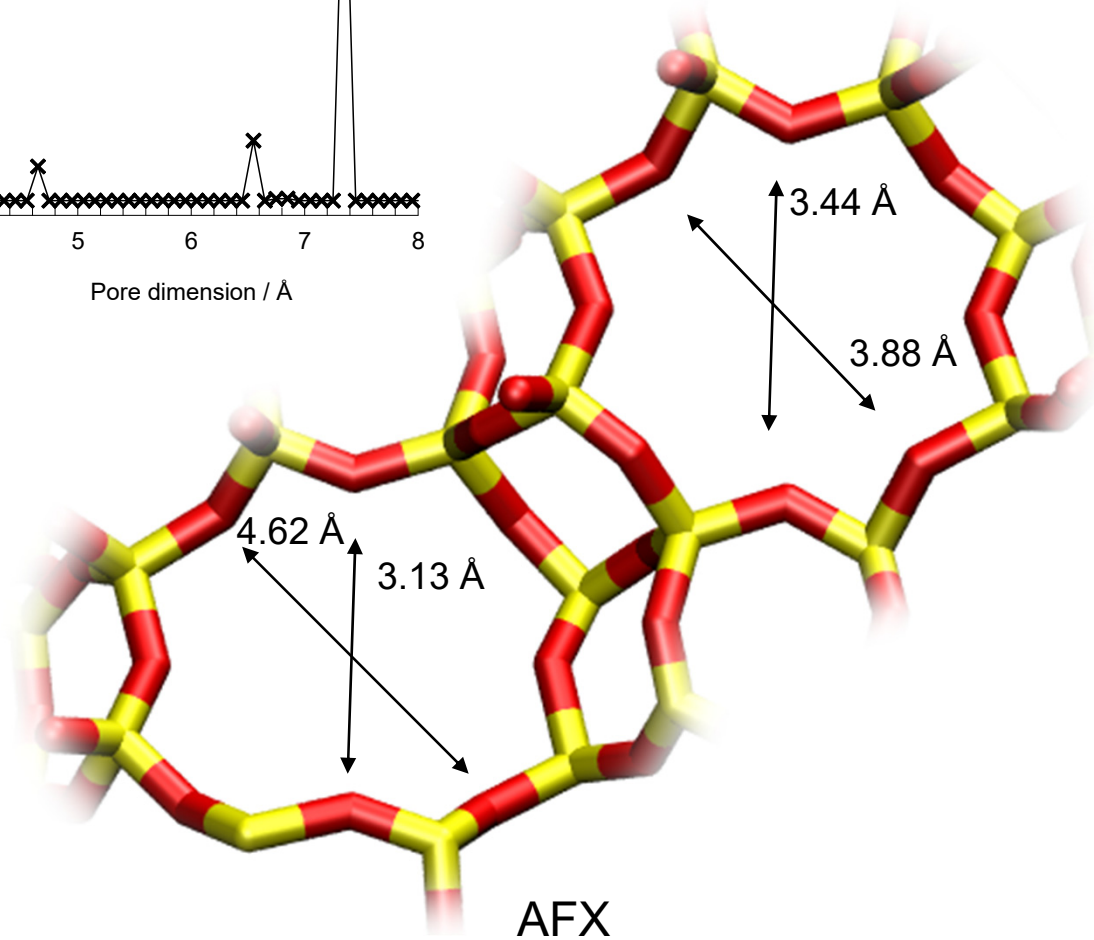


The window dimension calculated using the van der Waals diameter of framework atoms = 2.7 Å are indicated above by the arrows.

# CHA

Figure S31

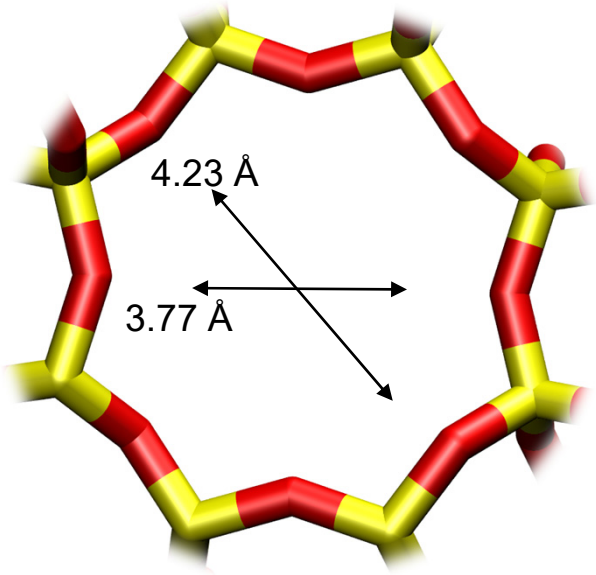


CHA

Snapshots showing location of $CH_4$ and $CO_2$

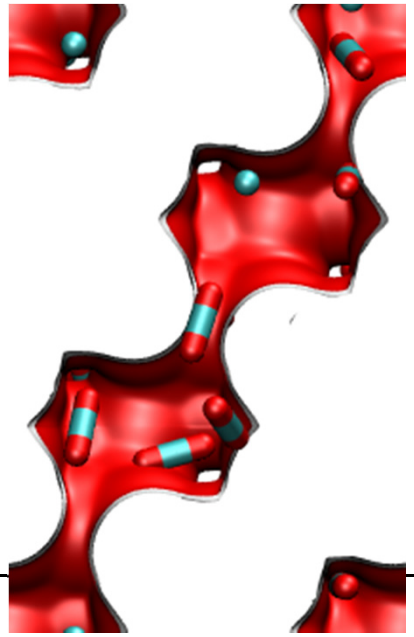

| | CHA |
|---|---|
| *a* /Å | 15.075 |
| *b* /Å | 23.907 |
| *c* /Å | 13.803 |
| Cell volume / Å$^3$ | 4974.574 |
| conversion factor for [molec/uc] to [mol per kg Framework] | 0.2312 |
| conversion factor for [molec/uc] to [kmol/m$^3$] | 0.8747 |
| $\rho$ [kg/m3] | 1444.1 |
| MW unit cell [g/mol(framework)] | 4326.106 |
| $\phi$, fractional pore volume | 0.382 |
| open space / Å$^3$/uc | 1898.4 |
| Pore volume / cm$^3$/g | 0.264 |
| Surface area /m$^2$/g | 758.0 |
| DeLaunay diameter /Å | 3.77 |

The window dimensions calculated using the van der Waals diameter of framework atoms = 2.7 Å are indicated above by the arrows.

# DDR

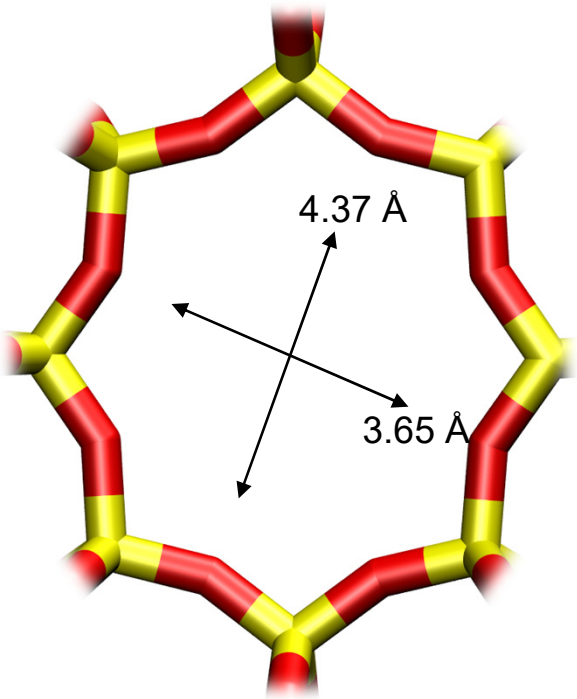


DDR

The window dimensions calculated using the van der Waals diameter of framework atoms = 2.7 Å are indicated above by the arrows.

Figure S32

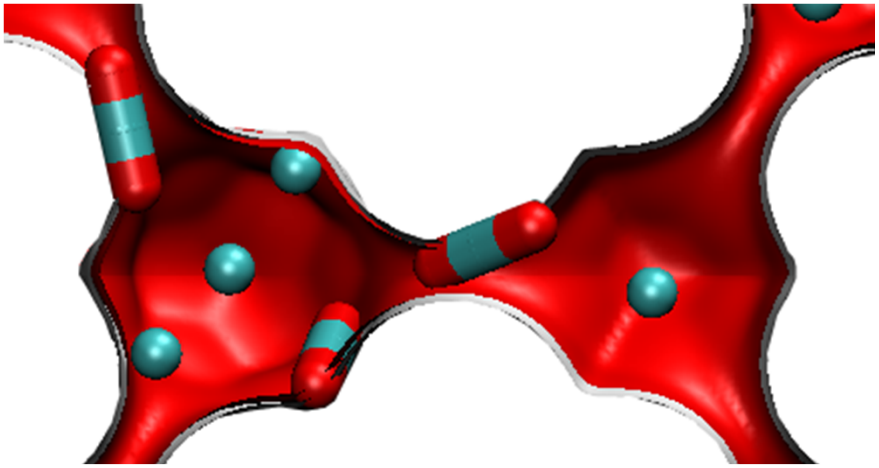

| | DDR |
|---|---|
| *a* /Å | 24.006 |
| *b* /Å | 13.86 |
| *c* /Å | 40.892 |
| Cell volume / Å$^3$ | 13605.72 |
| conversion factor for [molec/uc] to [mol per kg Framework] | 0.0693 |
| conversion factor for [molec/uc] to [kmol/m$^3$] | 0.4981 |
| $\rho$ [kg/m3] | 1759.991 |
| MW unit cell [g/mol(framework)] | 14420.35 |
| $\phi$, fractional pore volume | 0.245 |
| open space / Å$^3$/uc | 3333.5 |
| Pore volume / cm$^3$/g | 0.139 |
| Surface area /m$^2$/g | 350.0 |
| DeLaunay diameter /Å | 3.65 |

# ERI

Snapshots showing location of $CH_4$ and $CO_2$

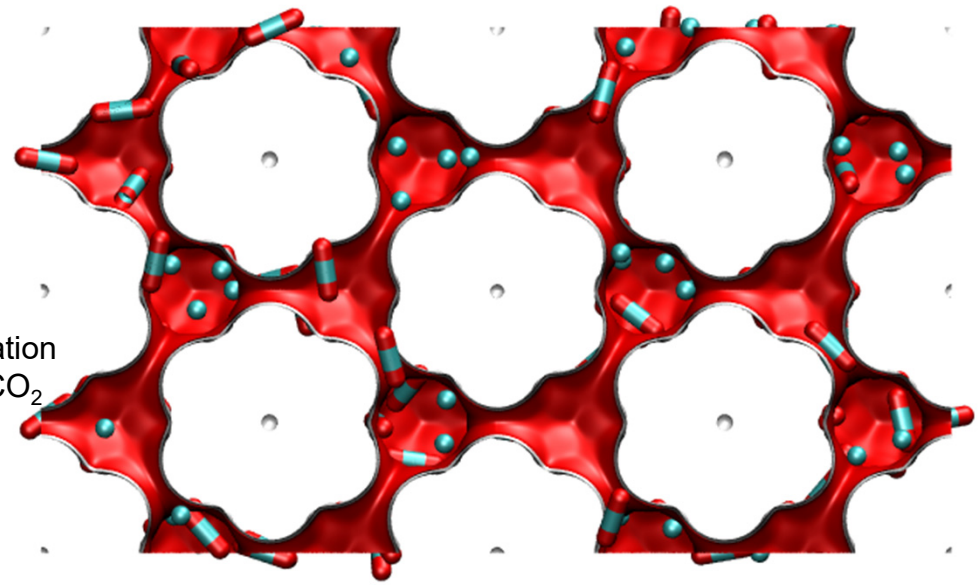

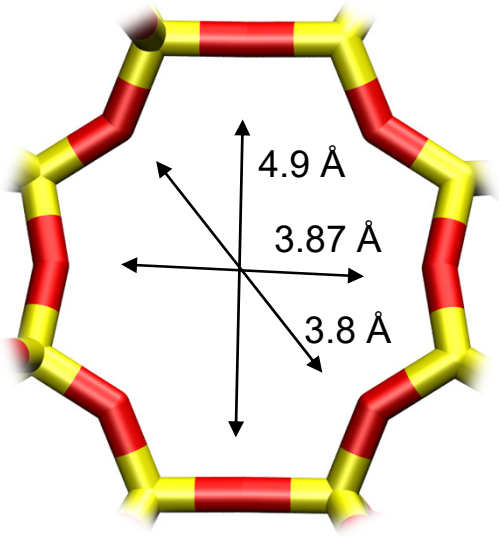


ERI

The window dimensions calculated using the van der Waals diameter of framework atoms = 2.7 Å are indicated above by the arrows.

| | ERI |
|---|---|
| *a* /Å | 22.953 |
| *b* /Å | 13.252 |
| *c* /Å | 14.81 |
| Cell volume / Å$^3$ | 4504.804 |
| conversion factor for [molec/uc] to [mol per kg Framework] | 0.2312 |
| conversion factor for [molec/uc] to [kmol/m$^3$] | 1.0156 |
| $\rho$ [kg/m3] | 1594.693 |
| MW unit cell [g/mol(framework)] | 4326.106 |
| $\phi$, fractional pore volume | 0.363 |
| open space / Å$^3$/uc | 1635.0 |
| Pore volume / cm$^3$/g | 0.228 |
| Surface area /m$^2$/g | 635.0 |
| DeLaunay diameter /Å | 3.81 |

# ITQ-29

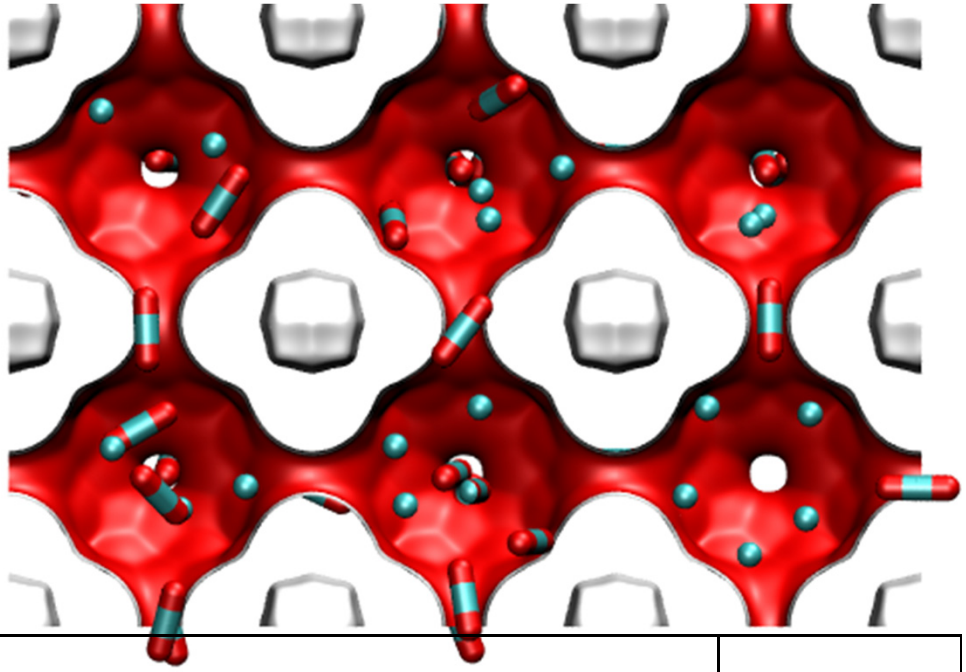

The structural information for ITQ-29 is not available in the IZA atlas and is taken from Corma, Nature, 437 (2004) 287. The window size is slightly smaller than that of LTA (all-silica).

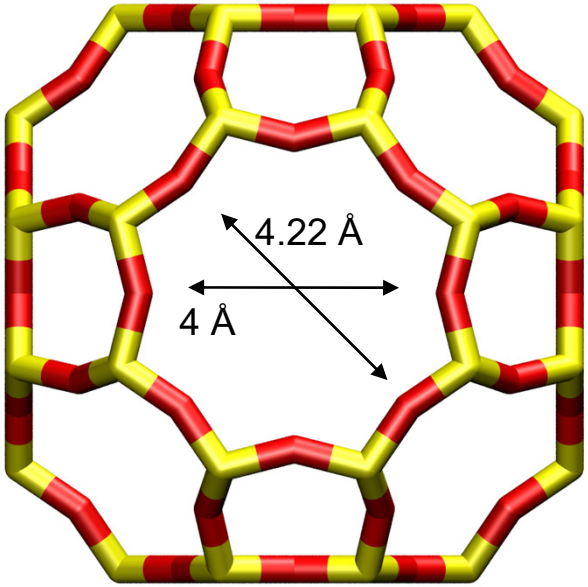


The window dimension calculated using the van der Waals diameter of framework atoms = 2.7 Å is indicated above by the arrows.

| | ITQ-29 |
|---|---|
| *a* /Å | 11.867 |
| *b* /Å | 11.867 |
| *c* /Å | 11.867 |
| Cell volume / Å$^3$ | 1671.178 |
| conversion factor for [molec/uc] to [mol per kg Framework] | 0.6935 |
| conversion factor for [molec/uc] to [kmol/m$^3$] | 2.4508 |
| $\rho$ [kg/m3] | 1432.877 |
| MW unit cell [g/mol(framework)] | 1442.035 |
| $\phi$, fractional pore volume | 0.405 |
| open space / Å$^3$/uc | 677.6 |
| Pore volume / cm$^3$/g | 0.283 |
| Surface area /m$^2$/g | 773.0 |
| DeLaunay diameter /Å | 3.98 |

# LTA (all-silica)

8-ring window of LTA

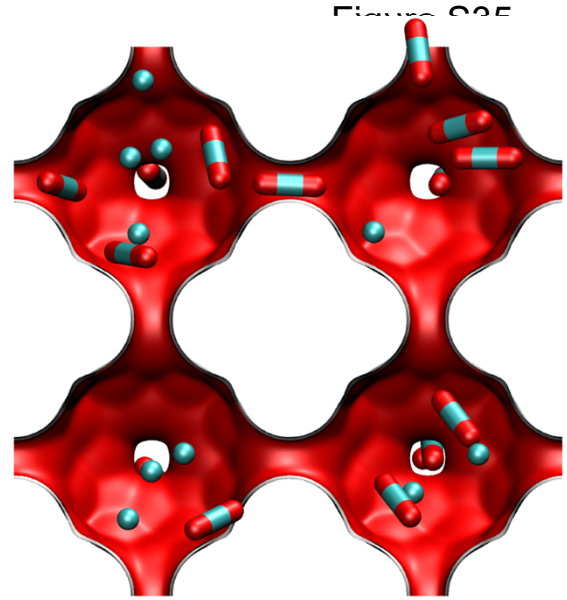

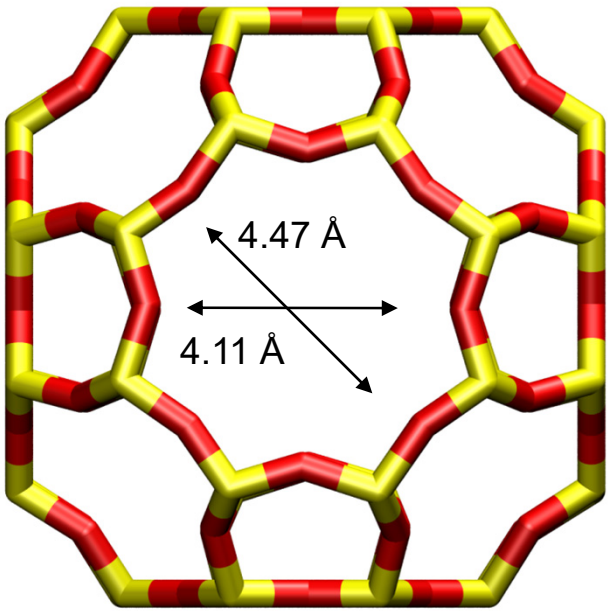


The window dimension calculated using the van der Waals diameter of framework atoms = 2.7 Å is indicated above by the arrows.

| | LTA |
|---|---|
| *a* /Å | 24.61 |
| *b* /Å | 24.61 |
| *c* /Å | 24.61 |
| Cell volume / Å$^3$ | 14905.1 |
| conversion factor for [molec/uc] to [mol per kg Framework] | 0.0867 |
| conversion factor for [molec/uc] to [kmol/m$^3$] | 0.2794 |
| $\rho$ [kg/m3] | 1285.248 |
| MW unit cell [g/mol(framework)] | 11536.28 |
| $\phi$, fractional pore volume | 0.399 |
| open space / Å$^3$/uc | 5944.4 |
| Pore volume / cm$^3$/g | 0.310 |
| Surface area /m$^2$/g | 896.0 |
| DeLaunay diameter /Å | 4.10 |

# LTA-5A

Figure S36

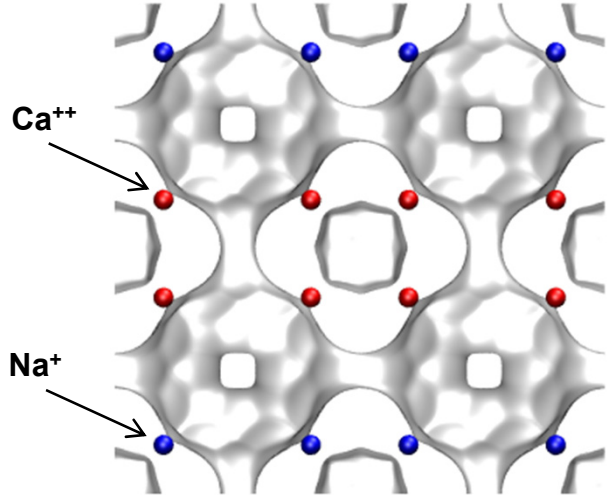


**LTA-5A (32 Na+, 32 Ca++)**

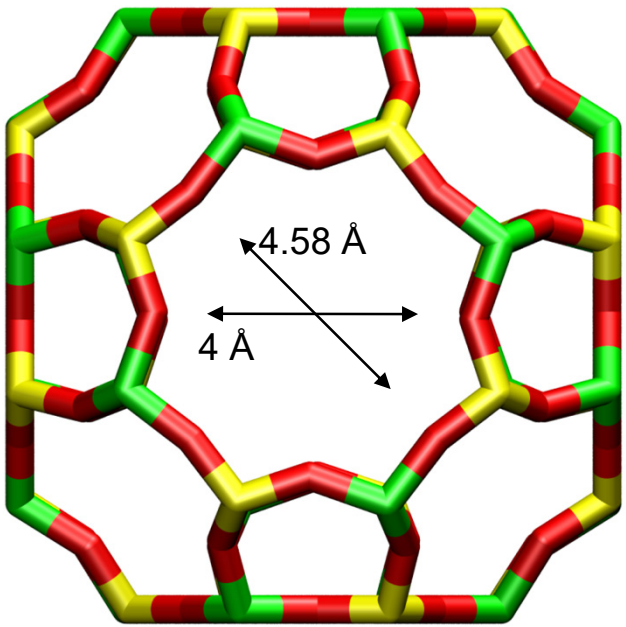


LTA-5A

The window dimension calculated using the van der Waals diameter of framework atoms = 2.7 Å is indicated above by the arrow.

| | LTA-5A |
|---|---|
| *a* /Å | 24.555 |
| *b* /Å | 24.555 |
| *c* /Å | 24.555 |
| Cell volume / Å$^3$ | 14805.39 |
| conversion factor for [molec/uc] to [mol per kg Framework] | 0.0744 |
| conversion factor for [molec/uc] to [kmol/m$^3$] | 0.2955 |
| $\rho$ [kg/m3] (with cations) | 1508.376 |
| MW unit cell [g/mol(framework+cations)] | 13448.48 |
| $\phi$, fractional pore volume | 0.380 |
| open space / Å$^3$/uc | 5620.4 |
| Pore volume / cm$^3$/g | 0.252 |
| Surface area /m$^2$/g | |
| DeLaunay diameter /Å | 4.00 |

# LTA-4A

Figure S37

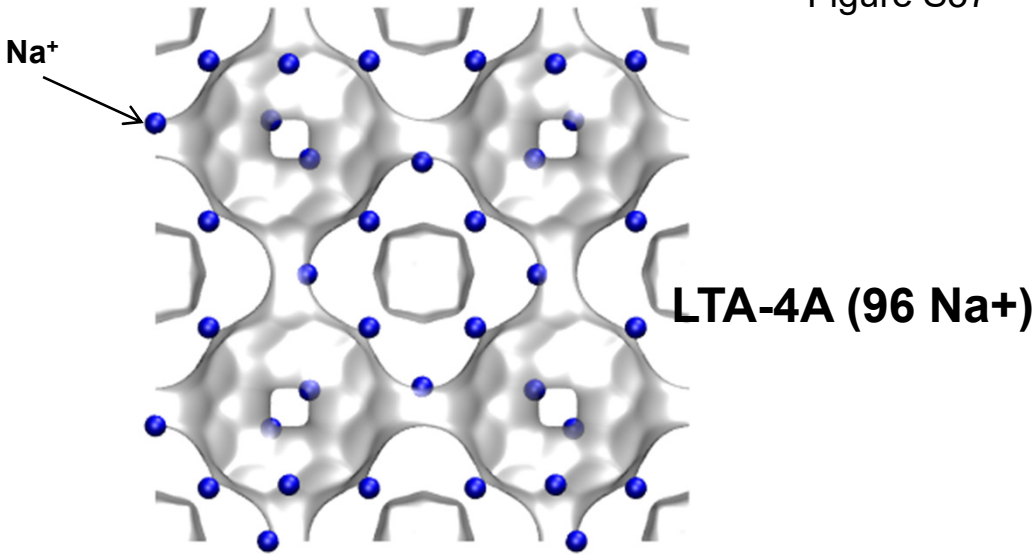


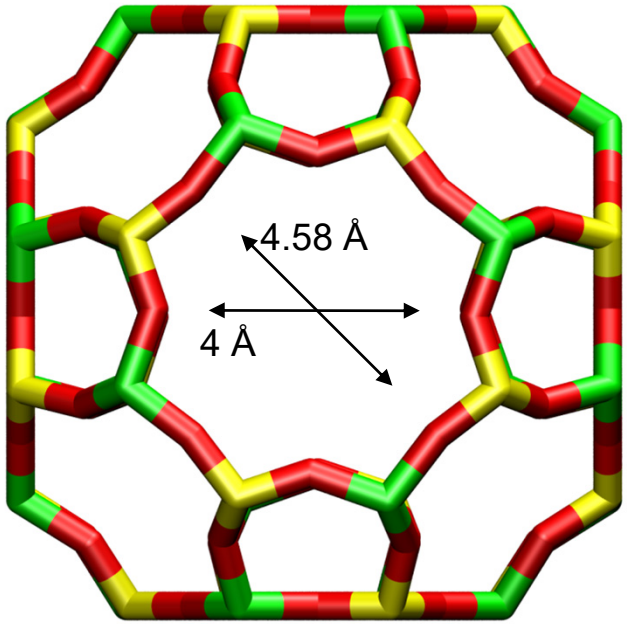


LTA-4A

The window dimension calculated using the van der Waals diameter of framework atoms = 2.7 Å is indicated above by the arrow.

Note that the $Na^+$ ions partially block the windows and therefore the diffusivities in LTA-4A are significantly lower than that for LTA Si. These cannot be determined from MD.

| | LTA-4A |
|---|---|
| *a* /Å | 24.555 |
| *b* /Å | 24.555 |
| *c* /Å | 24.555 |
| Cell volume / $Å^3$ | 14805.39 |
| conversion factor for [molec/uc] to [mol per kg Framework] | 0.0733 |
| conversion factor for [molec/uc] to [kmol/$m^3$] | 0.2991 |
| $\rho$ [kg/m3] (with cations) | 1529.55 |
| MW unit cell [g/mol(framework+cations)] | 13637.27 |
| $\phi$, fractional pore volume | 0.375 |
| open space / $Å^3$/uc | 5552.0 |
| Pore volume / $cm^3$/g | 0.245 |
| Surface area /$m^2$/g | |
| DeLaunay diameter /Å | 4.00 |

# ZIF-7

Figure S38

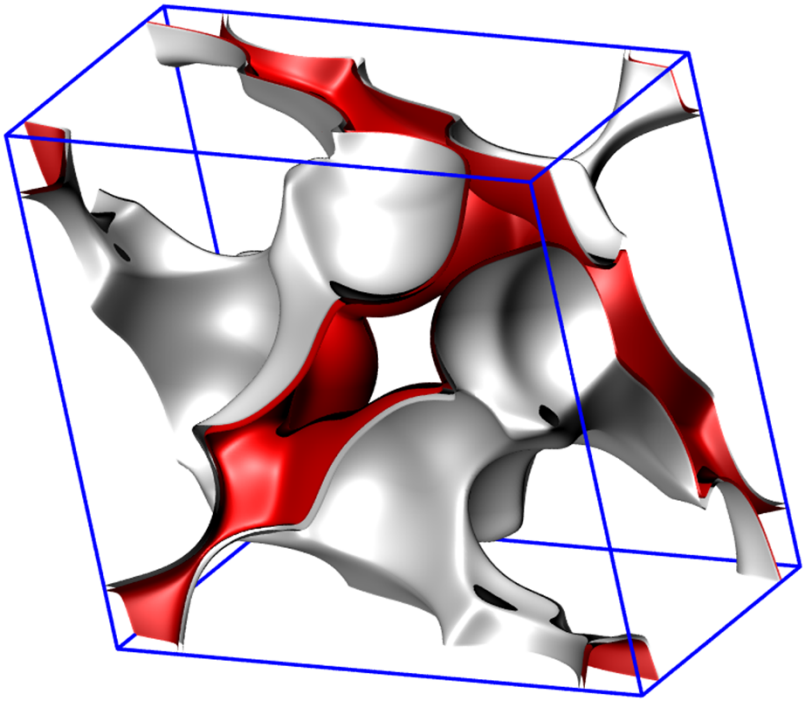

| | ZIF-7 |
|---|---|
| *a* /Å | 22.989 |
| *b* /Å | 22.989 |
| *c* /Å | 15.763 |
| Cell volume / Å$^3$ | 7214.557 |
| conversion factor for [molec/uc] to [mol per kg Framework] | 0.1855 |
| conversion factor for [molec/uc] to [kmol/m$^3$] | 0.8307 |
| $\rho$ [kg/m3] | 1240.903 |
| MW unit cell [g/mol(framework)] | 5391.274 |
| $\phi$, fractional pore volume | 0.277 |
| open space / Å$^3$/uc | 1999.0 |
| Pore volume / cm$^3$/g | 0.223 |
| Surface area /m$^2$/g | |
| DeLaunay diameter /Å | 3.26 |

# ZIF-8

Figure S39

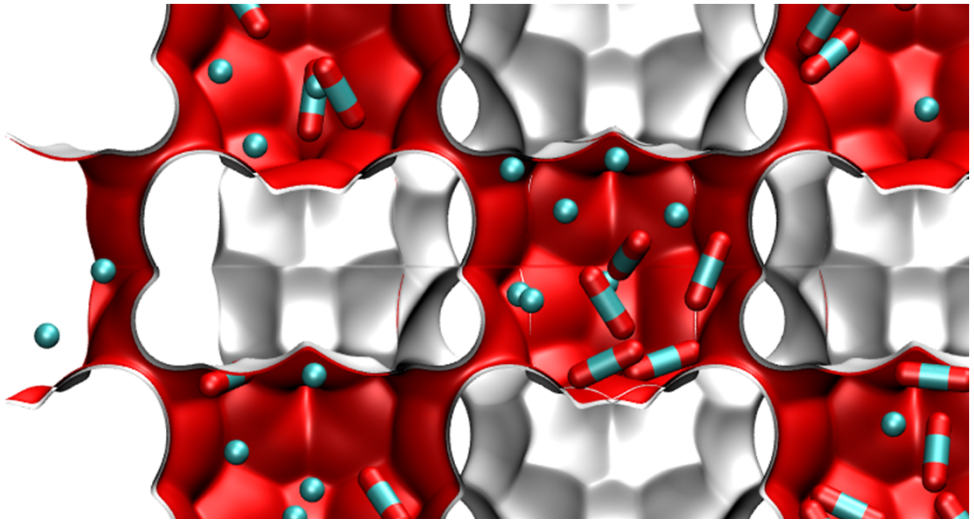

There are 2 cages per unit cell. The volume of one ZIF-8 cage is 1168 Å$^3$, significantly larger than that of a single cage of DDR (278 Å$^3$), or FAU (786 Å$^3$).

There are 2 cages per unit cell. To convert from molecules per cage to mol kg$^{-1}$, multiply by 0.7325.

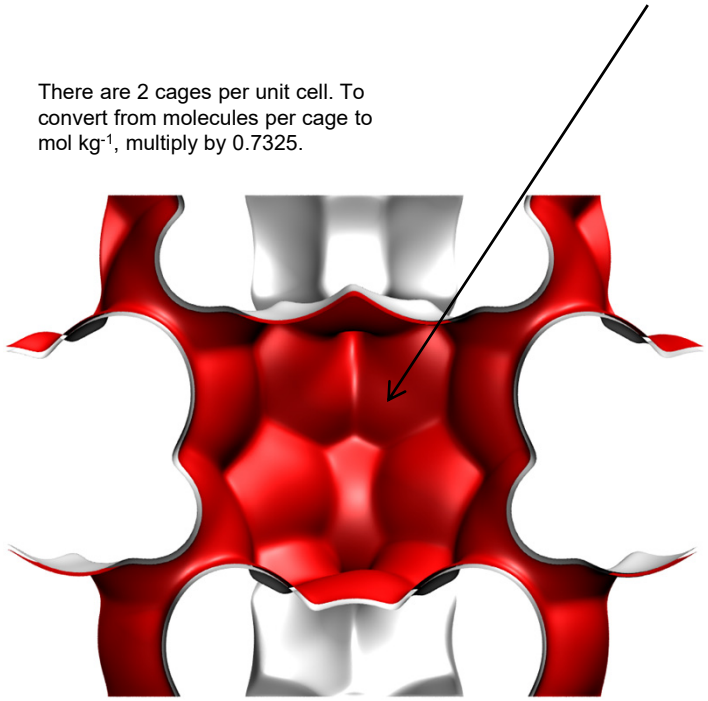

| | ZIF-8 |
|---|---|
| *a* /Å | 16.991 |
| *b* /Å | 16.991 |
| *c* /Å | 16.991 |
| Cell volume / Å$^3$ | 4905.201 |
| conversion factor for [molec/uc] to [mol per kg Framework] | 0.3663 |
| conversion factor for [molec/uc] to [kmol/m$^3$] | 0.7106 |
| $\rho$ [kg/m3] | 924.253 |
| MW unit cell [g/mol(framework)] | 2730.182 |
| $\phi$, fractional pore volume | 0.476 |
| open space / Å$^3$/uc | 2337.0 |
| Pore volume / cm$^3$/g | 0.515 |
| Surface area /m$^2$/g | 1164.7 |
| DeLaunay diameter /Å | 3.26 |

# KAUST-7

Figure S40

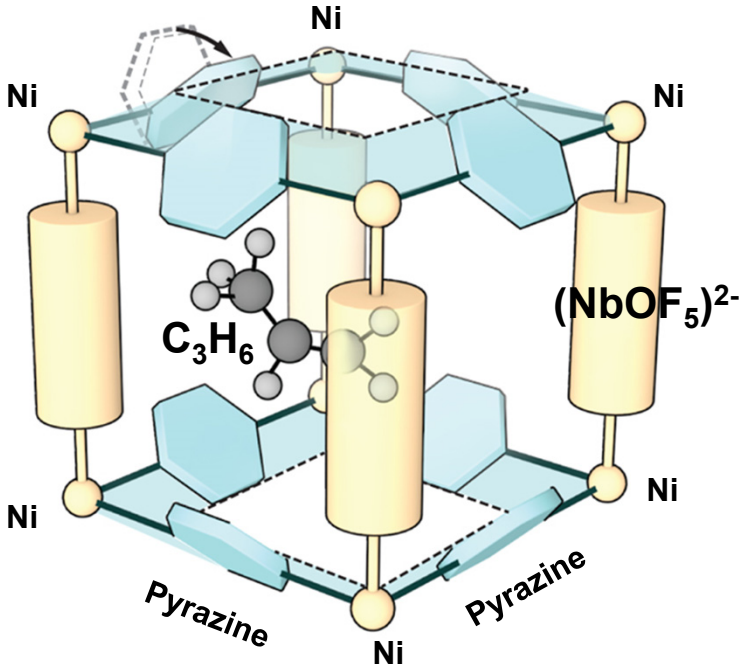


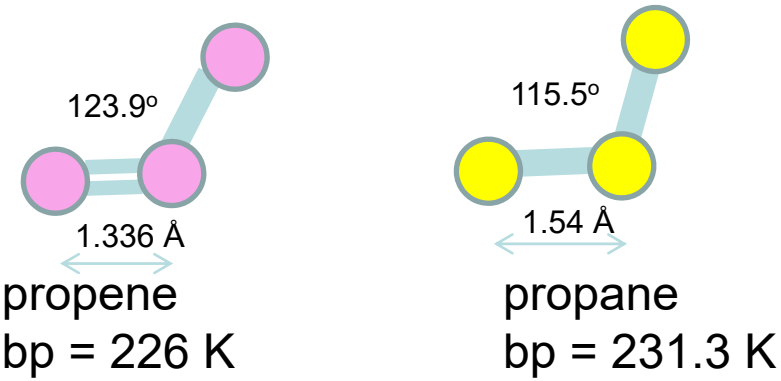


**The detailed structural information is provided in**
**Cadiau, A.; Adil, K.; Bhatt, P. M.; Belmabkhout, Y.; Eddaoudi, M. A Metal-Organic Framework–Based Splitter for Separating Propylene from Propane. Science 2016, 353, 137-140.**

# MFI pore landscape

Figure S41

| | MFI |
|---|---|
| *a* /Å | 20.022 |
| *b* /Å | 19.899 |
| *c* /Å | 13.383 |
| Cell volume / Å$^3$ | 5332.025 |
| conversion factor for [molec/uc] to [mol per kg Framework] | 0.1734 |
| conversion factor for [molec/uc] to [kmol/m$^3$] | 1.0477 |
| $\rho$ [kg/m3] | 1796.386 |
| MW unit cell [g/mol(framework)] | 5768.141 |
| $\phi$, fractional pore volume | 0.297 |
| open space / Å$^3$/uc | 1584.9 |
| Pore volume / cm$^3$/g | 0.165 |
| Surface area /m$^2$/g | 487.0 |
| DeLaunay diameter /Å | 5.16 |

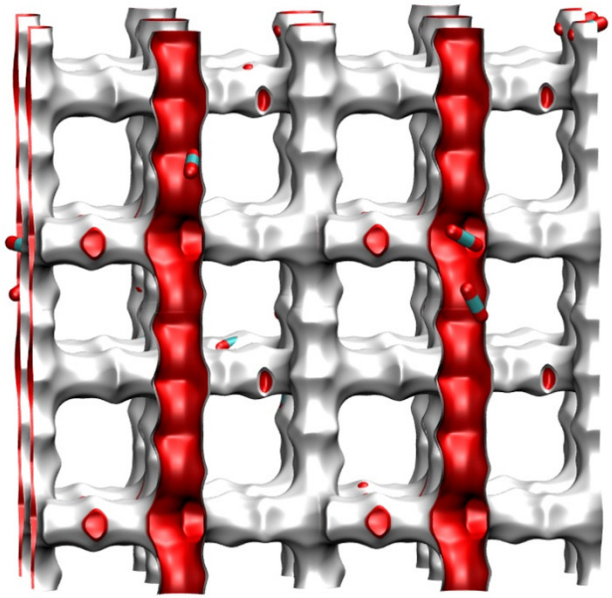

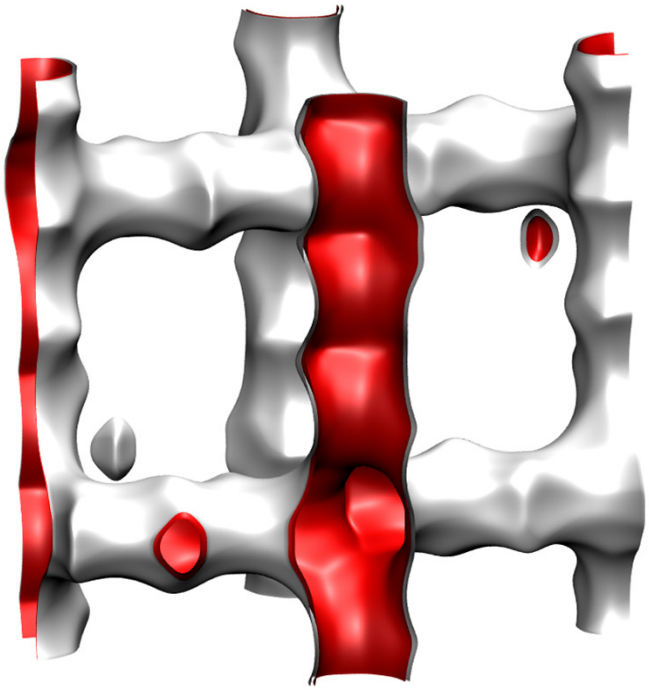

# MFI pore dimensions

Figure S42

10 ring channel of MFI viewed along [100]

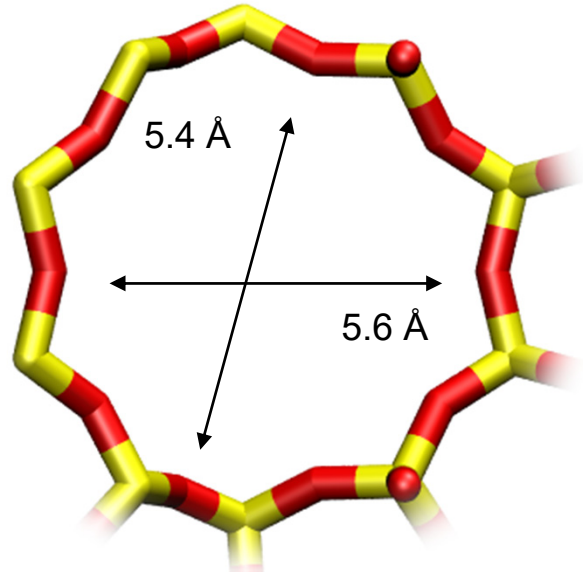


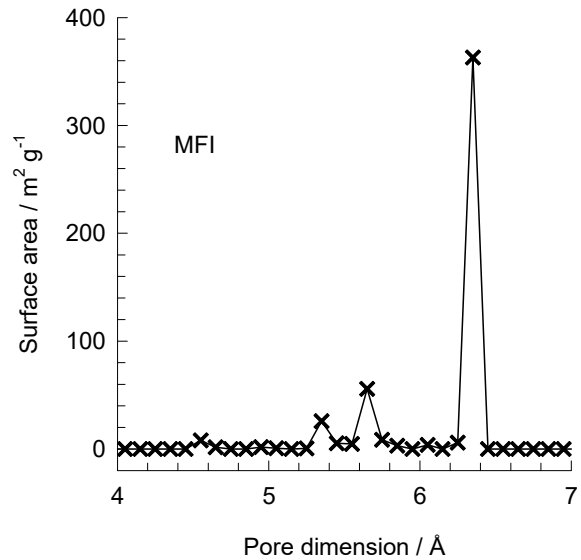


10 ring channel of MFI viewed along [010]

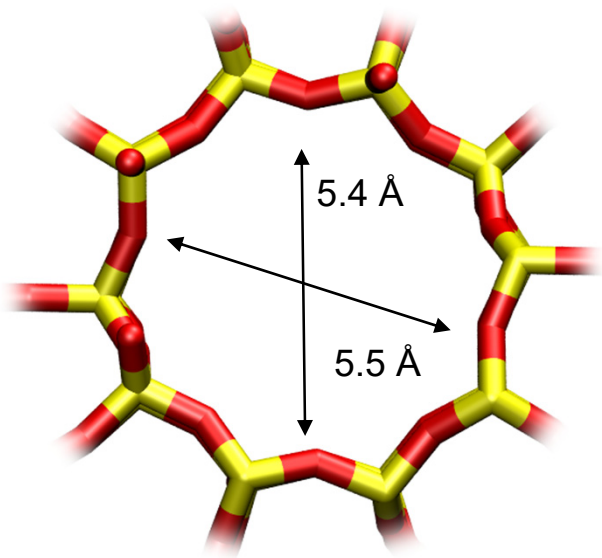


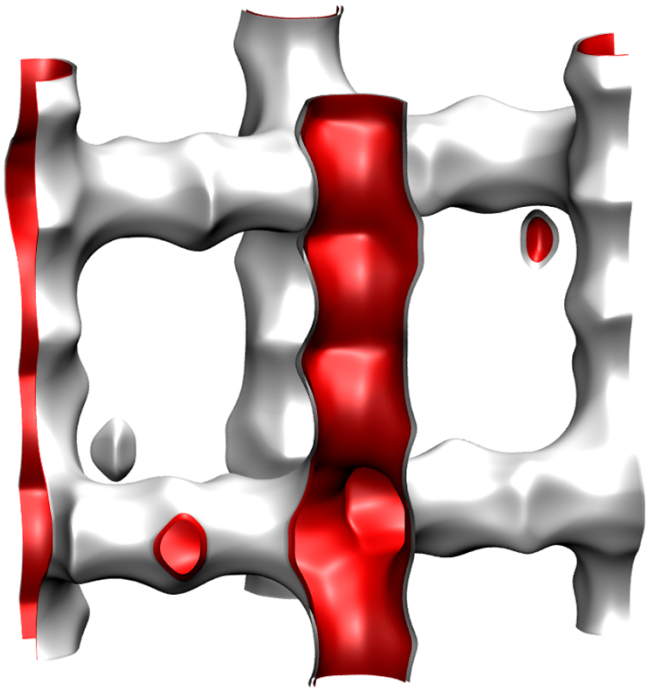

# ISV

Figure S43

ISV [1 0 0]

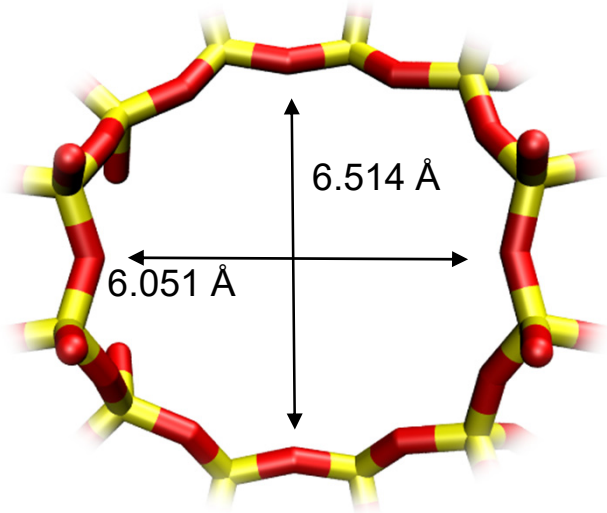


ISV [0 0 1]

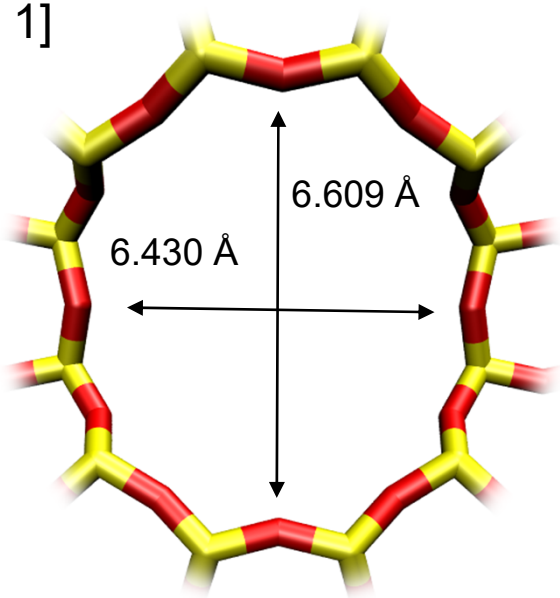


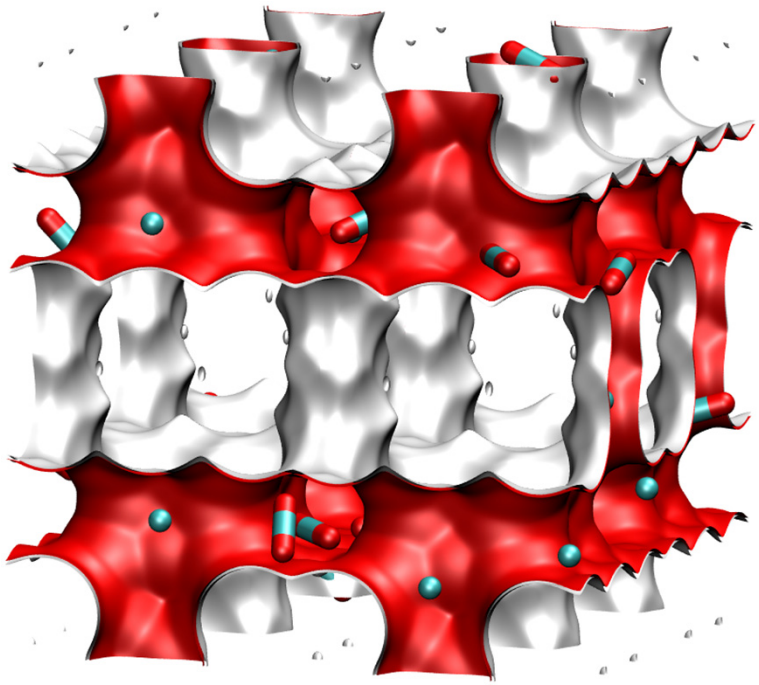

| | ISV |
|---|---|
| *a* /Å | 12.853 |
| *b* /Å | 12.853 |
| *c* /Å | 25.214 |
| Cell volume / Å$^3$ | 4165.343 |
| conversion factor for [molec/uc] to [mol per kg Framework] | 0.2600 |
| conversion factor for [molec/uc] to [kmol/m$^3$] | 0.9361 |
| $\rho$ [kg/m3] | 1533.027 |
| MW unit cell [g/mol(framework)] | 3845.427 |
| $\phi$, fractional pore volume | 0.426 |
| open space / Å$^3$/uc | 1773.9 |
| Pore volume / cm$^3$/g | 0.278 |
| Surface area /m$^2$/g | 911.0 |
| DeLaunay diameter /Å | 5.96 |

# BEA pore landscape

Figure S44

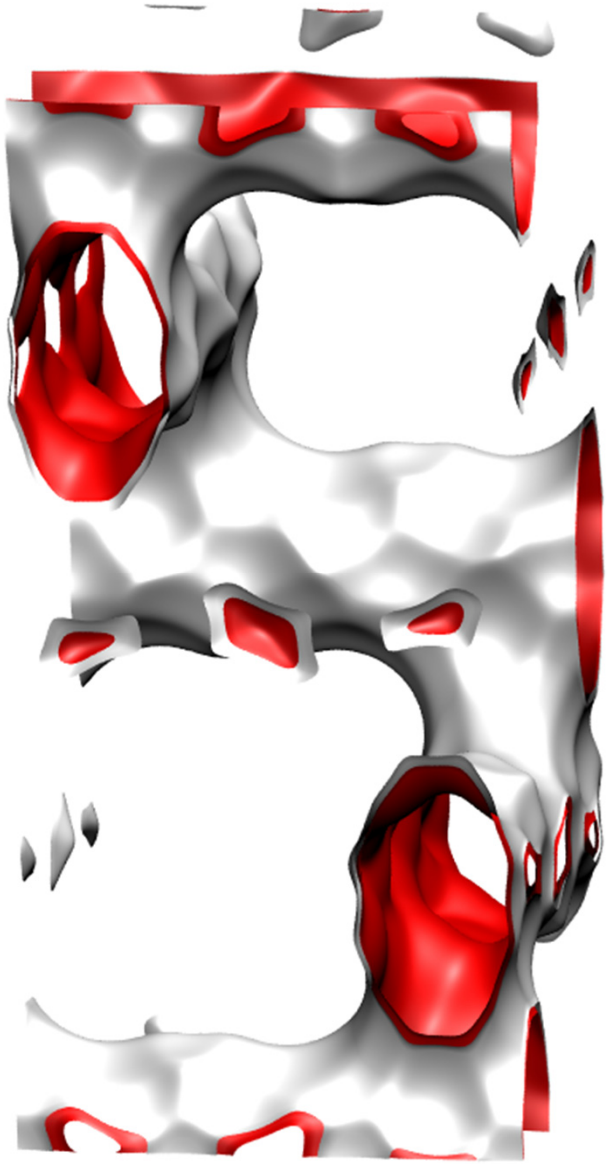

| | BEA |
|---|---|
| *a* /Å | 12.661 |
| *b* /Å | 12.661 |
| *c* /Å | 26.406 |
| Cell volume / Å$^3$ | 4232.906 |
| conversion factor for [molec/uc] to [mol per kg Framework] | 0.2600 |
| conversion factor for [molec/uc] to [kmol/m$^3$] | 0.9609 |
| $\rho$ [kg/m3] | 1508.558 |
| MW unit cell [g/mol(framework)] | 3845.427 |
| $\phi$, fractional pore volume | 0.408 |
| open space / Å$^3$/uc | 1728.1 |
| Pore volume / cm$^3$/g | 0.271 |
| Surface area /m$^2$/g | 923.0 |
| DeLaunay diameter /Å | 5.87 |

# BEA pore dimensions

This plot of surface area versus pore dimension is determined using a combination of the DeLaunay triangulation method for pore dimension determination, and the procedure of Düren for determination of the surface area.

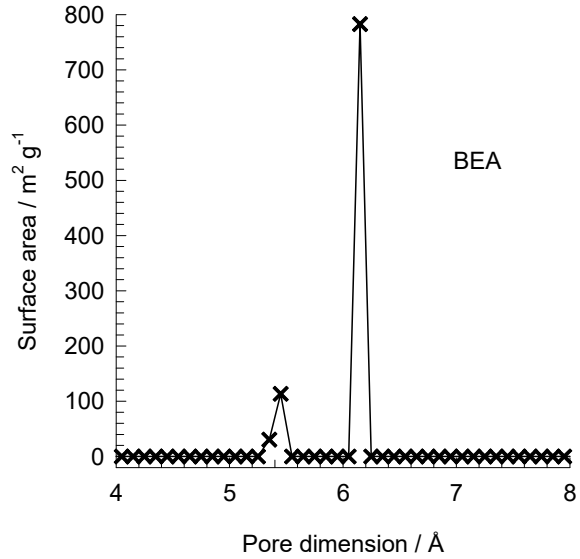


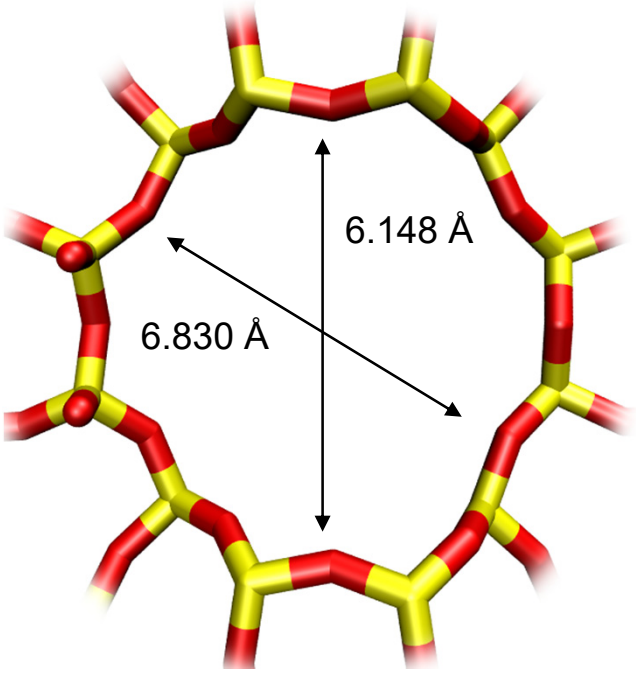


BEA [1 0 0]

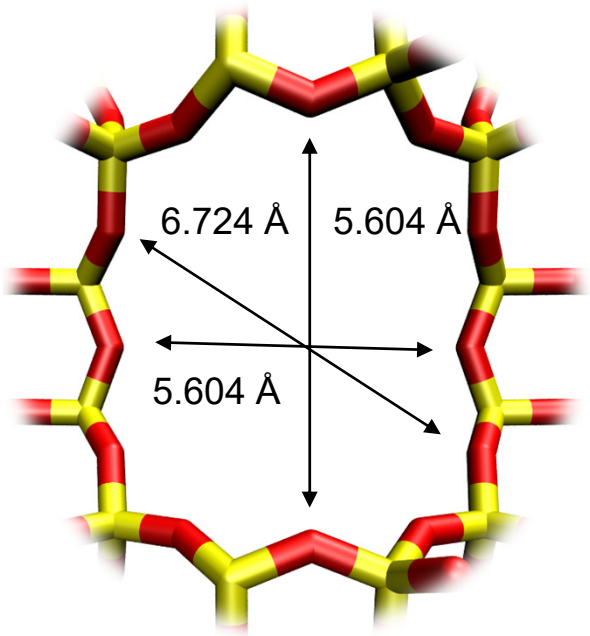


BEA [0 0 1]

# BOG pore landscape

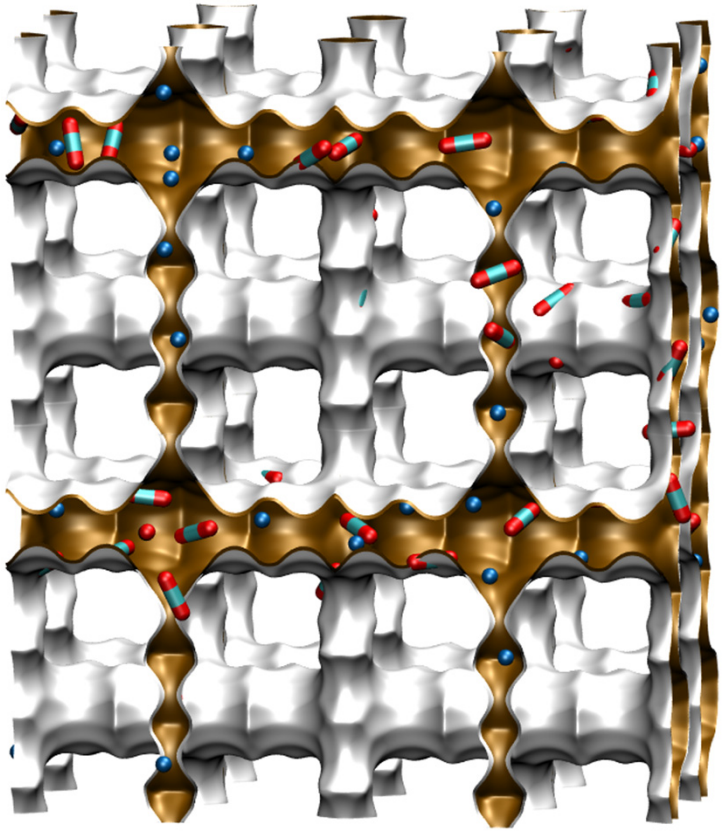

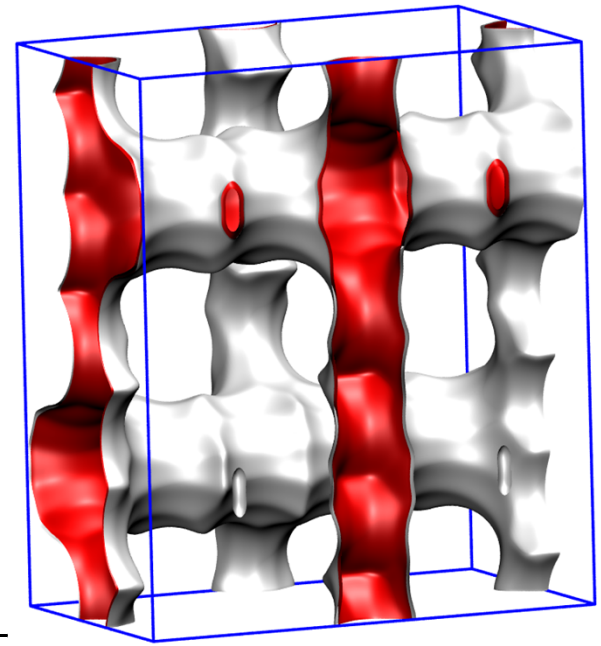

| | BOG |
|---|---|
| *a* /Å | 20.236 |
| *b* /Å | 23.798 |
| *c* /Å | 12.798 |
| Cell volume / Å$^3$ | 6163.214 |
| conversion factor for [molec/uc] to [mol per kg Framework] | 0.1734 |
| conversion factor for [molec/uc] to [kmol/m$^3$] | 0.7203 |
| $\rho$ [kg/m3] | 1995.523 |
| MW unit cell [g/mol(framework)] | 5768.141 |
| $\phi$, fractional pore volume | 0.374 |
| open space / Å$^3$/uc | 2305.4 |
| Pore volume / cm$^3$/g | 0.241 |
| Surface area /m$^2$/g | 758.0 |
| DeLaunay diameter /Å | 5.02 |

# BOG pore dimensions

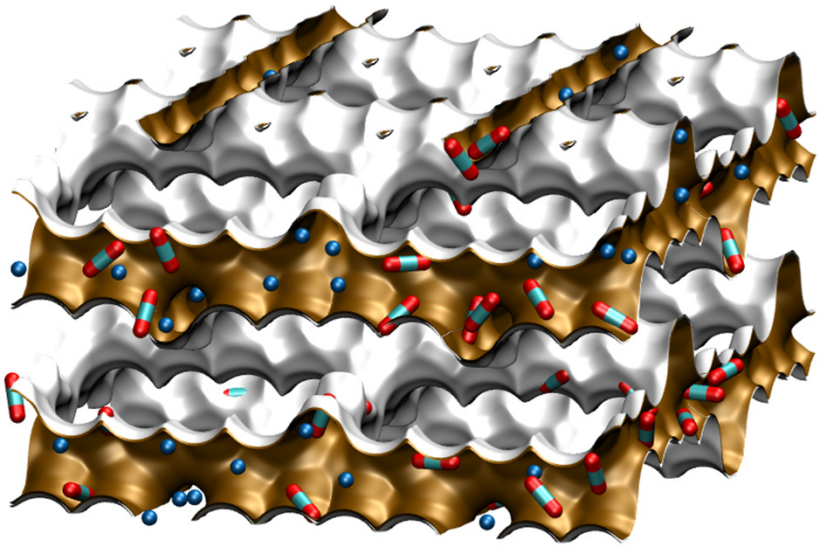

BOG has an intersecting channel system:
12-ring channels intersecting with 10-ring channels

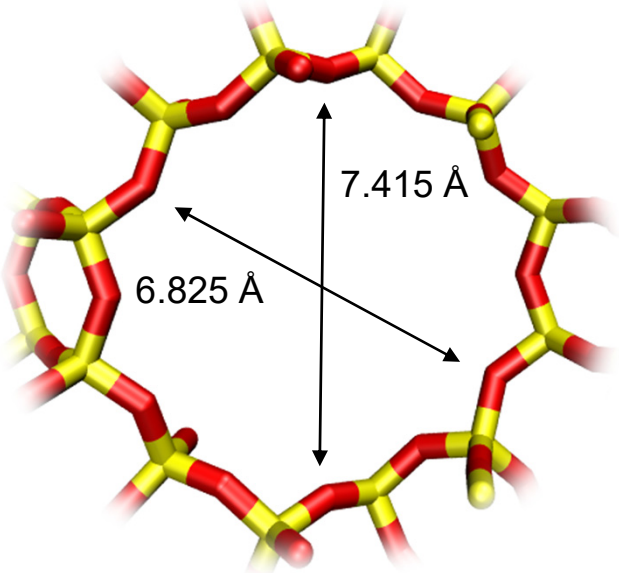


BOG [1 0 0]

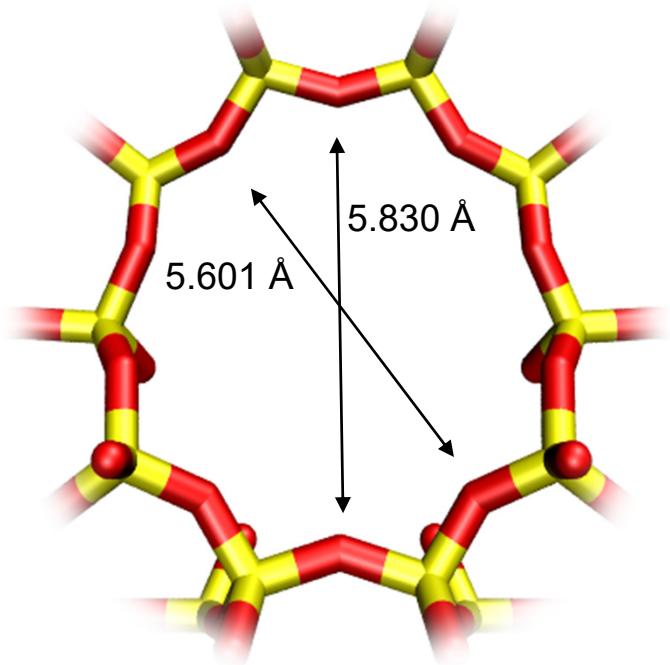


BOG [0 1 0]

# GME

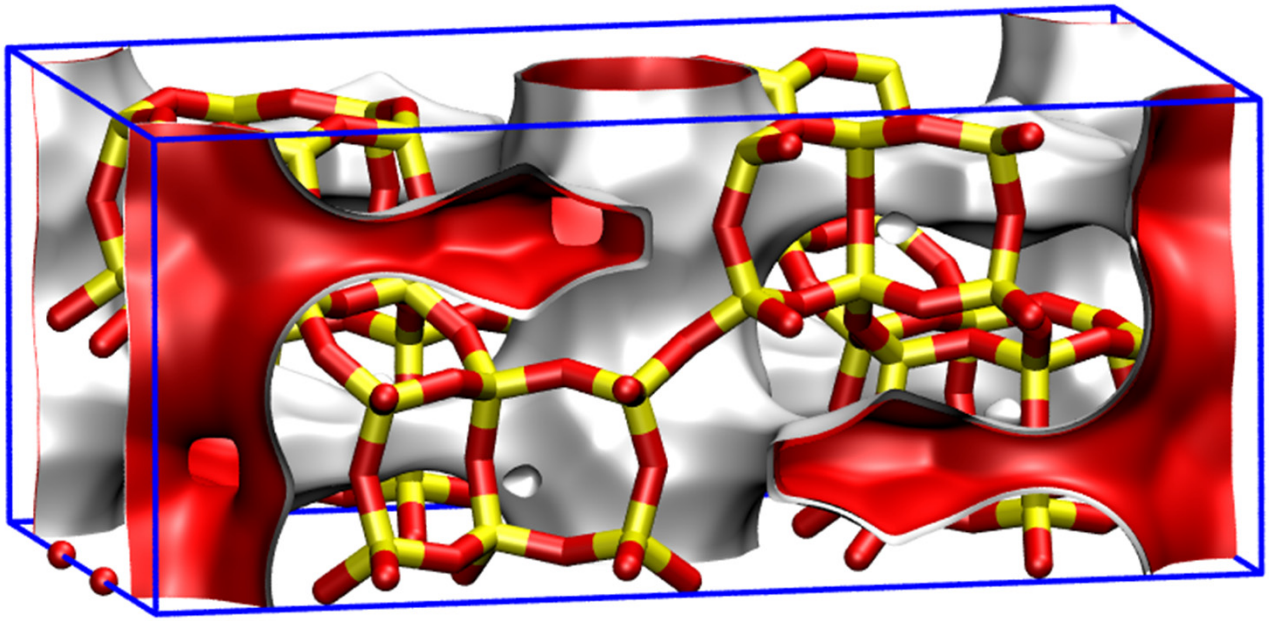

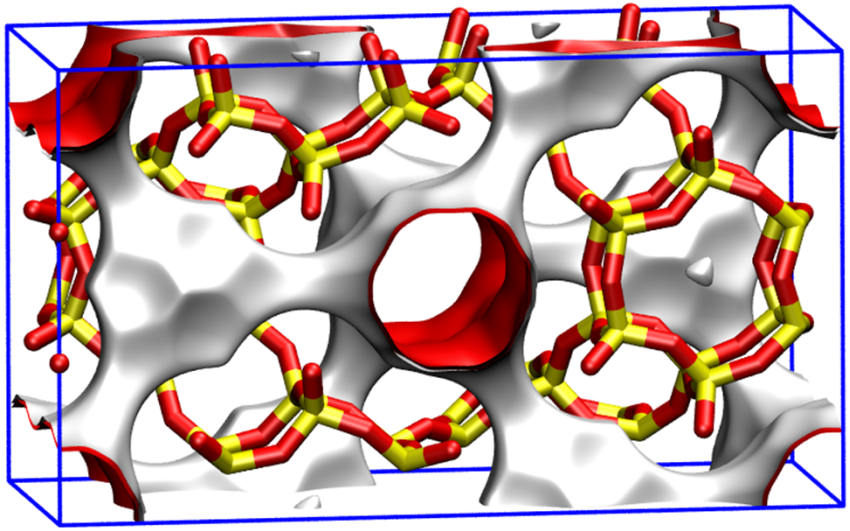

| | GME |
|---|---|
| *a* /Å | 23.826 |
| *b* /Å | 13.756 |
| *c* /Å | 10.064 |
| Cell volume / Å$^3$ | 3298.481 |
| conversion factor for [molec/uc] to [mol per kg Framework] | 0.3467 |
| conversion factor for [molec/uc] to [kmol/m$^3$] | 1.3090 |
| $\rho$ [kg/m3] | 1451.938 |
| MW unit cell [g/mol(framework)] | 2884.07 |
| $\phi$, fractional pore volume | 0.385 |
| open space / Å$^3$/uc | 1268.6 |
| Pore volume / cm$^3$/g | 0.265 |
| Surface area /m$^2$/g | 717.0 |
| DeLaunay diameter /Å | 7.09 |

# Zn(bdc)dabco

## landscapes

Figure S49

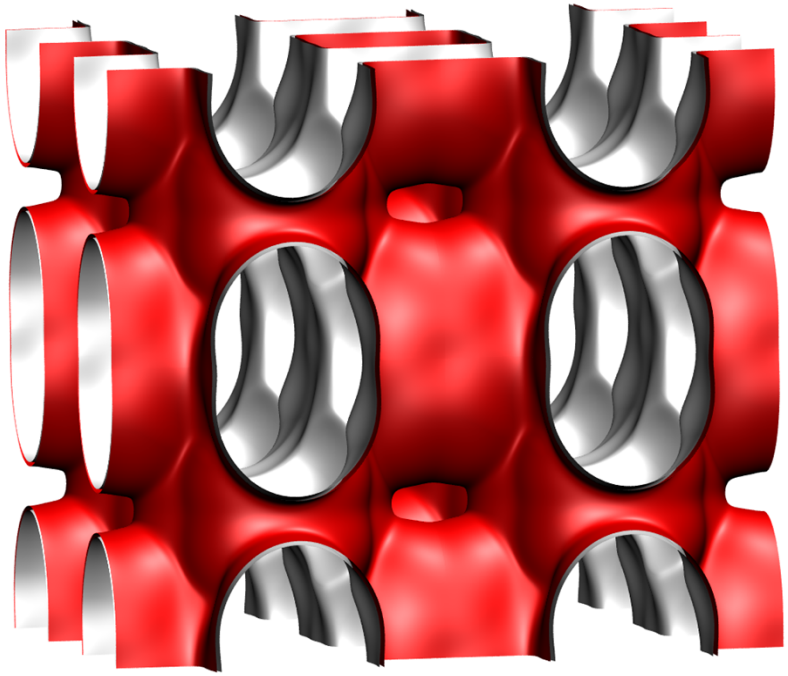

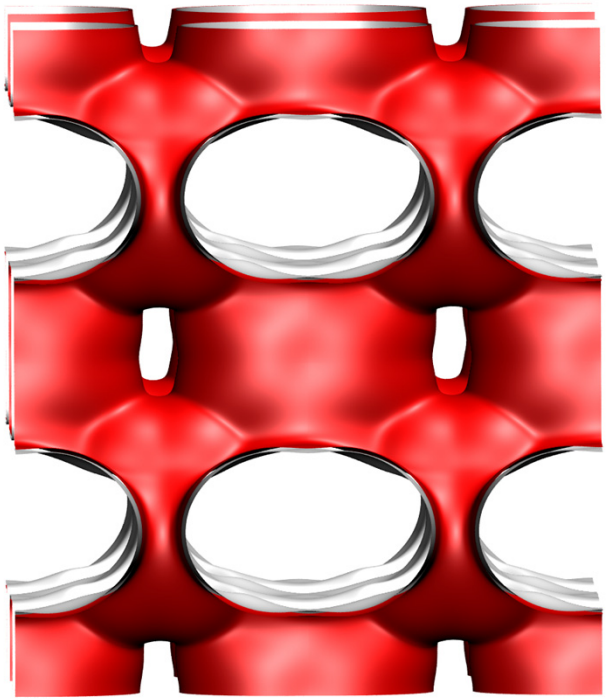

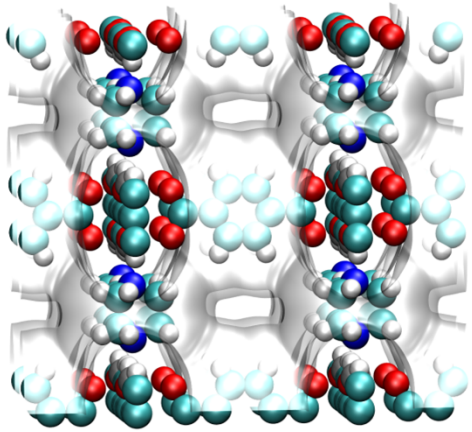

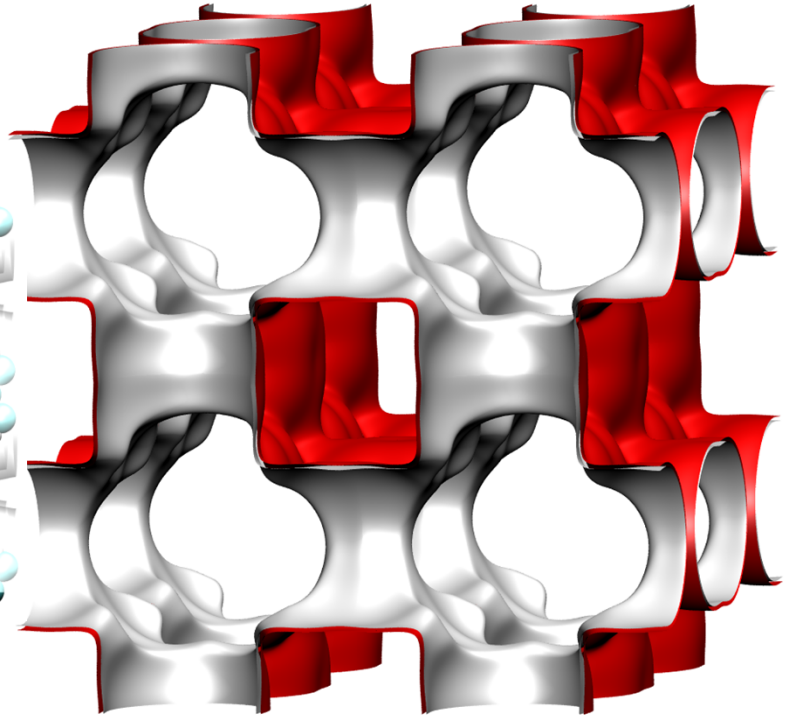

# Zn(bdc)dabco

## landscapes

*3D intersecting channels*

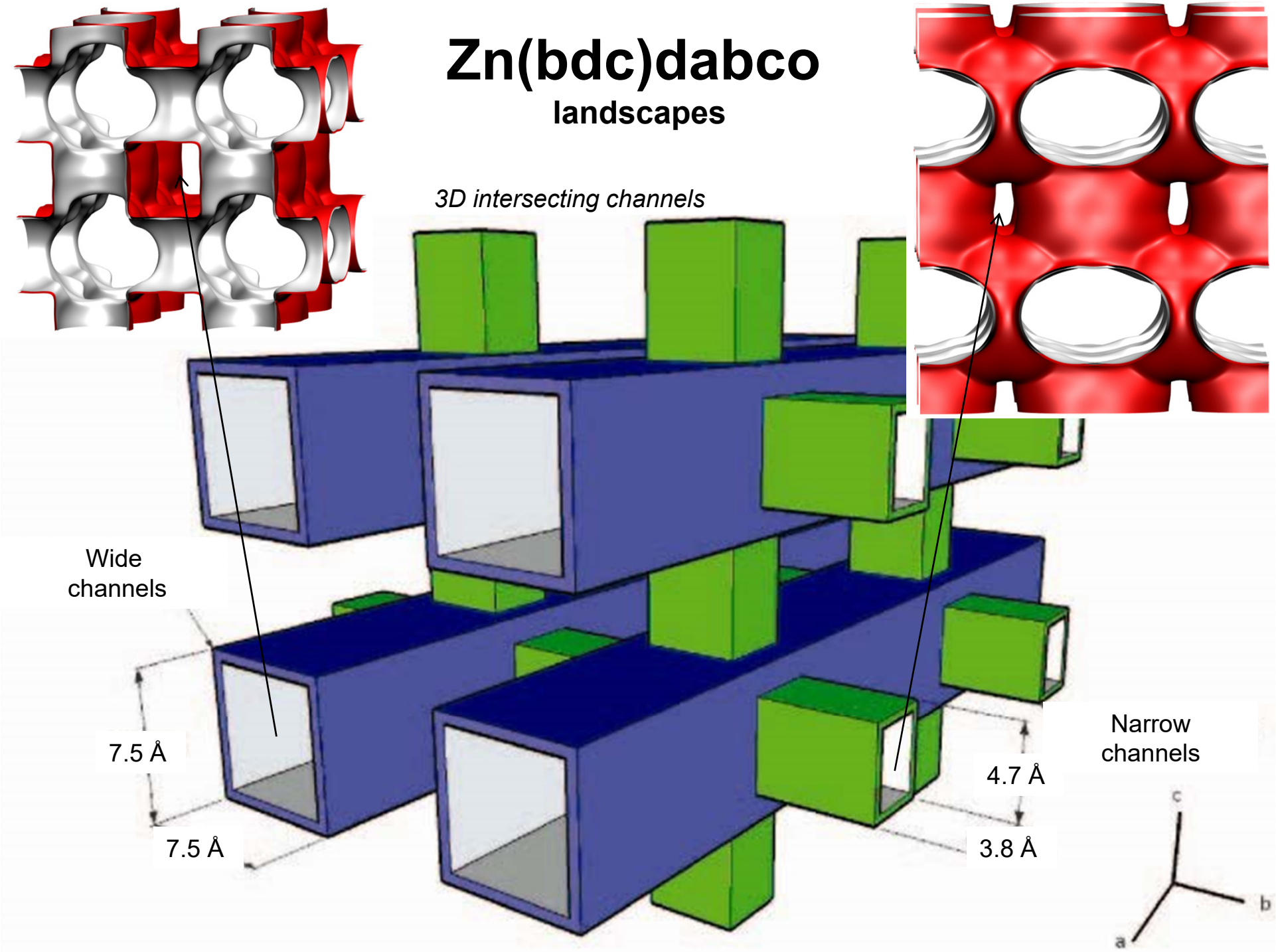

# Zn(bdc)dabco pore dimensions

Figure S51

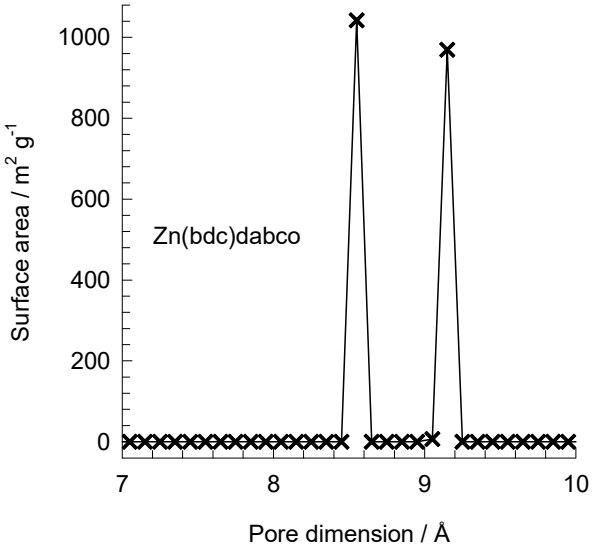


This plot of surface area versus pore dimension is determined using a combination of the DeLaunay triangulation method for pore dimension determination, and the procedure of Düren for determination of the surface area.

| | Zn(bdc)dabco |
|---|---|
| *a* /Å | 10.9288 |
| *b* /Å | 10.9288 |
| *c* /Å | 9.6084 |
| Cell volume / Å$^3$ | 1147.615 |
| conversion factor for [molec/uc] to [mol per kg Framework] | 1.7514 |
| conversion factor for [molec/uc] to [kmol/m$^3$] | 2.1867 |
| $\rho$ [kg/m3] | 826.1996 |
| MW unit cell [g/mol(framework)] | 570.9854 |
| $\phi$, fractional pore volume | 0.662 |
| open space / Å$^3$/uc | 759.4 |
| Pore volume / cm$^3$/g | 0.801 |
| Surface area /m$^2$/g | 2022.5 |
| DeLaunay diameter /Å | 8.32 |

# SIFSIX

Figure S52

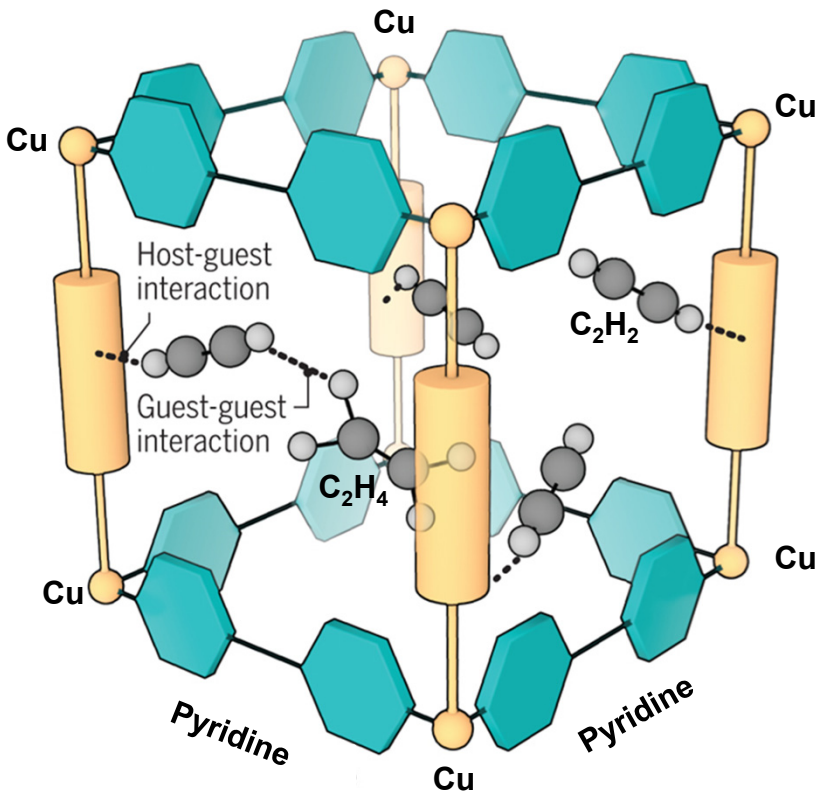


SIFSIX-1-Cu

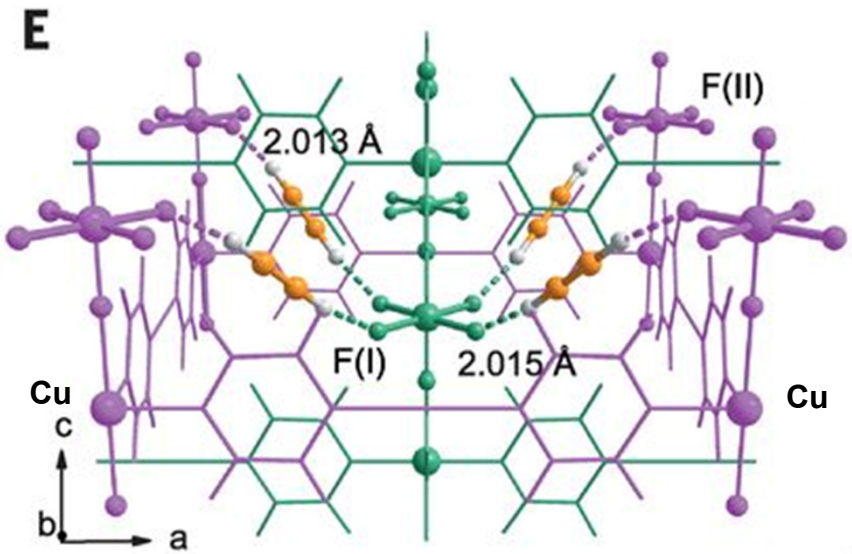


SIFSIX-2-Cu-i

**The detailed structural information is provided in**
**Cui, X.; Chen, K.; Xing, H.; Yang, Q.; Krishna, R.; Bao, Z.; Wu, H.; Zhou, W.; Dong, X.; Han, Y.; Li, B.; Ren, Q.; Zaworotko, M. J.; Chen, B. Pore Chemistry and Size Control in Hybrid Porous Materials for Acetylene Capture from Ethylene. Science 2016, 353, 141-144.**

# FAU (all-silica)

Figure S53

The volume of one FAU cage is 786 Å$^3$, larger in size than that of LTA (743 Å$^3$) and DDR (278 Å$^3$).

12-ring window of FAU

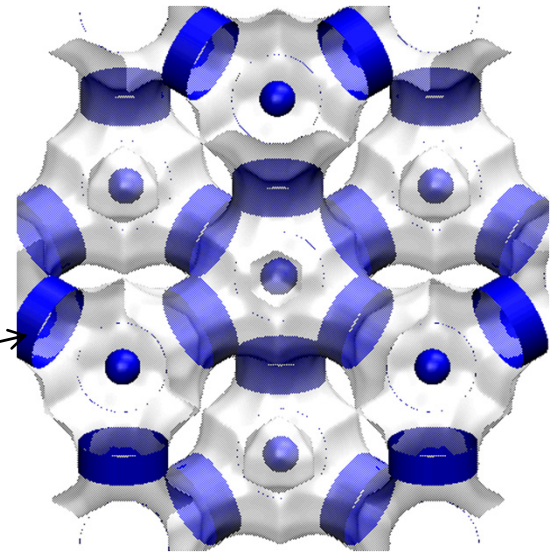

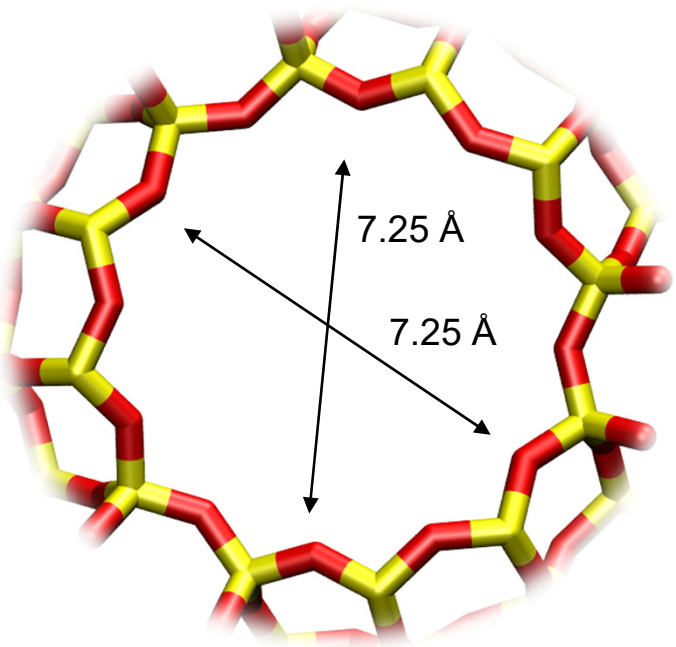


| | FAU-Si |
|---|---|
| *a* /Å | 24.28 |
| *b* /Å | 24.28 |
| *c* /Å | 24.28 |
| Cell volume / Å$^3$ | 14313.51 |
| conversion factor for [molec/uc] to [mol per kg Framework] | 0.0867 |
| conversion factor for [molec/uc] to [kmol/m$^3$] | 0.2642 |
| $\rho$ [kg/m3] | 1338.369 |
| MW unit cell [g/mol (framework)] | 11536.28 |
| $\phi$, fractional pore volume | 0.439 |
| open space / Å$^3$/uc | 6285.6 |
| Pore volume / cm$^3$/g | 0.328 |
| Surface area /m$^2$/g | 1086.0 |
| DeLaunay diameter /Å | 7.37 |

# NaY (138 Si, 54 Al, 54 Na+, Si/Al=2.55)

Figure S54

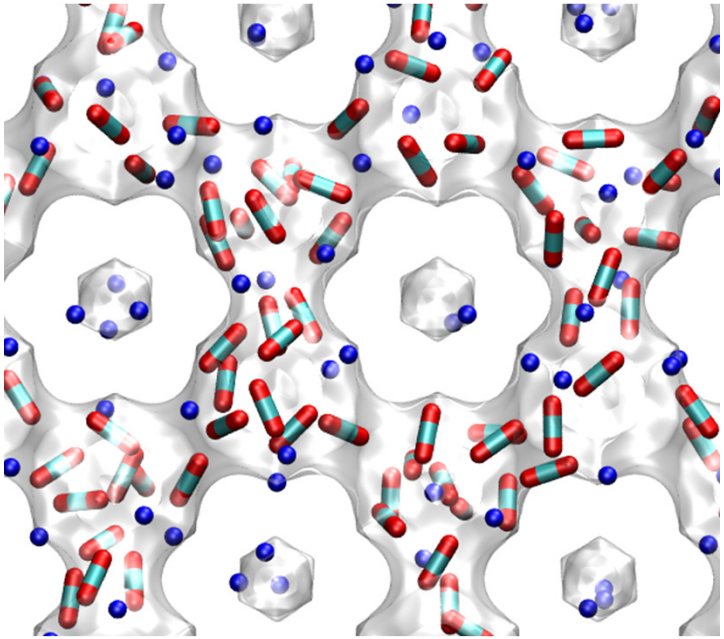

Blue spheres are cations

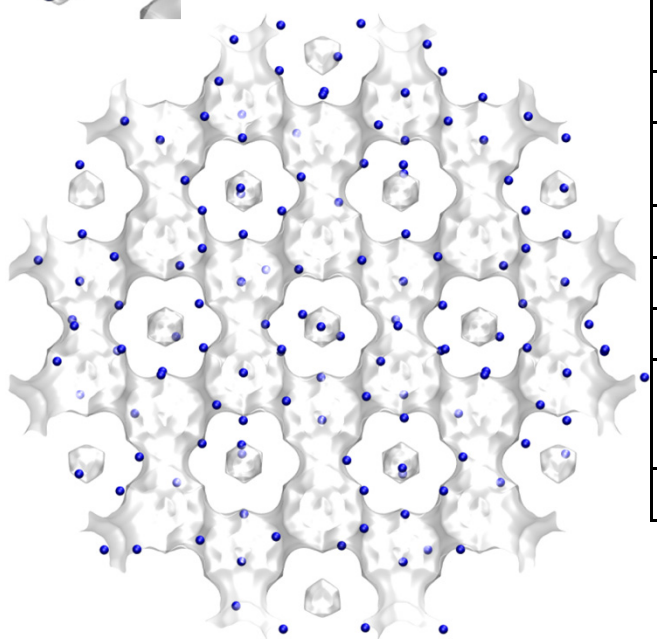

| | FAU-54Al |
|---|---|
| *a* /Å | 25.028 |
| *b* /Å | 25.028 |
| *c* /Å | 25.028 |
| Cell volume / Å$^3$ | 15677.56 |
| conversion factor for [molec/uc] to [mol per kg Framework] | 0.0786 |
| conversion factor for [molec/uc] to [kmol/m$^3$] | 0.2596 |
| $\rho$ [kg/m3] (with cations) | 1347.1 |
| MW unit cell [g/mol(framework+cations)] | 12718.08 |
| $\phi$, fractional pore volume | 0.408 |
| open space / Å$^3$/uc | 6396.6 |
| Pore volume / cm$^3$/g | 0.303 |
| Surface area /m$^2$/g | |
| DeLaunay diameter /Å | 7.37 |

# NaX (106 Si, 86 Al, 86 Na+, Si/Al=1.23)

Figure S55

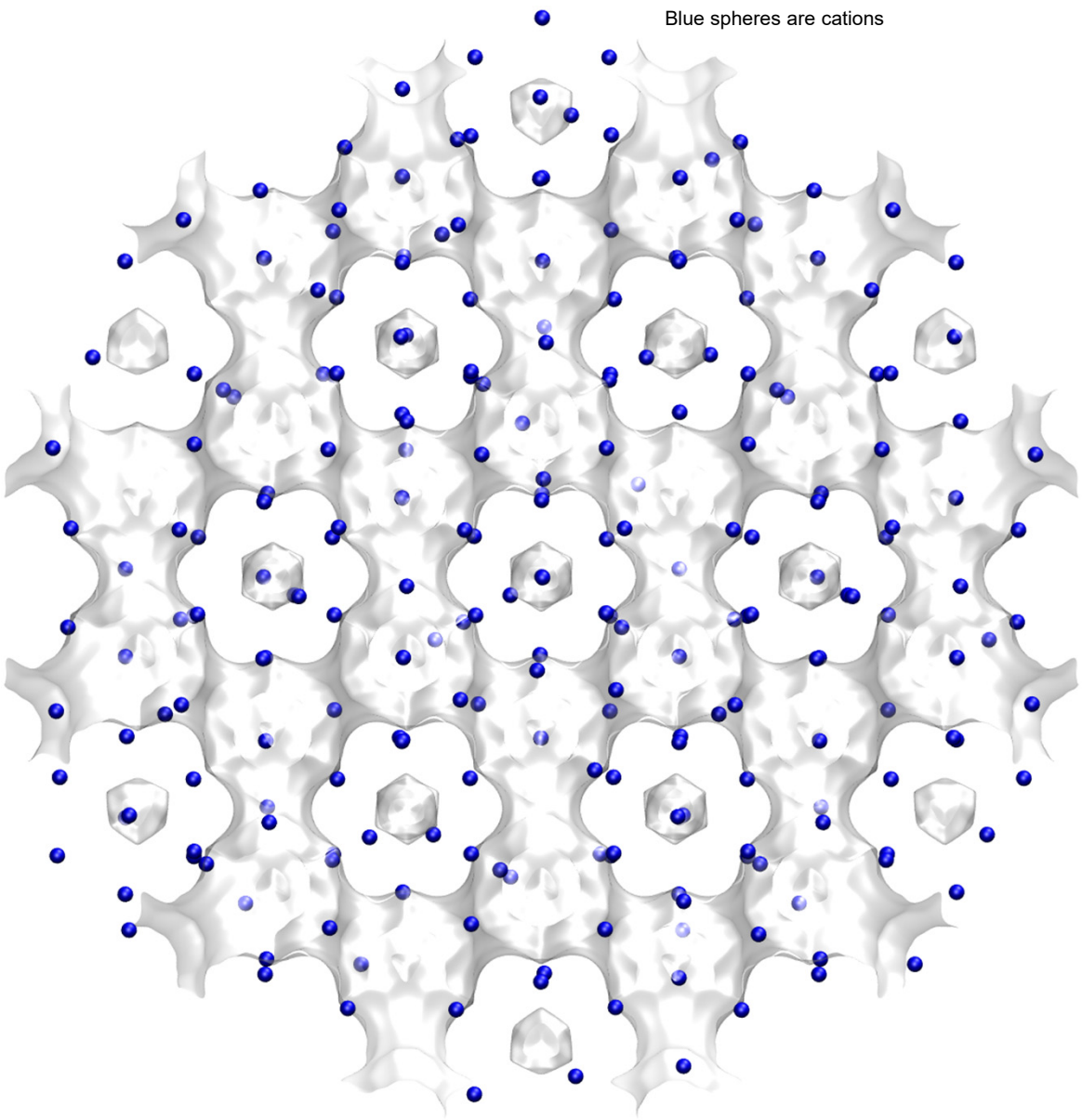


| | FAU-86Al |
|---|---|
| *a* /Å | 25.028 |
| *b* /Å | 25.028 |
| *c* /Å | 25.028 |
| Cell volume / Å$^3$ | 15677.56 |
| conversion factor for [molec/uc] to [mol per kg Framework] | 0.0745 |
| conversion factor for [molec/uc] to [kmol/m$^3$] | 0.2658 |
| $\rho$ [kg/m3] (with cations) | 1421.277 |
| MW unit cell [g/mol(framework+cations)] | 13418.42 |
| $\phi$, fractional pore volume | 0.399 |
| open space / Å$^3$/uc | 6248.0 |
| Pore volume / cm$^3$/g | 0.280 |
| Surface area /m$^2$/g | |
| DeLaunay diameter /Å | 7.37 |

# IRMOF-1 pore landscape

Figure S56

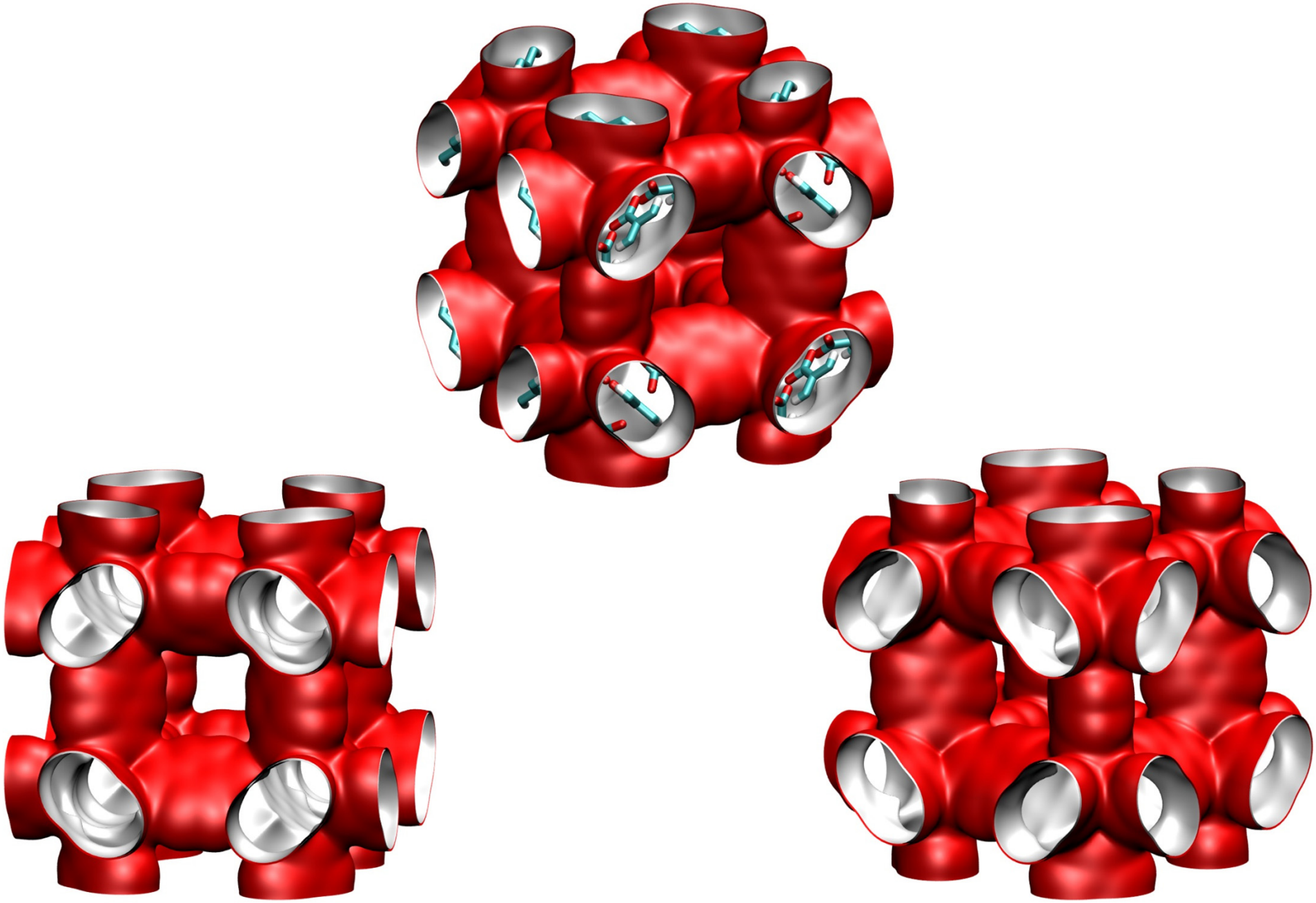

# IRMOF-1 pore dimensions

Figure S57

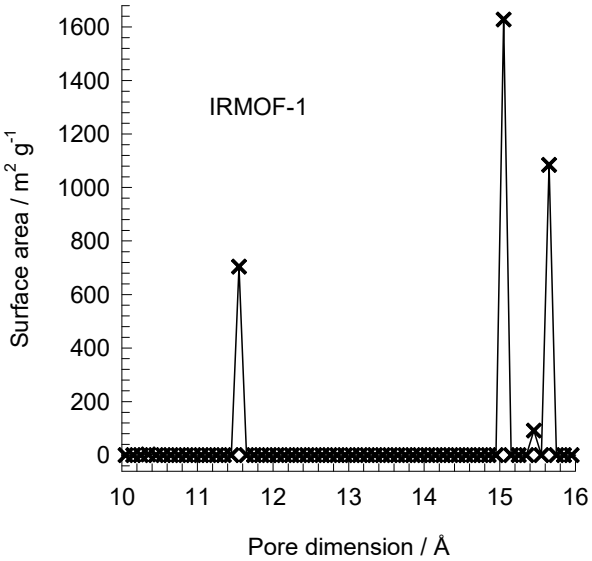


This plot of surface area versus pore dimension is determined using a combination of the DeLaunay triangulation method for pore dimension determination, and the procedure of Düren for determination of the surface area.

| | IRMOF-1 |
|---|---|
| *a* /Å | 25.832 |
| *b* /Å | 25.832 |
| *c* /Å | 25.832 |
| Cell volume / Å$^3$ | 17237.49 |
| conversion factor for [molec/uc] to [mol per kg Framework] | 0.1624 |
| conversion factor for [molec/uc] to [kmol/m$^3$] | 0.1186 |
| $\rho$ [kg/m3] | 593.2075 |
| MW unit cell [g/mol(framework)] | 6157.788 |
| $\phi$, fractional pore volume | 0.812 |
| open space / Å$^3$/uc | 13996.3 |
| Pore volume / cm$^3$/g | 1.369 |
| Surface area /m$^2$/g | 3522.2 |
| DeLaunay diameter /Å | 7.38 |

Figure S58

# CuBTC pore landscapes

The structural information for CuBTC (= $Cu_3(BTC)_2$ with BTC = 1,3,5-benzenetricarboxylate) have been taken from

S.S.Y. Chui, S.M.F. Lo, J.P.H. Charmant, A.G. Orpen, I.D. Williams, A chemically functionalizable nanoporous material $[Cu_3(TMA)_2(H2O)_3]_n$, Science 283 (1999) 1148-1150.
*The crystal structure of Chui et al. includes axial oxygen atoms weakly bonded to the Cu atoms, which correspond to water ligands. Our simulations have been performed on the dry CuBTC with these oxygen atoms removed.*

Q. Yang, C. Zhong, Electrostatic-Field-Induced Enhancement of Gas Mixture Separation in Metal-Organic Frameworks: A Computational Study, ChemPhysChem 7 (2006) 1417-1421.

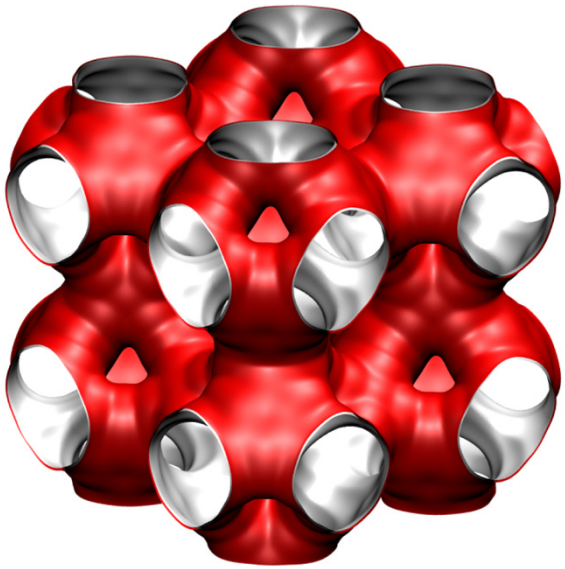

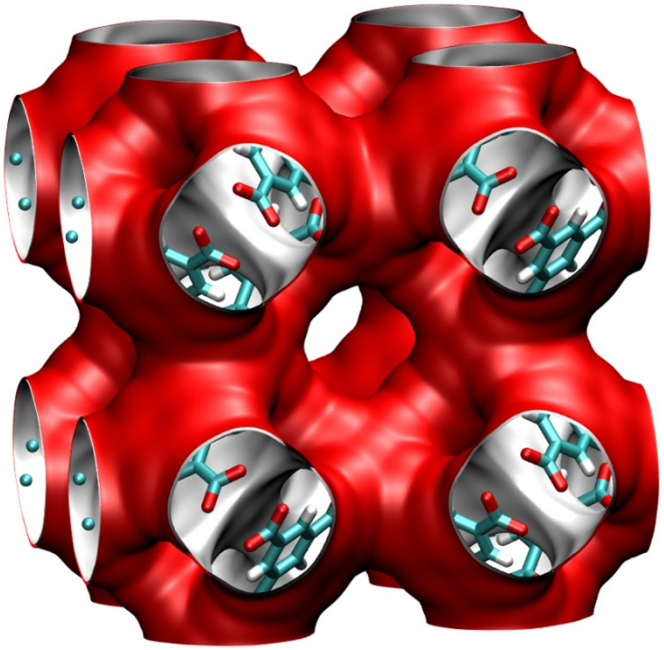

Snapshot of $CO_2/CH_4$ mixture

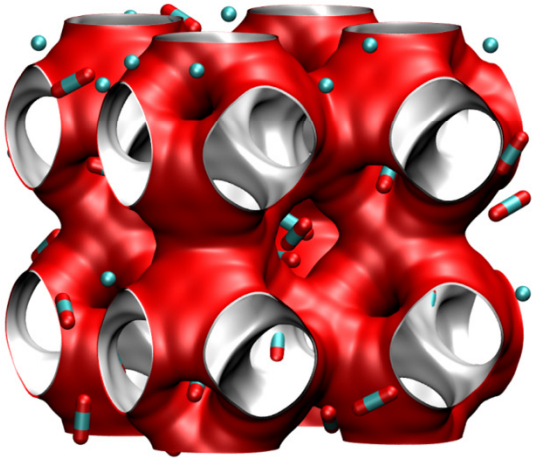

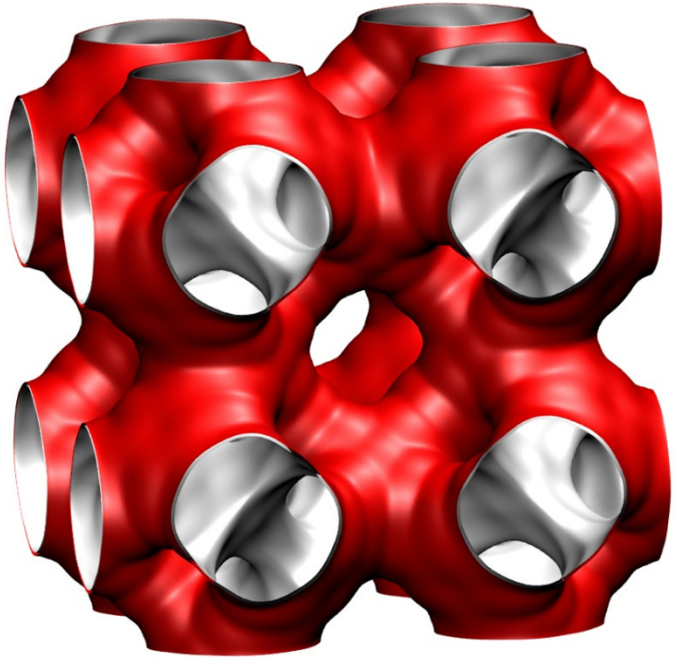

# CuBTC pore dimensions

Figure S59

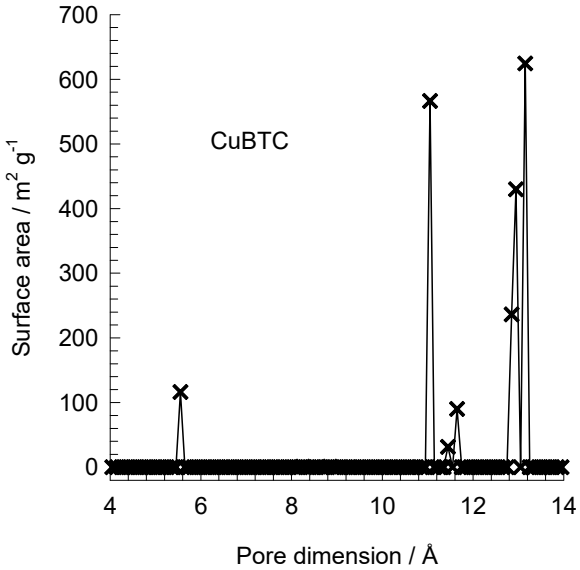


This plot of surface area versus pore dimension is determined using a combination of the DeLaunay triangulation method for pore dimension determination, and the procedure of Düren for determination of the surface area.

| | CuBTC |
|---|---|
| *a* /Å | 26.343 |
| *b* /Å | 26.343 |
| *c* /Å | 26.343 |
| Cell volume / Å$^3$ | 18280.82 |
| conversion factor for [molec/uc] to [mol per kg Framework] | 0.1034 |
| conversion factor for [molec/uc] to [kmol/m$^3$] | 0.1218 |
| $\rho$ [kg/m3] | 878.8298 |
| MW unit cell [g/mol(framework)] | 9674.855 |
| $\phi$, fractional pore volume | 0.746 |
| open space / Å$^3$/uc | 13628.4 |
| Pore volume / cm$^3$/g | 0.848 |
| Surface area /m$^2$/g | 2097.0 |
| DeLaunay diameter /Å | 6.23 |

The CuBTC structure consists of two types of “cages” and two types of “windows” separating these cages. Large cages are inter-connected by 9 Å windows of square cross-section. The large cages are also connected to tetrahedral-shaped pockets of ca. 6 Å size through triangular-shaped windows of ca. 4.6 Å size

Figure S60

# CuBTC framework

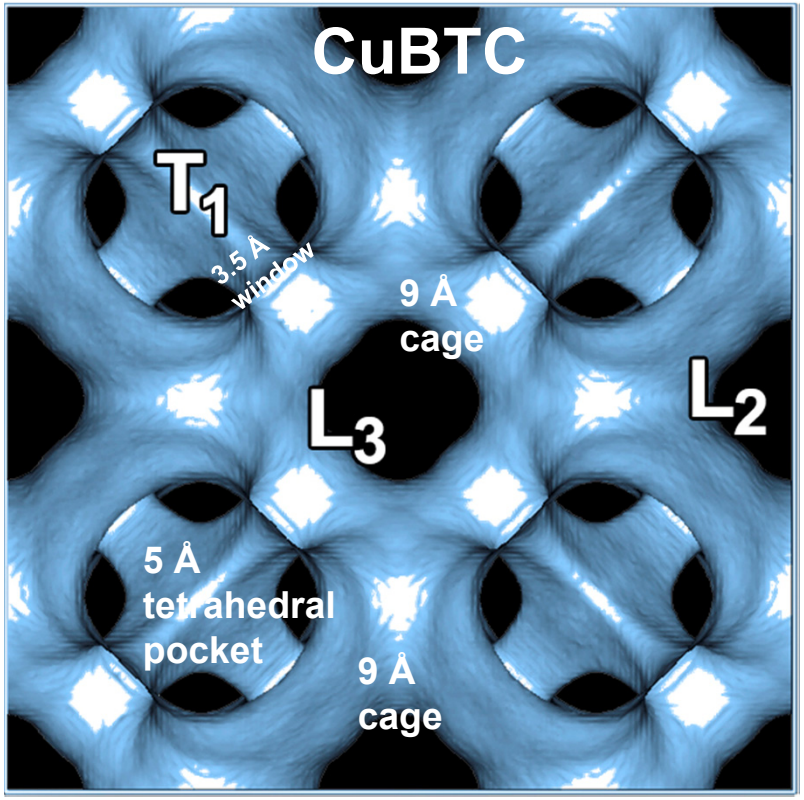


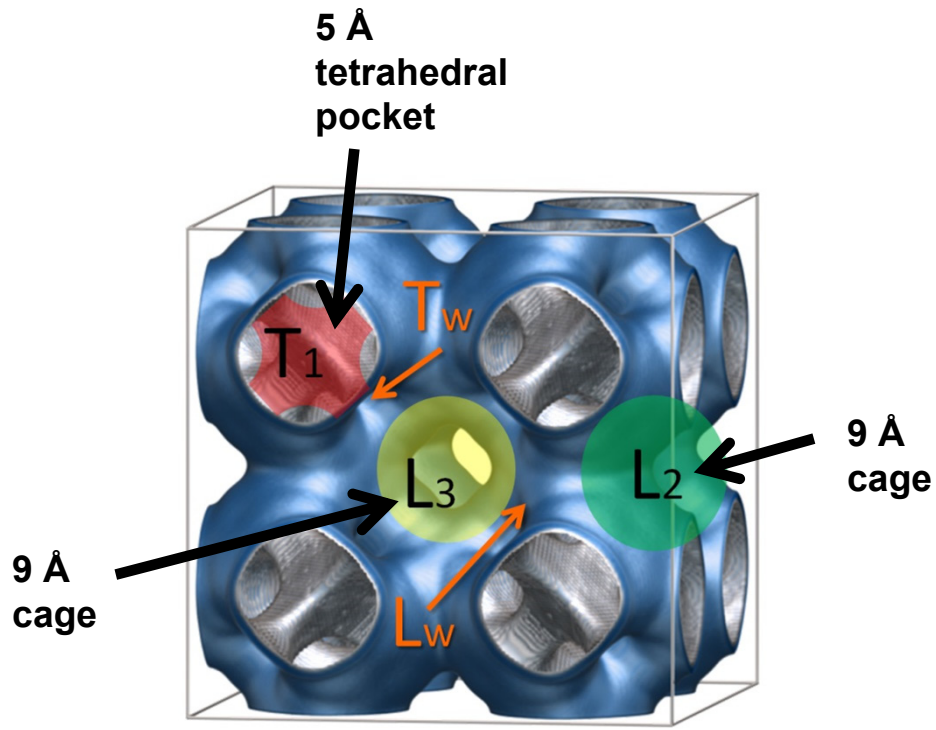

# MOF-177 pore landscape

Figure S61

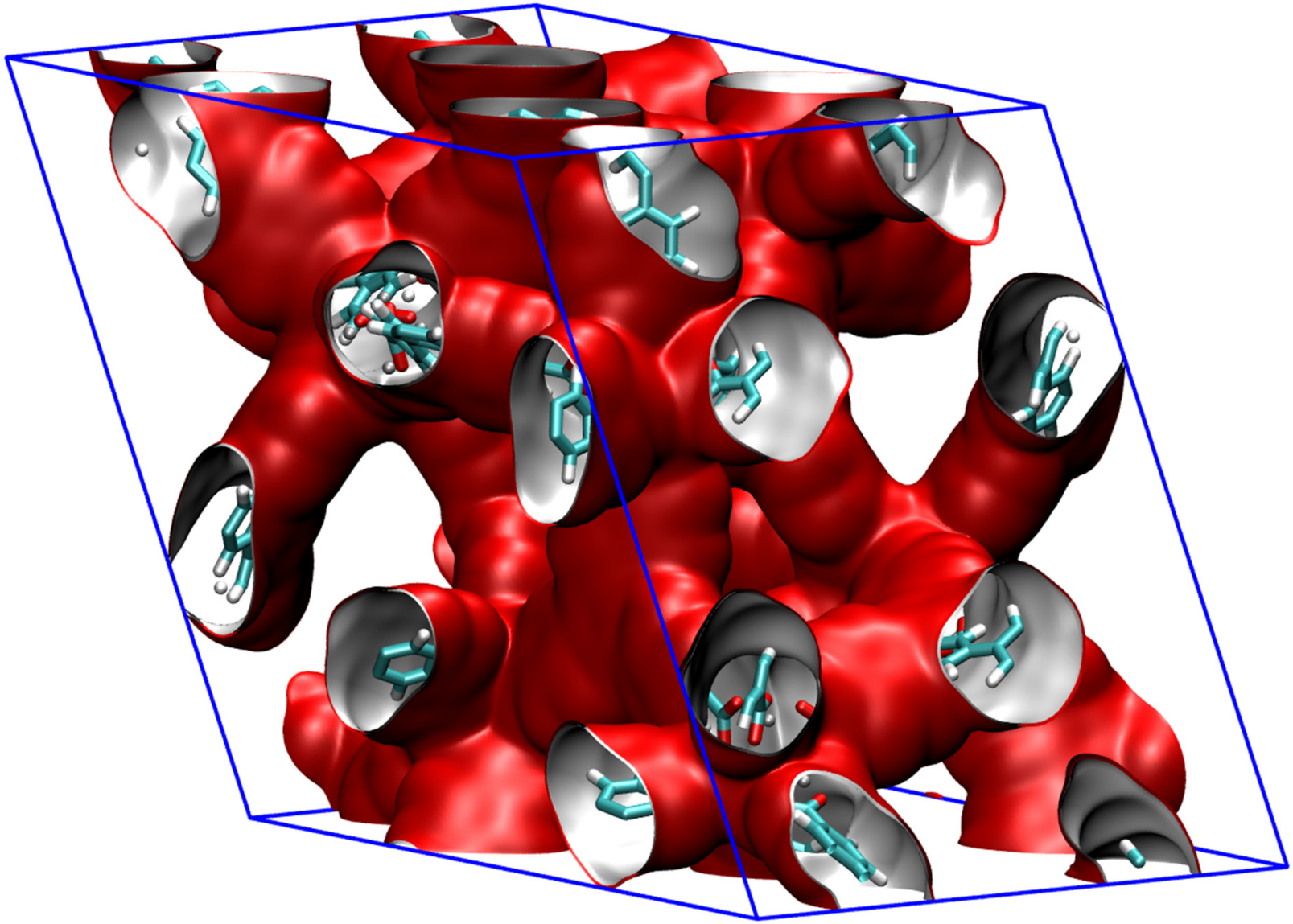

# MOF-177 pore dimensions

Figure S62

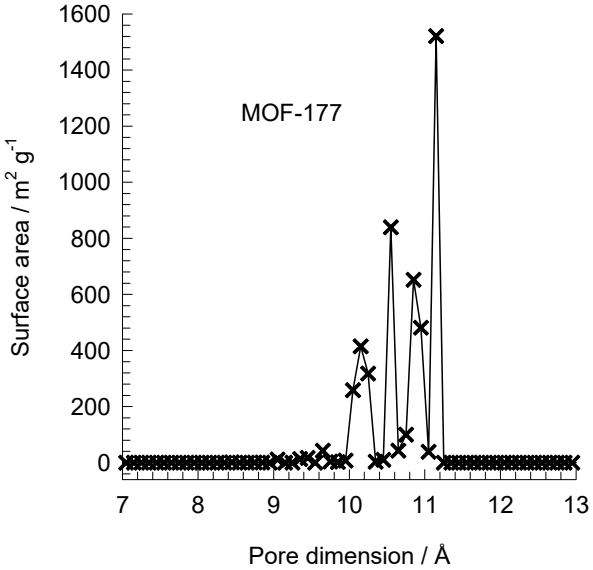


This plot of surface area versus pore dimension is determined using a combination of the DeLaunay triangulation method for pore dimension determination, and the procedure of Düren for determination of the surface area.

| | MOF-177 |
|---|---|
| *a* /Å | 37.072 |
| *b* /Å | 37.072 |
| *c* /Å | 30.033 |
| Cell volume / Å$^3$ | 35745.5 |
| conversion factor for [molec/uc] to [mol per kg Framework] | 0.1089 |
| conversion factor for [molec/uc] to [kmol/m$^3$] | 0.0553 |
| $\rho$ [kg/m3] | 426.5952 |
| MW unit cell [g/mol(framework)] | 9182.931 |
| $\phi$, fractional pore volume | 0.840 |
| open space / Å$^3$/uc | 30010.9 |
| Pore volume / cm$^3$/g | 1.968 |
| Surface area /m$^2$/g | 4781.0 |
| DeLaunay diameter /Å | 10.1 |

# MOF-177 snapshots of nC6/3MP/22DMB hexane isomers

Figure S63

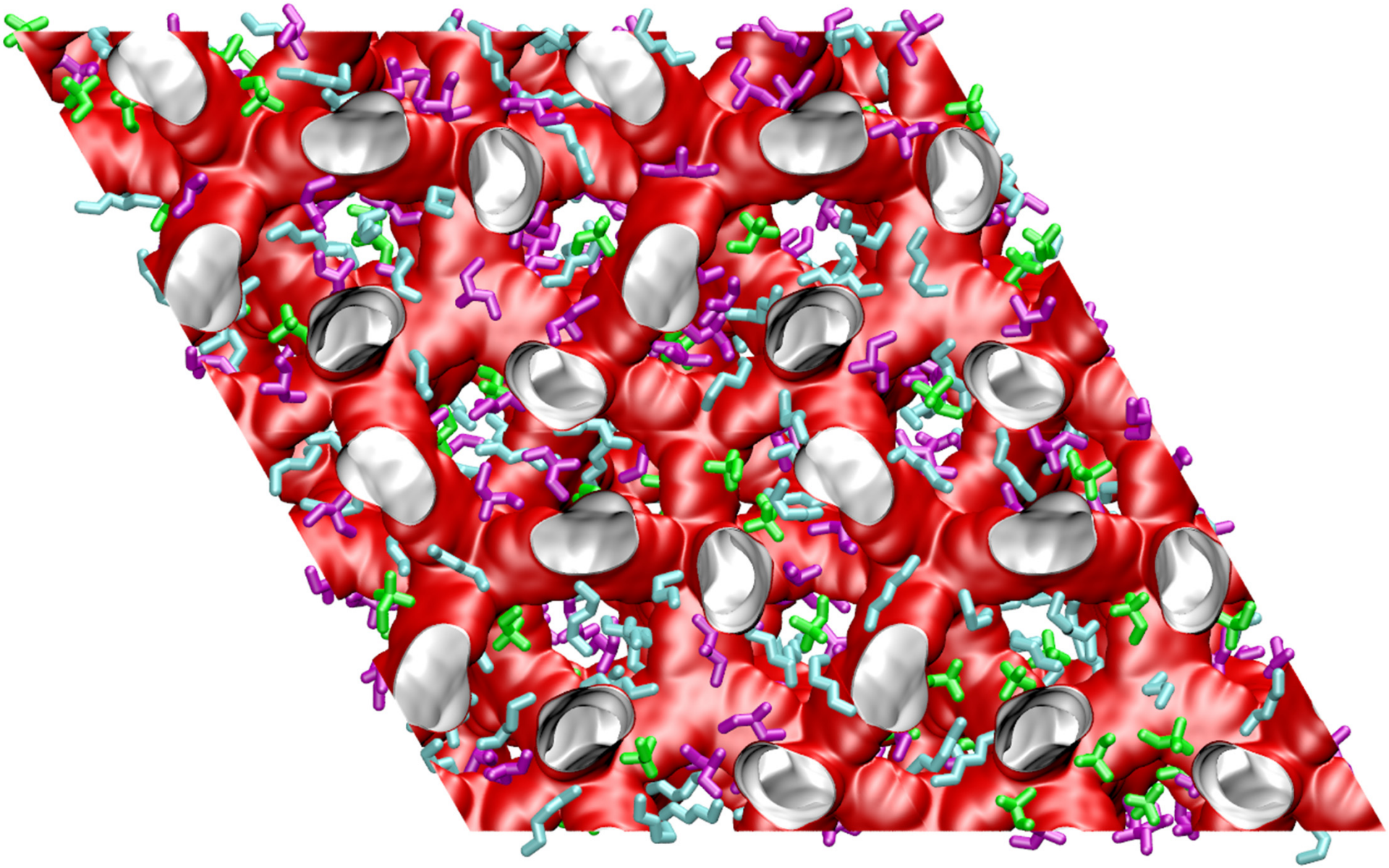

Figure S64

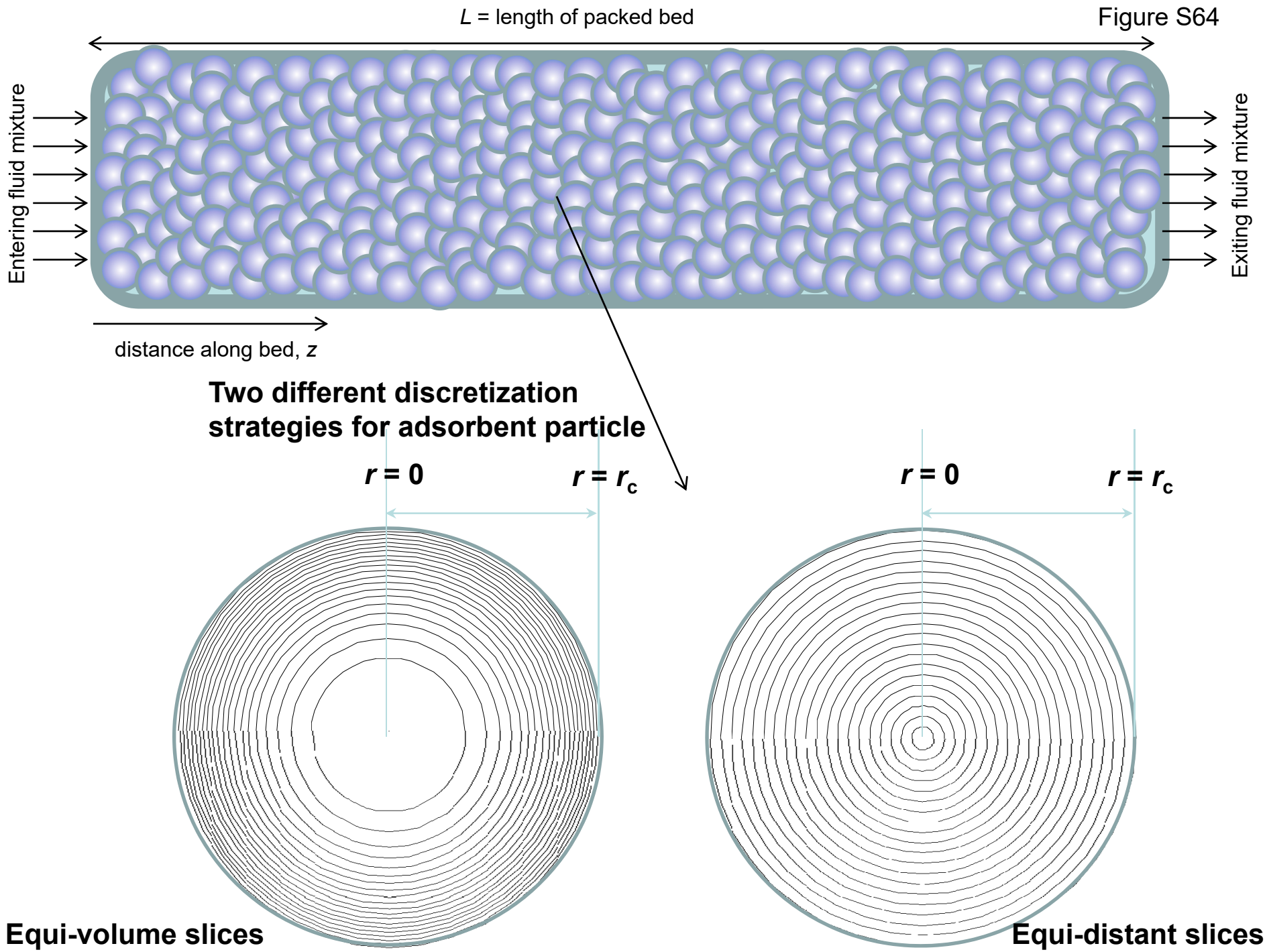
L = length of packed bed
Entering fluid mixture
Exiting fluid mixture
distance along bed, z
Two different discretization strategies for adsorbent particle
r = 0
r = rc
r = 0
r = rc
Equi-volume slices
Equi-distant slices

# Fixed bed breakthrough model

Figure S65

Component balance

$$\frac{1}{RT}\frac{\partial p_i}{\partial t} = -\frac{1}{RT}\frac{\partial (v p_i)}{\partial z} - \frac{(1-\varepsilon)}{\varepsilon}\rho\frac{\partial \bar{q}_i}{\partial t}; \quad i = 1,2,...n$$

Balance for mixture

$$\frac{1}{RT}p_t\frac{\partial (v(t,z))}{\partial z} = -\frac{(1-\varepsilon)}{\varepsilon}\rho\frac{\partial \bar{q}_t(t,z)}{\partial t}$$

Average loading within crystal

$$\bar{q}_i = \frac{3}{r_c^3}\int_0^{r_c} q_i r^2 dr$$

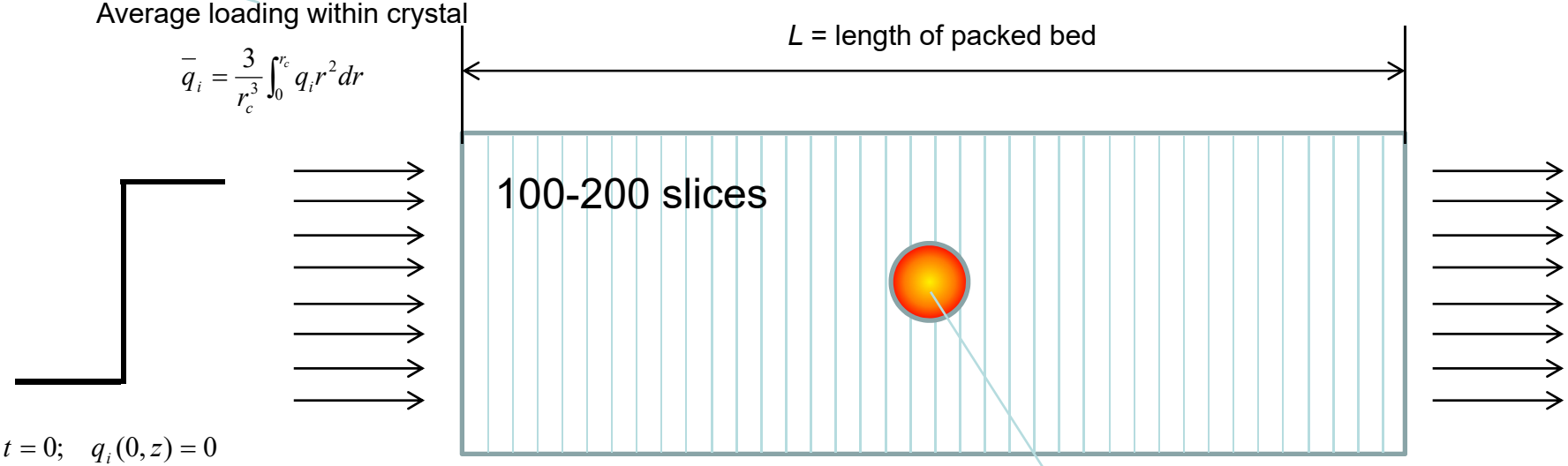


$$t = 0; \quad q_i(0,z) = 0$$

$$t \geq 0; \quad p_i(0,t) = p_{i0}; \quad u(0,t) = u_0$$

Uptake within crystal

$$\frac{\partial q_i}{\partial t} = -\frac{1}{\rho}\frac{1}{r^2}\frac{\partial}{\partial r}\left(r^2 N_i\right)$$

Equi-volume grid within crystal

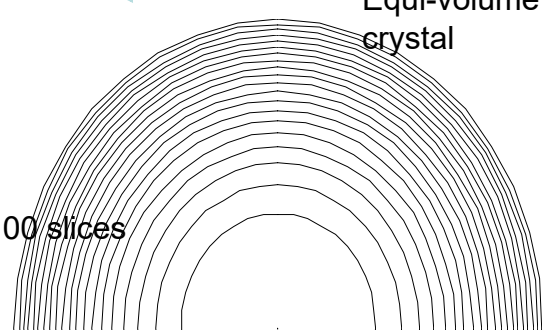


Maxwell-Stefan equations

$$-\rho\frac{q_i}{RT}\nabla\mu_i = \sum_{\substack{j=1 \\ j\neq i}}^{n}\frac{x_j N_i - x_i N_j}{Đ_{ij}} + \frac{N_i}{Đ_i}; \quad i = 1,2,..n$$

Figure S66

# Noble gases

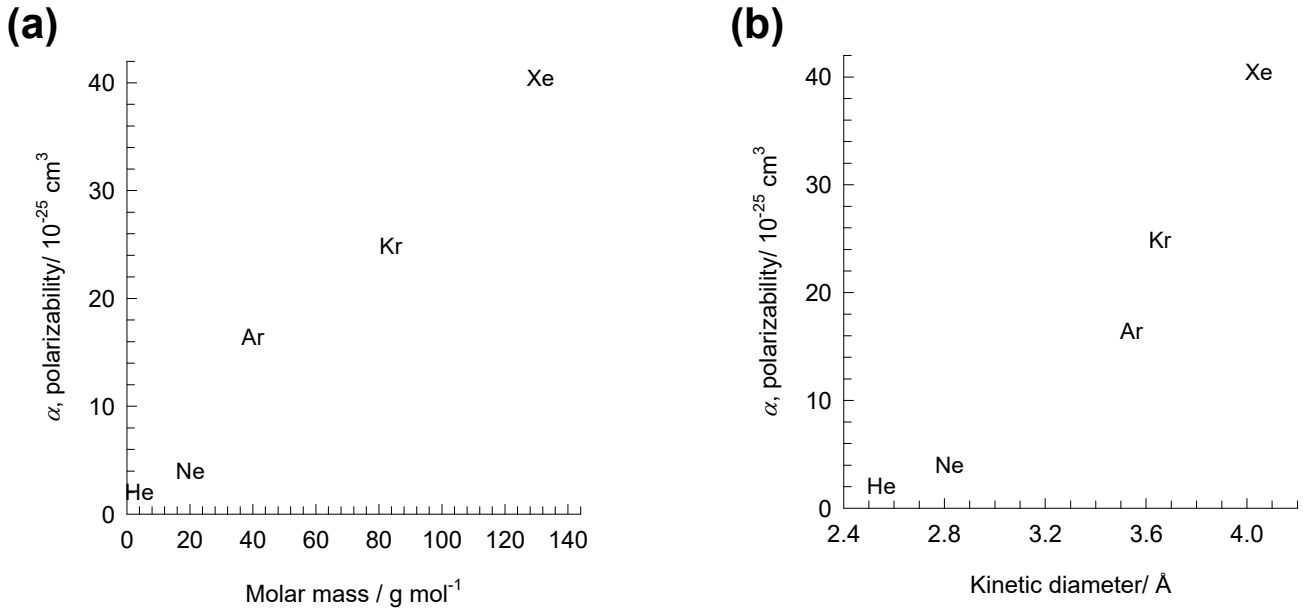


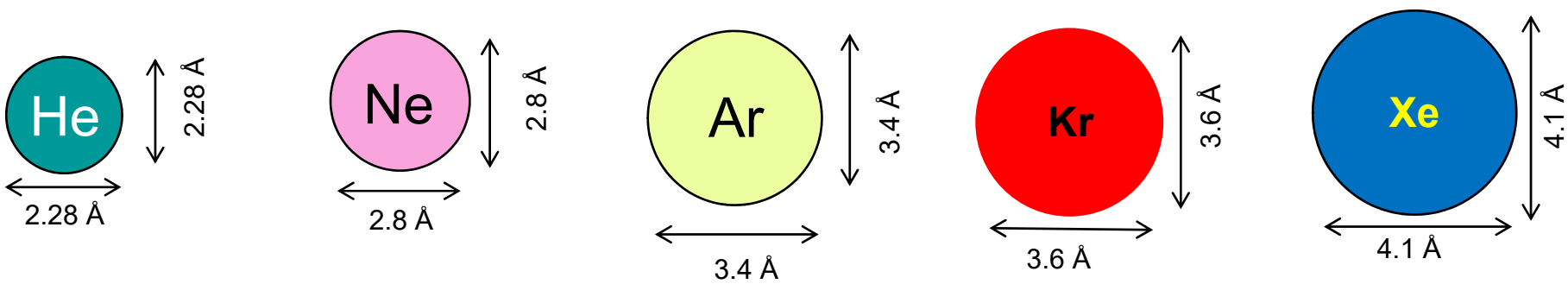

Figure S67

# Xe/Kr separations

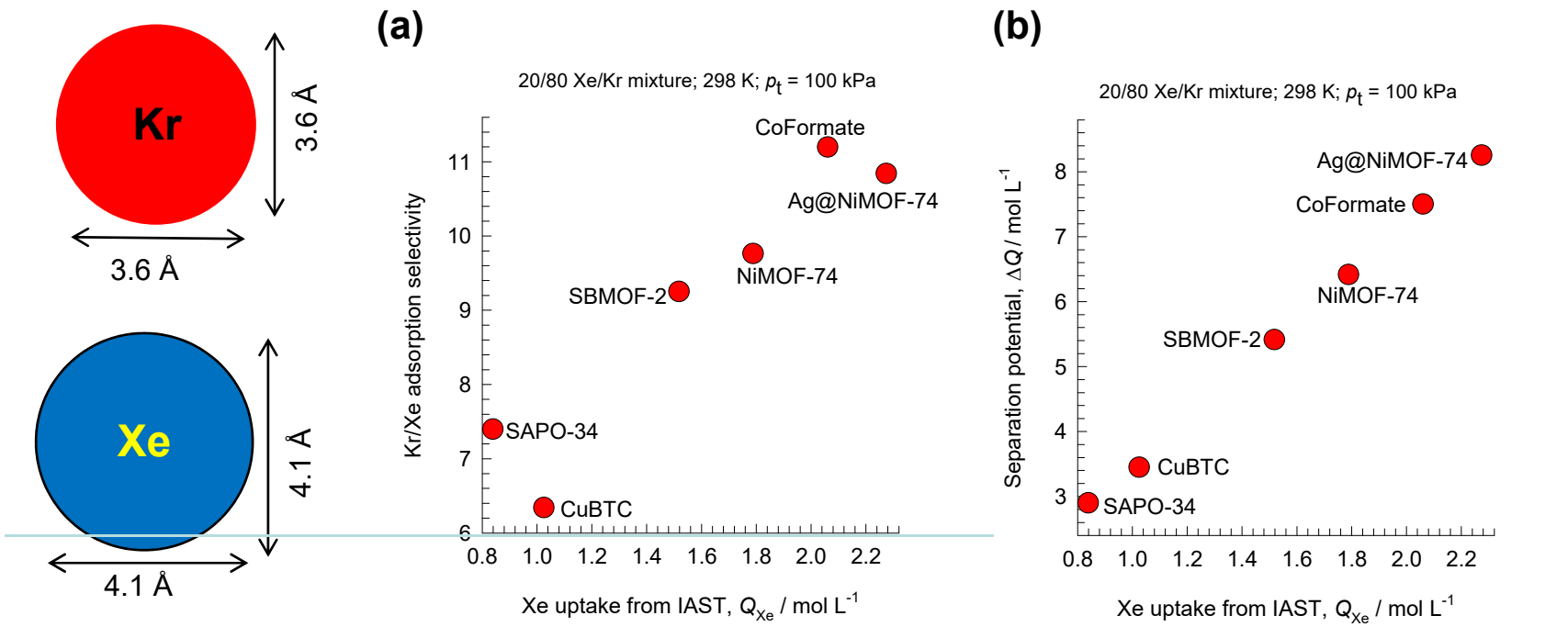

Figure S68

# Xe/Kr separations in fixed bed with CoFormate

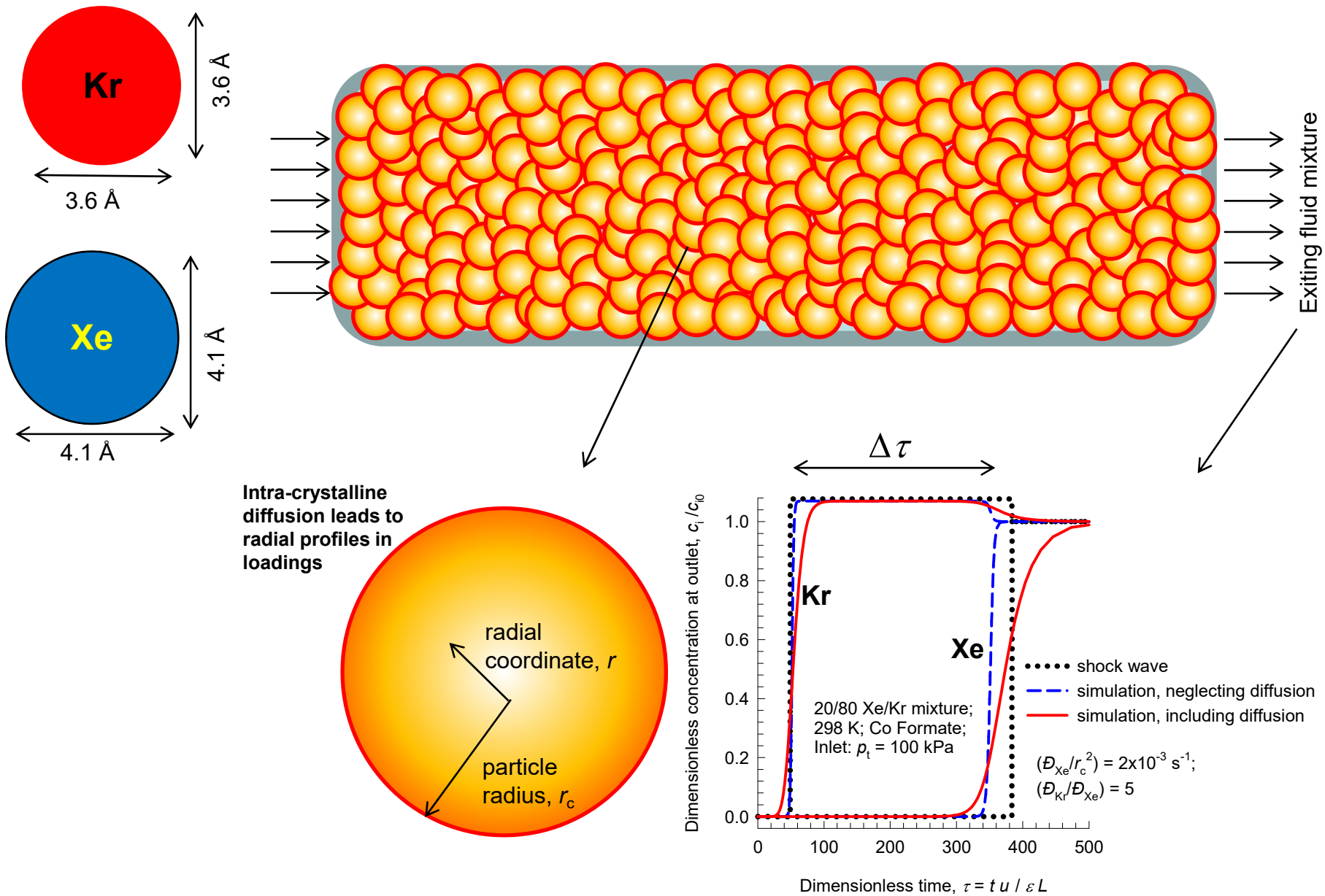

# Transient nC5/2MB breakthrough in fixed bed adsorber with ZIF-8
# Influence of intra-particle diffusion

Figure S69

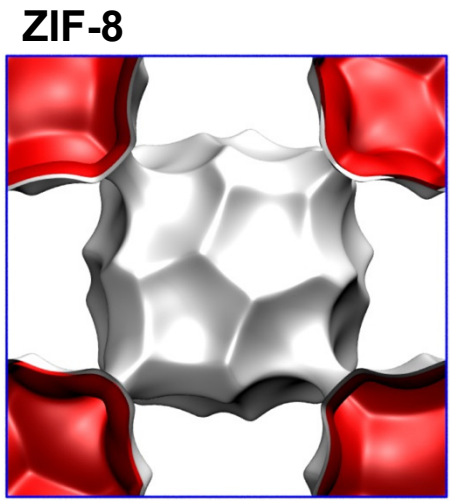


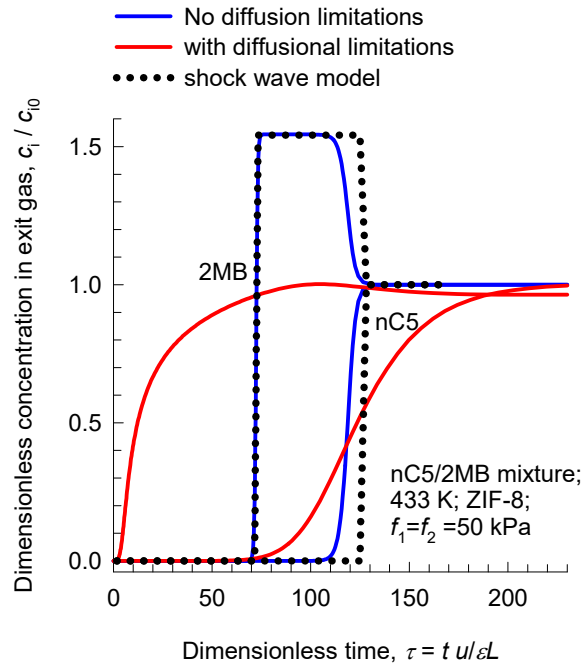

Figure S70

# Conventional hexane isomerization process

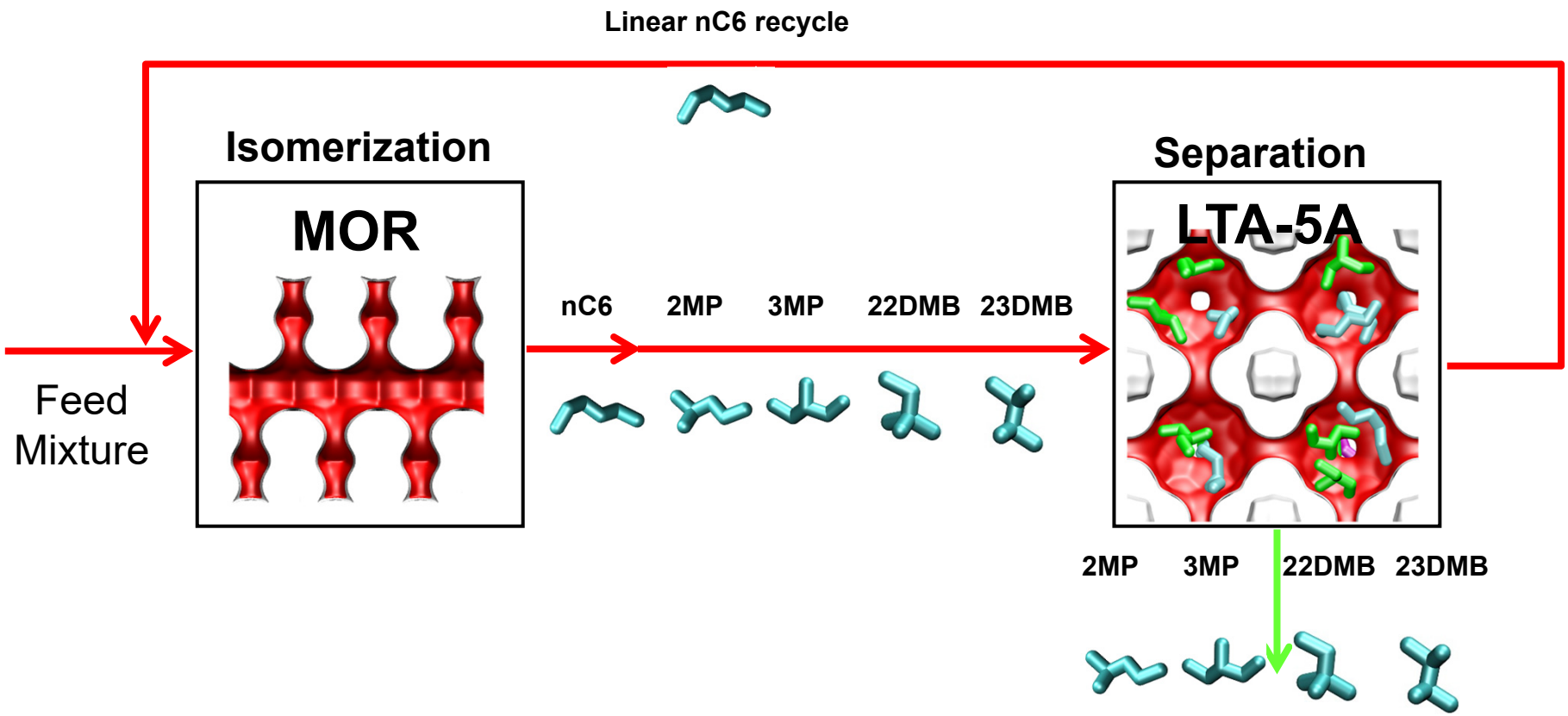

Figure S71

# Conventional hexane isomerization process

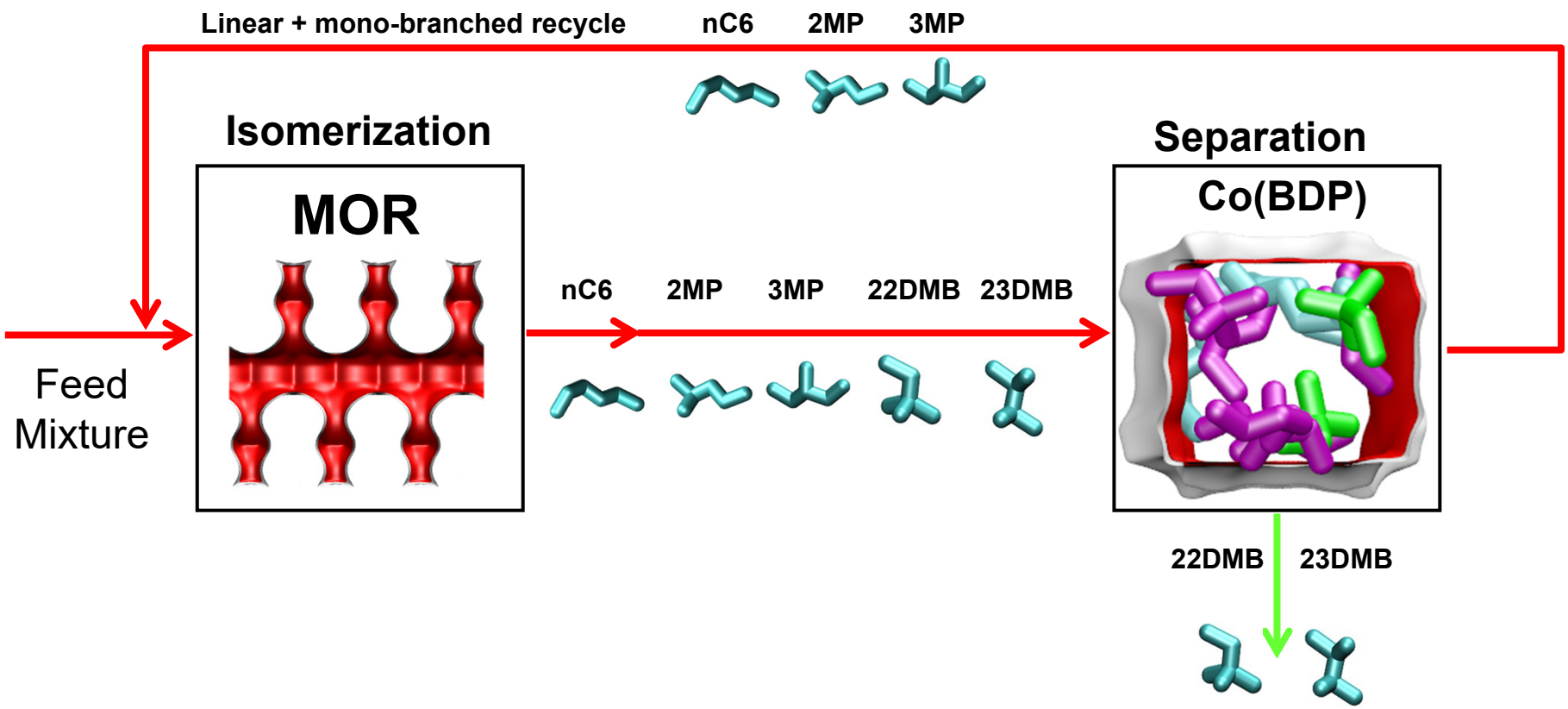

Figure S72

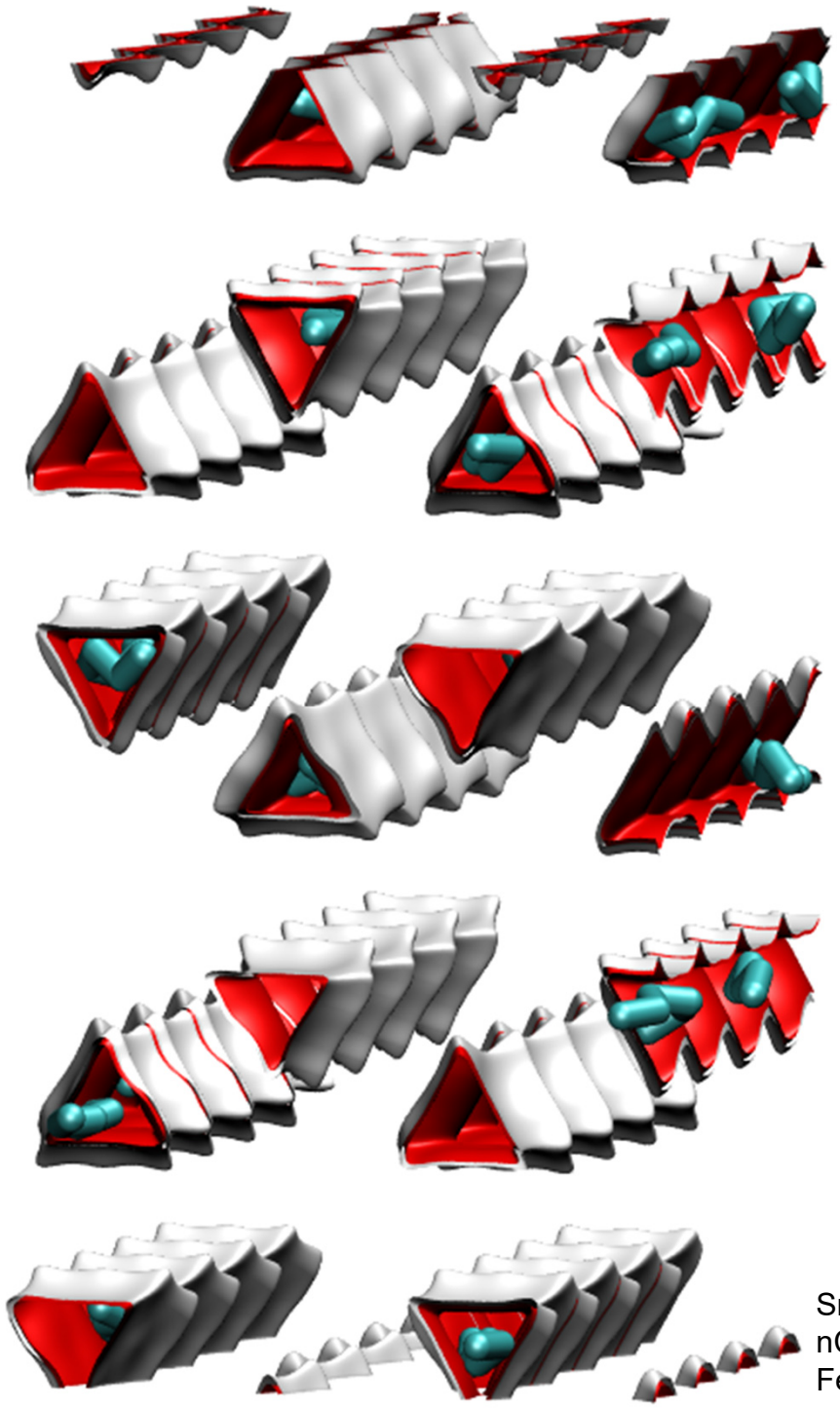

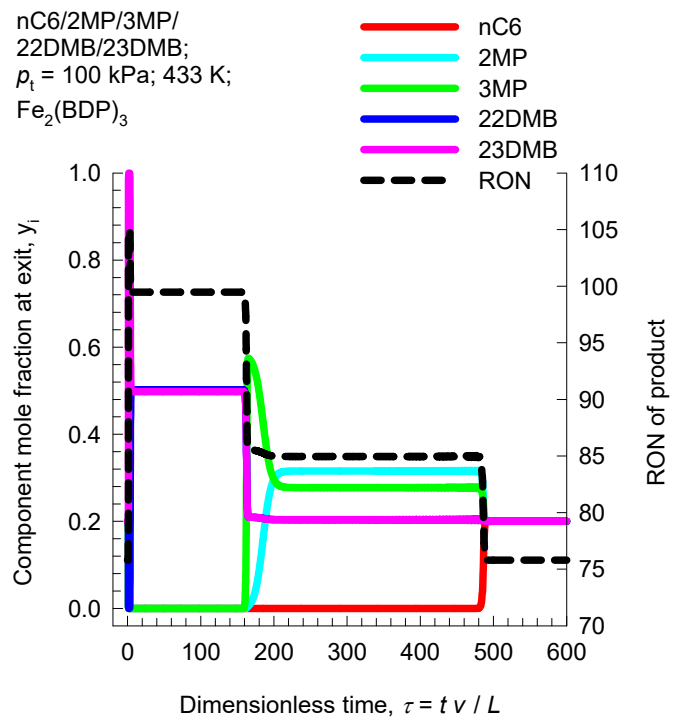


Snapshots showing the location of nC6 within the triangular channels of $Fe_2(BDP)_3$.

Figure S73

# Hexane isomers breakthrough in ZIF-77

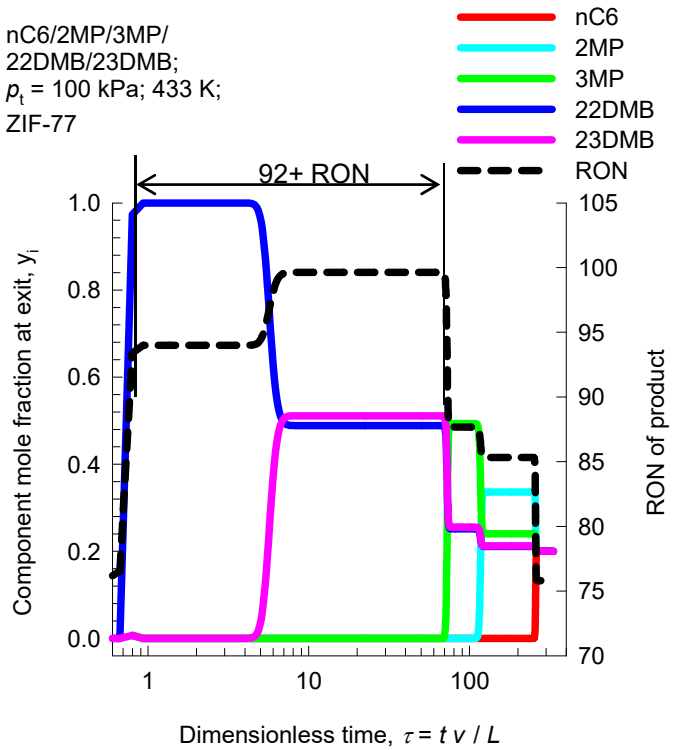


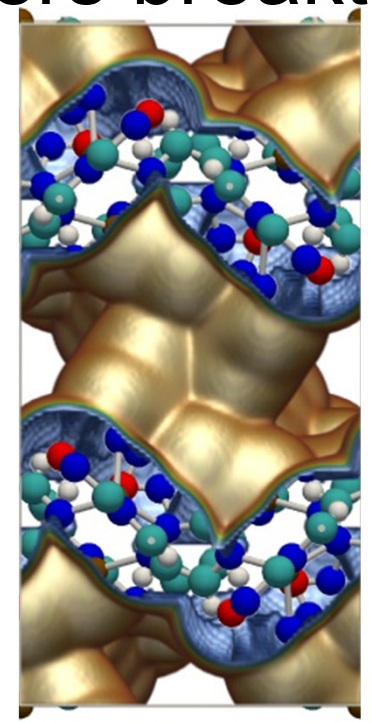

Pore landscape of ZIF-77

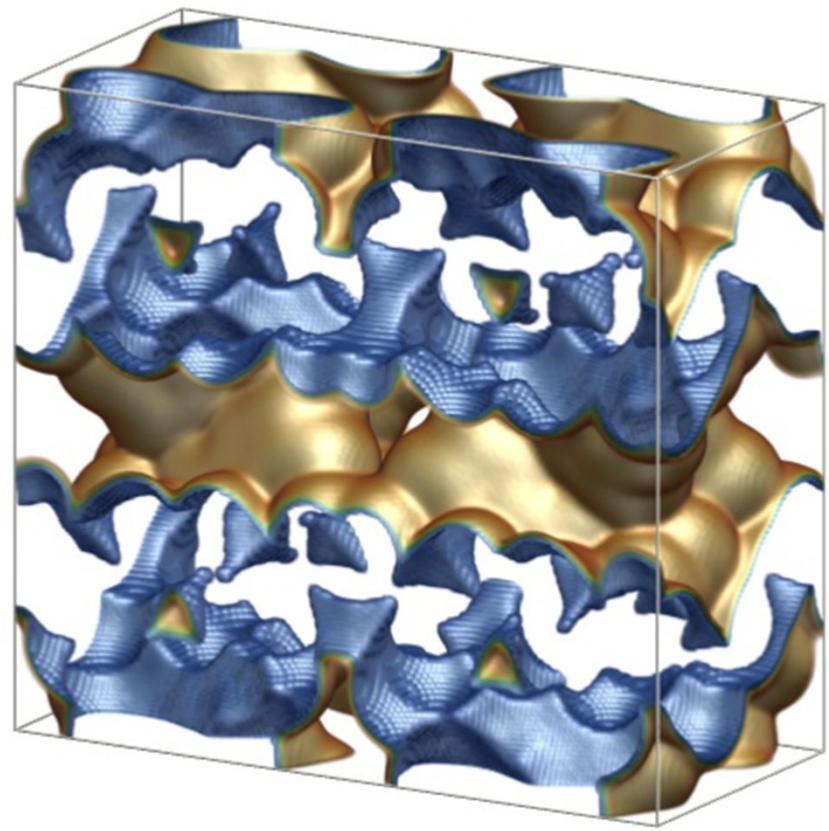

Figure S74

# Hexane isomers breakthrough in MFI

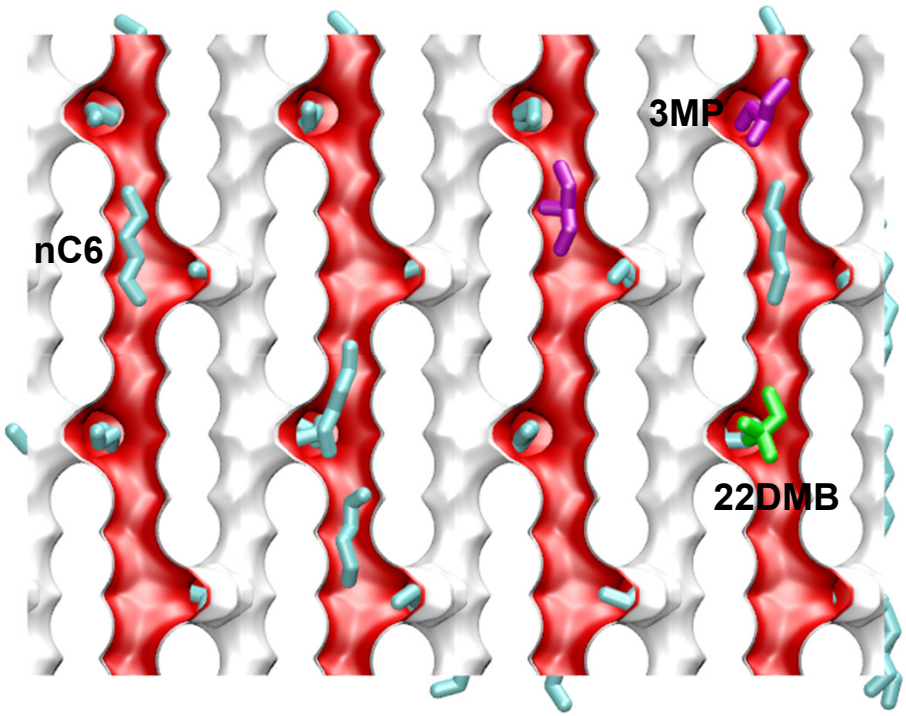


Snapshots showing the location of nC6, 3MP, and 22DMB within the intersecting channels of MFI.

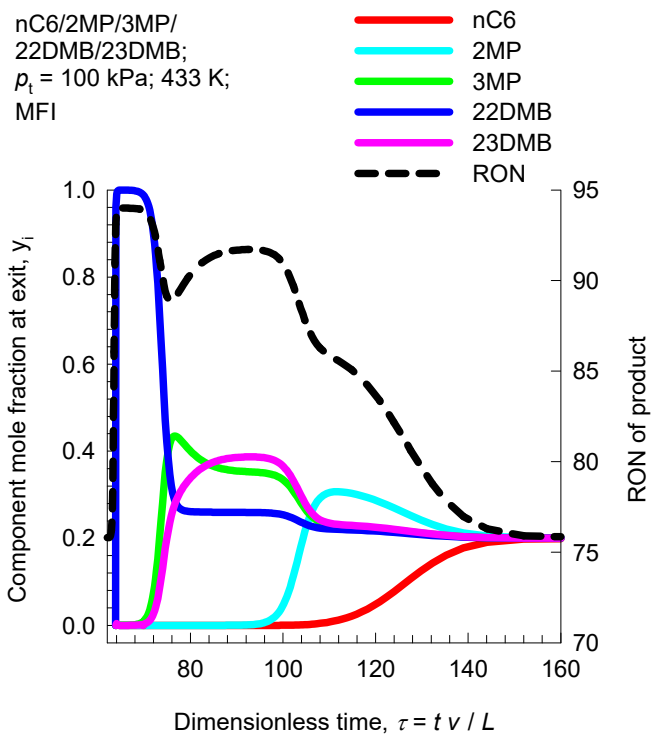

# Breakthrough simulations for Co(BDP)

Figure S75

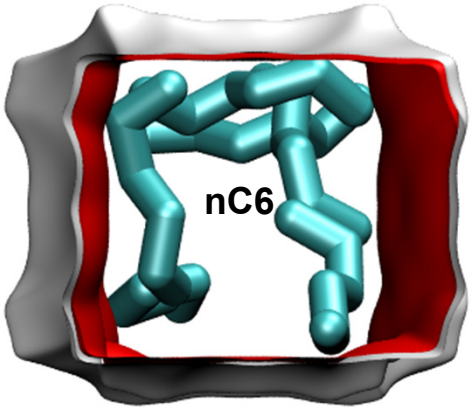


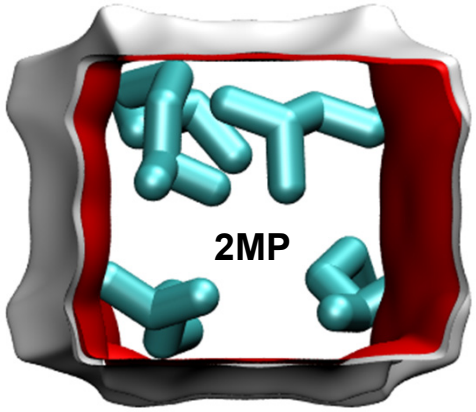


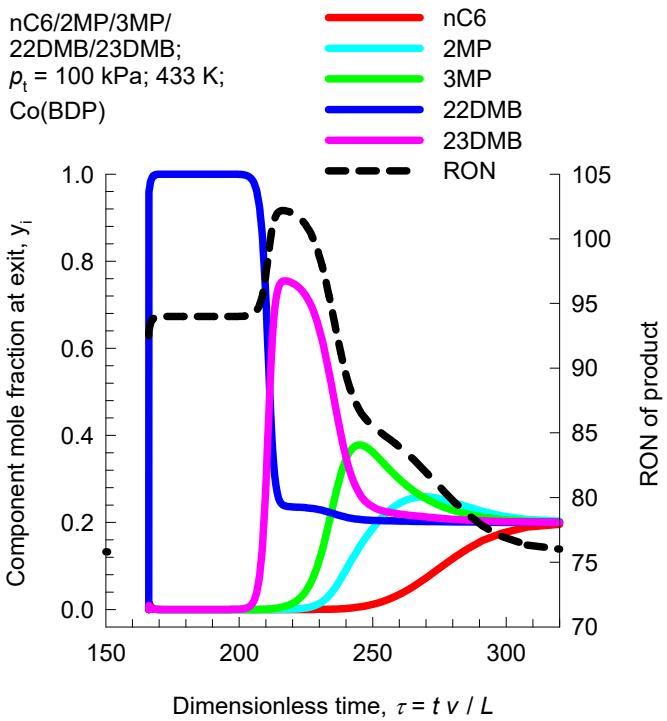


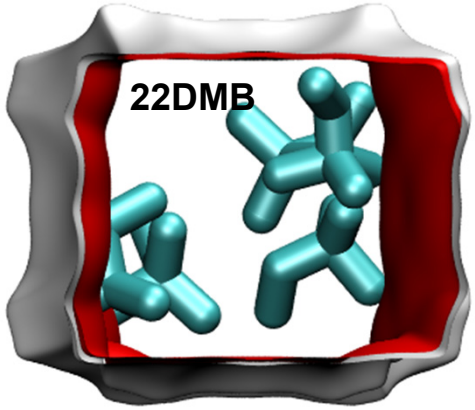

# Breakthrough simulations for MgMOF-74

Figure S76

**nC6**

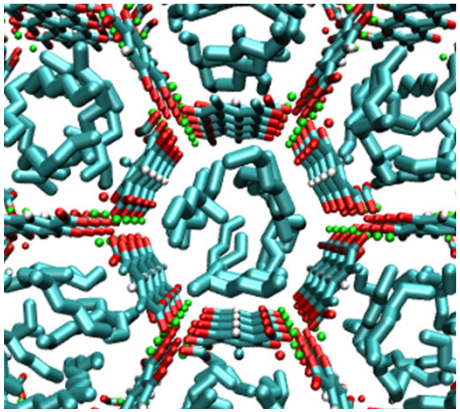

**2MP**

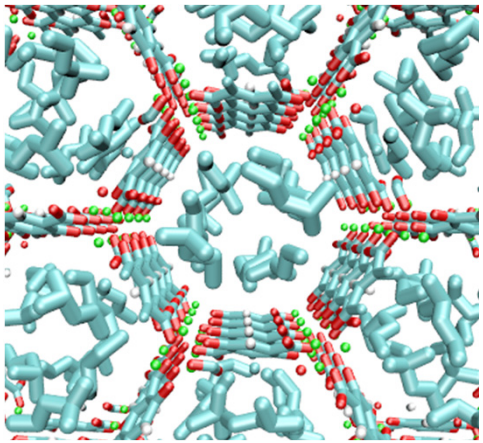

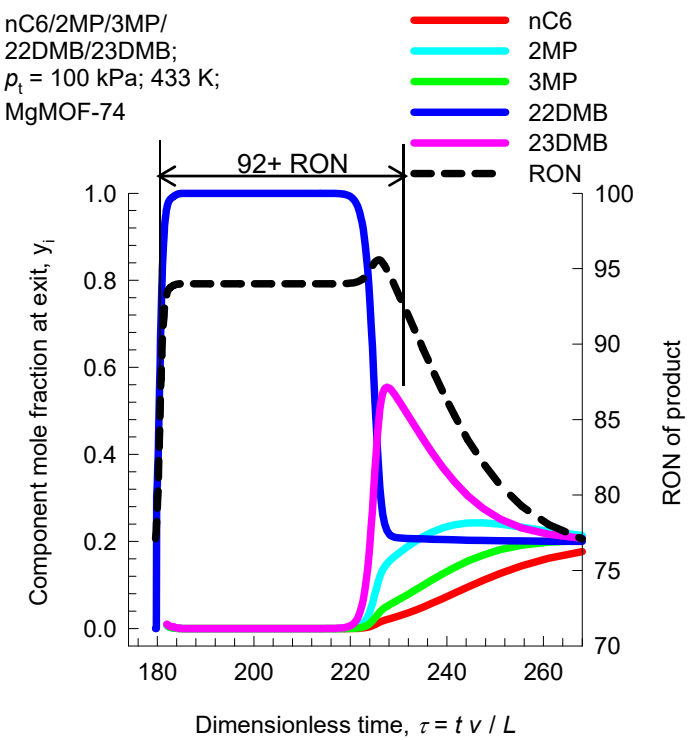


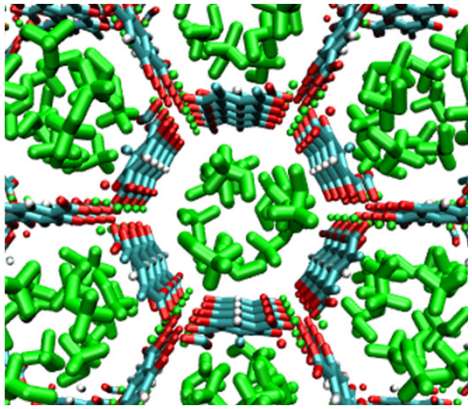

**22DMB**

# Breakthrough simulations for ZnMOF-74

Figure S77

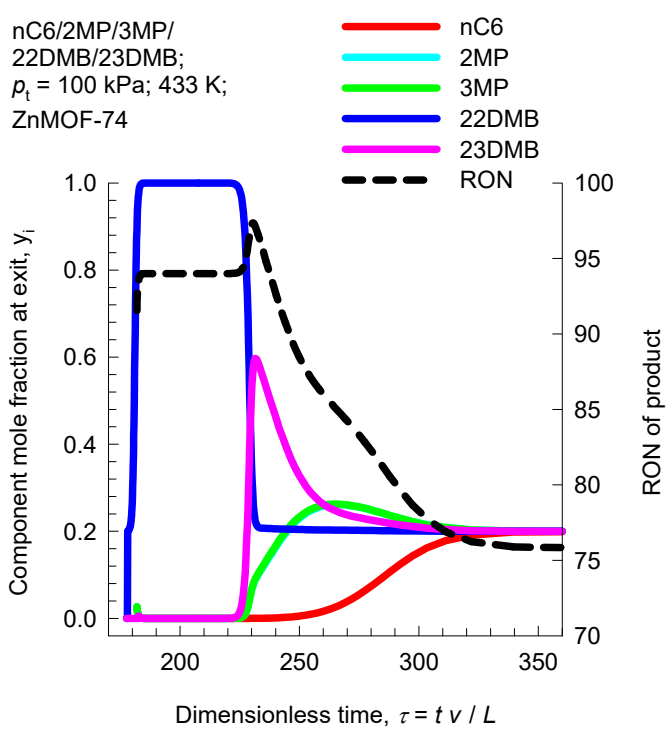


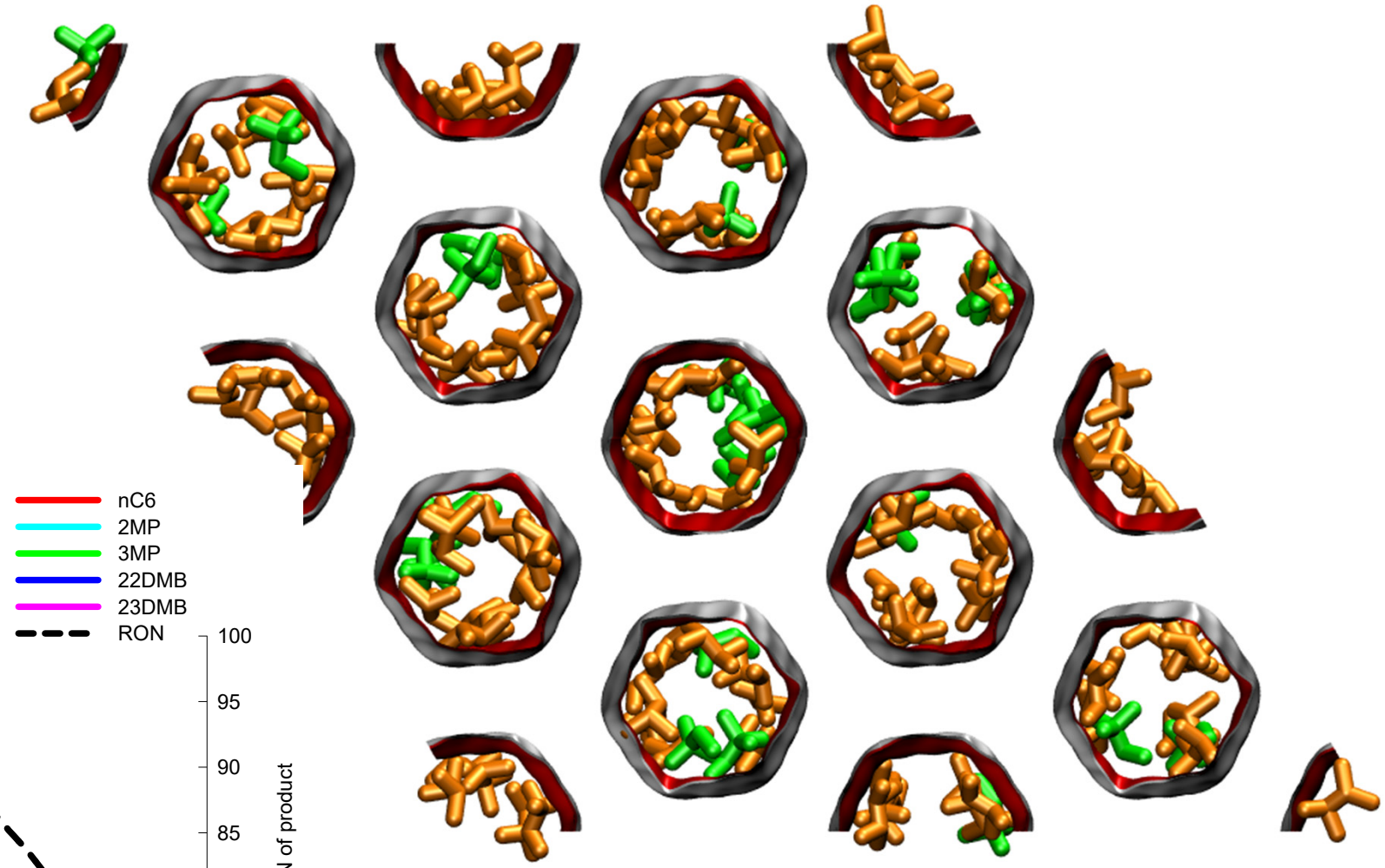

# Breakthrough simulations for ZIF-8

Figure S78

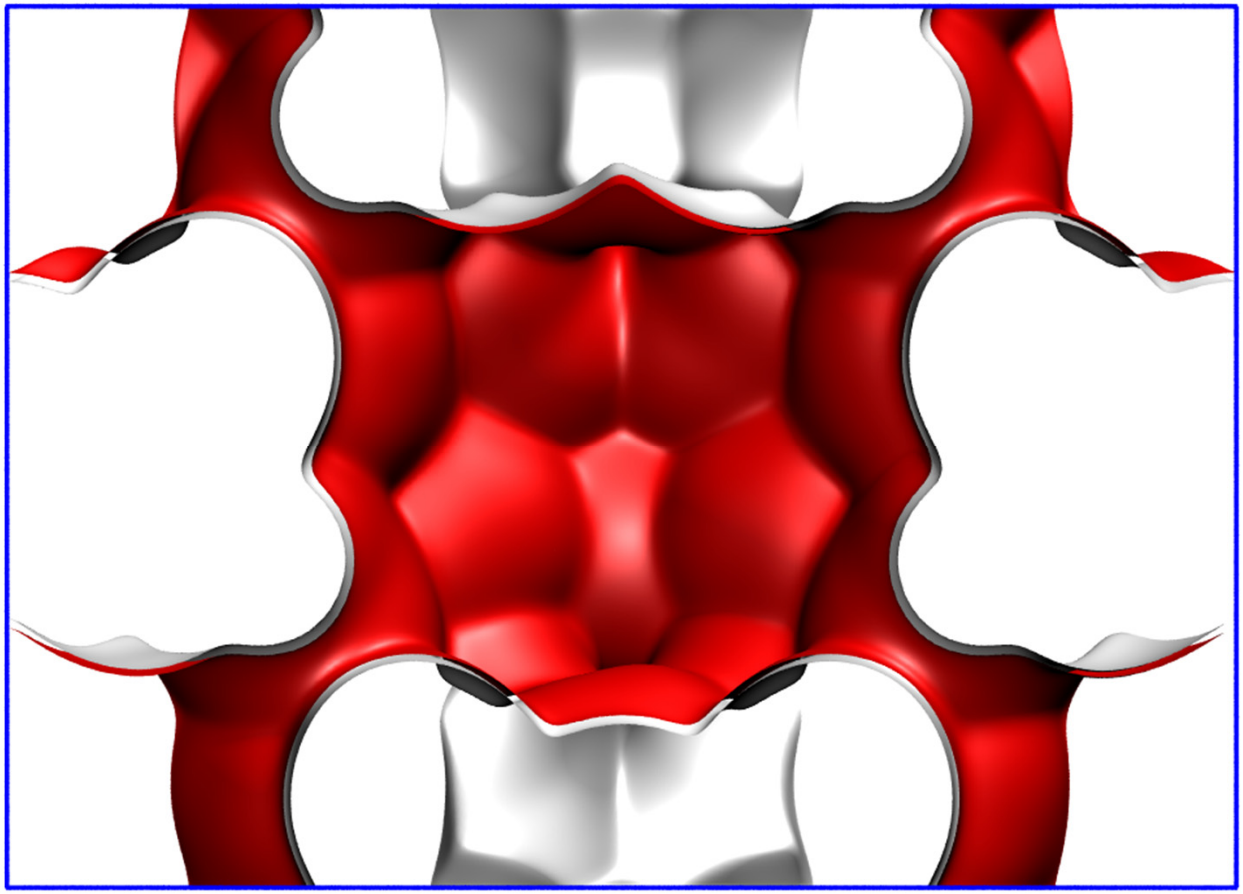

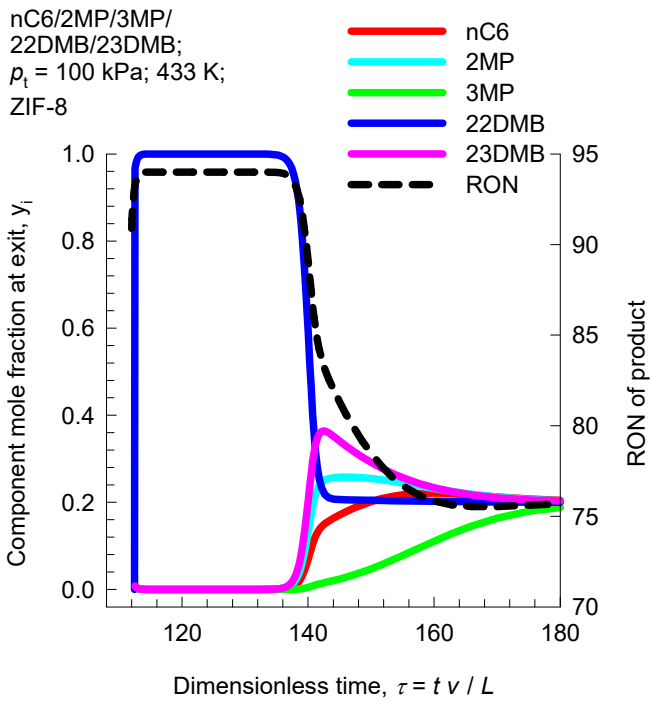

Figure S79

# Breakthrough simulations for BEA

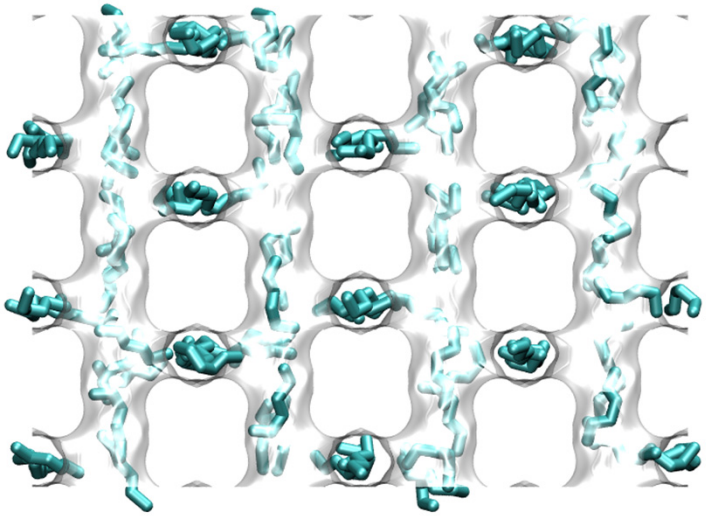

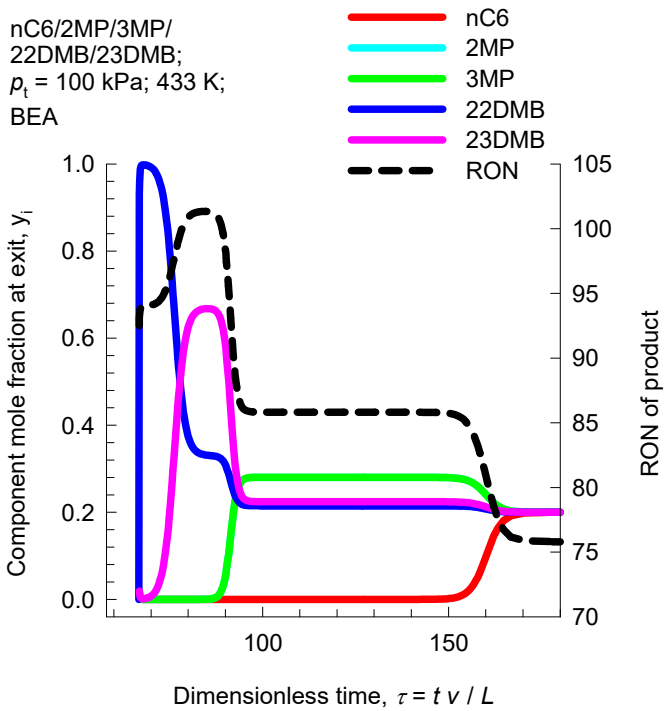


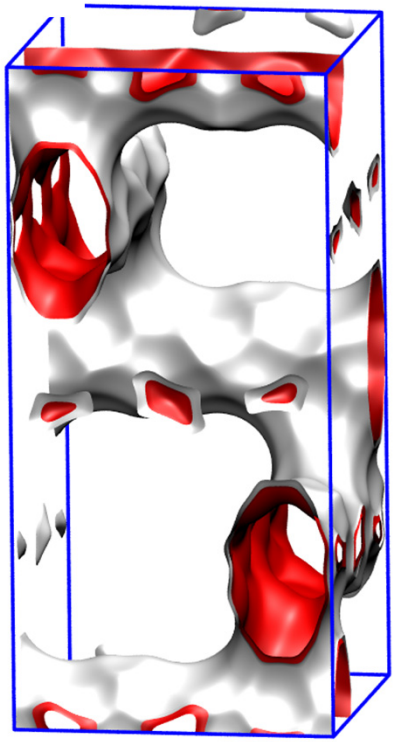

Figure S80

# Breakthrough simulations for ZnHBDC

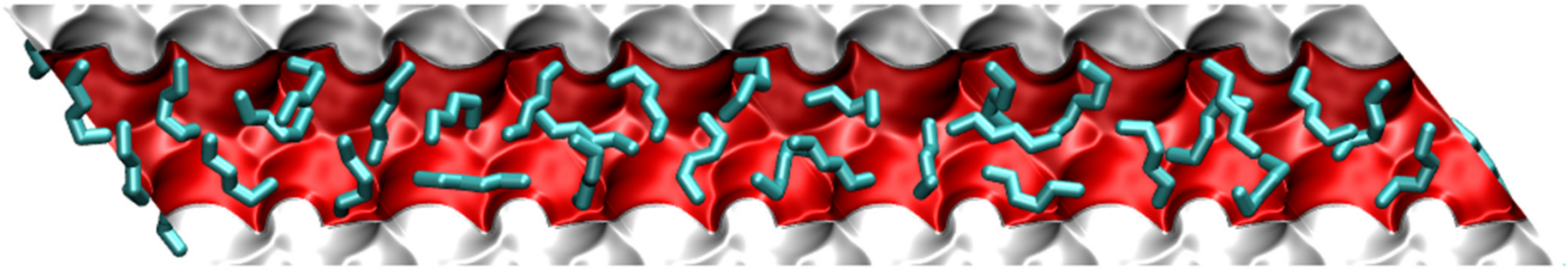

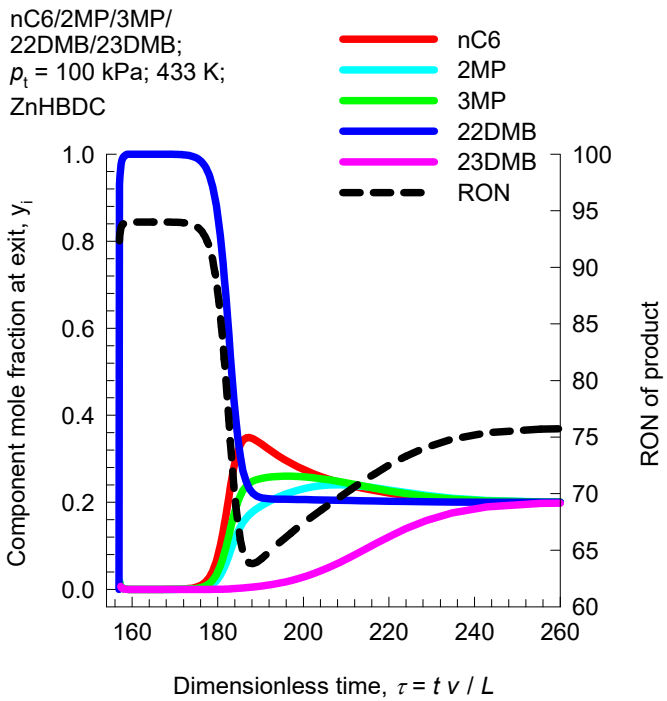


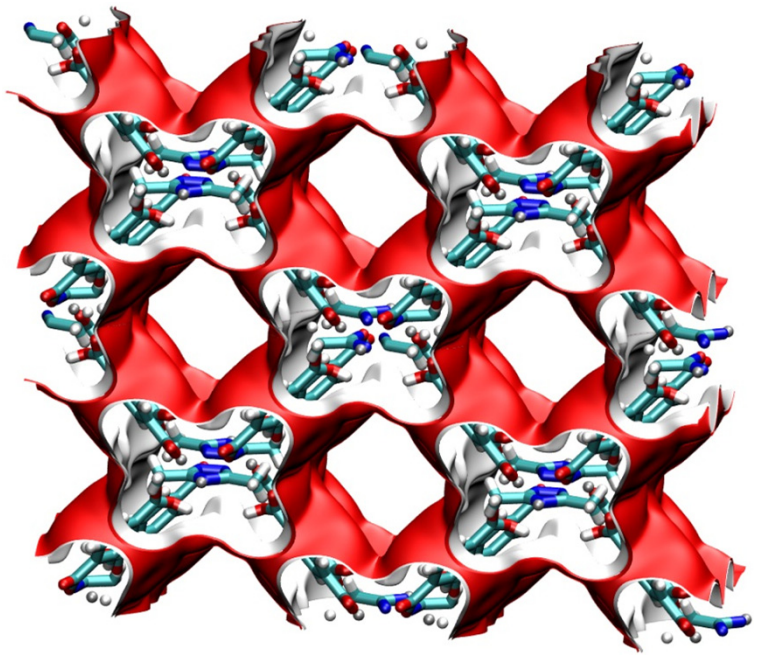

Figure S81

# Breakthrough simulations for Zn(bdc)dabco

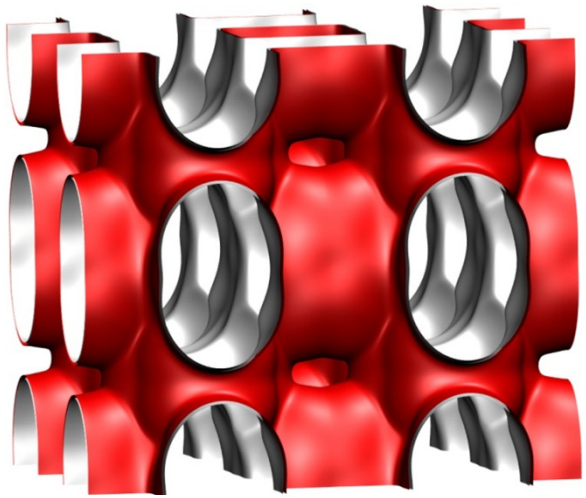

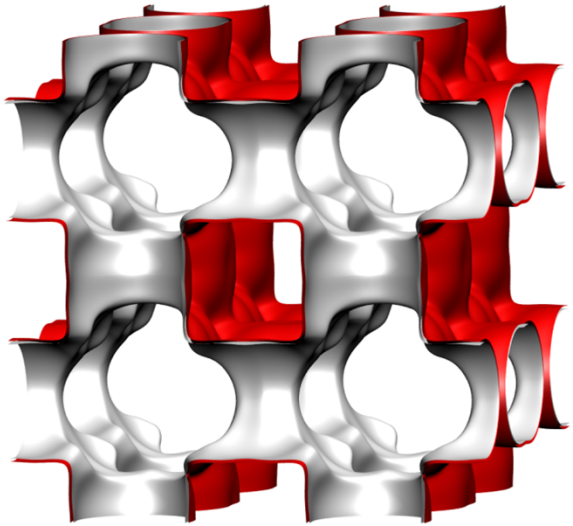

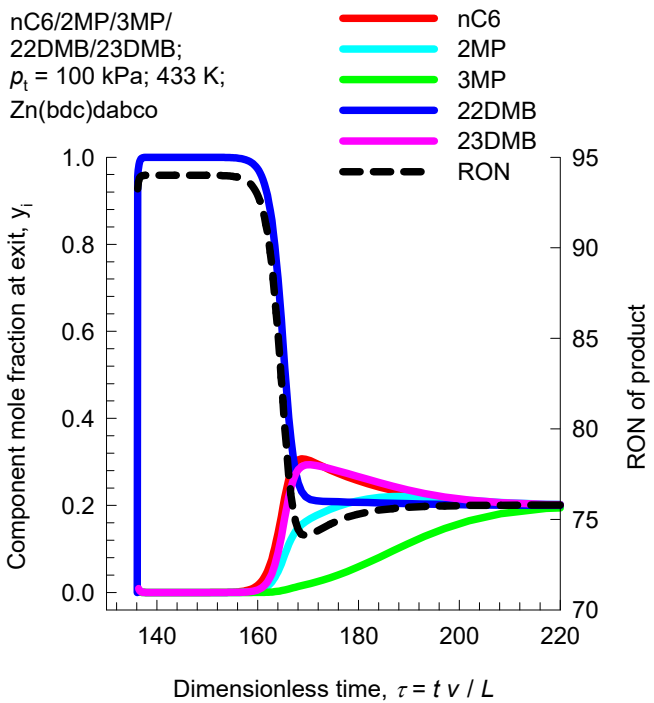

Figure S82

# Screening MOFs for hexanes isomer separation

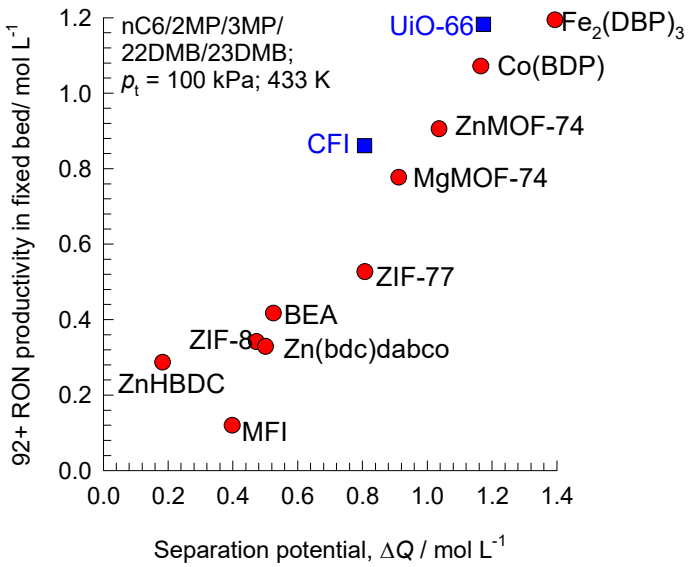


The blue symbols materials that exhibit the reverse adsorption hierarchy

Figure S83

# Adsorption/desorption cycles for UiO-66

Equilibrium breakthrough simulations

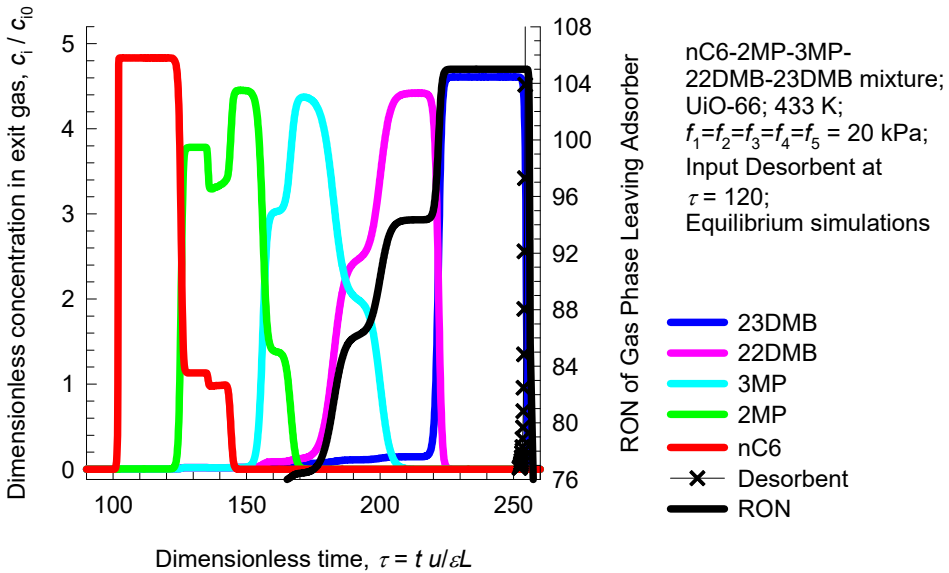


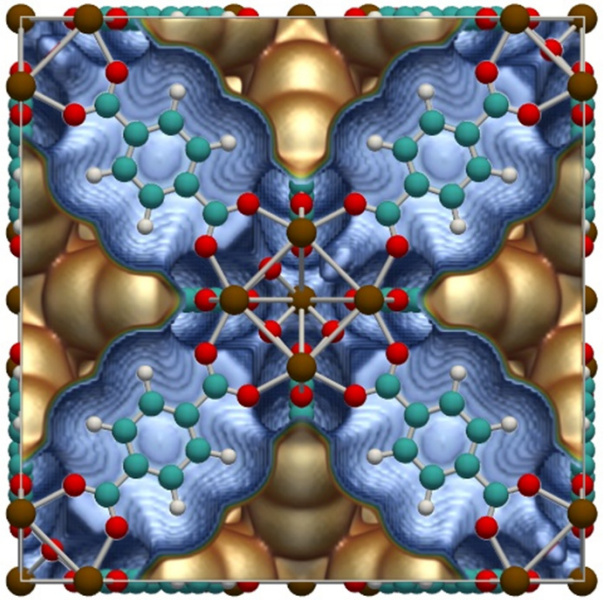

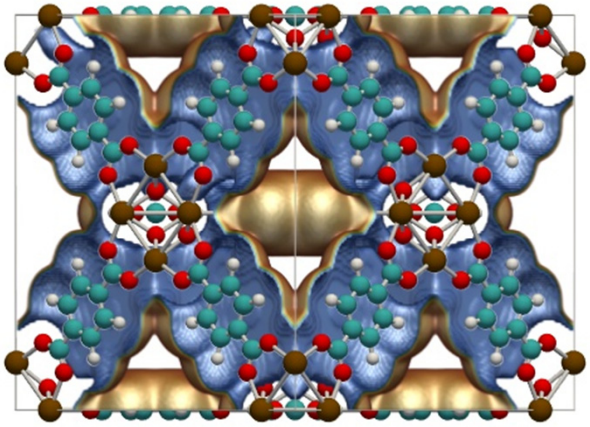

# Adsorption/desorption cycles for CFI

Figure S84

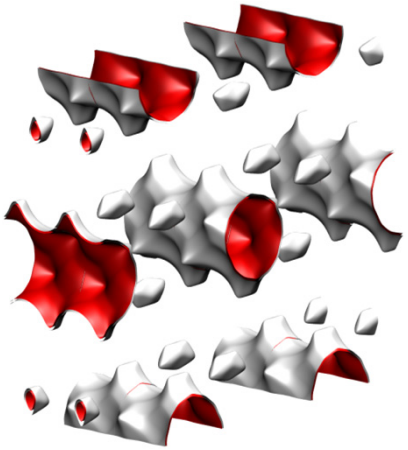

Length entropy effects cause the reverse adsorption hierarchy

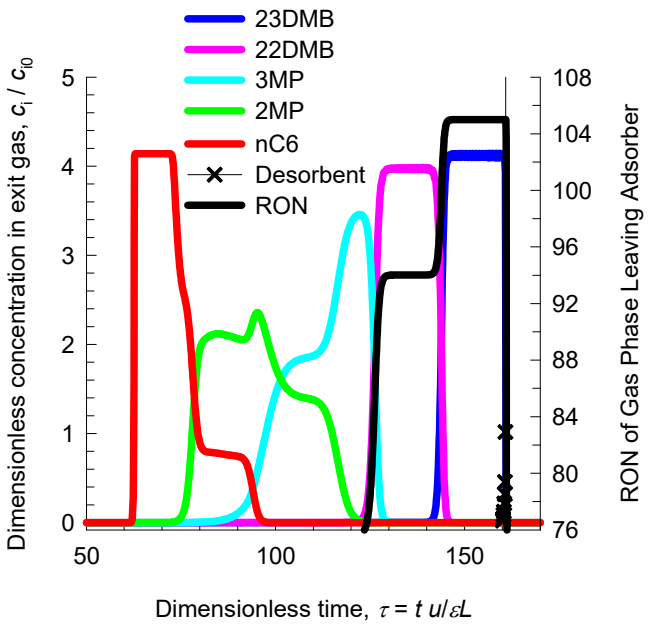


nC6-2MP-3MP-22DMB-23DMB mixture; CFI; 433 K; $f_1=f_2=f_3=f_4=f_5$ = 20 kPa; Input Desorbent at $\tau$ = 70; Equilibrium simulations

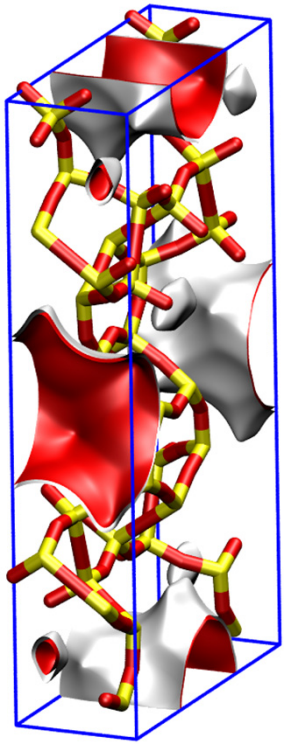

Figure S85

# Separations in the Petrochemicals Industry

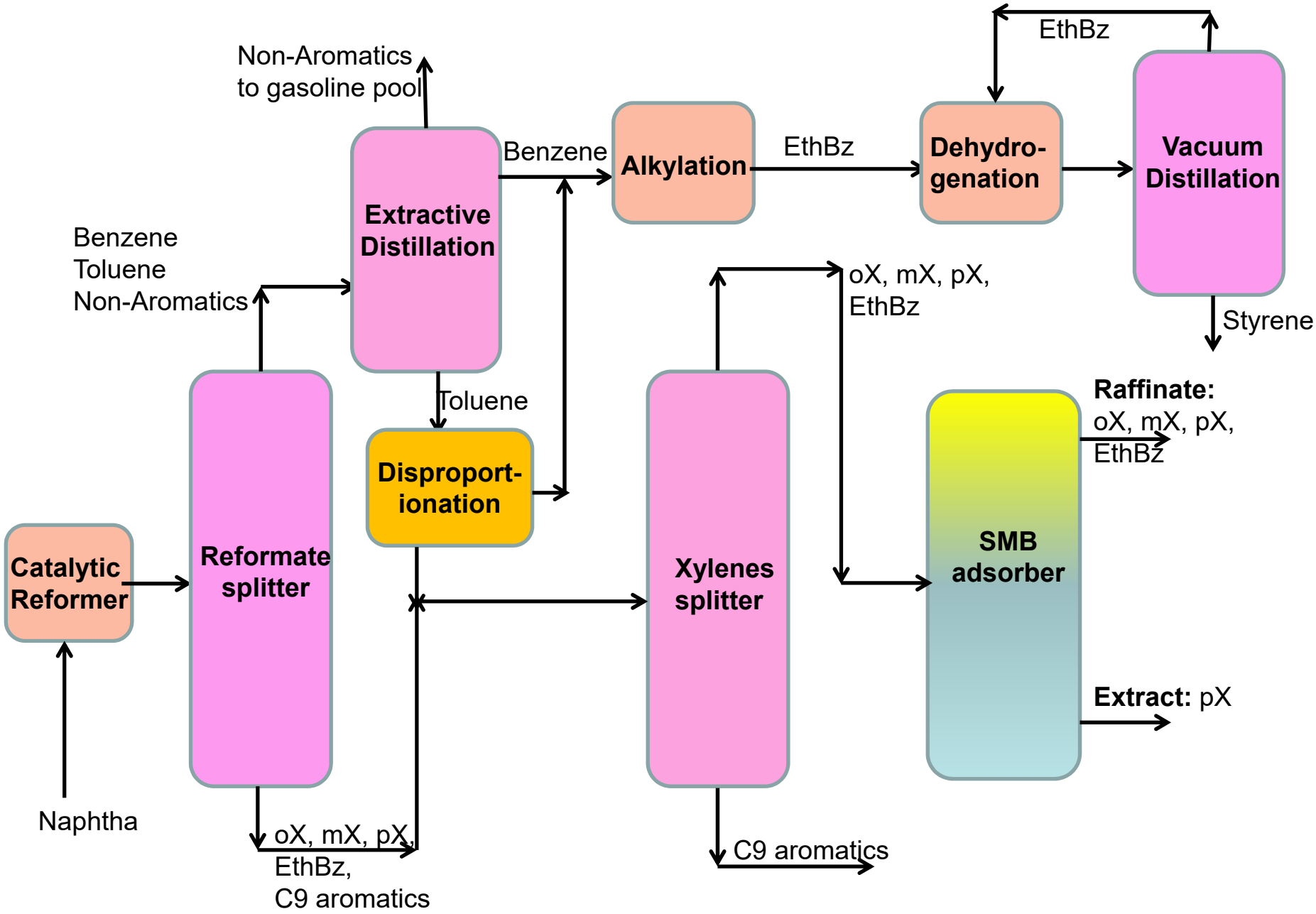

Figure S86

# Boiling point and freezing points of aromatics

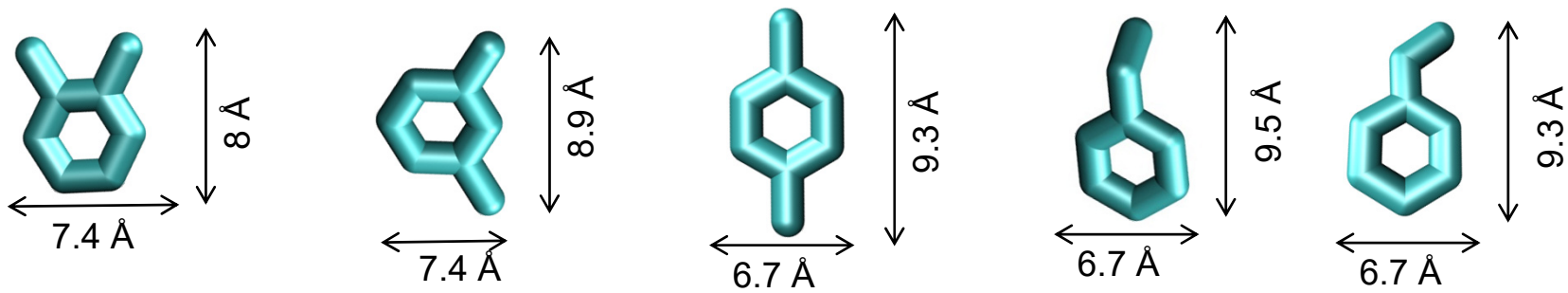


| | o-xylene (oX) | m-xylene (mX) | p-xylene (pX) | Ethylbenzene (EtBz) | Styrene (St) |
|---|---|---|---|---|---|
| **Boiling point** | 417.6 K | 412.3 K | 411.5 K | 409 K | 418.3 K |
| **Freezing point** | 248 K | 222 K | 286 K | 178 K | 242.5 K |

Highest freezing point; first crystals to form because it stacks best.

Figure S87

# SMB with BaX zeolite

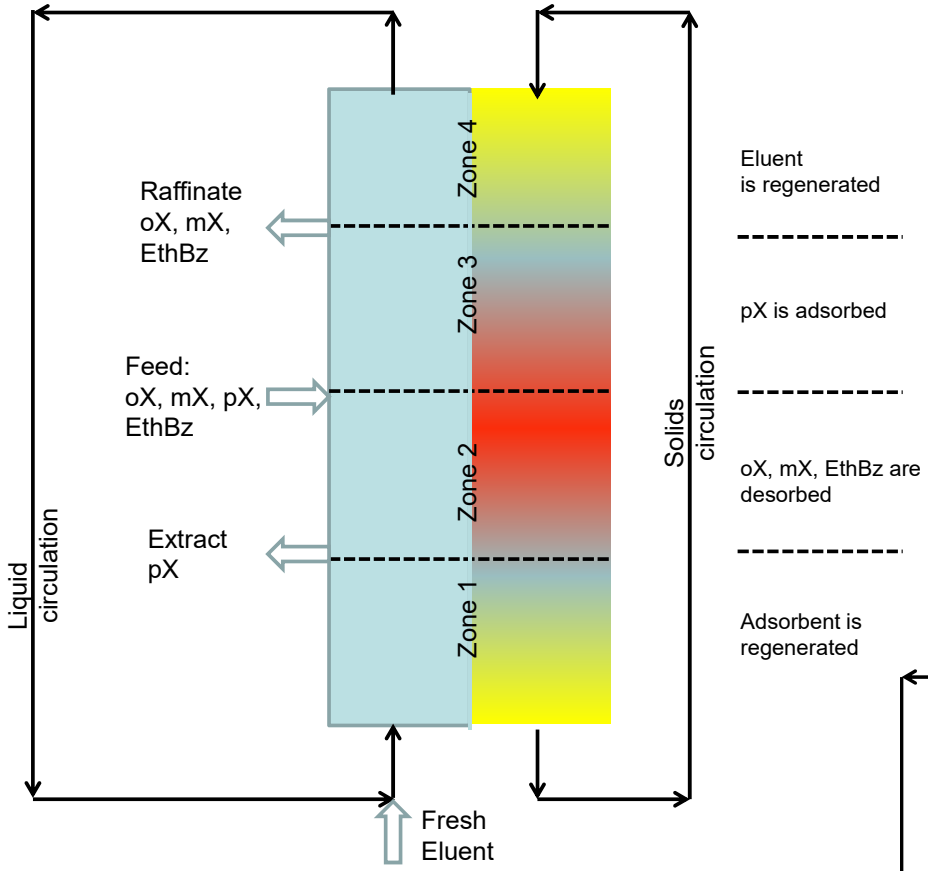


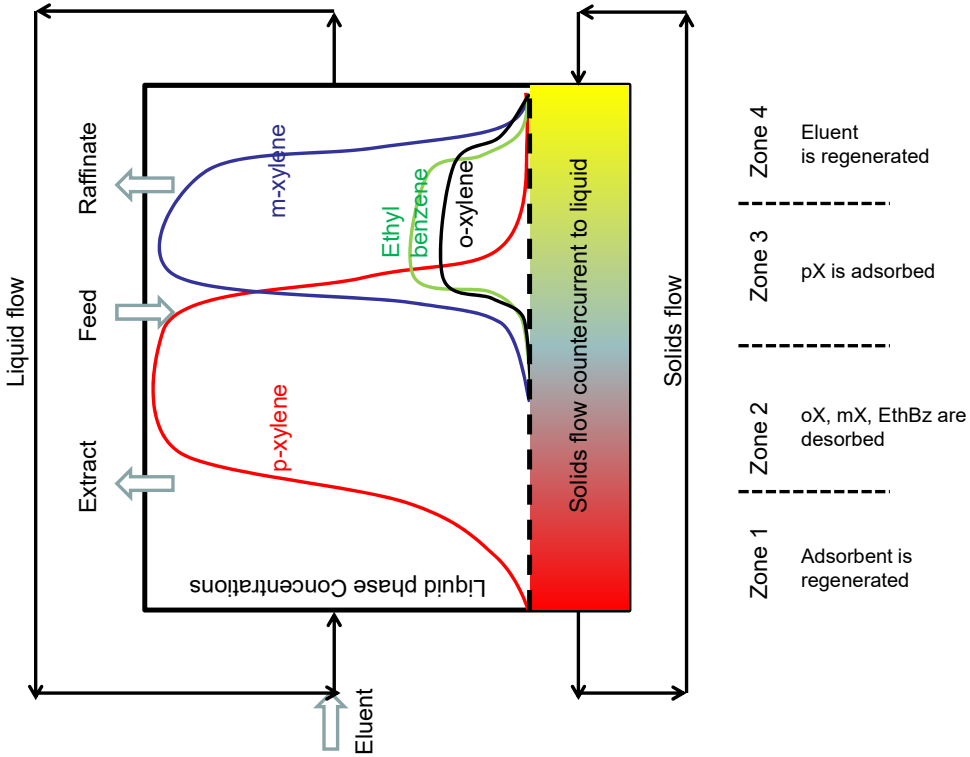

Figure S88

**(a) Stacking o-xylene in MIL-47**

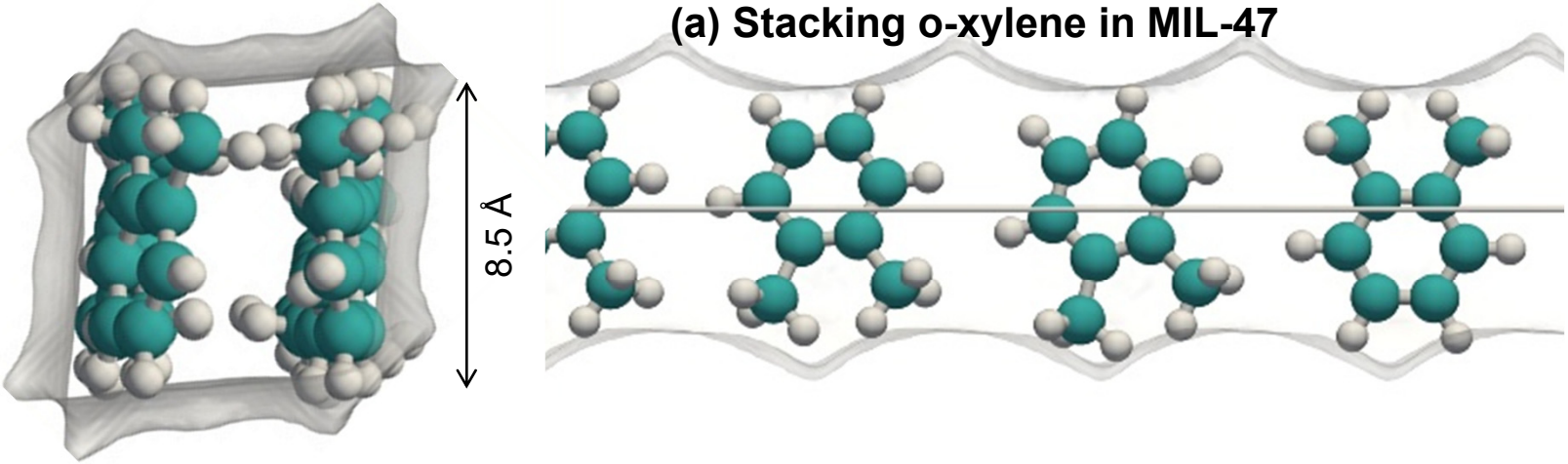


**(b) p-xylene stacking MAF-X8**

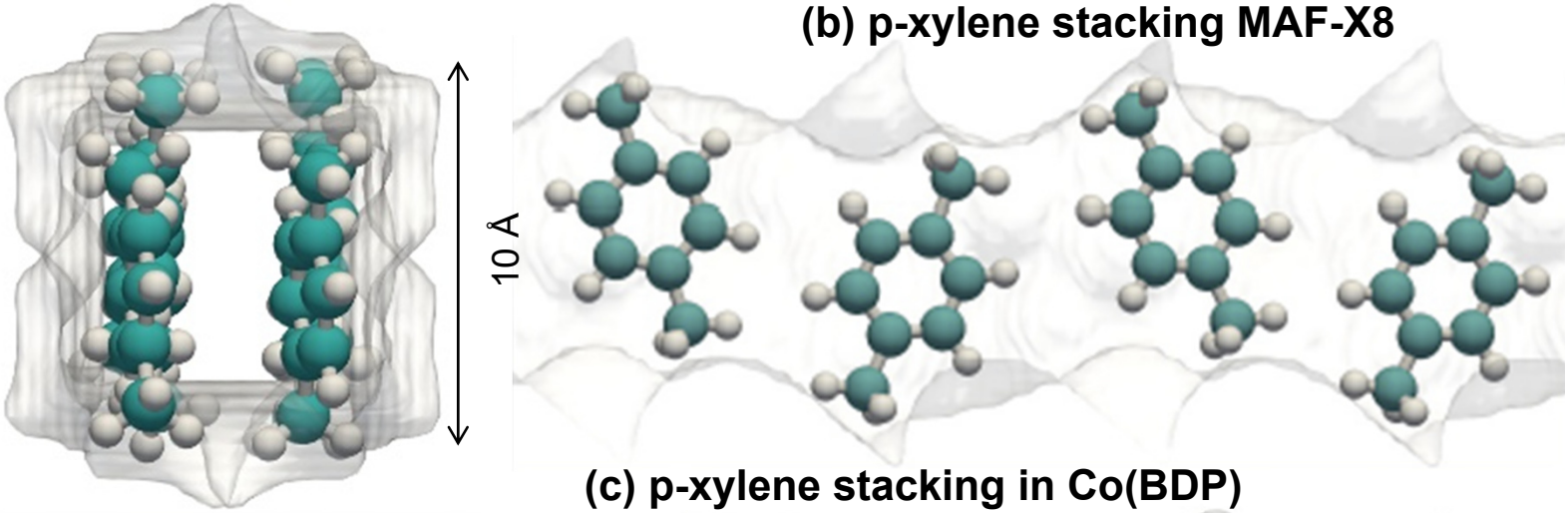


**(c) p-xylene stacking in Co(BDP)**

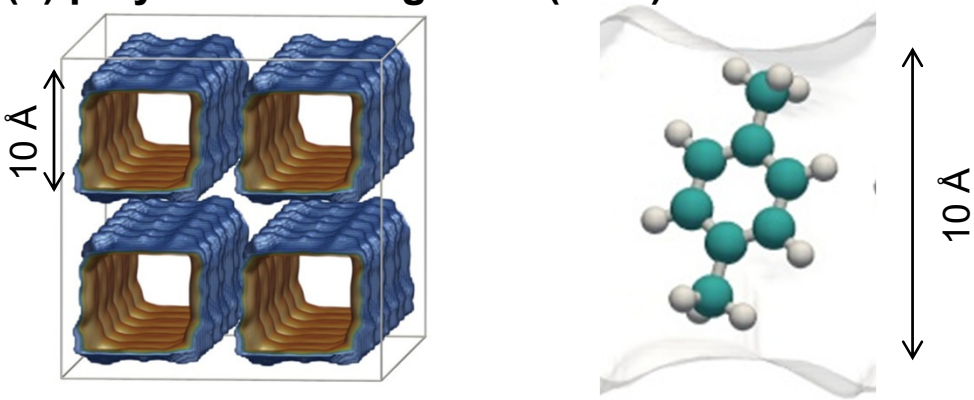

Figure S89

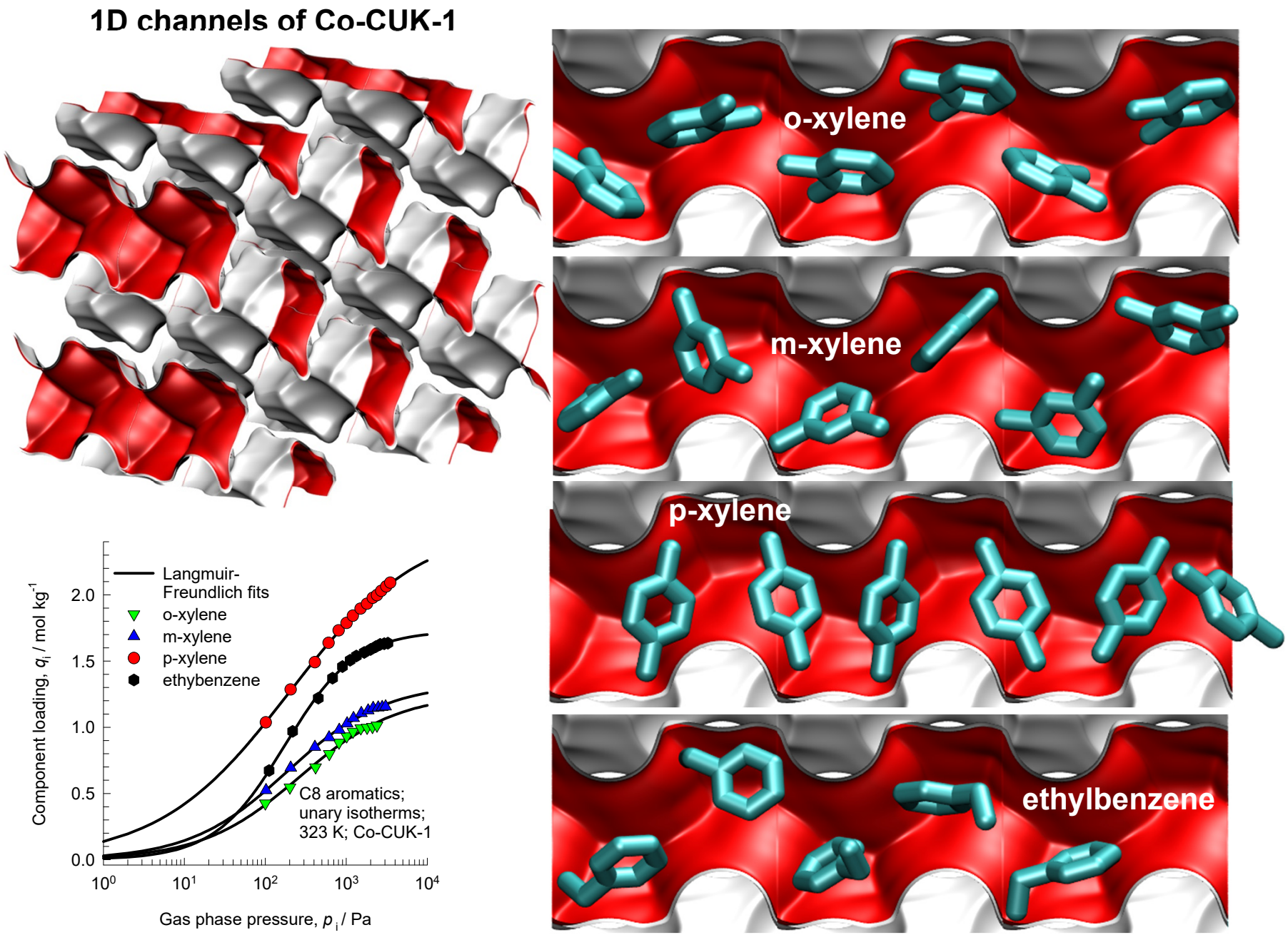
1D channels of Co-CUK-1
o-xylene
m-xylene
p-xylene
ethylbenzene
Langmuir-Freundlich fits
o-xylene
m-xylene
p-xylene
ethybenzene
C8 aromatics; unary isotherms; 323 K; Co-CUK-1
Component loading, $q_i$ / mol kg$^{-1}$
Gas phase pressure, $p_i$ / Pa
0.0
0.5
1.0
1.5
2.0
$10^0$
$10^1$
$10^2$
$10^3$
$10^4$

# Separating Xylene isomers

Figure S90

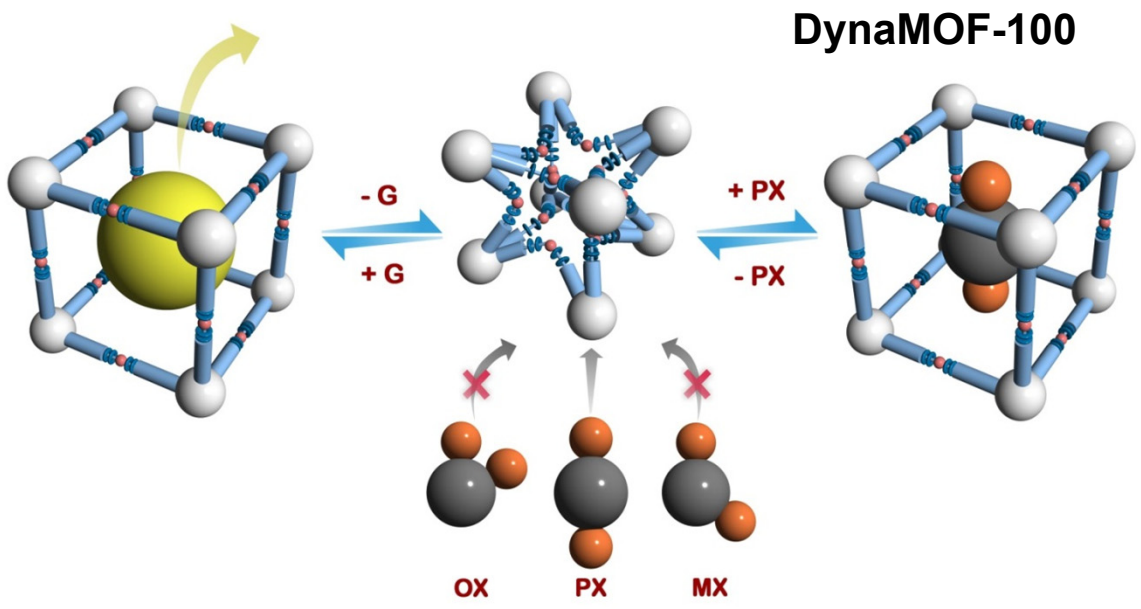

# Screening MOFs for Xylenes Separation

Figure S91

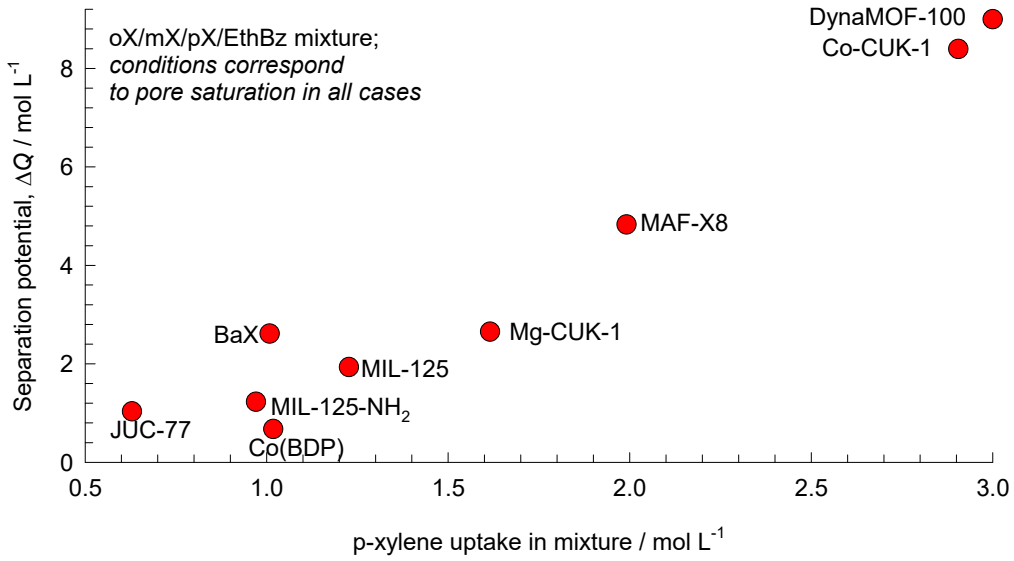

# Separating Ethylbenzene/Styrene

Figure S92

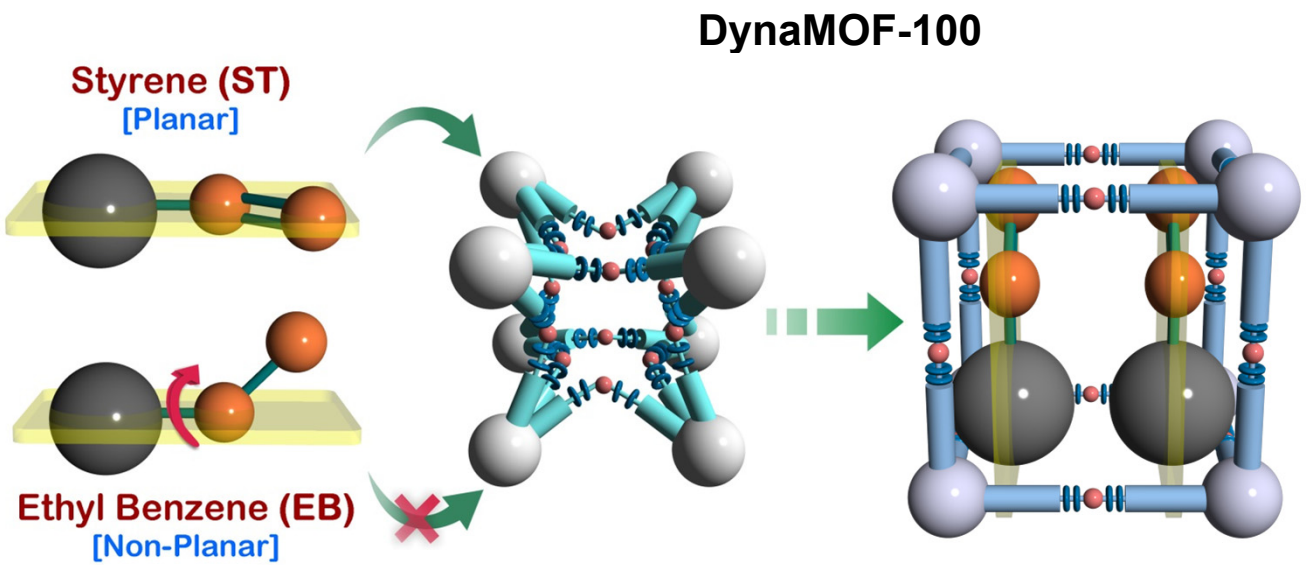

# Screening MOFs for Ethylbenzene/Styrene

Figure S93

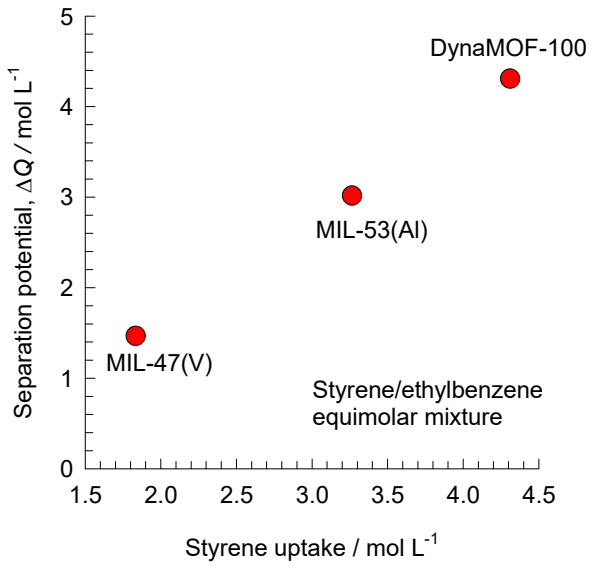

Figure S94

# Benzene/Cylcohexane separations

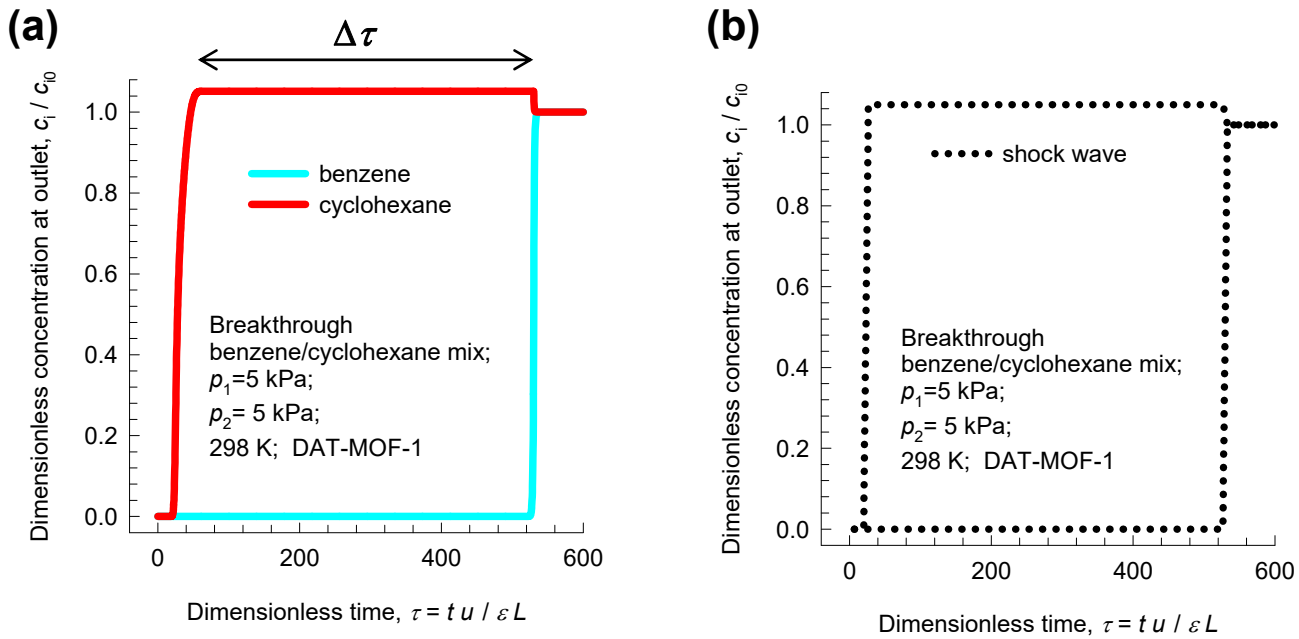

Figure S95

# Benzene/Cylcohexane separations